

UC Berkeley

UC Berkeley Electronic Theses and Dissertations

Title

Microscale devices for quantitative characterizations of human biology

Permalink

<https://escholarship.org/uc/item/04c203pg>

Author

Jeeawoody, Shaheen

Publication Date

2019

Peer reviewed|Thesis/dissertation

Microscale devices for quantitative characterizations of human biology

by

Shaheen Jeeawoody

A dissertation submitted in partial satisfaction of the

requirements for the degree of

Joint Doctor of Philosophy
with University of California, San Francisco

in

Bioengineering

in the

Graduate Division

of the

University of California, Berkeley

Committee in charge:

Professor Amy E. Herr, Chair
Professor Bo Huang
Professor Markita P. Landry

Fall 2019

Microscale devices for quantitative characterizations of human biology

Copyright 2019
By
Shaheen Jeeawoody

Abstract

Microscale devices for quantitative characterizations of human biology

by

Shaheen Jeeawoody

Joint Doctor of Philosophy

With University of California, San Francisco in Bioengineering

University of California, Berkeley

Professor Amy E. Herr, Chair

To understand the function and dysfunction of cells in biological organisms, it is important to characterize one of the key functional actors of the cell, proteins. With indications of poor correlation between mRNA expression and proteomic expression at the single cell level, *in vitro* assays directly quantifying protein expression, in both the spatial and temporal context, are needed. To span the extensive cellular heterogeneity in gene and protein expression and activity observed in cells and tissues, proteomic assays should interrogate single- and low-cell resolution with sufficiently high throughput to identify cellular sub-populations. These proteomic assays would also require sufficiently high selectivity and analytical sensitivity with which to interrogate protein isoforms and post-translational modifications. To address this measurement gap, we introduce and further develop proteomic assays towards these specifications.

We enhanced the analytical sensitivity of the ultrathin isoelectric focusing assay (IEF) with subsequent immunoblot, by developing a highly-porous hydrogel matrix as a new substrate for the assay. We characterized the effect of this 10-fold increase in gel porosity on the IEF separation performance, paired with a reagent modification that directly impacts separation performance. Additionally, we assessed the benefits of the increased porosity on the in-gel immunoblot.

Furthermore, we investigated the compartmentalization of protein lysate from single cells within the microwells embedded in the hydrogel substrate in our proteomic assays. We characterized the height of the fluid film between multi-material interfaces. We used numerical modeling and experimental validation to assess the contribution of the fluid film to the diffusive losses that reduce analytical sensitivity in our assays.

We then re-imagined the ultrathin IEF assay for a 100-fold increase in throughput by developing 3D projection electrophoresis. We interrogated the IEF separation

performance of this proof-of-concept high-throughput IEF assay with several optimizations. We conclude this section of this dissertation with an in-depth discussion of the potential further developments for this platform, towards a high-sensitivity, high-throughput proteomic assay with multiplexing capabilities.

In a parallel line of inquiry in this dissertation, to further understand and characterize cellular functions at a larger scale, *in vitro* biological models mimicking human physiology are needed. Due to inter-species differences in ion channels, biological pathways, and pharmacokinetic properties, animal models do not faithfully predict human cardiotoxicity. Human *in vitro* tissue models, with similar three-dimensional microenvironments to those found in *in vitro* human organs, that are predictive of human drug responses would be a significant advancement for understanding, studying, and developing new drugs and strategies for treating diseases. To assess the measurement needs in this space, we surveyed the breadth of *in vitro* cardiac devices mimicking human cardiac physiology.

The lipid storage and processing within adipose tissue strongly affects drug concentrations *in vivo*, and adipose tissue interacts with other organs via paracrine signals and fatty acid release, affecting the safety profiles of a large number of drug-like molecules. To address this measurement gap, we developed a microfluidic device with adipose tissue. We used numerical modeling and an analytical model to characterize the convective and diffusive transport within the device. We confirmed the maintenance of adipose cell viability and growth, extracellular matrix deposition, and adipose tissue functionality over two weeks.

We anticipate that the developments of analytical proteomic assays and *in vitro* biological models discussed in this dissertation will support quantitative characterizations of human biology, leading towards future development of targeted clinical therapies for improved length and quality of life.

To my family and friends

Table of Contents

Table of Contents.....	ii
List of Figures	iv
List of Tables.....	vi
Acknowledgements.....	vii
Chapter 1 : Introduction.....	1
Measurement gap: high-selectivity, high-throughput low-cell and single-cell proteomic assays	1
Measurement gap: <i>in vitro</i> biological tissue models mimicking human physiology.....	2
Dissertation overview.....	2
Chapter 2 : Ultrathin Isoelectric Focusing Performance Using Different Ampholyte Solutions	4
2.1 Introduction.....	4
2.2 Materials and Methods	5
2.3 Results and Discussion	7
2.4 Conclusions and Future Directions.....	12
Chapter 3 : Laterally Aggregated Polyacrylamide Gels for Immunoprobed Isoelectric Focusing	13
3.1 Introduction.....	13
3.2 Materials and Methods	14
3.3 Results and Discussion	19
3.4 Conclusions	31
Chapter 4 : Isoelectric Focusing Performance in Highly-Porous Polyacrylamide Gels Polymerized with Different Initiators.....	32
4.1 Introduction.....	32
4.2 Materials and Methods	32
4.3 Results and Discussion	37
4.4 Conclusions and Future Directions.....	46
Chapter 5 : Protein Diffusion from Microwells with Contrasting Hydrogel Domains	47
5.1 Introduction.....	47
5.2 Materials and Methods	49
5.3 Results and Discussion	52
5.4 Conclusions	63
Chapter 6 : Towards the Development of 3D Projection Electrophoresis for High-Throughput Single-Cell Isoelectric Focusing.....	64
6.1 Introduction.....	64
6.2 Materials and Methods	64
6.3 Results and Discussion	69
6.4 Conclusions and Future Directions.....	78
Chapter 7 : WAT-on-a-Chip: A Physiologically Relevant Microfluidic System Incorporating White Adipose Tissue	81

7.1 Introduction.....	81
7.2 Materials and Methods	82
7.3 Results and Discussion	87
7.4 Conclusions	94
Chapter 8 : <i>In Vitro</i> Cardiac Tissue Models: Current Status and Future Prospects	95
8.1 Introduction.....	95
8.2 Cell Sources for Cardiac Tissue Models.....	97
8.3 Cell Micropatterning for 2D Cardiomyocyte Alignment	99
8.4 Biomaterials Used to Generate 3D Cardiac Models	101
8.4.1 Natural Hydrogel-Based Cardiac Models.....	102
8.4.2 Synthetic Fibrous Cardiac Models	103
8.5 Microdevices for 3D Cardiac Models	105
8.6 Perspective and Conclusions.....	107
Chapter 9 : Conclusions and Future Directions.....	111
References.....	112
Appendices	129
Appendix 1 : Protocol: fabrication of porogen separation gels.....	129
Appendix 2 : Ultrathin IEF training bootcamp	133
Appendix 3 : Protocol: Ultrathin IEF assay with pI markers and tGFP protein (native lysis)	136
Appendix 4 : Protocol: Ultrathin scIEF assay with cells (native lysis).....	138
Appendix 5 : Protocol: Ultrathin scIEF assay with cells (denaturing lysis)	140
Appendix 6 : Protocol: slab IEF with purified protein ladder.....	142
Appendix 7 : Protocol: HTP scIEF fabrication of separation gels.....	148
Appendix 8 : Protocol: HTP scIEF fabrication of anolyte and catholyte gels.....	149
Appendix 9 : Protocol: HTP scIEF with purified protein ladder (native lysis).....	151
Appendix 10 : Protocol: desalted IEF cell lysate	154
Appendix 11 : MATLAB script for ultrathin IEF assay with pI markers and purified proteins.....	159
Appendix 12 : MATLAB script for ultrathin scIEF assay with cells	170
Appendix 13 : Characterization of background fluorescence in PA gels.....	175
Appendix 14 : Preliminary efforts towards the delivery of an IEF protein ladder via protein microparticles in the ultrathin IEF assay	178
Appendix 15 . Research eddies.....	180
Appendix 16 : Development of a lab cybersecurity SOP	182
Appendix 17 : Cell line authentication and mycoplasma testing certificates	187

List of Figures

Figure 2-1. Schematic of the ultrathin IEF assay.	8
Figure 2-2. Orthogonal view of the ultrathin IEF assay assembly on a widefield epifluorescence microscope.....	8
Figure 2-3. The SinuLyte® ampholytes demonstrated increased dpH/dx compared to the Polybuffer® ampholytes in the ultrathin IEF assay.....	9
Figure 2-4. Experimental assessment of the design space of the ultrathin IEF assay with SinuLyte® CA.	11
Figure 3-1. Generation of highly porous PA gels.	14
Figure 3-2. Gel weights measured in the equilibrium swelling ratio experiment.....	20
Figure 3-3. Characterization of highly porous PA gels.	21
Figure 3-4. Characteristic focusing of pI markers in PA gels over time.....	22
Figure 3-5. Electrical current during IEF.....	23
Figure 3-6. Cathodic drift during IEF in highly-porous PA gels.....	23
Figure 3-7. Highly porous PA gels are suitable for IEF.	25
Figure 3-8. Characteristic tGFP protein focusing in PA gels over time.	26
Figure 3-9. Characterization of photocapture efficiency in highly porous PA gels.....	27
Figure 3-10. Measurement of fluorescent intensity area-under-the-curve in photocapture efficiency measurements in PA gels.	28
Figure 3-11. Partition coefficient, K , is sensitive to PA gel formulation.	30
Figure 4-1. Swelling ratio in PA gels polymerized with different polymerization chemistries.....	39
Figure 4-2. Partitioning of IgG* in PA gels with different polymerization chemistries. ...	41
Figure 4-3. Gel microarchitecture is not disrupted by exposure to hydrogen-bond-disrupting detergents, indicating stable gel crosslinking.	42
Figure 4-4. IEF is disrupted in gels polymerized with the LAP photoinitiator, as characterized using pI markers.....	44
Figure 4-5. Electrical current during IEF in PA gels of different polymerization chemistries.....	45
Figure 4-6. IEF performance in gels of different polymerization chemistries using tGFP protein.....	45
Figure 5-1. The fluid film is created by capping the bottom gel with a lid layer.	53
Figure 5-2. In the absence of a fluid layer, numerical simulations indicate that the lid material determines the concentration distribution of the protein source material diffusing out of the microwell.....	55
Figure 5-3. Experimental validation of protein release from a spherical source located in a hydrogel microwell.	58
Figure 5-4. His-tagged protein release from Ni surface functionalized magnetic microparticles.....	59
Figure 5-5. Fluorescent bead tracking reveals advection introduced by lid gel placement.	60
Figure 5-6. The protein solute concentration in the microwell depends on H , K_{eq} , and D for GFP in various materials, as determined by numerical simulations.....	62
Figure 6-1. Experimental characterization of pI's of fluorescently-labeled proteins in IEF protein ladder.....	71

Figure 6-2. Waste products after 5 ultracentrifugation washes reveals an excess of unconjugated dye from the conjugation process.....	72
Figure 6-3. Schematic of high-throughput IEF platform using 3D projection electrophoresis.....	74
Figure 6-4. Rhinohide™ increases porosity of gels, without significant differences between Rhinohide™ lots.....	75
Figure 6-5. The filter paper hydration chamber is not required to maintain the hydration state of the separation gel after 60 s electrophoresis in the HTP IEF assay.....	75
Figure 6-6. The HTP IEF assay yields reproducible separations of the fluorescently-labeled IEF protein ladder at 60 s electrophoresis.....	77
Figure 7-1. Schematic concept of the WAT-on-a-chip.....	88
Figure 7-2. Fabrication of the multilayer PDMS–PET hybrid MPS.....	89
Figure 7-3. Characterization of transport processes inside the MPS.....	90
Figure 7-4. Physiologically relevant adipose tissue in the MPS.....	92
Figure 7-5. The MPS enables maintenance of viability and functionality of adipose tissue.....	93
Figure 8-1. Overview of <i>in vitro</i> cardiac tissue model.....	96
Figure 8-2. Micropatterned 2D cardiac models.....	101
Figure 8-3. Biomaterial-based 3D cardiac models.....	105
Figure 8-4. Microdevice-based 3D cardiac models.....	107
Figure 10-1. Increases in background and noise from standard PA gels were observed specifically from UV exposure of gels containing BPMA.....	177
Figure 10-2. High background and noise from the PA gel immunoblots were decreased several fold in the LAP-polymerized PA gels.....	177
Figure 10-3. Inverted fluorescence micrograph of Protein G indicates a disrupted pH gradient.....	180
Figure 10-4. Mask inadvertently damaged via exposure to high-intensity UV light.....	181
Figure 10-5. Visual characterization of the porosity of highly-porous PA gels.....	182

List of Tables

Table 2-1. Composition of IEF lid gels for the ampholyte study.	7
Table 3-1. Composition of PA porogen gels.....	16
Table 3-2. Composition of IEF lid gel.....	18
Table 4-1. Composition of polyacrylamide gels with different chemistries.	34
Table 4-2. Composition of IEF lid gel.....	37
Table 5-1. Partition and diffusion coefficient values for GFP in the range of layer materials characterized in this study.....	53
Table 6-1. Composition of HTP IEF anolyte and catholyte gels.....	68
Table 6-2. Proteins and fluorescence labels in the in-house-designed IEF protein ladder.	70
Table 6-3. The theoretical isoelectric points and molecular weights of several HER2 isoforms indicates the need for an IEF assay capable of separating proteins with a ΔpI_{\min} under 0.04. ^{4,161,162,164,165,182}	80
Table 8-1. Generation of cardiomyocytes from human pluripotent stem cells.....	98
Table 8-2. Analysis of <i>in vitro</i> cardiac tissue models and the corresponding mechanical, electrophysiological, and biological outcomes.	109
Table 10-1. Gel nomenclature for the brief study on gel background and noise.	176
Table 10-2. Conditions of gel exposure for the brief study on gel background and noise.	176
Table 10-3. Composition of IEF lid gel for the protein microparticle study.	179

Acknowledgements

If I had to sum up my years at UC Berkeley and UCSF in one sentence, this is what I would say: community is everything, and I am eternally grateful to mine.

Dr. Amy Herr is a phenomenal scientist and engineer and an inspirational role model. Her insistence on precise language, professionalism, and enthusiasm are all hallmarks of my graduate experience. From spending several hours before my qualifying exam reviewing slides with me on Skype, to leading intense research discussions during subgroup meetings, to surprising me with moments of sponsorship and grand opportunities, she is a dedicated mentor. I have learned from and appreciated every moment of my experience with Amy as my PhD advisor. Thank you, Amy.

I had the great honor and pleasure of working with so many brilliant and kind researchers in the Herr lab. I cherish many moments of intellectual curiosity, laughter, commiseration, invaluable insight, celebration, and triumph with everyone in this lab. This dissertation has been guided throughout by brief conversations that redirected research directions and sparked collaborations. A special note of gratitude and appreciation goes to John (rotation mentor!), Kevin, Elaine, Julea, Héctor, Eli, Ginny, Ali, Sam, Alisha, Anjali, Yizhe, Kristine, Andoni, Louise, Alden, Heather, Gabi, Ana, Qiong, Burcu, Philippe, Azim, Isao, and Peggy. Go Team IEF!

I am also grateful for the opportunity early in my graduate career to work with Dr. Kevin Healy, whose guidance and support were much appreciated, especially with the steep learning curve to this new research direction. Much gratitude and appreciation go to Peter, Willie, Anurag, Aline, Kevin T., Kento, Shane, Eda, Zhen, and Steven. I would like to express my gratitude to both my dissertation committee, Dr. Markita Landry and Dr. Bo Huang, and my qualifying exam committee, Dr. Aaron Streets, Dr. Phil Messersmith, Dr. Bo Huang, and Dr. Danica Chen, for their extensive and thoughtful advice and input. I'm also grateful to my rotation mentors and multiple BioE faculty with timely guidance.

I would like to thank the organizations that funded this dissertation work, including the National Science Foundation's Graduate Research Fellowship and the National Institutes of Health. This research support was essential and much appreciated.

Many individuals, campus facilities, and organizations were integral to this work. I am grateful to Catherine Dea; Jeanne Powers; Dave Rogers, Thom Opal, and the other staff at Stanley Hall; Dr. Paul Lum and Dr. Naima Azgui at the QB3-Berkeley Biomolecular Nanotechnology Center; the Berkeley Stem Cell Center; and Dr. Mary West at the QB3 Cell and Tissue Analysis Facility. Dr. Holly Aaron, Jen-Yi Lee, and Feather Ives at the CRL Molecular Imaging Center provided invaluable assistance with confocal laser scanning microscopy. I found an unexpected pleasure in safety discussions with Celia Shryne and others at Berkeley EH&S, and a sense of awe for Lily Mirels' practical advice and Kristin Olson's sheer competence and grace.

Dr. Noé Lozano and Meltem Erol, thank you for your invaluable insight, mentorship, and dedication to DEI efforts. Working with the GPS, SSEA, EDP, SWE, BEAST, GWE, Hacking 4 Impact, and BASIS teams, among others, are all treasured memories and transformative experiences. I am grateful to Dr. Fan Yang for taking a chance on an inexperienced and enthusiastic undergrad, and for her extensive guidance. I learned so much from Anusuya, Janice, Stephanie, and others in the Yang lab.

I do not have the words to accurately describe how fundamental my family and friends were in this dissertation. Xinyi, Christina, Sally, and Kayla, thank you for the balanced advice, compassion, and the cheer of our almost-weekly lunches and various explorations and celebrations. To Ren, Mila, the Gills, and the Huynh's – you're all essential and cherished parts of the foundation of my life.

Loulou, Mom, and Dad, thank you for your guidance, patience, unwavering support, love, and enthusiastic encouragement of all things science. None of this would have been possible without you.

Merci à tous.

Chapter 1: Introduction

Measurement gap: high-selectivity, high-throughput low-cell and single-cell proteomic assays

Understanding the function and dysfunction of cells in biological organisms, it is important to characterize one of the key functional actors of the cell, proteins. With indications of poor correlation between mRNA expression and proteomic expression at the single cell level,^{1,2} *in vitro* assays directly quantifying proteoform expression are an important area of ongoing development. Interrogations of protein expression, isoforms, post-translational modifications, localization and trafficking, activity, and degradation, in both the spatial and temporal context, would provide an expanded view of proteomic activity within the cell.³⁻⁷ However, to span the extensive cellular heterogeneity in gene and protein expression and activity observed in cells and tissues,^{4,8,9} proteomic assays should interrogate single- and low-cell resolution with sufficiently high throughput to identify cellular sub-populations. These proteomic assays would also require sufficiently high selectivity and analytical sensitivity with which to interrogate protein isoforms and post-translational modifications.

Selectivity in protein identification is often conferred by antibody affinity; however, the development and application of site-specific antibodies for every protein isoform and post-translational modification serves as a major limiting factor. Liquid chromatography-mass spectrometry^{10,11} specifically identifies phosphorylation site(s) and enables quantitative ratiometric analysis of protein activation, but has not yet been demonstrated at single cell resolution.¹² While powerful *de facto* tools to interrogate protein expression in single cells at high throughput with either surface marker information or spatial information, flow cytometry and immunocytochemistry both rely on site-specific antibodies and introduce fixation artifacts. Multiple methods leverage physicochemical properties of protein isoforms in addition to immunoaffinity of a pan-antibody, rather than relying on site-specific antibodies. Single-cell Western blotting leverages both size separation and immunoaffinity at single cell resolution, and currently is limited at 4 kDa molecular weight differences.³ Capillary isoelectric focusing,¹³ mini-gel isoelectric focusing,¹⁴ and surface isoelectric focusing¹⁵ use charge-based proteomic separations, in addition to immunoaffinity, but again have not been demonstrated at single cell resolution. Specifically, isoelectric focusing (IEF) uses a pH gradient, canonically generated by a solution of carrier ampholyte species, to separate proteins by isoelectric point (pI), or the pH at which the protein is net neutrally charged.¹⁶ The cutting-edge single-cell mass spectrometry assay^{17,18} interrogates high-expression protein isoforms, serving as an assay for both discovery and targeted studies.

As a complementary proteomic assay for targeted studies, the Herr lab introduced the single cell isoelectric focusing (scIEF) technique using an ultrathin hydrogel substrate¹⁹⁻²¹ to leverage minute differences in protein net charge, in addition to immunoaffinity. Further advancement of this assay towards the ultimate goal of a high-selectivity, high-throughput proteomic assay at single cell resolution is critical for adoption in interrogations of cellular function and dysfunction.

Measurement gap: *in vitro* biological tissue models mimicking human physiology

Much of the promise in the stem cell field revolves around personalized medicine, especially with the discovery of human induced pluripotent stem cells (hiPSCs)^{22,23}. One approach with great potential for generating personalized treatments to use hiPSCs to develop minimally-functional tissues integrated in microfluidic chips. Due to inter-species differences in ion channels, biological pathways, and pharmacokinetic properties, animal models do not faithfully predict human cardiotoxicity. Human *in vitro* tissue models that are predictive of human drug responses would be a significant advancement for understanding, studying, and developing new drugs and strategies for treating diseases. Traditional 2D *in vitro* systems, although informative,^{24,25} cannot accurately mimic the complex 3D conditions of the *in vivo* microenvironment.²⁶ In contrast, 3D models are characterized by establishment of adhesion complexes and tissue polarity and by changes in cytoskeletal structure and cell volume, that are significantly different from those found in cells cultured as monolayers. As a result, the translational results in 2D conditions are fundamentally different from those in 3D.²⁷

Complementing the myriad organ-on-a-chip platforms developed using mouse and human iPSCs,^{28–31} the Healy lab, in collaboration with the Lee, Willenbring, Conklin, and Stahl labs, have developed cardiac and liver microfluidic chips with cells derived from wild-type and patient-specific hiPSCs³² (and unpublished data). To effectively recapitulate human physiology using these microphysiological systems, inclusion of adipose tissue is essential. The lipid storage and processing within adipose tissue strongly affects drug concentrations *in vivo*, and adipose tissue interacts with other organs via paracrine signals and fatty acid release, affecting the safety profiles of a large number of drug-like molecules.

Dissertation overview

In this dissertation, we sought to address both the need for high-selectivity, high-throughput proteomic assays at single- to low-cell resolution, and the need for *in vitro* assays better mimicking human physiology. This dissertation spans research efforts in both directions.

In the first part of this dissertation, we address the need for additional developments in the single-cell proteomic assays, specifically within the electrophoretic cytometry space. In Chapter 2, we characterize the performance of the ultrathin IEF assay with a replacement of the ampholyte solution, a critical reagent that directly impacts separation performance. Furthermore, we leverage separation science theory to regain lost performance metrics from this reagent substitution in this ultrathin IEF assay.

In Chapter 3, we enhance the analytical sensitivity of the ultrathin isoelectric focusing assay with subsequent immunoblot. We develop a highly-porous hydrogel matrix as a new substrate for the assay. We characterize the effect of this 10-fold increase in gel porosity on the IEF separation performance. Additionally, we assess the benefits of the increased porosity on the in-gel immunoblot.

Chapter 4 details the development of a parallel investigation of highly-porous hydrogel matrices via photo-polymerization. We characterize the performance of the ultrathin IEF assay with these novel matrices, and report the incompatibility of this polymerization chemistry with IEF.

In Chapter 5, we investigate the compartmentalization of protein lysate from single cells within the microwells embedded in the hydrogel substrate for our electrophoretic cytometry assays. We characterize the height of the fluid film between multi-material interfaces. Furthermore, we use numerical modeling and experimental validation to assess the contribution of this fluid film to the diffusive losses that reduce analytical sensitivity in our assays.

In Chapter 6, we enhance the ultrathin IEF assay for a 100-fold increase in throughput by developing 3D projection electrophoresis. In order to characterize this assay reproducibly, we design a fluorescently-labeled IEF protein ladder for future inclusion with single cells or other biological samples. We demonstrate a proof-of-concept IEF separation in this new assay, termed “high throughput IEF” (HTP IEF). In addition, we interrogate the IEF separation performance of this assay with several optimizations. We conclude this chapter with an in-depth discussion of the potential further developments for this platform.

In the latter part of this dissertation, we address the need for *in vitro* tissue models with characteristics similar to those found in human physiology, specifically within the organ-on-a-chip space. In Chapter 7, we design and develop the first microfluidic organ-on-a-chip device with adipose tissue, named “WAT-on-a-chip.” We use numerical modeling and an analytical model to characterize the convective and diffusive transport within the device. We characterize the viability of the adipose tissue for over two weeks. Furthermore, we confirm the maintenance of adipose functionality by staining the extracellular matrix within the tissue and by visually assessing adipocyte cell growth and lipid droplet formation.

In Chapter 8, we survey the breadth of *in vitro* cardiac devices mimicking human cardiac physiology. We discuss the essential developments in cardiomyocyte generation, biomaterial substrates, and microdevices in this research space. We compare the mechanical, electrophysiological, and biological outcomes of these *in vitro* models, and discuss the ideal *in vitro* cardiac tissue model for biological studies, disease modeling, drug screening, and design of tailored therapeutic responses in line with precision medicine efforts.

Finally, in Chapter 9, we summarize the work in this dissertation and discuss potential future research directions. The appendix includes multiple protocols and analysis scripts used in this work, as well as shorter research inquiries.

Chapter 2: Ultrathin Isoelectric Focusing Performance Using Different Ampholyte Solutions

2.1 Introduction

Isoelectric focusing (IEF) is a preparatory and analytical technique for separating proteins, among other macromolecules, by isoelectric point (pI), or the pH at which the protein is net neutrally charged. This separation necessitates a pH gradient, increasing from anode to cathode, across which the proteins electrophorese under an applied electric field and focus to their pI. Over the last 60+ years, multiple methods have been developed and characterized for creating the pH gradient required for IEF.^{16,33} Of particular interest and adoption are ampholytes (abbreviated “CA”), applied in slab IEF,³⁴ surface IEF,¹⁵ capillary IEF with and without subsequent immunoblot,^{13,35} microfluidic IEF,³⁶ ultrathin IEF with subsequent immunoblot,^{19–21} and many other platforms. An effective ampholyte solution for IEF is defined as a heterogenous solution of species, typically zwitterionic, that span a specific range of pI’s. Each ampholyte species should have both high buffering capacity and high conductivity at its pI, among other characteristics.¹⁶ According to the law of pH monotony, upon application of an electric field, the CA stack in order of pI across the separation axis, building from the anode and cathode inwards, to create an ideally-linear pH gradient.¹⁶

Commercially-available CA solutions provide incomplete information on the particular IEF performance enabled by each CA mixture, making non-experimental comparisons difficult. For example, the Polybuffer® CA are reported by the manufacturer to generate a linear pH gradient for resolving pI differences of 0.4 with a buffering capacity of 0.070–0.080 mmol/mL.³⁷ A solution of polyamino-polycarboxylic acids, the SinuLyte® CA are reported by the manufacturer to resolve pI differences of 0.1, with “up to 1.5 to 2.5 higher” buffering capacity “compared to established ampholytes,” but with no information on the linearity of the generated pH gradient.³⁸ In contrast, the Zoom® CA are mixtures of ampholytes with “sulfonate and carboxylic acid groups at one end, and free primary and secondary amino groups at the other,” resulting in molecules with molecular weights ranging from 400 to 700 Daltons. The manufacturer specifies the conductivity and pH gradient ranges for a 2% solution, but provides no information on the linearity of the generated pH gradient in IEF.³⁹ Recent work by Righetti et al. used mass spectrometry to experimentally characterize the buffering capacity and composition of four established and commercially-available CA most commonly used in IEF platforms: Ampholine (polyamino-polycarboxylic acids),⁴⁰ Pharmalyte, Bio-Lyte, and Servalyt (polyamino-polysulfonic-polycarboxylic acids). This work highlighted a need for the identification of additional alkaline ampholytes.^{41,42} Comparative experimental studies have characterized the utility of the Polybuffer CA as a less expensive replacement for established ampholyte solutions.⁴³ Without this missing information on the precise composition, buffering capacity, and IEF performance of CA solutions, integration with IEF modeling software such as Simul5⁴⁴ for non-experimental optimization of IEF separations is hampered.

Recently the Herr lab has developed an IEF assay¹⁹ (abbreviated “ultrathin IEF” or “ultrathin scIEF” with single cells) using an ultrathin hydrogel substrate, designed to separate proteins from arrays of single cells. This technique used Polybuffer® CA to form a pH 4-7 gradient, which spans 50-70% of the pI’s of the human proteome.^{45,46} Given both our interest in refining the ultrathin IEF assay to interrogate protein isoforms and post-translational modifications, as well as commercial discontinuation of the Polybuffer® CA’s in 2015, we experimentally compare the performance of the ultrathin IEF assay using Polybuffer® versus SinuLyte® CA. Then, we use our knowledge of IEF theory to modify assay parameters for high-resolution separations of proteins with the SinuLyte® CA. We complete this short study with a discussion of alternative methods for generating pH gradients in IEF platforms.

2.2 Materials and Methods

Reagents

Silicon wafers (University Wafer 1156), SU8 3050 photoresist (MicroChem), a custom in-house-designed mask (CAD/ART Services), GelSlick® (Lonza 50640), standard glass slides (VWR), dichlorodimethyl silane (Sigma 440272), 3-(trimethoxysilyl)propyl methacrylate (Sigma 440159), methanol (Sigma 179337), glacial acetic acid (Sigma 8817-46), 30%T 29:1 acrylamide/bis-acrylamide solution (Sigma A3574), 40%T 29:1 acrylamide/bis-acrylamide solution (Sigma A7802), 1.5 M pH 8.8 TrisHCl (TekNova T1588), N-[3-[(3-benzoylphenyl)formamido]propyl] methacrylamide (BPMA, custom synthesized by PharmAgra Labs), ammonium persulfate (APS, Sigma A3678), N,N,N',N'-tetramethylethylenediamine (TEMED, Sigma T9281), UV photoinitiator 2,2'-Azobis[2-methyl-N-(2-hydroxyethyl)propionamide] (VA086, Wako Chemicals 61551), borosilicate glass sheets (McMaster-Carr 8476K62), and permanent lab markers (VWR 52877-310) were used to fabricate materials in this study.

IEF was conducted using the immobilines pKa 3.6 and pKa 9.3 acrylamido buffers (Sigma 01716, 01738), Polybuffer ampholytes (Sigma P9652, lot SLBD5427V), SinuLyte® pH 4-7 ampholytes (Sigma 05087, lot BCBJ7449V), an ABS electrophoresis device designed and printed in-house, graphite electrodes (Bio-Rad 1702980), 0.5 mm gel spacers (CBS Scientific MVS0510-R), and TritonX-100 detergent (Sigma X100). Tris-buffered saline with Tween-20 (TBS-T, CST 9997S) was used for gel incubation and wash steps.

The proteins and molecules used in this study were fluorescent pI markers 4.5, 5.5, 6.6, and 6.8 (Sigma 89149, 77866, 73376, 89508), henceforth termed “pI markers,” and BSA (Sigma A7030).

Wafer and Separation Gel Fabrication

SU8 fabrication on a silicon wafer was conducted following a standard protocol.³ Briefly, a custom mask with rails spaced 22 mm apart was used to fabricate features of 40 μm in height (confirmed by optical profilometry) in SU8 on a silicon wafer. After wafer treatment with dichlorodimethyl silane, polyacrylamide (abbreviated “PA”) precursor

solutions were created containing 1% of each of the pI markers 4.5, 5.5, 6.6, and 6.8 (from 1-3 mg/mL stock solutions from manufacturer). The mixed and degassed precursor solutions were combined with APS/TEMED and introduced to the silanized wafer. Gel polymerization onto silanized half-glass slides occurred for 20 minutes at room temperature, protected from light. After fabrication, these PA gels were used immediately for the IEF assay. For this study, we use the canonical notation of %T as the total acrylamide monomer concentration (w/v) in solution, and %C as the ratio of bis-acrylamide crosslinker concentration to the total acrylamide monomer concentration.⁴⁷ We use a 6%T 3.3%C PA gel polymerized with APS/TEMED.¹⁹

IEF

Ultrathin IEF was conducted as previously described¹⁹ with minor modifications to accommodate purified protein solutions. During the 20-minute polymerization time of the PA gels described above, the 3-component IEF lid was fabricated using either a 1:100 dilution of the stock 40% SinuLyte® ampholytes for a final concentration of 0.4%, or a 1:10 dilution of the stock Polybuffer® ampholytes. **Table 2-1** lists the components of two types of lid gels used in this study, which was polymerized for 4 minutes per component (in the order of anolyte, catholyte, and focusing region) at 20 mW/cm² light intensity using a 390 nm UV long-pass filter (Edmund Optics) on an OAI Model 30 Collimated UV light source.

The PA gel and lid gel were assembled in the IEF device previously described,¹⁹ and set on an Olympus IX-71 inverted microscope with an Olympus UPlanFi 4× (NA 0.13) objective and a EMCCD Camera iXon2 (Andor), with imaging settings loaded into MetaMorph software (7.10.1.161, Molecular Devices). After a 30 s delay for the soluble reagents in the focusing lid gel to diffuse into the PA gel, IEF was conducted by applying 690 V for 12-25 minutes using the Power-Pac high-voltage power supply device (HVPS, Bio-Rad 1645056). During this focusing period, pI markers were imaged using a UV-longpass filter cube (XF100-1, Omega Optical) at 2.5 minute intervals. The lab markers used to denote the gel edges along the separation axis is fluorescent in the UV-longpass channel and visible in brightfield imaging.

Micrographs were analyzed using an in-house MATLAB (R2015b, MathWorks) script^{6,48,49} adapted to this microwell-free variant of the IEF (code in **Appendix 11**). Briefly, the micrographs were segmented into regions of interest (ROIs), converted into line plots averaged across the width of the ROI (maintaining the separation axis), and background-subtracted using the average background intensity across the ROI. Gaussian curve fitting to the line plots led to the extraction of the peak height, peak location, peak width, area under the curve, SNR, and other assay-specific parameters from each ROI. Validation of the Gaussian curve fits is conducted analytically ($R^2 \geq 0.7$ and signal-to-noise ratio $SNR \geq 3$) and confirmed manually. For the images taken on the Olympus microscope setup, 1 pixel corresponds to 4 μm .

Statistical Analysis

Linear regression fit was performed using an in-house MATLAB script.

Table 2-1. Composition of IEF lid gels for the ampholyte study.

Components of the 3-part lid gel used for lysis and electrophoresis in this study, for both the Polybuffer® and SinuLyte® CA solutions.

Polybuffer® Lid gel components	pH 4 anolyte	Focusing region	pH 10 catholyte
Polyacrylamide gel	15% T 3.3% C 0.2% VA-086	15% T 3.3% C 0.2% VA-086	15% T 3.3% C 0.2% VA-086
IEF reagents and detergents		1:10 dilution of stock Polybuffer® ampholytes 1% TritonX-100	
Boundary conditions	13.5 mM pKa 3.6 immobiline 6.4 mM pKa 9.3 immobiline		5.6 mM pKa 3.6 immobiline 14.4 mM pKa 9.3 immobiline

SinuLyte® Lid gel components	pH 4 anolyte	Focusing region	pH 10 catholyte
Polyacrylamide gel	15% T 3.3% C 0.2% VA-086	15% T 3.3% C 0.2% VA-086	15% T 3.3% C 0.2% VA-086
IEF reagents and detergents		1:100 dilution of stock solution (0.4% final) SinuLyte® ampholytes 1% TritonX-100	
Boundary conditions	13.5 mM pKa 3.6 immobiline 6.4 mM pKa 9.3 immobiline		5.6 mM pKa 3.6 immobiline 14.4 mM pKa 9.3 immobiline

2.3 Results and Discussion

To interrogate IEF performance in the ultrathin IEF assay, we slightly modified the previously-developed ultrathin scIEF assay¹⁹ to accommodate purified protein solutions. **Figure 2-1A and B** depict the difference in separation gel between the scIEF and non-single-cell IEF variants of this assay, namely the removal of the microwells. After the requisite solutions are diffusively introduced to the microwell-free IEF variant of the ultrathin separation gel, the lid gel is stacked on the separation gel (**Figure 2-1C, D**) for subsequent IEF (**Figure 2-1E**).

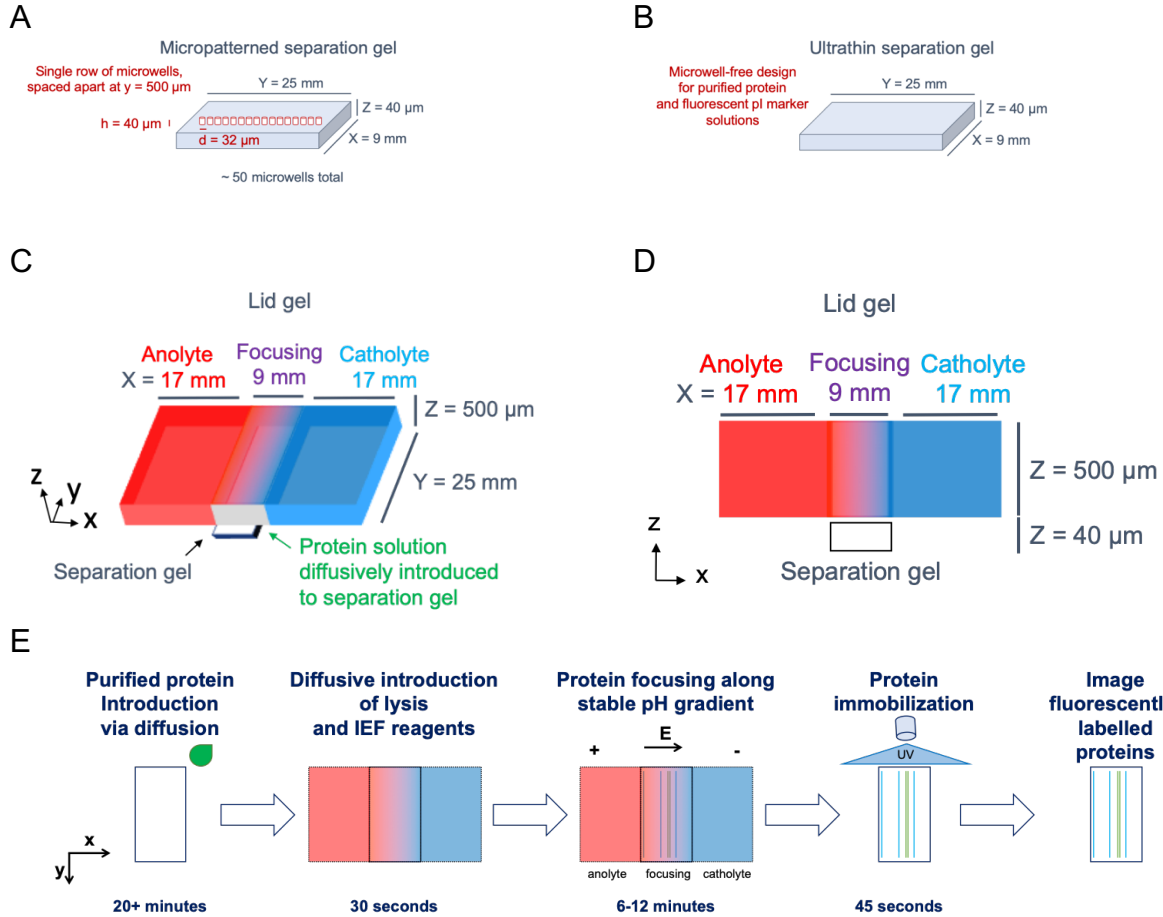


Figure 2-1. Schematic of the ultrathin IEF assay.

(A) Orthogonal view of the ultrathin PA separation gel, patterned with microwells in the ultrathin scIEF assay. (B) Orthogonal view of the ultrathin PA separation gel in the ultrathin IEF assay. (C) Orthogonal view of the assembly of gels within the ultrathin IEF chamber. (D) Side view of the assembly of gels in the ultrathin IEF assay. (E) The workflow of the ultrathin IEF assay, from gel incubation with protein solution through protein electrophoretic separation, immobilization, and imaging.



Figure 2-2. Orthogonal view of the ultrathin IEF assay assembly on a widefield epifluorescence microscope.

IEF device is black with purple edging, adhered to the microscope stage. Gel is oriented with anolyte boundary towards the top of the image with the red connector.

IEF Performance with Different Ampholyte Solutions

We investigated the formation and stability of the pH gradients formed with either the Polybuffer® or SinuLyte® CA. To monitor and then characterize the pH gradient formed, we generated pH gradients that included four fluorescently-labeled pI markers (pI 4.5, 5.5, 6.6, and 6.8). To characterize the pH gradient at equilibrium, we assessed IEF with each CA solution by considering the slope of each pH gradient, dpH/dx . To determine dpH/dx , each of the focused pI marker concentration distributions were fit to a Gaussian curve. Using the peak locations and knowledge of the ampholyte composition, we then used a linear regression fit of the pI markers to estimate the pH gradient properties. The dpH/dx was quantified as $0.61 \pm 0.06 \text{ mm}^{-1}$ with Polybuffer® CA and $0.84 \pm 0.19 \text{ mm}^{-1}$ with SinuLyte® CA over time (Figure 2-3A, mean \pm standard deviation for time course of $n=1$ gel). For the same separation axis in ultrathin IEF, the dpH/dx was measured at 0.40 mm^{-1} for the Polybuffer® ampholytes over a pH 4-9 gradient.¹⁹

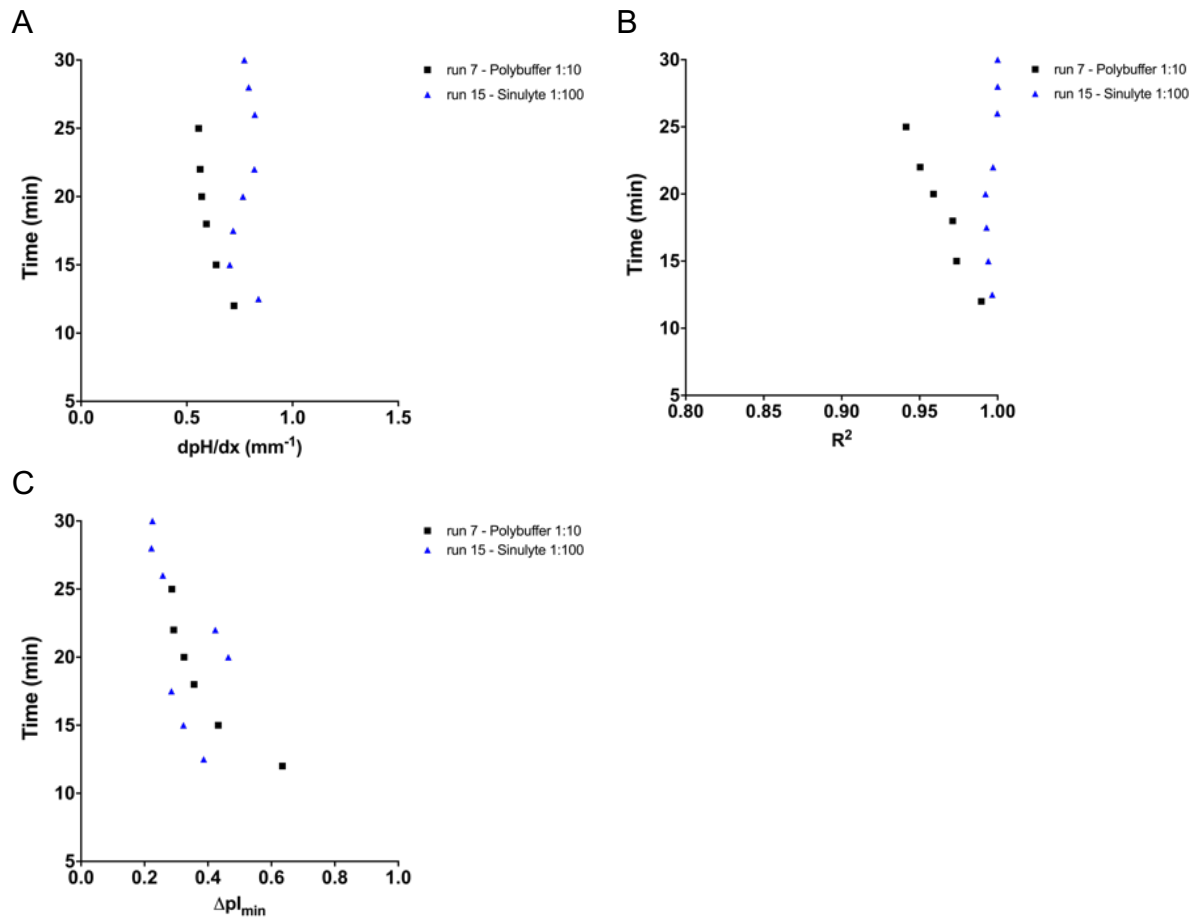


Figure 2-3. The SinuLyte® ampholytes demonstrated increased dpH/dx compared to the Polybuffer® ampholytes in the ultrathin IEF assay.

(A) dpH/dx , (B) R^2 statistic for the linear fit, and (C) ΔpI_{min} is reported over time for $n=1$ gel with the SinuLyte® CA (black) and Polybuffer® CA (blue) for the pI markers.

To assess the linearity of the pH gradient, we measured the mean R^2 statistic for the linear fits. We quantified $R^2 = 0.96 \pm 0.02$ with Polybuffer® CA and 0.997 ± 0.003 with

SinuLyte® CA (**Figure 2-3B**, mean \pm standard deviation over time for n=1 gel). Discussion. The Polybuffer® CA used previously in a similar ultrathin IEF platform demonstrated 1.00 ± 0.00 linearity.^{19,20}

We evaluated the minimum difference in pI for which two neighboring proteins are fully resolved (ΔpI_{min}), a unitless metric determined by **Equation 2-1**.¹⁶ Using the pI markers (**Figure 2-3C**), we measured the ΔpI_{min} as 0.38 ± 0.13 with Polybuffer® CA and 0.32 ± 0.09 with SinuLyte® CA (mean \pm standard deviation over time for n=1 gel). The smallest measured ΔpI_{min} in this timeframe was 0.28 with Polybuffer® CA and 0.22 with SinuLyte® CA. However, the Polybuffer® CA used previously in a similar ultrathin IEF platform demonstrated ΔpI_{min} of 0.13 ± 0.02 over a pH 4-7 gradient.¹⁹ Researcher handling aside, this analysis indicated that the SinuLyte® CA may have negatively affected the separation performance of this ultrathin IEF assay.

$$\Delta pI_{min} = 3 * \frac{dpH}{dx} * \sigma_{protein} = 3 * \sqrt{\frac{D * \frac{dpH}{dx}}{E * -\frac{du}{dpH}}}$$

Equation 2-1. ΔpI_{min} quantified for proteins focused in an IEF assay.¹⁶

IEF Optimization with SinuLyte® Ampholytes

We next modified the parameters of this IEF assay using the SinuLyte® CA to regain the IEF performance previously observed with the Polybuffer® CA. Specifically, **Equation 2-1** describes ΔpI_{min} as a function of the protein-specific parameters (the diffusivity of the protein in-gel or D , and the electrophoretic mobility shift across the pH gradient or du/dpH) and the assay-specific parameters (the strength of the applied electric field or E , and dpH/dx). Electric field strength is dependent on the applied voltage V and the separation length L ($E = V / L$).¹⁶ In order to investigate the design space of the ultrathin IEF assay with SinuLyte® CA, we started with the experimental conditions used in **Figure 2-3**: $L = 9$ mm, CA content = 0.4%, and $V = 600$ V, and systematically modified L , CA content, and V both analytically and experimentally.

It is important to note that these experiments were designed with small sample size to rapidly assess the design space of the ultrathin IEF assay. Further research into the IEF separation performance and reproducibility at each of these conditions is required.

From a theoretical perspective, increasing the separation length in this IEF assay would result in a decrease in the slope of the pH gradient dpH/dx and a decrease in the electric field strength. Experimentally modifying the separation length did not result in a large change in the ΔpI_{min} (**Figure 2-4A**). Further research is required in this, due to the small sample size.

In addition, assessing the optimal concentration of ampholytes for a robust IEF separation was essential, since insufficient ampholytes at any one pI would reduce the

buffering capacity at that pI, negatively impacting separation resolution. We anticipated that, above the threshold for sufficient buffering capacity, an increase in CA concentration would not change the separation performance of the assay. We observed no large change in the ΔpI_{min} (**Figure 2-4B**). To preserve reagents, we maintained the 0.4% CA content.

Finally, increasing the applied voltage would theoretically increase the electric field strength, thereby sharpening IEF focusing and resulting in a smaller ΔpI_{min} . From this set of experiments, we identified that the increase in the applied voltage was sufficient to achieve a ΔpI_{min} near 0.1 (**Figure 2-4C**). Subsequent characterization of the IEF separation performance under these conditions (L = 9 mm, CA content = 0.4%, V = 690V) yielded $\Delta pI_{min} = 0.16 \pm 0.02$ (mean \pm standard deviation for n=3 gels, measured at 12 minutes of IEF, averaged over 3 pI markers, **Figure 3-7D**).

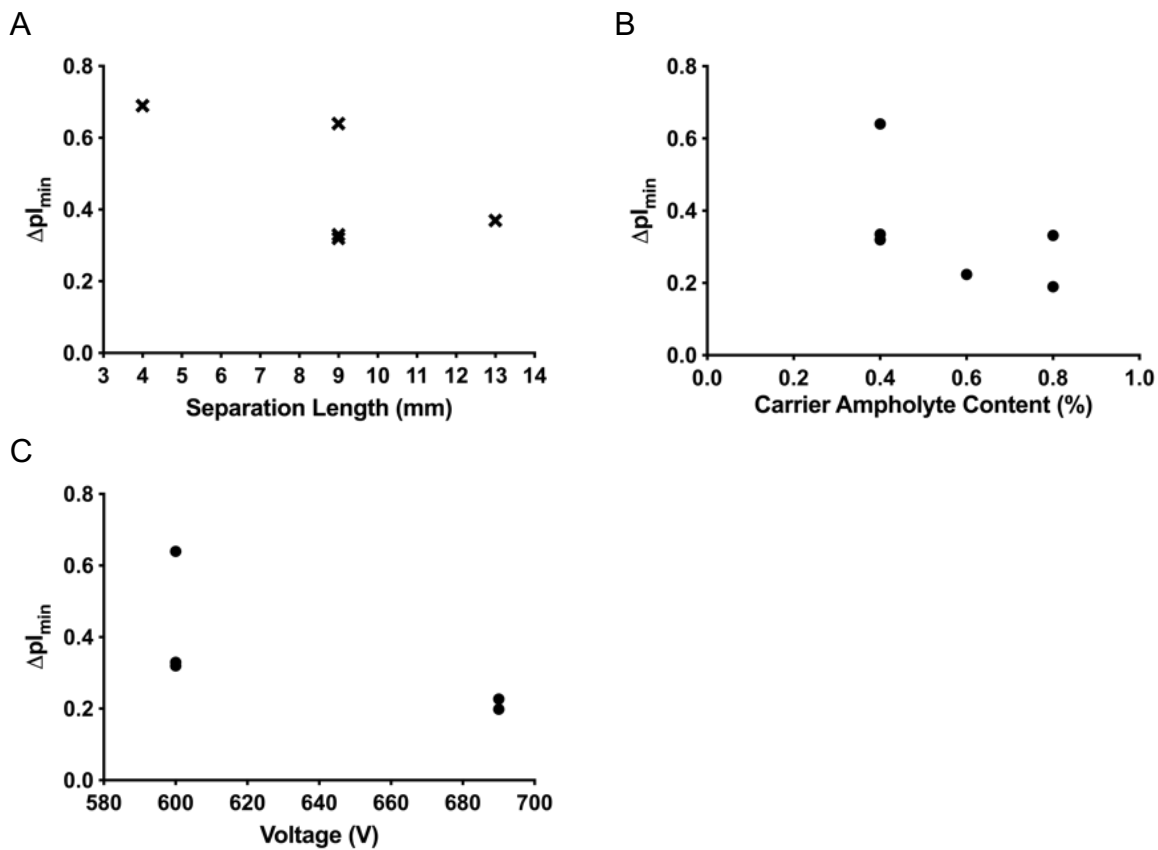


Figure 2-4. Experimental assessment of the design space of the ultrathin IEF assay with SinuLyte® CA.

ΔpI_{min} averaged over time for the 3 pI markers, in the ultrathin IEF assay with modifications to (A) the separation axis with 600 V applied voltage, (B) the concentration of SinuLyte® CA with 600V applied voltage over a 9 mm separation axis and (B) the applied voltage with a 9 mm separation axis, for n=1-3 gels.

2.4 Conclusions and Future Directions

In this work, we modified the ultrathin IEF assay to accommodate a replacement ampholyte solution, and investigated how this modification affected IEF separation performance. We leveraged IEF separation theory to optimize assay parameters in order to regain IEF separation performance, reaching a $\Delta pI_{min} = 0.16 \pm 0.02$. More recently, the ΔpI_{min} for Zoom® CA was characterized as 0.11 for a similar ultrathin IEF assay across a pH 4-7 gradient,²¹ indicating that alternate CA solutions might confer higher IEF performance in the same assay format.

Given the limited information on the composition and chemical properties of commercially-available ampholyte solutions,^{16,41} as well as the risk for discontinuation of products, there is a clear need to design less-variable pH gradients that are not reliant on ampholytes. Out of the range of alternate methods for generating pH gradients,^{16,33,50} including the “natural” pH gradient generated by splitting water molecules into H⁺ and OH⁻ ions upon application of an electric field,⁵¹ and the thermally-generated pH gradient,⁵² we find that the creation of an immobilized pH gradient (IPG)^{50,53,54} would be a significant development in this particular ultrathin IEF assay. Notably, a pre-formed and immobilized pH gradient in the PA gel would allow researchers to specifically design a pH range for the target proteins of interest, and would ideally remove any technical variation in the location of specific pI's along the separation axis.

Chapter 3: Laterally Aggregated Polyacrylamide Gels for Immunoprobed Isoelectric Focusing

This work was performed in collaboration with Dr. Kevin A. Yamauchi and Alison Su.

3.1 Introduction

Polyacrylamide gels (abbreviated “PA”) are widely used for electrophoretic analysis and characterization of proteins.^{55–57} Used in important protein electrophoresis modalities^{16,58}, PA gels offer exceptional separation resolution because (1) the pore size of the gel approximates the average diameter of globular proteins, making the gel a high-performance sieving matrix and (2) the porous gel retards molecular diffusion, as compared to electrophoresis in free solution (i.e., capillary zone electrophoresis, CZE; capillary isoelectric focusing, cIEF).

In addition to acting as a separation medium for electrophoresis, PA gels offer auxiliary functions. For example, after slab-gel 2DE, the gel matrix is used to transfer specific focused proteins to mass spectrometry (MALDI) for definitive target identification, with the gel physically cut out of the slab, and transferred to the mass spectrometer.⁵⁹ Another example is Western blotting,^{60–62} where proteins are separated by size and then probed with immunoreagents, thus facilitating target identification using an immunoassay. Western blotting confers high selectivity, but may not afford detection resolution suitable for post-translational modifications and/or splice variants. Such proteoforms may not have detectable molecular mass differences.

Appending an immunoassay to isoelectric focusing (IEF) can provide the resolving power necessary to measure a broader swath of proteoforms. IEF separates protein targets based on differences in isoelectric point (pI), not size.¹⁶ During IEF, species electromigrate through a pH gradient, stopping at the position in the gradient where the local pH and the pI of the target are equal. Protein targets then ‘focus’ at this position, with a sustained applied electric field and stable pH gradient. Unlike the PA gel of western blotting (protein sizing), the PA gel of IEF need not function as a molecular sieving matrix. When developed in a miniaturized format, IEF can operate with enhanced heat dissipation (i.e., Joule heating), reduced reagent and sample consumption, and improved separation performance (rapid separation times).

While immunoblotting formats often rely on physical transfer of separated protein targets from the separation lane to a large-pore-size blotting membrane^{14,63,64}, immunoprobed IEF formats have, instead, covalently immobilized separated proteins to the functionalized walls of the IEF separation capillary^{13,65} or, in our case, covalently immobilized protein peaks into a PA gel separation matrix.^{66–69} but only as an anti-convective media (during IEF) and an immobilization scaffold for the subsequent immunoprobing (immunoassay).

Consequently, we sought to assess the role of PA gel porosity and microarchitecture in immunoprobed IEF with in-gel target detection. We considered both PA gel formulations

similar to slab-gel and published formats (i.e., 6%T 3.3%C PA gel; mean pore radius = 5-92 nm and fiber radius ~0.5 nm,^{70,71} depicted schematically in **Figure 3-1A**), as well as PA gels designed to offer larger mean pore radius characteristics by inducing lateral aggregation by including a preformed hydrophilic polymer (i.e., PEG) during PA gel polymerization.⁷² Incorporation of PEG creates a bi-modal pore size distribution in the resultant hydrogel, with open fluidic spaces formerly occupied by the porogen and small pores created between bundles of polyacrylamide^{70,73,74} For these “highly porous” PA gel formulations, the mean pore radius can be ~250 nm (i.e., 5%T, 4%C PA gel incorporating 2% PEG with PA bundle radius at 150 nm, depicted schematically in **Figure 3-1C**), a 100-fold increase.⁷⁰ After PA gel polymerization, the unfunctionalized PEG freely diffuses out of the PA hydrogel matrix. However, a small fraction of the PEG is thought to remain in the PA gel as a semi-interpenetrating network, which may inhibit in-gel diffusion of soluble species.⁷²

Specifically, for immunoprobed IEF, we address questions regarding the anti-convective characteristics of highly porous PA gels during IEF and, during immunoprobing, target immobilization to the PA gel matrix, introduction of antibody probe into the PA gels, and removal of unbound antibody probe (background) which impact detection performance.

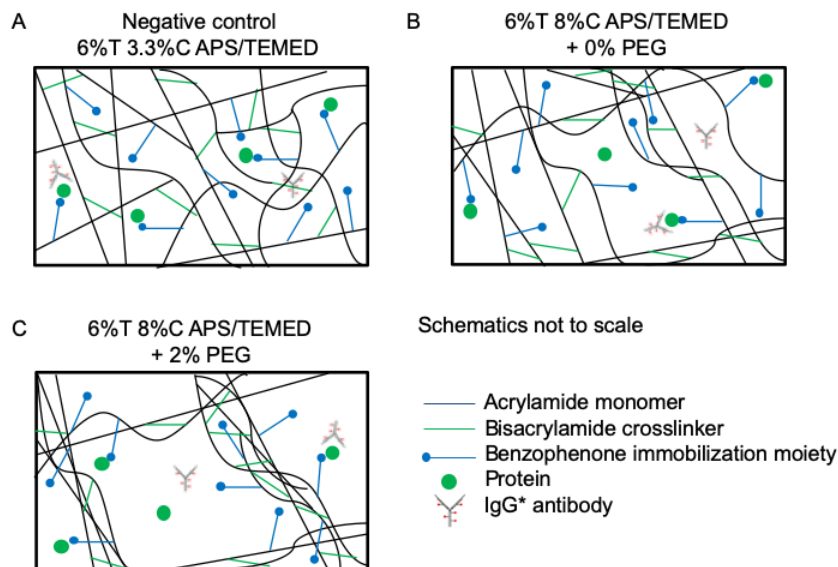


Figure 3-1. Generation of highly porous PA gels.

(A) Depiction of random organization of porous microarchitecture in the negative control gels. (B) Depiction of bimodal distribution of pores in 0% PEG gels, with the voids formed from aggregation of the bis-acrylamide crosslinker at high concentration. (C) Depiction of bimodal distribution of pores in 2% PEG gels, with the voids formerly filled with hydrophilic 10 kDa PEG. Protein and fluorescently-labeled IgG* antibody depicted relative to the pores. Schematics not to scale.

3.2 Materials and Methods

Reagents

Borofloat wafers (University Wafer 516), SU8 3050 photoresist (MicroChem), titanium diisopropoxide bis(acetylacetonate) (Sigma 325252), anhydrous isopropanol (Sigma 278475), a custom in-house-designed mask (CAD/ART Services), GelSlick® (Lonza 50640), standard glass slides (VWR), dichlorodimethyl silane (Sigma 440272), 3-(trimethoxysilyl)propyl methacrylate (Sigma 440159), methanol (Sigma 179337), glacial acetic acid (Sigma 8817-46), 30%T 29:1 acrylamide/bis-acrylamide solution (Sigma A3574), 40%T 29:1 acrylamide/bis-acrylamide solution (Sigma A7802), bis-acrylamide powder (Sigma 146072), 1.5 M pH 8.8 TrisHCl (TekNova T1588), N-[3-[(3-benzoylphenyl)formamido]propyl] methacrylamide (BPMA, custom synthesized by PharmAgra Labs), ammonium persulfate (APS, Sigma A3678), N,N,N',N'-tetramethylethylenediamine (TEMED, Sigma T9281), UV photoinitiator VA086 (Wako Chemicals 61551), 10 kDa poly(ethylene glycol) (PEG, Sigma 92897), borosilicate glass sheets (McMaster-Carr 8476K62), #1.5H glass coverslips (Ibidi 0107999097), μ -Slide 4 well glass-bottom chambered coverslips (Ibidi 80427), Array-It Hybridization Cassettes (AHC1x16, Array-It), and permanent lab markers (VWR 52877-310) were used to fabricate materials in this study.

IEF was conducted using the immobilines pKa 3.6 and pKa 9.3 acrylamido buffers (Sigma 01716, 01738), SinuLyte® pH 4-7 ampholytes (Sigma 05087), an ABS electrophoresis device designed and printed in-house, graphite electrodes (Bio-Rad 1702980), 0.5 mm gel spacers (CBS Scientific MVS0510-R), and TritonX-100 detergent (Sigma X100). Tris-buffered saline with Tween-20 (TBS-T, CST 9997S) was used for gel incubation and wash steps.

The proteins and molecules used in this study were fluorescent pl markers 4.5, 5.5, and 6.6 (Sigma 89149, 77866, 73376), henceforth termed “**pl markers**,” BSA (Sigma A7030), purified recombinant turboGFP (Evrogen FP522, lot 55201240718) termed “**tGFP**” (a variant of the GFP with increased fluorescence, MW 27 kDa), primary rabbit-anti-turboGFP antibody (Pierce PA5-22688, lots UA2694351 and UA2718271), secondary polyclonal antibody AlexaFluor-647-labeled donkey-anti-rabbit (Invitrogen A-31573) termed “**IgG***.” The IgG* degree of labeling is reported by the manufacturer as 5 fluorophores per molecule for lot 1964354 (Invitrogen).

Wafer and Gel Fabrication

SU8 fabrication on a glass wafer was conducted following a standard protocol.³ Briefly, a custom mask with rails spaced 22 mm apart was used to fabricate features of 40 μ m in height (confirmed by optical profilometry) in SU8 on a borofloat wafer. After wafer treatment with GelSlick®, polyacrylamide (abbreviated “**PA**”) gels were fabricated on the wafer and polymerized onto silanized half glass slides. **Table 3-1** lists the critical components of each gel condition, using 10 kDa PEG as the preformed hydrophilic polymer and leveraging porogen gel fabrication conditions developed by Righetti and colleagues (further details in **Appendix 1**).⁷⁰ After fabrication, gels were incubated for 16-24 hours in 1 \times TBS-T to allow for diffusion of soluble PEG porogen out of the PA gel network, thus forming the voids depicted in **Figure 3-1B and C**, then rinsed in DI water for 30 minutes before use.

For this study, we use the canonical notation of %T as the total acrylamide monomer concentration (w/v) in solution, and %C as the ratio of bis-acrylamide crosslinker concentration to the total acrylamide monomer concentration.⁴⁷ To distinguish the six PA gel conditions, as outlined in **Table 3-1**, we define the 6%T 3.3%C APS/TEMED gels as “**benchmarking gels**,” the 6%T 8%C APS/TEMED + 0% PEG gels as “**negative control gels**,” the 6%T 8%C APS/TEMED + 0.5% PEG gels as “**0.5% PEG highly porous PA gels**,” the 6%T 8%C APS/TEMED + 1% PEG gels as “**1% PEG highly porous PA gels**,” the 6%T 8%C APS/TEMED + 1.5% PEG gels as “**1.5% PEG highly porous PA gels**,” and the 6%T 8%C APS/TEMED + 2% PEG gels as “**2% PEG highly porous PA gels**.” The PA gel matrix is formed from incorporation of acrylamide monomers and bis-acrylamide crosslinkers into a randomly organized hydrogel network, inducing heterogeneity in pore size.^{75–77}

Table 3-1. Composition of PA porogen gels.

Primary components of all gel conditions used in this work, following standard gel fabrication techniques in ⁴⁸. Highlighting indicates modifications from the 6%T 3.3%C APS/TEMED negative control gel condition, for ease of comparison between PA gel conditions. Concentrations reported as % are %w/v.

Gel nomenclature	Bench- marking	Negative control	0.5% PEG Highly porous gel	1% PEG Highly porous gel	1.5% PEG Highly porous gel	2% PEG Highly porous gel
Acrylamide content	6% T	6% T	6% T	6% T	6% T	6% T
Bisacrylamide : acrylamide ratio	3.3% C	8% C	8% C	8% C	8% C	8% C
10 kDa PEG	0.0%	0.0%	0.5%	1.0%	1.5%	2.0%
Polymerization chemistry	APS / TEMED	APS / TEMED	APS / TEMED	APS / TEMED	APS / TEMED	APS / TEMED
BPMA photo- immobilization moiety	5 mM	5 mM	5 mM	5 mM	5 mM	5 mM

Thermodynamic Partitioning

We used confocal imaging to measure the thermodynamic partitioning coefficient of IgG* into the PA gels⁶⁸. After silanization of the μ -Slide chambered coverslips, gels were fabricated using wafer molds with 40 μ m feature heights within these containers and incubated in TBS-T for 24 hours. Gels were then exposed to 1:20 dilution of IgG* solution (from 2 mg/mL stock solution from manufacturer, spun down to remove aggregates) in 2% BSA / TBS-T for > 2 hours to equilibrium. Confocal imaging experiments were conducted on an inverted Zeiss LSM 710 AxioObserver at the CRL Molecular Imaging Center. Images were acquired at room temperature using a 40 \times water immersion objective (LD C-Apochromat 40 \times / 1.1 NA W Corr M27, Zeiss) with the correction collar manually assessed to optimal calibration at 0.150 mm. IgG* within the chambered coverslips was imaged using a HeNe633 laser at 17% power, using the MBS488/561/633 beam splitter and the Zen 2010 software (Zeiss). Z-stack images

were acquired with a step size of $z=0.70\ \mu\text{m}$ and a field of view of $x=y=212.55\ \mu\text{m}$, and analyzed using an in-house Fiji (1.52i, NIH) script.

Equilibrium Swelling Ratio

The equilibrium swelling ratio was conducted using Flory-Rehner theory.^{47,78–80} After fabrication of PA gels on glass slides with $500\ \mu\text{m}$ spacers to define gel height, gels were weighed immediately on an Ohaus Adventurer Pro weigh station to determine the “fabrication” weight, then incubated in $1\times$ TBS-T for 24 hours for PEG diffusion out of the gel. After 12 hours of DI water incubation, the equilibrated gel was weighed again for the “hydration” weight, dehydrated fully with a nitrogen gas stream, and weighed a third time for the “dehydration” weight.

IEF and Photocapture Efficiency

The thin-film IEF was conducted as previously described¹⁹ with minor modifications to accommodate purified protein solutions (further details in **Appendix 3**). First, gels with a height of $40\ \mu\text{m}$ were rinsed in DI water and then the fluid layer was wicked off the top of the gel. Next, the gel was incubated in $40\ \mu\text{L}$ of a solution of 1% each of the pl markers 4.5, 5.5, and 6.6 (from 1-3 mg/mL stock solutions from manufacturer), and 10% v/v tGFP (from $37\ \mu\text{M}$ stock from manufacturer) for 30 minutes at room temperature, protected from light. The 3-component IEF lid was fabricated using a 1:100 dilution of the stock 40% Sinulyte ampholytes for a final concentration of 0.4%. **Table 3-2** lists the components of the lid gel, which was polymerized for 4 minutes each at $20\ \text{mW}/\text{cm}^2$ light intensity using a 390 nm UV long-pass filter (Edmund Optics) on an OAI Model 30 Collimated UV light source.

The PA gel and lid gel were assembled in the IEF device previously described,¹⁹ and set on an Olympus IX-71 inverted microscope with an Olympus UPlanFi $4\times$ (NA 0.13) objective and a EMCCD Camera iXon2 (Andor), with imaging settings loaded into MetaMorph software (7.10.1.161, Molecular Devices). After a 30 s delay for the soluble reagents in the focusing lid gel to diffuse into the PA gel, IEF was conducted by applying 690 V for 12 minutes using the Power-Pac high-voltage power supply device (HVPS, BioRad 1645056). During this focusing period, pl markers were imaged using a UV-longpass filter cube (XF100-1, Omega Optical) at 2.5-min intervals, and tGFP was imaged using a GFP filter cube (XF100-3, Omega Optical) 1 minute subsequently. After 12 minutes of focusing, protein photo-immobilization was induced by application of UV at 100% intensity for 45 s with the Hamamatsu LC8 (Hamamatsu Photonics K.K.), sweeping across the gel assembly at 1.6 cm above the gels. After protein photo-immobilization, gels were rinsed in TBS-T for 30 minutes to remove uncaptured species, and imaged with the same settings. The lab markers used to denote the gel edges along the separation axis is fluorescent in the UV-LP channel and visible in brightfield imaging.

Micrographs were analyzed using an in-house MATLAB (R2015b, MathWorks) script^{6,48} adapted to this microwell-free variant of the IEF (code in **Appendix 11**). Briefly, the micrographs were segmented into regions of interest (ROIs), converted into line plots

averaged across the width of the ROI (maintaining the separation axis), and background-subtracted using the average background intensity across the ROI. Gaussian curve fitting to the line plots enables extraction of the peak height, peak location, peak width, area under the curve, signal-to-noise ratio (SNR), and other assay-specific parameters from each ROI. Validation of the Gaussian curve fits is conducted analytically ($R^2 \geq 0.7$ and signal-to-noise ratio $SNR \geq 3$) and confirmed manually. For the images taken on the Olympus microscope, 1 pixel is $4 \mu\text{m} \times 4 \mu\text{m}$.

Table 3-2. Composition of IEF lid gel.

Components of the 3-part lid gel used for lysis and electrophoresis in the ultrathin IEF assay.

Lid gel components	pH 4 anolyte	Focusing region	pH 10 catholyte
Polyacrylamide gel	15% T 3.3% C 0.2% VA-086	15% T 3.3% C 0.2% VA-086	15% T 3.3% C 0.2% VA-086
IEF reagents and detergents		0.4% final SinuLyte® ampholytes 1% TritonX-100	
Boundary conditions	13.5 mM pKa 3.6 immobiline 6.4 mM pKa 9.3 immobiline		5.6 mM pKa 3.6 immobiline 14.4 mM pKa 9.3 immobiline

Immunoprobng Efficiency

Assessment of immunoprobng efficiency in hydrated gels was conducted as previously described.^{81,82} Briefly, gels on full glass slides were rinsed in DI water, dried with a nitrogen stream, and assembled into a 16-well Array-It Hybridization Cassette (2 columns of 8 wells each). The gel region in each well was rehydrated in 100 μL 2% BSA / TBS-T for 30 min. Each well in the left column was exposed to 50 μL of 200 nM tGFP protein diluted in 2% BSA / TBS-T for 30 min, while each well in the right column was exposed to 50 μL of 2% BSA / TBS-T as blanks. Proteins were immobilized to the photoactive gel by application of 18 mW/cm^2 UV for 300 s using the OAI Model 30 Collimated UV light source.

After gels were rinsed in TBS-T for 30 min to remove uncaptured molecules, the gels were immunoprobnged for tGFP using a standard immunoprobng protocol.⁴⁸ Briefly, gels were exposed to 80 μL of 1:10 dilution of primary rabbit-anti-tGFP antibody in 2% BSA / TBS-T (667 nM and 1:10 dilution of secondary donkey-anti-rabbit-647 antibody in 2% BSA/TBS-T (1333 nM in solution).

Gels were imaged on the GenePix 4300A microarray scanner (Molecular Devices) for native GFP fluorescence in the 488 channel and immunoprobnged fluorescence signal in the 647 channel. Images were analyzed using an in-house Fiji script. Briefly, each well was segmented into a region of interest (ROIs) avoiding edge effects, and background-

subtracted using the average “background” intensity in an adjacent blank ROI, for which the “background” was the gel autofluorescence in the absence of protein. This analysis yielded average fluorescence intensity and immunoprobng efficiency from each ROI. The SNR for each ROI was calculated by defining the “signal” as average fluorescence intensity in the protein-containing ROI, and the “noise” as the standard deviation of the “background” defined above. For the images acquired by the GenePix scanner, 1 pixel is 5 $\mu\text{m} \times 5 \mu\text{m}$.

Statistical Analysis

To compare the means of the 3+ gel conditions in this study, we first assessed for normality using a Q-Q test. After identification that the distributions of means did not follow a normal distribution, we assessed statistical significance using a one-way ANOVA’s with Kruskal-Wallis test. To compare pairs of gel conditions, we applied a post-hoc Dunn’s multiple comparison test with $p < 0.05$ (*), using GraphPad Prism version 8.1.1. The number of experimental replicates ($n = 3$ gels) was determined *a priori*. Linear regression fit was performed using an in-house MATLAB script.

3.3 Results and Discussion

We assessed three key functions of the laterally aggregated, photoactive PA gels in immunoprobng IEF: (i) acting as an anti-convective medium during IEF, (ii) acting as a scaffold for UV-induced immobilization of IEF bands, and (iii) facilitating heterogeneous immunoassays of the immobilized protein targets. The following sections investigate each aspect, starting with a physical characterization of the gel formulations.

Physical Characterization of Highly Porous PA Gels

For this study, we designed and fabricated a panel of PA gel formulations comprised of **highly porous PA gels** polymerized in the presence of hydrophilic polymer (0.5% - 2.0% 10 kDa PEG, 6%T, 8%C), **negative control gels** (0% PEG, 6%T, 8%C), and **benchmarking gels** (0% PEG, 6%T, 3.3%C). Three notes on rationale: first, benchmarking gels were included to facilitate comparison of this study to other immunoprobng IEF studies¹⁹. Second, as compared to the benchmarking gel formulations, the highly porous PA gel formulations contain an increased bis-acrylamide crosslinker concentration for mechanical robustness, with APS/TEMED polymerization conditions consistent among all gel formulations (**Table 3-1**). Third, PA gel porosity increases both via incorporation of PEG at increasing molecular weights and increasing concentration.⁷⁰ For this study, we chose to selectively vary the concentration of 10 kDa PEG with the PA gel precursor solution, because lower molecular weight PEG requires higher PEG concentrations to induce lateral aggregation (e.g., 25% for 1 kDa PEG).⁷⁰

After gel fabrication, we sought to characterize the dependence of matrix porosity on PEG concentration. Using the equilibrium swelling ratio assay, we first sought to validate the relevance of the assay to the gel formulations under study (**Figure 3-1**). To address this question, we observed a slight gel swelling as PEG diffuses out of the PA gels during equilibration of a newly-fabricated gel with a surrounding solution (**Figure**

3-2). The slight swelling suggests extensive water retention. As compared to the dry dehydrated state, the swelling confirms that the equilibrium swelling ratio assay is applicable to scrutinize the highly porous PA gels.⁸⁰

Next, using the equilibrium swelling ratio assay, we can determine the equilibrium swelling ratio (Q) defined in **Equation 3-1**, where mass hydrated gel and mass dehydrated gel are the mass of each gel when measured in the hydrated and dehydrated states, respectively^{47,77,78}.

$$Q = \frac{\text{mass}_{hydrated\ gel}}{\text{mass}_{dehydrated\ gel}}$$

Equation 3-1. Equilibrium swelling ratio in PA gels.

In first comparing benchmarking gels to negative control gels, we observed a decrease in Q with the increase in bis-acrylamide crosslinker concentration (**Figure 3-3**). Comparison of Q values in the PA gel formulations studied here fall into the range of previously reported values for PA gels with 0% PEG (Q = 17.63±0.83; PA gel 10%T, 3%C gel formulation; different chemical polymerization⁸³). In comparison to the benchmarking gel formulation (3.3%C), we observed slightly increased opacity in the negative control gel formulation and highly porous PA gel formulations, all of which contained 8%C bis-acrylamide.

In next comparing the negative control gels (0% PEG) to the highly porous PA gels, we observed a statistically significant increase in Q for the 2% PEG highly porous gel formulation (p < 0.05, **Figure 3-3**). Similarly, comparison to the benchmarking gel showed a significant increase in Q for the 2% PEG gel (p < 0.05, one-way ANOVA performed with Kruskal-Wallis test and post-test Dunn’s multiple comparison test). Swelling behavior in the highly porous PA gel formulations is corroborated by similar behavior in highly porous PA matrices observed by other groups.⁷⁴

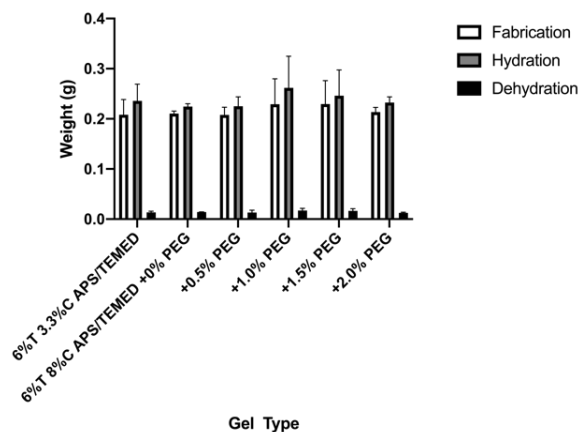


Figure 3-2. Gel weights measured in the equilibrium swelling ratio experiment.

The weight of the gels was measured immediately after fabrication, after incubation in solution to equilibrium, and after drying. Mean and standard deviation depicted for n=3 gels.

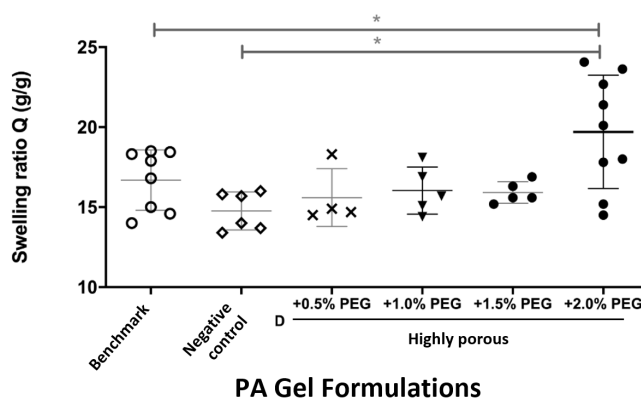


Figure 3-3. Characterization of highly porous PA gels.

Equilibrium swelling ratio reports larger average pore size in 2% PEG-containing PA gel formulations. Swelling ratio (Q) for benchmark gel formulation (0% PEG, 6%T, 3.3%C) is 16.7 ± 1.89 , for negative control gel formulation (0% PEG, 6%T, 8%C) is 14.8 ± 1.19 and for highly porous PA gels (0.5% to 2.0% PEG, 6%T, 8%C) is maximum at 19.7 ± 3.54 for the 2% PEG formulation. Mean and standard deviation; $n=4-9$ gels; significance determined by one-way ANOVA with Kruskal-Wallis test and post-test Dunn's multiple comparison test with $p < 0.05$ (*).

Taken together, the inclusion of 2% PEG in the PA gel formulation significantly increases Q , indicating an increase in gel porosity as desired. Consequently, our study focuses on this gel (2% PEG, 6%T, 8%C) as the matrix through which to understand the three key functions of the gel in immunoprobed IEF: as an anti-convective medium, a scaffold for protein immobilization, and an immunoassay substrate.

IEF in Highly Porous PA Gels

Next, to understand the PA gel formulations as anti-convective media for IEF, we investigated IEF behavior during the focusing and equilibrium stages, for an ampholyte system. During IEF focusing, proteins electrophorese along a pH gradient to the point in the gradient that matches the isoelectric point (pI) of that respective species (i.e., the pH at which a protein molecule is net neutrally-charged). Once at the pI position, IEF balances diffusive band broadening with a restorative electrophoretic force, thus forming a pseudo-equilibrium electrophoretic separation.^{16,84-86} The pH gradient follows the law of pH monotony.¹⁶ Performing IEF in a matrix reduces convection-associated dispersion along the separation axis, yielding sharply-focused protein bands.⁸⁷ In addition to affecting convection, the PA gel porosity should affect the electrophoretic mobility and diffusivity of target species (and ampholytes), under certain conditions.

We first characterized the formation and stability of IEF pH gradients formed in the benchmarking, negative control, and 2% PEG PA gel formulations. To monitor IEF, we included three fluorescently labeled pI markers ($pI = 4.5, 5.5,$ and 6.6) as indicators of pH gradient formation (**Figure 3-4**). As a proxy for the duration required to establish a stable pH gradient, we monitored until the stable formation of a Gaussian concentration distribution for each pI marker. In the negative control and 2% PEG PA gel formulation

(8%C), the focusing time was ~5 min. In the benchmarking gel formulation (3.3%C), the focusing time was ~7.5 min. In all cases, the electrical current decreased during the same periods of time, as expected as ampholytes form a pH gradient (**Figure 3-5**).^{35,84}

PA gels are known to support cathodic drift during and after IEF pH gradient focusing. The drift of the stable pH gradient is generated by electroosmotic flow arising from applying an electric field to a fluid in a PA gel matrix, which includes slightly negatively charged polyacrylamide chains.⁸⁸ To estimate the cathodic drift velocity, we measured the velocity of the 6.6 pI marker (from the 7.5 min to 10 min timepoint of elapsed IEF time) in IEF performed in the benchmarking, negative control, and 2% PEG PA gel formulations. We observed a statistically significant difference in the drift velocity of the pI marker between the benchmarking (6%T, 3.3%C) and negative control (6%T, 8%C) gel formulations (benchmarking gel: 0.06±0.02 mm/min; negative control: 0.17±0.01 mm/min; mean ± standard deviation; n=3 gels; one-way ANOVA with Kruskal-Wallis test and post-test Dunn's multiple comparison test, **Figure 3-6**). Reported values of cathodic drift during IEF in PA gels are similar (i.e., 0.021±0.003 mm/min in thin-film IEF,²⁰ ~0.07 mm/min in microchannel IEF,³⁶ and ~0.1 mm/min in slab IEF⁸⁸). Finally, in considering the 2% PEG gels, we observed a cathodic drift velocity of the pI marker (0.08±0.02 mm/min) that was not statistically different from the benchmarking or negative control gel formulations, thus indicating that the 2% PEG PA gel formulation reduces convection during IEF, as desired. We hypothesize that the negative control gels, with increased bis-acrylamide content compared to the benchmarking gels, might exhibit increased negative charge per unit volume, yielding increased electroosmotic flow through the PA gel and increased drift velocity.

Time	Benchmarking gel	Negative control gel	2% PEG Highly porous gel
Brightfield			
0 min IEF			
1			
2.5			
5			
7.5			
10	 A 4.5 5.5 6.6 B Linear fit $y = 0.36x + 3.3$ $R^2 = 0.93$	 A 4.5 5.5 6.6 B Linear fit $y = 0.37x + 3.0$ $R^2 = 0.93$	 A 4.5 5.5 6.6 B Linear fit $y = 0.38x + 2.46$ $R^2 = 0.91$

Figure 3-4. Characteristic focusing of pI markers in PA gels over time.

Representative inverted micrographs of fluorescent pI markers focusing in IEF pH gradient over the 12 minute timeframe. "A" denotes the edge of the pH 4 boundary condition on the left. pH gradient spans pH 4-7 from left to right. "B" denotes the edge of the pH 10 boundary condition. "4.5," "5.5," and "6.6" denote the pI markers that focus as pH 4.5, 5.5, and 6.6, respectively.

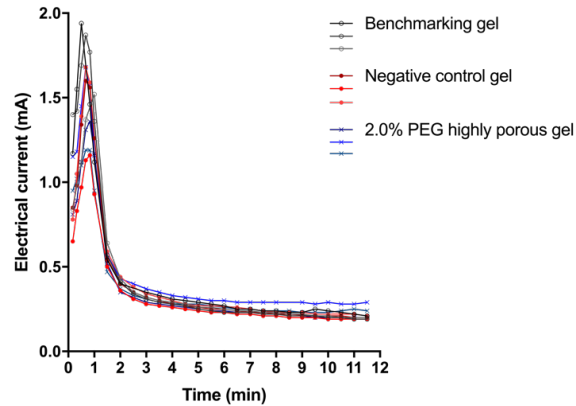


Figure 3-5. Electrical current during IEF.

Each line indicates the electrical current for a single experimental run. Gray lines indicate the benchmarking gels, red the negative control gels, and blue the 2% PEG highly porous gels.

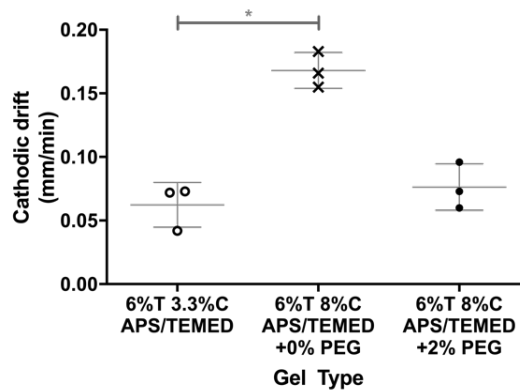


Figure 3-6. Cathodic drift during IEF in highly-porous PA gels.

Cathodic drift is significantly different between the negative control and the 0% PEG gels. Mean and standard deviation marked by vertical lines for $n=3$ gels per condition. One-way ANOVA with Kruskal-Wallis test and post-test Dunn's multiple comparison test was conducted with $p < 0.05$ (*).

We next characterized both the linearity and slope (dpH/dx) of the IEF pH gradient at equilibrium (10 min of elapsed IEF separation time, **Figure 3-7**). The three fluorescently labeled pI markers were here, again, used as indicators of pH gradient (**Figure 3-7A**, **Figure 3-4**). To assess the linearity of each pH gradient, we compared the mean R^2 statistic for linear fits of pI marker value *versus* location along the gradient. We hypothesized no notable impact on either parameter among the three gel formulations, as ampholyte focusing is dependent on the separation axis length, anolyte and catholyte conditions, and the ampholyte composition, not the hydrogel network.¹⁶ We observed no significant difference in the slope or the linearity of the pH gradients, among the three gel formulations (**Figure 3-7B-C**; one-way ANOVA performed with Kruskal-Wallis test and post-test Dunn's multiple comparison test). The linearity and pH gradient slope are similar to previously reported values in anti-convective media.^{19,20}

To conservatively estimate the minimum pI difference for which two neighboring protein peaks are fully resolved¹⁶ (ΔpI_{min}), we assessed the triad of fluorescently labeled pI

markers through the relationship in **Equation 3-2**, where dpH/dx is the slope of the pH gradient and $\sigma_{protein}$ is a measure of the peak quarter-width (i.e., standard deviation of the Gaussian fit to the fluorescence intensity profile when focused). The estimated ΔpI_{min} is considered conservative, as the diffusivity of the pI markers is expected to be substantially larger than a moderate-sized protein. The pI markers studied have molecular masses that are 2 orders of magnitude smaller than a moderate-sized protein (e.g., tGFP at 27,000 Da vs 285 Da for a pI marker). Nevertheless, estimates of ΔpI_{min} using the pI markers give an indication of the expected suitability of IEF resolution in the 2% PEG highly porous PA gels.

$$\Delta pI_{min} = 3 * \frac{dpH}{dx} * \sigma_{protein}$$

Equation 3-2. ΔpI_{min} quantified for proteins focused in an IEF assay.

For the 2% PEG highly porous PA gel formulation, we observed a ΔpI_{min} that was statistically larger than that of the negative control gel formulation (**Figure 3-7D**). The ΔpI_{min} values estimated for the 2% PEG PA gel and negative control PA gel were 0.20 ± 0.03 and 0.12 ± 0.01 (mean \pm standard deviation; $n=3$ gels), respectively. While differences in the ΔpI_{min} between the negative control and benchmarking gels were not statistically significant (one-way ANOVA performed with Kruskal-Wallis test and post-test Dunn's multiple comparison test). The benchmarking PA gel formulation had $\Delta pI_{min} = 0.16 \pm 0.02$.

Next, to estimate a less conservative ΔpI_{min} , IEF analysis was performed on the well-characterized, fluorescent model protein tGFP, which focuses into 2-3 isoform peaks⁶⁷ depending on IEF performance and design. In tGFP analysis via IEF, the 2% PEG highly porous PA gel supported a $\Delta pI_{min} = 0.07 \pm 0.02$ (mean \pm standard deviation; $n=3$ gels, **Figure 3-9B**). The benchmarking PA gel formulation had a $\Delta pI_{min} = 0.11 \pm 0.03$, with a similar ΔpI_{min} measured for the negative control ($\Delta pI_{min} = 0.12 \pm 0.02$). The tGFP protein focused into two isoform peaks⁶⁷ for all replicate IEF analyses in the 2% PEG PA gels, and in one of three replicated in the negative control gels (**Figure 3-8, Figure 3-9A**).

Comparison to other published IEF performance suggests that the 2% PEG highly porous PA gels offer ΔpI_{min} performance *on par* with or exceeding that of commonly used formats, including capillary IEF⁸⁹ and others (benchmarking gels, $\Delta pI_{min}=0.13 \pm 0.02$ using Polybuffer® ampholytes over a pH 4-7 gradient¹⁹; IEF in free solution, $\Delta pI_{min}=0.11$ for adherent-cell IEF platforms using Zoom® ampholytes over a pH 4-7 gradient²¹). Analysis of the 2% PEG highly porous PA gel formulation suggests the matrix is suitable as an anti-convective media for high performance IEF, which is important to resolving protein isoforms and post-translational modifications.

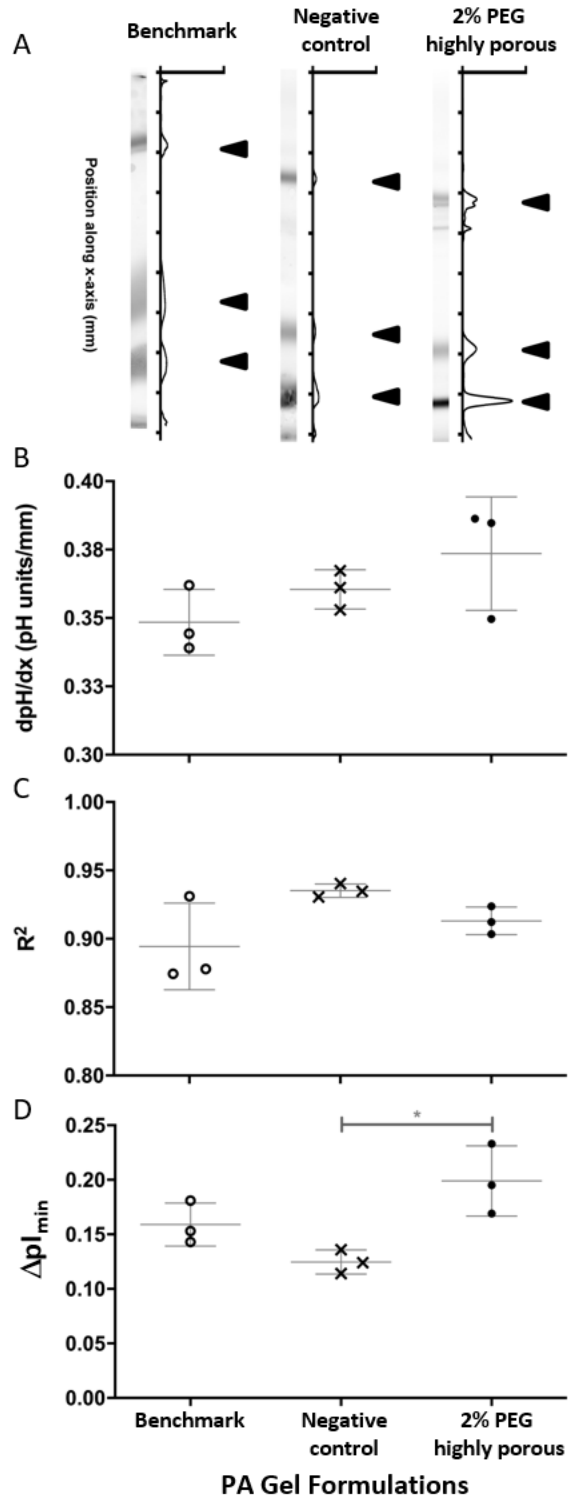


Figure 3-7. Highly porous PA gels are suitable for IEF.

(A) Representative inverted micrographs and intensity plots of IEF-focused pI markers (4.5, 5.5, and 6.6 markers, black arrows) at 10 min elapsed separation time. Y-axis indicates fluorescence intensity. (B) Slope of pH gradient is not significantly different between the gel conditions. (C) R² statistic for linear regression fit of the 3 pI markers is not significantly different between pH gradient linearity between the

gel conditions. (D) The minimum resolvable pI difference (ΔpI_{min}) is significantly different between highly porous PA gel formulations with 0% PEG (negative control) and 2% PEG. For all graphs, mean and standard deviation marked by horizontal lines for n=3 gels per condition. One-way ANOVA with Kruskal-Wallis test and post-test Dunn's multiple comparison test was conducted with $p < 0.05$ (*).

Immunoprobng Efficiency in Highly Porous PA Gels

After IEF analysis, focused proteins are immobilized and probed using an immunoassay to complete the immunoprobed IEF assay. The PA gel formulations studied here have been designed to support in-situ immunoprobng, a transfer-free immunoblotting design. Transfer-free blotting reduces losses during re-solubilization of IEF-focused protein targets, which is advantageous to the analytical sensitivity of the IEF assay. In-situ immunoprobng uses the PA gel matrix as a scaffold for protein target immobilization, followed by an in-gel immunoassay on each immobilized protein target. Light-based blotting (immobilization) toggles the IEF matrix from an anti-convective media to the immobilization scaffold. One common approach to light-based blotting uses photoactivation (UV) of a light-sensitive monomer polymerized into each PA gel (i.e., benzophenone N-[3-[(3-benzoylphenyl)formamido]propyl] methacrylamide, BPMA). Upon UV activation, BPMA abstracts hydrogen from neighboring C—H bonds, thus irreversibly crosslinking protein targets to the gel matrix.^{3,90}

For the transfer-free immunoblotting design, we first assessed each PA gel formulation as an immobilization scaffold. We define photocapture efficiency, η , in **Equation 3-3**, where $tGFP_{pre-immobilization}$ and $tGFP_{post-immobilization}$ are the areas-under-the-curve (AUCs) of focused protein (tGFP) before exposure of the protein peak to UV light and after exposure to UV light, respectively (**Figure 3-9A**).

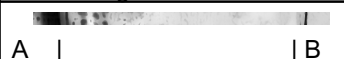

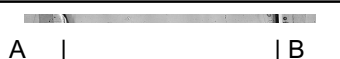





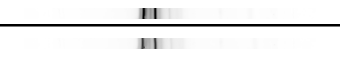
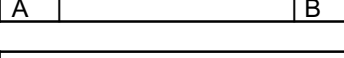
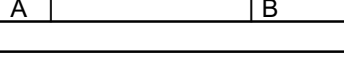
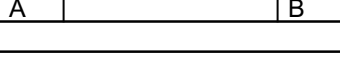



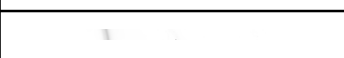




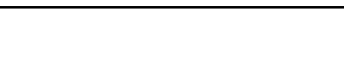
Time	Benchmarking gel	Negative control gel	2% PEG Highly porous gel
Brightfield			
3.5 min IEF			
6			
8.5			
11			
Post-immobilization Brightfield			
Post-immobilization			

Figure 3-8. Characteristic tGFP protein focusing in PA gels over time.

Representative inverted micrographs of purified recombinant tGFP protein focusing in IEF pH gradient over the 12 minute timeframe. “A |” denotes the edge of the pH 4 boundary condition on the left. pH gradient spans pH 4-7 from left to right. “| B” denotes the edge of the pH 10 boundary condition.

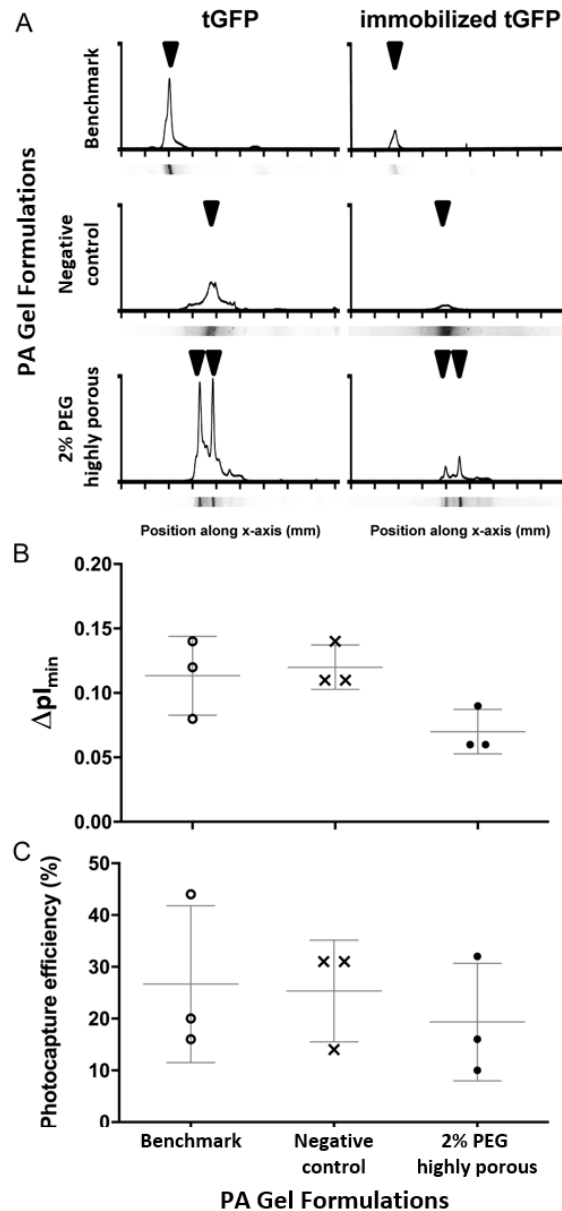


Figure 3-9. Characterization of photocapture efficiency in highly porous PA gels.(A) Representative inverted micrographs and intensity plots of IEF-focused tGFP (arrows) at 11 min of IEF (left) and after tGFP immobilization and wash (right). Y-axis indicates fluorescence intensity. (B) Estimated minimum resolvable pI difference, using the most abundant isoforms, shows no significant difference between gel formulations. (C) tGFP photocapture efficiency (η) over all tGFP isoforms indicates no significant difference. For all graphs, mean and standard deviation marked by vertical lines for $n=3$ gels per condition. One-way ANOVA with Kruskal-Wallis test and post-test Dunn's multiple comparison test was conducted with $p<0.05$ (*).

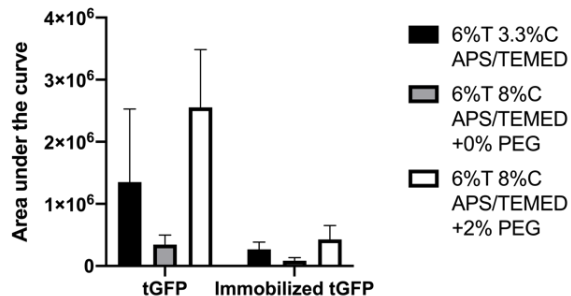


Figure 3-10. Measurement of fluorescent intensity area-under-the-curve in photocapture efficiency measurements in PA gels.

tGFP AUC indicates high technical variation from the pre-immobilization measurement. Mean and standard deviation reported for $n=3$ gels per condition. One-way ANOVA with Kruskal-Wallis test and post-test Dunn's multiple comparison test was conducted with $p < 0.05$ (*).

We expect the increased pore size in the highly porous PA matrices to reduce η not due to the dimensions of the pores, but rather due to the sequestration of benzophenone immobilization moieties within the PA bundles. To assess the impact of the pore dimensions on photocapture efficiency, we first use the predicted molar volume of the benzophenone immobilization moiety⁹¹ to estimate that an individual benzophenone group occupies 0.279 nm³ of volume. Using the PA pore sizes from SEM characterization⁷⁰ of 2.5 nm radius for 5%T 4%C PA gels and 250 nm radius for 5%T 4%C + 2% PEG PA gels, we estimate that benzophenone groups occupy 0.084% of the volume of a single pore in a negative control PA gel, and similarly 0.084% of the volume of a single pore in the highly porous 2% PEG PA gels. This estimate assumes that the incorporation rate of hydrophobic BPMA into the hydrophilic PA chains during gel polymerization is not disrupted by the presence of hydrophilic PEG and the resultant lateral chain aggregation of PA in the highly porous 2% PEG gels. Thus, the same benzophenone occupancy would occur in these PA gels regardless of pore dimensions. Given a diffusivity of tGFP in a 6%T 3.3%C gel as $D = 31.3 \mu\text{m}^2/\text{s}$ ⁶⁷, we estimate the time for tGFP diffusing across a single pore to be 4 orders of magnitude smaller than the 45 s of UV-induced immobilization. The limiting factor affecting photocapture efficiency therefore is not the dimension of the pore, but rather the number of active BPMA sites on the surface of the large PA pores for protein immobilization.

Competitive occupation of the active BPMA sites for protein immobilization is of concern in the ultrathin IEF platform. During IEF and protein photocapture, the PA gels contain not only the 3.7 μM tGFP protein used as a model protein in this study, but also the ampholytes solution and TritonX-100. During the IEF stage, the 4 mM total solution of ampholytes stacks into individual bands of each ampholyte to form the pH gradient. During subsequent UV activation of BPMA, these ampholytes would likely compete with tGFP, and over any protein species of interest, for those active BPMA sites. However, this assessment is limited by a lack of information on the concentration distribution of commercially available ampholytes, as well as the relative binding affinity of each ampholyte species to BPMA.

We experimentally quantified η in these gels. Across all three gel formulations, no difference was measured in the η values (benchmarking gels, $\eta = 27 \pm 15\%$; negative control gels, $\eta = 25 \pm 10\%$; 2% PEG gels, $\eta = 19 \pm 11\%$; mean \pm standard deviation; $n=3$ gels, **Figure 3-9C**). Using the benchmarking gel formulation, immunoprobed IEF on tGFP from single mammalian cell lysate (a more complex sample matrix) was performed with $\eta = 17 \pm 1.5\%$.¹⁹ Note that the protein loading was not designed to control the total volume (and concomitantly, mass) of sample introduced to the gel (**Figure 3-10**). The CV (calculated as the standard deviation divided by the mean) of the pre-immobilization tGFP AUC was quantified as 87% for the negative control gels, 44% for the 0% PEG gels, and 36% for the 2% PEG gels. The CV of the post-immobilization tGFP AUC was 42% for the negative control gels, 56% for the 0% PEG gels, and 52% for the 2% PEG gels. Analyses of η for the 2% PEG highly porous PA gel formulation suggests that this material is a suitable scaffold for UV-induced protein immobilization.

$$\eta = \frac{AUC \text{ tGFP post - immobilization}}{AUC \text{ tGFP pre - immobilization}}$$

Equation 3-3. η for proteins immobilized in the PA gels using the benzophenone moiety.

For the transfer-free immunoblotting design, we next assessed the performance of the in-situ immunoassay (immunoprobings) step. Performing an immunoassay on target immobilized in a hydrogel brings makes consideration the thermodynamic partitioning (K) characteristics of the hydrogel important. Gel microarchitecture affects the size-exclusion phenomena observed with small-pore gels and large-molecular-weight soluble species.^{69,92,93} Typically dominated by size-exclusion mechanisms, the thermodynamic partitioning reduces the concentration of immunoprobe in the gel, as compared to in free solution, and impacts binding kinetics of the immunoassay. In turn, the concentration of immunoprobe in the gel impacts the analytical sensitivity of the immunoprobed IEF assay, as well as reagent consumption.

First, given the relationship between PEG concentration and resultant porosity of each PA gel formulation, we sought to measure the partition coefficient (K) of a canonical immunoprobe (IgG*, a fluorescently labeled primary antibody), using the following relationship^{69,77,92} in **Equation 3-4**. Here, IgG* fluorescence_{gel} is the fluorescent signal from the labeled immunoprobe in the gel, IgG* fluorescence_{solution} is the fluorescence signal of the labeled immunoprobe in the gel, autofluorescence_{gel, blank} is the background autofluorescence in the gel without IgG*, and autofluorescence_{solution, blank} is the autofluorescence in the solution without IgG*.

$$K = \frac{IgG^* \text{ fluorescence}_{gel} - \text{autofluorescence}_{gel, blank}}{IgG^* \text{ fluorescence}_{solution} - \text{autofluorescence}_{solution, blank}}$$

Equation 3-4. Partition coefficient K for IgG* in PA gels.

As PEG concentration increases, we anticipate K will also increase. Increased K directly increases the concentration of immunoreagent available for the downstream immunoassay, impacting assay sensitivity.⁶⁹ The value of K ranges from 0 (no entry of the soluble species into the gel at equilibrium) to 1.0 (near-equivalent concentrations of

the soluble species between free solution and the gel at equilibrium) for species with no specific interactions with the gel network.

As reported in **Figure 3-11**, we observed a partition coefficient for the 2% PEG highly porous PA gels that was significantly larger than both the benchmarking gels and negative control gels (benchmarking gels, $K = 0.11 \pm 0.01$; negative control gels, $K = 0.20 \pm 0.01$; 2% PEG highly porous PA gels, $K = 0.35 \pm 0.02$; mean \pm standard deviation; $n = 3-6$ gels). The observed K values are corroborated by wide-field epifluorescence microscopy of PA gel formulations similar to our benchmarking gel formulations.³ Characterization of PA gels created under lateral chain aggregation conditions by scanning electron microscopy (SEM) reports similar porosity.⁷⁰

The two-fold increase in K between the benchmarking gels and negative control gel is hypothesized to arise from bis-acrylamide aggregating into bundles in the higher %C formulation, as has been previously observed (20%C and 60%C PA gels)⁹⁴, and corroborated by freeze-etched transmission electron microscopy (TEM) of similar PA gel formulations⁹⁵ and an observed decrease in elastic modulus⁹⁶ (10%C PA gels versus lower %C PA gels).

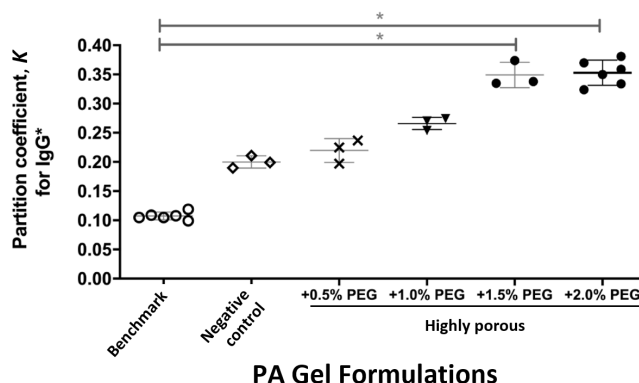


Figure 3-11. Partition coefficient, K , is sensitive to PA gel formulation.

Partitioning of AlexaFluor-647-labeled donkey-anti-rabbit antibody (IgG*) into the hydrogel network indicates a statistically significant increase in K due to the gel formulation and incorporation of the PEG. Mean and standard deviation marked for $n=3-6$ gels per condition.

Lastly, we sought to compare the dependence of background signal on the gel formulation, after in-gel immunoassay completion. Background signal can be attributed to immunoprobe retained in the PA gel after each round of washing. High background signal can degrade detection sensitivity and is an acute challenge in PA gel immunoassay formats. Here, we considered an immunoassay probed by an unlabeled primary polyclonal antibody to the target, followed by detection using a fluorescently labeled secondary polyclonal antibody. We sought a well-characterized protein target, and so opted to employ the naturally fluorescent tGFP protein.

The post-immunoassay background signal in the 2% PEG highly porous PA gels was 2x and 3x lower than background signal measured in the benchmarking gels and negative

control gels, respectively (benchmarking gels, 1850 ± 1060 AFU; negative control gels, 1290 ± 380 AFU; 2% PEG highly porous PA gels, 606 ± 72 AFU). We attribute the lower background measured in the highly porous PA gels to reduced entropic trapping of antibody probes in these larger pore size matrices. Freely diffusing molecules are known to become trapped in regions of hydrogel pore-size inhomogeneity.⁹³ In these larger pore size regions, molecules can be trapped in a free energy minimum. Entropic trapping is particularly relevant for macromolecules of intermediate size.⁹³ Immunoreagents such as antibodies (5-8 nm hydrodynamic radius^{97,98}) would be expected to be entropically trapped in the negative control PA gels (5-92 nm mean pore radius^{70,71}). In the 2% PEG highly porous PA gels, however, the estimated mean pore radius is substantially larger (~ 250 nm; **Figure 3-1C**).⁷⁰

The observed decrease in background signal during immunoprobings in the 2% PEG highly porous PA gels is attributed to reduced entropic trapping of antibody probes in hydrogel. Reduced entropic trapping would facilitate more effective washout of both the primary and secondary antibodies during the immunoprobings steps. Overcoming the high post-immunoprobings background signal makes the 2% PEG highly porous PA gels an attractive material in which to perform immunoprobings IEF.

3.4 Conclusions

We sought to design a PA gel to enhance performance of the immunoassay stage of immunoprobings IEF, while maintaining the separations performance of IEF stage. Here, we utilized lateral aggregation during PA gel polymerization to increase the mean pore size of PA gels. To do this, we devised PA gel formulations that included the hydrophilic polymer PEG. We validated that we created significantly larger porous PA gels and observed a significant increase in antibody partitioning into the gel matrix. Comparing the highly porous polyacrylamide gel to benchmarking gels (utilized in previous immunoprobings IEF assays), we observed no significant impact on the formation or stability of the IEF pH gradient, and an improvement in separation resolution. Consequently, the highly porous PA gels are suitable for IEF analysis of protein targets. In the subsequent immunoassay stage, the large pore size gels allow for more effective washout (removal) of unbound immunoreagent at immunoassay completion. The highly porous PA matrices therefore serve to support high performance IEF separations while providing an immobilization scaffold that is well-suited for heterogeneous immunoassays needed for selective target readout.

Chapter 4: Isoelectric Focusing Performance in Highly-Porous Polyacrylamide Gels Polymerized with Different Initiators

This work was performed in collaboration with Dr. Kevin A. Yamauchi.

4.1 Introduction

Since the development of isoelectric focusing (IEF) in the 1960's by Svensson and Vesterberg, extensive research has gone into the design of an ideal substrate specifically for IEF as an analytical assay. Polyacrylamide (PA) gels serve as an anti-convective substrate for IEF-based separations of proteins.¹⁶ As a precursor to investigating the performance of the IEF immunoblot in highly porous PA gels (**Chapter 3**), we considered the mechanism by which these highly porous PA gels were created. In Righetti et al,⁷⁰ the pre-formed polymer poly(ethylene glycol) (PEG) was incorporated into the gel precursor solution as a porogen. During polymerization, acrylamide monomers form chains that are interconnected and stabilized by bis-acrylamide crosslinkers, resulting in a randomly-organized three-dimensional hydrogel network of heterogeneous pore size on the order of 2.5 nm. The hydrophilic PEG induces lateral aggregation of the PA chains into bundles at an estimated 150 nm radius. After polymerization, the PEG freely diffuses out of the PA gel matrix, creating large water-filled voids of an estimated mean pore radius of 250 nm, and much smaller pores within the PA bundles.⁷⁰

The mechanism for inducing PA gel polymerization in Righetti et al⁷⁰ is one of the canonical initiator/catalyst pairs for free radical polymerization of hydrogels, ammonium persulfate (APS) and N,N,N',N'-tetramethylethylenediamine (TEMED). The timeframe of PA polymerization by APS/TEMED is reported to be ~15-20 min for initial gel stability and ~ 2 hours for reaction completion.⁷⁵ During this extended timeframe, the diffusion of PEG out of the gel matrix into the free solution sink may result in the partial collapse of the laterally aggregated PA chains in the gravitational field. Thus, we investigated if use of a photoinitiator to rapidly initialize gel polymerization would result in larger pores in the PA gel matrix. Specifically, we considered two photoinitiators: 2,2'-azobis[2-methyl-N-(2-hydroxyethyl)propionamide] (VA-086)^{99,100} or lithium phenyl-2,4,6-trimethylbenzoylphosphinate (LAP).¹⁰¹ LAP exhibits increased absorbance within visible light and near-UV ranges, resulting in more rapid activation of the initiators in the PA precursor solution and subsequently more rapid PA gel polymerization, compared to VA-086.

In this study, we interrogated how different gel chemistries, from bis-acrylamide content and polymerization initiators to the incorporation of PEG as a porogen, change gel microstructure. To characterize use of these gels for the recently-developed IEF immunoblot assay,¹⁹ we investigated both antibody partitioning into the gels and the performance of IEF within these modified PA gels.

4.2 Materials and Methods

Reagents

Borofloat wafers (University Wafer 516), SU8 3050 photoresist (MicroChem), titanium diisopropoxide bis(acetylacetonate) (Sigma 325252), anhydrous isopropanol (Sigma 278475), a custom in-house-designed mask (CAD/ART Services), GelSlick® (Lonza 50640), standard glass slides (VWR), dichlorodimethyl silane (Sigma 440272), 3-(trimethoxysilyl)propyl methacrylate (Sigma 440159), methanol (Sigma 179337), glacial acetic acid (Sigma 8817-46), 30%T 29:1 acrylamide/bis-acrylamide solution (Sigma A3574), 40%T 29:1 acrylamide/bis-acrylamide solution (Sigma A7802), bis-acrylamide powder (Sigma 146072), 1.5 M pH 8.8 TrisHCl (TekNova T1588), N-[3-[(3-benzoylphenyl)formamido]propyl] methacrylamide (BPMA, custom synthesized by PharmAgra Labs), ammonium persulfate (APS, Sigma A3678), N,N,N',N'-tetramethylethylenediamine (TEMED, Sigma T9281), UV photoinitiator 2,2'-Azobis[2-methyl-N-(2-hydroxyethyl)propionamide] (VA086, Wako Chemicals 61551), UV photoinitiator LAP (LAP, Allevi), 10 kDa poly(ethylene glycol) (PEG, Sigma 92897), borosilicate glass sheets (McMaster-Carr 8476K62), 4-well plates (ThermoFisher 267061), parafilm (Bemis PM-999), glass coverslips (VWR 48366), and permanent lab markers (VWR 52877-310) were used to fabricate materials in this study.

IEF was conducted using the immobilines pKa 3.6 and pKa 9.3 acrylamido buffers (Sigma 01716, 01738), SinuLyte® pH 4-7 ampholytes (Sigma 05087, lot BCBJ7449V), an ABS electrophoresis device designed and printed in-house, graphite electrodes (Bio-Rad 1702980), 0.5 mm gel spacers (CBS Scientific MVS0510-R), and TritonX-100 detergent (Sigma X100). Tris-buffered saline with Tween-20 (TBS-T, CST 9997S) was used for gel incubation and wash steps. Urea (Sigma U5378), thiourea (Sigma T8656), and CHAPS (SAFC RES1300C) were used as detergents.

The proteins and molecules used in this study were fluorescent pl markers 4.5, 5.5, and 6.6 (Sigma 89149, 77866, 73376), henceforth termed “pl markers,” BSA (Sigma A7030), and purified recombinant turboGFP (Evrogen FP522, lot 55201240718) termed “tGFP” (a variant of the GFP with increased fluorescence, MW 27 kDa), and secondary polyclonal antibody AlexaFluor-647-labeled donkey-anti-rabbit (Invitrogen A-31573) termed “IgG*.” The IgG* degree of labeling is reported by the manufacturer as 5 fluorophores per molecule for lot 1964354 (Invitrogen).

Wafer and Gel Fabrication

SU8 fabrication on a borofloat wafer was conducted following a standard protocol.³ Briefly, a custom mask with rails spaced 22 mm apart was used to fabricate features of 40 μm in height (confirmed by optical profilometry) in SU8 on the wafer. After wafer treatment with GelSlick®, PA gels were fabricated on the wafer and polymerized onto silanized half glass slides. **Table 4-1** lists the critical components of each gel condition, using 10 kDa PEG as the preformed hydrophilic polymer and leveraging porogen gel fabrication conditions developed by Righetti and colleagues.⁷⁰ Chemical polymerization was implemented using APS and TEMED as the initiator and catalyst, respectively. Photopolymerization was implemented using VA-086 or LAP as the initiator and polymerized for 4 or 1 minutes, respectively, at 20 mW/cm² light intensity using a 390 nm UV long-pass filter (Edmund Optics) on an OAI Model 30 Collimated UV light source. See **Appendix 1** for further details.

Table 4-1. Composition of polyacrylamide gels with different chemistries.

Primary components of all gel conditions used in this study, following standard gel fabrication techniques in ⁴⁸. Highlighting and bolding indicate modifications from the 6%T 3.3%C APS/TEMED gel condition, for ease of comparison between PA gel conditions.

Gel nomenclature	3.3%C APS/TEMED	8%C APS/TEMED	8%C APS/TEMED + 2.0% PEG
Acrylamide content	6%T	6%T	6%T
Bisacrylamide : acrylamide ratio	3.3%C	8%C	8%C
10 kDa PEG	0.0%	0.0%	2.0%
Polymerization chemistry	APS / TEMED	APS / TEMED	APS / TEMED
BPMA photo- immobilization moiety	5 mM	5 mM	5 mM

Gel nomenclature	3.3%C APS/TEMED + 2.0% PEG	3.3%C VA-086 + 2.0% PEG	3.3%C LAP	3.3%C LAP + 2.0% PEG
Acrylamide content	6%T	6%T	6%T	6%T
Bisacrylamide : acrylamide ratio	3.3%C	3.3%C	3.3%C	3.3%C
10 kDa PEG	2.0%	2.0%	0.0%	2.0%
Polymerization chemistry	APS / TEMED	VA-086	LAP	LAP
BPMA photo- immobilization moiety	5 mM	5 mM	5 mM	5 mM

Gel nomenclature	8%C LAP +0.0% PEG	8%C LAP + 0.5% PEG	8%C LAP + 1.0% PEG	8%C LAP + 1.5% PEG	8%C LAP + 2.0% PEG
Acrylamide content	6%T	6%T	6%T	6%T	6%T
Bisacrylamide : acrylamide ratio	8%C	8%C	8%C	8%C	8%C
10 kDa PEG	0.0%	0.5%	1.0%	1.5%	2.0%
Polymerization chemistry	LAP	LAP	LAP	LAP	LAP
BPMA photo- immobilization moiety	5 mM	5 mM	5 mM	5 mM	5 mM

After fabrication, gels were incubated for 16-24 hours in 1× TBS-T to allow for diffusion of soluble PEG porogen out of the PA gel network, thus forming large water-filled voids, then rinsed in DI water for 30 minutes before use.

For this study, we use the canonical notation of %T as the total acrylamide monomer concentration (w/v) in solution, and %C as the ratio of bis-acrylamide crosslinker concentration to the total acrylamide monomer concentration.⁴⁷ We distinguish the many PA gel conditions by %C, polymerization chemistry, and %PEG content, as outlined in **Table 4-1**.

Equilibrium Swelling Ratio

The equilibrium swelling ratio was conducted using Flory-Rehner theory.^{47,78–80} After fabrication of PA gels on glass slides with 500 μm spacers to define gel height, gels were weighed immediately on an Ohaus Adventurer Pro weigh station to determine the “fabrication” weight, then incubated in 1× TBS-T for 24 hours for PEG diffusion out of the gel. After 12 hours of DI water incubation, the equilibrated gel was weighed again for the “hydration” weight, dehydrated fully with a nitrogen gas stream, and weighed a third time for the “dehydration” weight.

Thermodynamic Partitioning

We used the thermodynamic partitioning method using wide-field epifluorescence^{3,92} to interrogate IgG* partitioning into the PA gels. We created a device for gel fabrication on a glass slide with 500 μm spacers (CBS Scientific, MVS0510-R) oriented to leave a free solution “well” in the center of the gel. This resulted in total gel dimensions of X = 15 mm, Y = 18 mm, and Z = 500 μm (including the free solution “well”) and free solution “well” dimensions of X = 8 mm, Y = 4 mm, and Z = 500 μm. This gel height was selected to reduce the relative effect of the IgG*-containing free solution fluid layer between the gel and the coverslip during the subsequent imaging. After fabrication of PA gels on silanized half glass slides with 500 μm feature heights, gels were rinsed in TBS-T solution, and exposed to 50 nM of IgG* solution (from 2 mg/mL stock solution from manufacturer, spun down to remove aggregates) in 2% BSA / TBS-T in 4-well plates (5 mL per well containing 3 gels on 1/3 glass slides) sealed with parafilm for 51 hours to equilibrium (3* τ = 22.2 hours). The calculated time to equilibrium (τ = 8.07 hr) was calculated using 1D model of diffusion ($\tau = x^2 / 2D$), where $x = \sim 500$ μm gel height, and $D = 4.3$ μm²/s for the diffusivity of IgG* in an 8%T 2.6%C PA gel.¹⁰² Blank gels were exposed to TBS-T solution in the same method for the same time.

The gels were sequentially removed from solution and assembled for imaging. The bottoms of the glass slides were blotted dry; additional solution was added to the free solution “well,” and a coverslip was gently slid over the entire gel to inhibit dehydration during imaging. The gels were then set on an Olympus IX-71 inverted microscope with an Olympus UPlanFi 4× (NA 0.13) objective and an EMCCD Camera iXon2 (Andor), with imaging settings loaded into MetaMorph software (7.10.1.161, Molecular Devices). The IgG* was imaged using a Cy5 filter cube (49009, Chroma) promptly, and subsequently imaged using brightfield imaging to identify features.

The same gels were subsequently incubated in a detergent solution designed to disrupt hydrogen bonds (7M urea, 2M thiourea, 1% TritonX-100, CHAPS in DI water) in a 4-well plate (5 mL per well containing 3 gels on 1/3 glass slides) overnight for 8-12 hours to equilibrium. The calculated time to equilibrium ($\tau = 26.04$ min) was calculated using 1D model of diffusion ($\tau = x^2 / 2D$), where $x = \sim 500$ μm gel height, and $D=80$ $\mu\text{m}^2/\text{s}$ for the diffusivity of TritonX-100 in free solution.¹⁹ Of the 4 detergents used in this study, TritonX-100 has the lowest free solution diffusivity and therefore the highest time to equilibrate in-gel).¹⁹ After rinsing the gels in TBS-T, the gels were then exposed to the same dilution of IgG* solution as previously described for the same time, assembled, and imaged using the same settings. Images were analyzed using an in-house MATLAB script to extract the average fluorescence intensity of the gel and the free solution.

IEF

The ultrathin IEF was conducted as previously described¹⁹ with minor modifications to accommodate purified protein solutions (further details in **Appendix 3**). Briefly, gels of height 40 μm were briefly rinsed in DI water, with the fluid layer wicked off the top of the gel, then incubated in 40 μL of a solution of 1% each of the pI markers 4.5, 5.5, and 6.6 (from 1-3 mg/mL stock solutions from manufacturer), and 10% tGFP (from 37 μM stock from manufacturer) for 30 minutes at room temperature, protected from light. The 3-component IEF lid was fabricated using a 1:100 dilution of the stock 40% SinuLyte® ampholytes for a final concentration of 0.4%. **Table 4-2** lists the components of the lid gel, which was polymerized for 4 minutes per component (in the order of catholyte, anolyte, and focusing region) at 20 mW/cm² light intensity using a 390 nm UV long-pass filter (Edmund Optics) on an OAI Model 30 Collimated UV light source.

The PA gel and lid gel were assembled in the IEF device previously described,¹⁹ and set on an Olympus IX-71 inverted microscope with an Olympus UPlanFi 4 \times (NA 0.13) objective and a EMCCD Camera iXon2 (Andor), with imaging settings loaded into MetaMorph software (7.10.1.161, Molecular Devices). After a 30 s delay for the soluble reagents in the focusing lid gel to diffuse into the PA gel, IEF was conducted by applying 690 V for 12 minutes using the Power-Pac high-voltage power supply device (HVPS, Bio-Rad 1645056). During this focusing period, pI markers were imaged using a UV-longpass filter cube (XF100-1, Omega Optical) at 2.5 minute intervals, and tGFP was imaged using a GFP filter cube (XF100-3, Omega Optical) 1 minute subsequently. After protein photo-immobilization, gels were rinsed in TBS-T for 30 minutes to remove uncaptured species, and imaged with the same settings. The lab markers used to denote the gel edges along the separation axis is fluorescent in the UV-longpass channel and visible in brightfield imaging.

Micrographs were analyzed using an in-house MATLAB (R2015b, MathWorks) script^{6,48,49} adapted to this microwell-free variant of the IEF (code in **Appendix 11**). Briefly, the micrographs were segmented into regions of interest (ROIs), converted into line plots averaged across the width of the ROI (maintaining the separation axis), and background-subtracted using the average background intensity across the ROI. Gaussian curve fitting to the line plots led to the extraction of the peak height, peak

location, peak width, area under the curve, SNR, and other assay-specific parameters from each ROI. Validation of the Gaussian curve fits is conducted analytically ($R^2 \geq 0.7$ and signal-to-noise ratio $SNR \geq 3$) and confirmed manually. For the images taken on the Olympus microscope setup, 1 pixel corresponds to 4 μm .

Statistical Analysis

To compare the means of the 3+ gel conditions assessed in this study, we first assessed for normality using a Q-Q test. After identification that the distributions of means did not follow a normal distribution, we assessed statistical significance using the one-way ANOVA's with Kruskal-Wallis test. To compare specific pairs of gel conditions, we applied a post-hoc Dunn's multiple comparison test with $p < 0.05$ (*), using GraphPad Prism version 8.1.1. Linear regression fit was performed using an in-house MATLAB script.

Table 4-2. Composition of IEF lid gel.

Components of the 3-part lid gel used for lysis and electrophoresis in this study.

Lid gel components	pH 4 anolyte	Focusing region	pH 10 catholyte
Polyacrylamide gel	15% T 3.3% C 0.2% VA-086	15% T 3.3% C 0.2% VA-086	15% T 3.3% C 0.2% VA-086
IEF reagents and detergents		0.4% final SinuLyte® ampholytes 1% TritonX-100	
Boundary conditions	13.5 mM pKa 3.6 immobiline 6.4 mM pKa 9.3 immobiline		5.6 mM pKa 3.6 immobiline 14.4 mM pKa 9.3 immobiline

4.3 Results and Discussion

Physical Characterization of Highly Porous PA Gels with Different Polymerization Chemistries

For this study, we designed, fabricated, and assessed eleven hydrogel materials. Matching the gel condition previously characterized in ultrathin IEF,¹⁹ the negative control gel contains no PEG porogen and is thus composed of 6%T 3.3%C PA with the polymerization reaction initiated by APS and TEMED. We interrogate the effect of increasing bis-acrylamide crosslinker concentration to provide additional mechanical robustness to the PA gel network (3.3%C versus 8%C). We also interrogate the effect of polymerization initiators (chemical polymerization via APS/TEMED, photopolymerization via VA-086, and photopolymerization via LAP). Finally, in a subset of gel conditions, we incorporated 0.5% to 2% of 10 kDa PEG as the preformed

hydrophilic polymer to create increasingly porous PA gels, as reported in **Table 4-1**. We immersed each gel in a 1× TBS-T solution for 16-24 hours for diffusive removal of PEG, then rinsed in DI water before use. We observed slightly increased opacity in all of the PA gel conditions containing 8%C bis-acrylamide, compared to the gels containing 3.3%C bis-acrylamide.

First, we used the equilibrium swelling ratio assay (**Figure 4-1A**) to indirectly characterize the porosity of the PA gels in this study. We then calculated the unitless metric of swelling ratio (Q) using **Equation 4-1**.^{47,77,78} Q was measured for the full set of gel conditions (16.5±1.94 in 3.3%C APS/TEMED, 27.1±0.99 in 3.3%C APS/TEMED + 2.0% PEG, 46.5±5.52 in 3.3%C VA-086 + 2.0% PEG, 33.5±0.95 in 3.3%C LAP + 2.0% PEG, 17.3±4.05 in 8%C APS/TEMED, 23.5±0.71 in 8%C APS/TEMED + 2.0% PEG, 19.2±1.12 in 8%C LAP + 0.0% PEG, 21.3±0.81 in 8%C LAP + 1.0% PEG, and 23.7±1.00 in 8%C LAP + 2.0% PEG, with mean ± standard deviation; n=3-14 gels, **Figure 4-1B**). The observed Q for four sets of gels were statistically significant from each other: the 3.3%C APS/TEMED vs the 3.3%C LAP + 2.0% PEG, the 3.3%C APS/TEMED versus the 3.3%C VA-086 + 2.0% PEG, the 3.3%C VA-086 + 2.0% PEG versus the 3.3%C LAP + 2.0% PEG, and the 3.3%C VA-086 + 2.0% PEG versus the 8%C APS/TEMED.

The incorporation of 2.0% PEG into the 3.3%C APS/TEMED gel condition increased Q 1.6-fold. Increases in Q were also observed between the 8%C APS/TEMED and 8%C APS/TEMED + 2.0% PEG gel conditions, and between the 8%C LAP and the 8%C LAP + 2.0% PEG gel conditions. These match the expected function of PEG as a porogen to induce lateral aggregation of the PA chains, resulting in a highly porous PA gel network.⁷⁰

Of the 3 gel conditions with 3.3%C and 2% PEG (the second through fourth conditions in **Figure 4-1B**), the gels polymerized with VA-086 exhibited the highest Q and therefore the largest pores, but with increased variation. At this low %C, photopolymerization with either VA-086 or LAP distinctly changed the resulting pore size for these highly porous PA gels, compared to the chemical polymerization via APS/TEMED. Since the polymerization time varies between these two polymerization initiation methods (1-4 min vs 20 min), perhaps this rapid gel photopolymerization is sufficient to stabilize the large pores generated by the phase separation of PEG and PA during polymerization.

Interestingly, this initiator-induced difference in Q did not hold at higher bis-acrylamide concentrations. Specifically, the Q for the 8%C APS/TEMED + 2.0% PEG gels is not statistically significant from that of the 8%C LAP + 2.0% PEG gels (the fifth and last conditions in **Figure 4-1B**). We observed no significant difference in Q between all of the gel conditions with 8%C (the right-most conditions in **Figure 4-1B**), suggesting that this increased bis-acrylamide content might limit the porosity increase observed in the porogen-containing gel conditions.

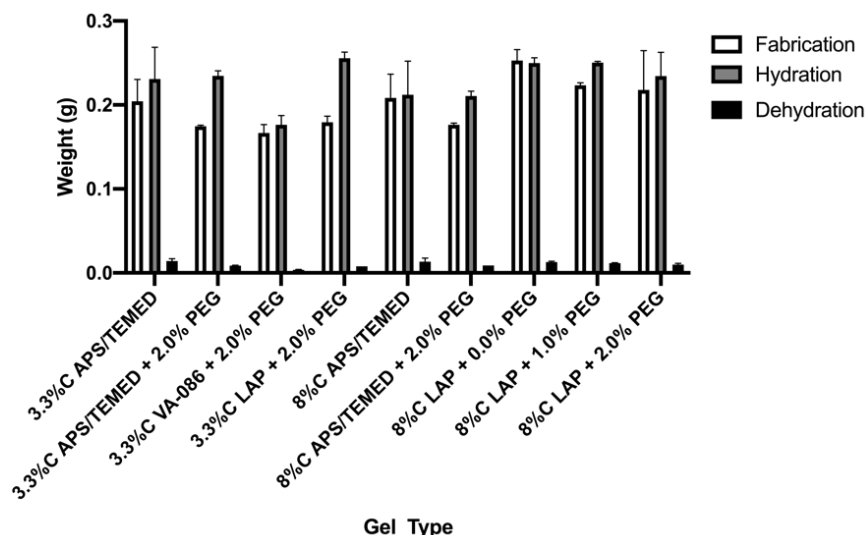
These Q measurements also indicates that by selecting the appropriate polymerization chemistry, PA gel porosity may be easily tunable to suit a range of macromolecule sizes

for electrophoretic cytometry assays. It is important to note that the equilibrium swelling ratio is a bulk measurement taken in open air without control for ambient air temperature or gel dehydration, for which the fabrication and hydration measurements are disproportionately affected; thus, Q serves as an indirect measurement of gel porosity.

$$Q = \frac{\text{mass}_{hydrated\ gel}}{\text{mass}_{dehydrated\ gel}}$$

Equation 4-1. Equilibrium swelling ratio in PA gels.

A



B

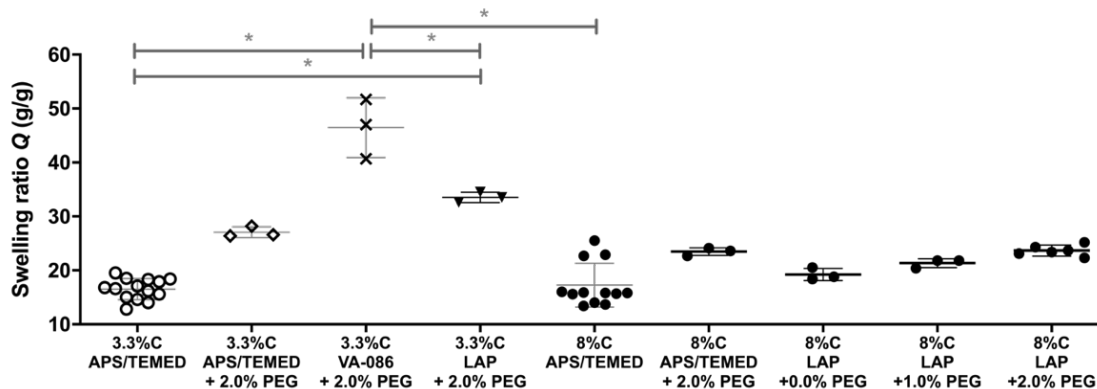


Figure 4-1. Swelling ratio in PA gels polymerized with different polymerization chemistries.

(A) Gel weights measured in equilibrium swelling ratio experiment after fabrication (white); after incubation in solution to equilibrium (gray), and after drying (black). (B) The swelling ratio (Q) varied significantly due to polymerization initiator, bis-acrylamide content, and PEG porogen content at the same 6%T gel composition. This indirectly indicates a change in gel porosity. Mean and standard deviation marked by vertical lines for $n=3-12$ gels per condition. One-way ANOVA with Kruskal-Wallis test and post-test Dunn's multiple comparison test with $p < 0.05$ (*).

Characterization of Partitioning in Highly Porous PA Gels with Different Polymerization Chemistries

Next, we sought to characterize the partition coefficient (K) of AlexaFluor-647-labeled antibody probes (>150 kDa, IgG*) in multiple gel conditions using **Equation 4-2**. K ranges from 0 (no entry of the soluble species into the gel at equilibrium) to <1 (near-equivalent concentrations of the soluble species between free solution and the gel at equilibrium) for species with no specific interactions with the gel network. Increased K directly increases the concentration of immunoreagent available for a subsequent immunoassay, affected assay sensitivity.⁶⁹ K was measured for a range of gel conditions (0.14±0.04 in 3.3%C APS/TEMED, 0.29±0.13 in 8%C APS/TEMED, 0.34±0.09 in 3.3%C LAP, 0.39±0.04 in 8%C LAP +0.0% PEG, 0.41±0.01 in 8%C LAP +0.5% PEG, 0.52±0.02 in 8%C LAP +1.0% PEG, 0.59±0.02 in 8%C LAP +1.5% PEG, 0.74±0.08 in 8%C LAP +2.0% PEG, with mean ± standard deviation; n=3-9 gels pooled from multiple experiments, **Figure 4-2**). We observed a statistically-significant difference between the 3.3%C APS/TEMED gel and the 8%C LAP +1.0%, 8%C LAP +1.5%, and 8%C LAP +2% PEG gels. This significant increase in K in the 8%C LAP +PEG gels not only is an indirect indicator of an increase in gel porosity, but allows for tunability in the desired partitioning behavior of IgG* in a PA gel fabricated using this particular polymerization chemistry, resulting in tunable in-gel immunoblots with IgG*.

A 2.5-fold increase in K was observed between the 3.3%C APS/TEMED and the 3.3%C LAP gel condition. This matches the observation with the Q measurement that gel polymerization chemistry affects gel porosity.

We also observed a large variation in K measurements in the 8%C APS/TEMED gel condition, notably across multiple gels in the same experiment and across multiple experimental runs. Further investigation is needed to identify the source of this variation.

$$K = \frac{[IgG^*]_{gel} - [IgG^*]_{gel,blank}}{[IgG^*]_{solution} - [IgG^*]_{solution,blank}}$$

Equation 4-2. Partitioning of IgG* in PA gels.

It is important to note that the wide-field microscopy method used here to measure the in-gel and in-solution IgG* fluorescence also includes a thin IgG*-containing fluid layer between the hydrated gel and the coverslip on top of the gel. As reported in **Chapter 5**, this fluid layer between a 6%T PA gel and a glass substrate has been quantified as ~1.7 μm. We expect that this IgG*-containing fluid layer on top of the gel would result in a much brighter “gel” fluorescence measurement (via wide-field microscopy) than is accurate, an effect that would be much more muted for the IgG*-containing fluid layer on top of the IgG*-containing free solution “well.” Thus, this particular method of measuring K would be slightly skewed high. This hypothesis has been experimentally validated via quantification of K in the same gels sequentially via wide-field microscopy and confocal laser scanning microscopy (using the latter method, an IgG*-containing fluid layer on top of the gel is visible and verifiable in a z-stack and would not skew the in-gel fluorescence measurement).⁶⁸ As reported in **Chapter 3**, a novel method for measuring K reported vastly differing K values for the same PA gel conditions, fabricated by the same researcher using the same protocol. Specifically, for the 6%T 3.3%C APS/TEMED gel condition, K via wide-field microscopy was measured as

0.14±0.04, while K via confocal laser scanning microscopy was measured as 0.11±0.01 (**Figure 3-3A**). Nevertheless, one still can compare the relative differences in K in PA gels polymerized by different gel conditions reported here by this method.

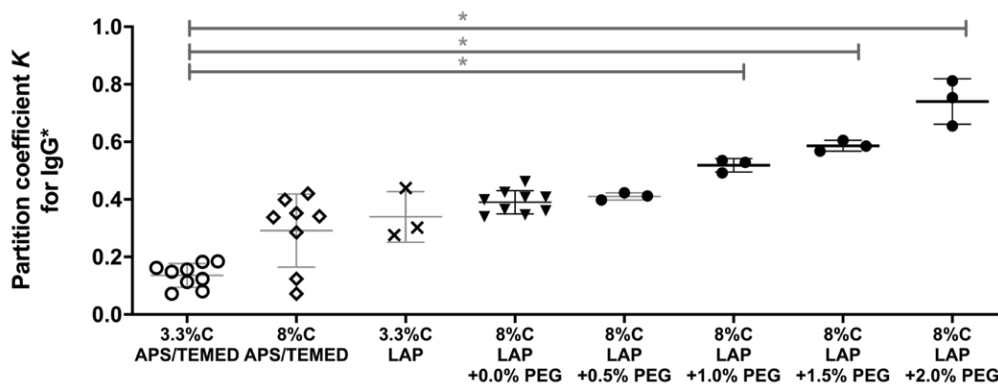


Figure 4-2. Partitioning of IgG* in PA gels with different polymerization chemistries.

Partitioning of AlexaFluor-647-labeled donkey-anti-rabbit antibody (IgG*) into the hydrogel network indicates a statistically significant increase in K due to the combinatorial change in gel bis-acrylamide content, polymerization initiator, and incorporation of the PEG porogen at the same 6%T gel composition. This indirectly indicates a change in gel porosity. Mean and standard deviation marked by vertical lines for $n=3-9$ gels per condition. One-way ANOVA with Kruskal-Wallis test and post-test Dunn's multiple comparison test with $p<0.05$ (*).

Of the gels reported in **Figure 4-2**, a subset was maintained for assessment of the stability of the gel microarchitecture. During hydrogel polymerization, hydrophilic PEG acts as a porogen, resulting in the formation of bundles of laterally aggregated PA chains.^{70,103,104} After hydrogel polymerization, the PEG diffuses out of the PA gel network, which should be stably crosslinked. A small fraction of the PEG is thought to remain in the PA gel as a semi-interpenetrating network, which may inhibit in-gel diffusion of soluble species.⁷² To characterize the stability of the gel microarchitecture, we exposed the gels to a detergent solution (7M urea, 2M thiourea, 1% TritonX-100, and 3.6% CHAPS, matching the denaturing lysis condition for the ultrathin IEF assay). Chaotropes, such as urea and thiourea, disrupt hydrogen bonding but cannot destabilize the covalent bonds of a PA gel. After detergent exposure, we used the same partitioning experiment on these gels, with the expectation that any gel microarchitecture disruption would reduce IgG* partitioning into the gel. K was quantified for the same set of 3 gels per condition before detergent treatment (0.39±0.04 in 8%C LAP +0.0% PEG, 0.41±0.01 in 8%C LAP +0.5% PEG, 0.52±0.02 in 8%C LAP +1.0% PEG, 0.59±0.02 in 8%C LAP +1.5% PEG, 0.74±0.08 in 8%C LAP +2.0% PEG, with mean ± standard deviation; $n=3$ gels, blue data points in **Figure 4-3**) and after detergent treatment (0.38±0.01 in 8%C LAP +0.0% PEG, 0.42±0.02 in 8%C LAP +0.5% PEG, 0.53±0.01 in 8%C LAP +1.0% PEG, 0.59±0.01 in 8%C LAP +1.5% PEG, 0.75±0.01 in 8%C LAP +2.0% PEG, with mean ± standard deviation; $n=3$ gels, red data points in **Figure 4-3**). We observed minimal difference in K due to the detergent exposure, indicating that the porogen gels were stably crosslinked.

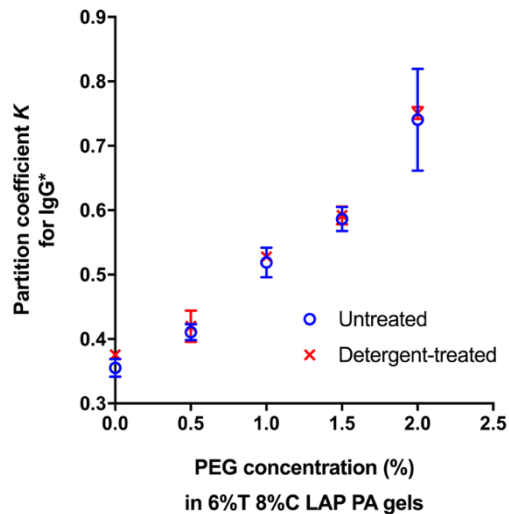


Figure 4-3. Gel microarchitecture is not disrupted by exposure to hydrogen-bond-disrupting detergents, indicating stable gel crosslinking.

We observed minimal difference in the partitioning of IgG* into the 6%T 8%C LAP gels before (blue circles) and after (red X's) exposure to hydrogen-bond-disrupting detergents. Mean and standard deviation depicted for n=3 gels.

IEF in Highly Porous PA Gels with Different Polymerization Chemistries

Next, we interrogated if gels with different gel polymerization chemistries maintained their suitability as an anticonvective media for IEF protein separations.

For this, we used a subset of gels studied previously: the 6%T 3.3%C APS/TEMED gel condition previously characterized in the ultrathin IEF assay as a negative control,¹⁹ the 6%T 8%C LAP + 0.0% PEG gel condition to investigate the role of bis-acrylamide and polymerization initiator, and 6%T 8%C LAP + 2.0% PEG gel condition to investigate a large-pore gel condition mimicking those reported in Righetti et al.⁷⁰

We investigated the formation and stability of the pH gradients formed in the hydrogels. To monitor and then characterize the pH gradient formed, we generated pH gradients that included three fluorescently-labeled pl markers (pl 4.5, 5.5, and 6.6). As an indicator of pH gradient formation – IEF having reached equilibrium – we utilized the pl markers (**Figure 4-4A**) and quantitatively identified the timepoint at which the peak center of the Gaussian fit of the focused fluorescent band of each pl marker shifts between consecutive measurements by the same rate (defined as cathodic drift), and at which the peak width does not significantly decrease between consecutive measurements. We measured ~7.5 min for the pH gradient to focus in all 3 gel conditions.

To further characterize IEF focusing and stability in the PA gels, the electrical current was measured during IEF for all gel conditions (**Figure 4-5**). The observed drop in electrical current within the first 2 minutes of IEF confirms that the ampholytes did focus

to their respective pI, reduce their electrophoretic migration, and stack across the separation axis to form the pH gradient, as previously reported in IEF.^{35,84}

To characterize the pH gradient at equilibrium, we assessed IEF in each material by considering the slope of each pH gradient, dpH/dx . To determine dpH/dx , each of the 3 focused pI marker concentration distributions were fit to a Gaussian curve at 10 min of elapsed separation time (**Figure 4-4A**). This timepoint was selected to exceed the time-to-focus measured previously, to measure IEF separation resolution reliably in a stable pH gradient across all gel conditions. Using the peak locations and knowledge of the ampholyte composition, we then used a linear regression fit of the 3 pI markers to estimate the pH gradient properties. The dpH/dx was quantified as $0.35 \pm 0.01 \text{ mm}^{-1}$ in the 3.3% APS/TEMED gels, $0.35 \pm 0.03 \text{ mm}^{-1}$ in the 8% LAP + 0.0% PEG gels, and $0.32 \pm 0.01 \text{ mm}^{-1}$ in the 8% LAP + 2.0% PEG gels (**Figure 4-4B**, mean \pm standard deviation; $n=3$ gels). The 2% PEG gels demonstrated no significant effect on the shape of pH gradient. This is as expected, since the focusing of the SinuLyte® ampholytes is dependent on the separation axis length and the ampholytes themselves, not the hydrogel network.¹⁶ For the same separation axis in ultrathin IEF, the dpH/dx was measured at 0.40 mm^{-1} for the Polybuffer® ampholytes over a pH 4-9 gradient.¹⁹

To assess the linearity of the pH gradient, we next measured the mean R^2 statistic for the linear fits. We quantified $R^2 = 0.89 \pm 0.03$ in the 3.3% APS/TEMED gels, 0.83 ± 0.05 in the 8% LAP + 0.0% PEG gels, and 0.79 ± 0.01 in the 8% LAP + 2.0% PEG gels (**Figure 4-4C**, mean \pm standard deviation; $n=3$ gels). There was no significant difference in the linearity of the gradient via the R^2 statistic to the linear fit of the pH gradient, between the 3.3% APS/TEMED gels and both of the LAP-polymerized gels. However, the linearity of the pH gradient should be near 1.00 for a well-designed ampholyte solution, and should be independent of the gel microarchitecture. Here we employ SinuLyte® ampholytes, for which no information is available from the manufacturer about the pH gradient linearity. In comparison, the Polybuffer® ampholytes used previously in a similar ultrathin IEF platform demonstrated 1.00 ± 0.00 linearity.^{19,20} This observed non-linear and compressed region in the pH gradient between pI markers 5.5 and 6.6 in the 8% LAP + 0.0% PEG and 8% LAP + 2.0% PEG gels, as well as the poor separation resolution between these two pI markers in these two gel conditions, indicates that the LAP is disrupting the pH gradient.

We next evaluated the minimum difference in pI for which two neighboring proteins are fully resolved (ΔpI_{min}), a unitless metric determined by **Equation 4-3**.¹⁶ Using the pI markers (**Figure 4-4D**), we measured the ΔpI_{min} as 0.16 ± 0.02 in the 3.3% APS/TEMED gels, 0.20 ± 0.03 in the 8% LAP + 0.0% PEG gels, and 0.19 ± 0.03 in the 8% LAP + 2.0% PEG gels (mean \pm standard deviation; $n=3$ gels).

$$\Delta pI_{min} = 3 * \frac{dpH}{dx} * \sigma_{protein}$$

Equation 4-3. ΔpI_{min} quantified for proteins focused in an IEF assay.

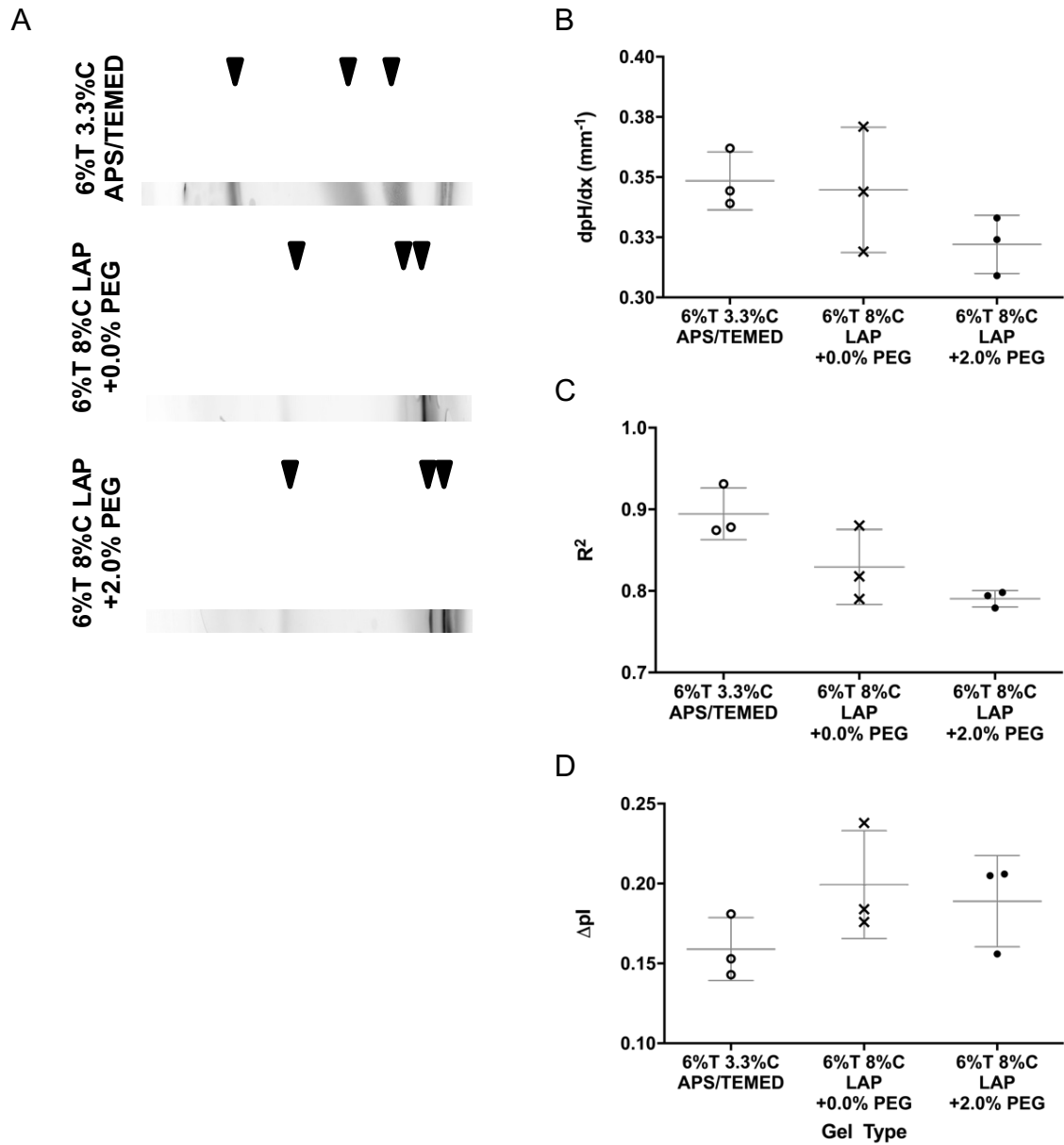


Figure 4-4. IEF is disrupted in gels polymerized with the LAP photoinitiator, as characterized using pI markers.

(A) Representative inverted micrographs and intensity plots of the in-gel focused pI 4.5, 5.5, and 6.6 markers (arrows) in the native IEF platform at 10 minutes. (B) Slope of the pH gradient is not significantly different between the gel conditions. (C) R² statistic for the linear regression fit of the 3 pI markers is not significantly significant between the gel conditions. (D) ΔpI_{min} is not significantly significant between the gel conditions. For all graphs, mean and standard deviation marked by vertical lines for n=3 gels per condition. One-way ANOVA with Kruskal-Wallis test and post-test Dunn's multiple comparison test was conducted with p<0.05 (*).

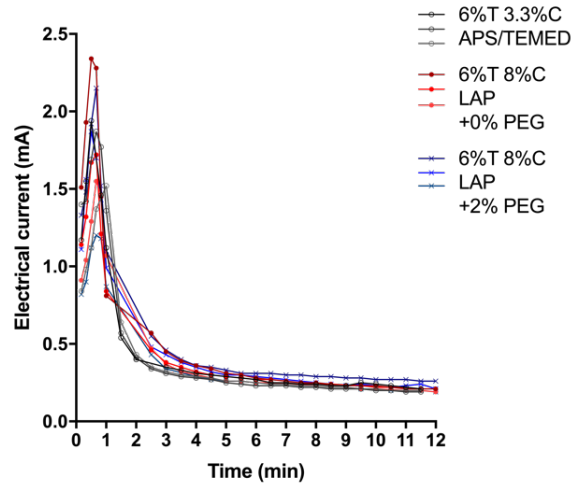


Figure 4-5. Electrical current during IEF in PA gels of different polymerization chemistries.

Electrical current measured during IEF experiment for all 3 conditions. Each line indicates a single experimental run. Gray lines indicate the 3.3%C APS/TEMED gels, red 8%C LAP + 0.0% PEG, and blue 8%C LAP + 2.0% PEG.

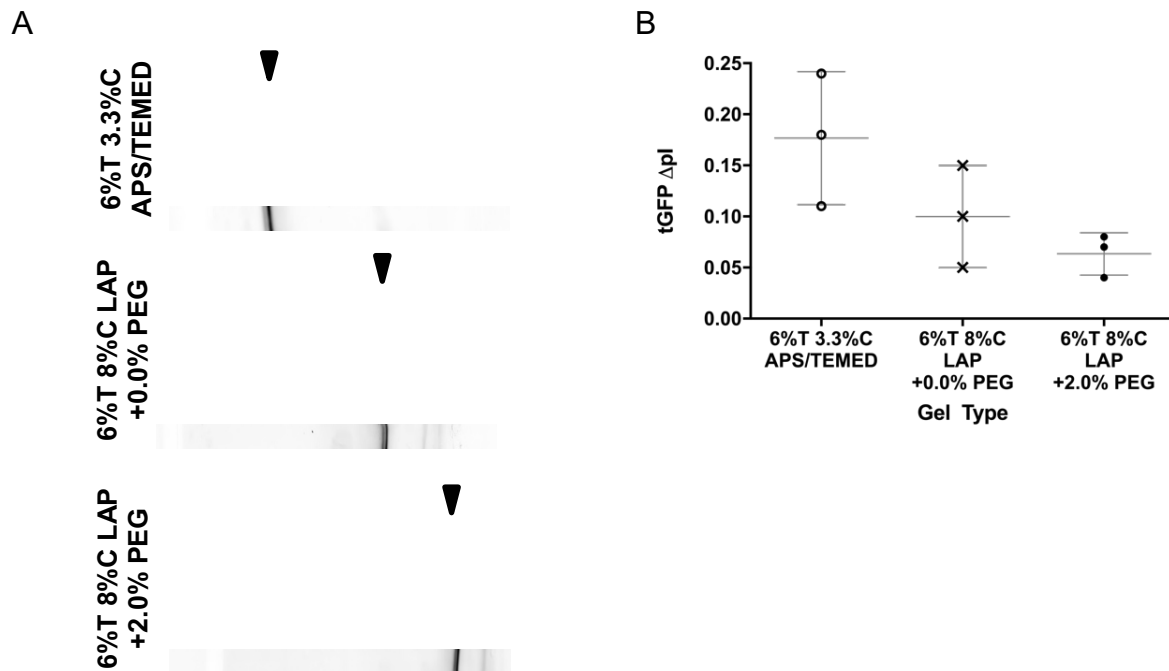


Figure 4-6. IEF performance in gels of different polymerization chemistries using tGFP protein.

(A) Representative inverted micrographs and intensity plots of the focused tGFP (arrow) in the native IEF platform at 11 minutes. (B) ΔpI_{min} did not significantly differ between the gel conditions. Mean and standard deviation marked by vertical lines for $n=3$ gels per condition. One-way ANOVA with Kruskal-Wallis test and post-test Dunn's multiple comparison test was conducted with $p<0.05$ (*).

Using the model protein tGFP, we characterized the ΔpI_{min} as 0.18 ± 0.07 in the 3.3%C APS/TEMED gels, 0.10 ± 0.05 in the 8%C LAP + 0.0% PEG gels, and 0.06 ± 0.02 in the 8%C LAP + 2.0% PEG gels (mean \pm standard deviation; $n=3$ gels, **Figure 4-6**). It is

unclear why the focused tGFP protein band (pI ~4.5 via IEF in a microfluidic channel)¹⁹ shifts towards the catholyte in the 8%C LAP + 0.0% PEG and 8%C LAP + 2.0% PEG (**Figure 4-6A**), especially compared to the band location of the pI 4.5 marker run in the same experimental run (**Figure 4-4A**). Inclusion of a fluorescently-labeled purified protein IEF ladder with the tGFP protein (**Chapter 6**) could provide additional information on potential disruption of the pH gradient by LAP.

This investigation indicates that the highly porous PA gels polymerized with LAP result in nonlinear pH gradients in IEF, notably a compressed gradient near pH 5.5-6.6, and as such are unsuitable matrices for IEF.

4.4 Conclusions and Future Directions

We investigated the role of gel chemistry in modifying the PA gel microarchitecture, while preserving the 6%T content of the PA gels. Notably, with modifications to the bis-acrylamide content, the method of gel polymerization, and the incorporation of PEG as a porogen, we observed a 2.8-fold increase in the swelling ratio of specific PA gel conditions. We further observed a 5.3-fold increases in IgG* partitioning in these highly porous PA gel matrices. The observed partitioning measurements in the series of 8%C LAP +PEG gels were unaffected by exposure to hydrogen-bond-disrupting detergents, suggesting that the gels were stably crosslinked. From a subset of PA gel conditions, we observed that gel photopolymerization via LAP resulted in a nonlinear pH gradient in IEF. PA gels polymerized with LAP are therefore unsuitable as a substrate for IEF across pH 4-7, within which the pI's of ~50-70% of the human proteome lie.^{45,46}

Further research is needed into the mechanism by which the incorporation of LAP into the PA gel network would induce nonlinearity of the pH gradient in IEF. During gel polymerization, the free radical formed from activation of the LAP photoinitiator converts unreacted acrylamide monomers into free radicals, that subsequently combine with unreacted acrylamide monomers and bisacrylamide crosslinkers to form the PA gel network. Thus, the 294 Da LAP itself is not part of the gel network and should rapidly diffuse out of the gel after gel polymerization during the extended wash step described in these experiments. If some fraction of LAP remains within the gel, two potential hypotheses might explain the observed disrupted IEF in the 8%C LAP + 0.0% PEG and 8%C LAP + 2.0% PEG. One hypothesis is that the LAP might affect the pH of the entire PA gel, which might then disrupt the pH 5.5-6.6 region of the pH gradient generated by the ampholytes in IEF. Alternatively, perhaps the LAP interacts with the ampholytes that stack to form the pH 5.5-6.6 region, thereby disrupting the pH gradient selectively within this range. These hypotheses are informed by the observation that the inclusion of 250 mM imidazole (an ampholyte of pI ~6.1)¹⁶ in the focusing region of the IEF lid gel disrupted the formation of the pH gradient in this ultrathin IEF assay (**0**). Perhaps these gel compositions might be useful in interrogating proteins with pI's above pH 7, provided a stable and linear pH gradient is observed in these gels above pH 7.

Chapter 5: Protein Diffusion from Microwells with Contrasting Hydrogel Domains

This work was performed in collaboration with Dr. Elaine J. Su, and is reproduced with permission of AIP Publishing from EJ Su, S Jeeawoody, AE Herr. “Protein diffusion in materials with heterogeneous partition coefficients.” *APL Bioengineering*. 2019;3:026101.

5.1 Introduction

Molecular transport through hydrogels is important across a wide range of bioengineering systems, including tissue engineering, drug delivery, and single-cell assays. In hydrogels, diffusion of macromolecules from one phase to another (i.e., liquid to hydrogel) is hindered by thermodynamic partitioning. The equilibrium partition coefficient, K_{eq} , is defined as the ratio of concentration of solute in the gel to that in liquid:

$$K_{eq} = \frac{C_{gel}}{C_{liquid}} \quad (1)$$

Where C is the solute mass per volume, C_{gel} is the solute concentration in the hydrogel, and C_{liquid} is the solute concentration in the liquid phase.^{92,105} In the absence of attractive interactions (e.g., van der Waals forces or electrostatic interactions⁷⁷ between the solute and the gel), the partition coefficient is described by Ogston’s model, which depends on the polymer volume fraction, chain radius, and the size and shape of the solute molecule.¹⁰⁶ Empirically, the partition coefficient in gels is quantitatively determined by measuring the relative concentration of a fluorescent species in the solution phase and in the hydrogel phase for a given multi-material system.^{3,19,92}

In addition to equilibrium solute concentrations, time-dependent and diffusion-driven solute concentration gradients – both within a single material and between materials – are important. For example, understanding drug delivery to the bloodstream or transport capabilities of cellular waste products out of capsules both benefit from understanding these types of concentration distributions.^{107–113} Within homogeneous hydrogels such as polyacrylamide (PA), which have mobile polymer chains, solute diffusion in hydrogels behaves according to a scaled hydrodynamic model¹¹⁰ and can be empirically determined.^{92,111} In hydrogels with immobile polymer chains (e.g., alginate), the diffusion coefficient (D) of small molecular species can be described by a hydrogel obstruction model.¹¹⁰ When placed in a liquid bath, the transport of solute from the gel phase into the liquid phase can be characterized by using non-steady-state measurements. Using such approaches, the D of small solute species was found to be 5-50% lower in gel than in the surrounding water.¹⁰⁹ The importance of material type and properties on in-gel and out-of-gel diffusion has necessitated development of methods to rapidly determine D of a solute in hydrogel systems.¹¹⁴

In general, the diffusion of a solute through a heterogeneous medium depends on the solubility and diffusivity of the solute in the different material domains and the geometry

of the domains.¹¹⁵ Although various studies have reported on particle diffusion in locally heterogeneous hydrogels^{116,117} and in hybrid [e.g., poly(ethylene oxide)-poly(acrylic acid) (PEO-PAA)] hydrogels,¹¹⁸ few studies have reported on solute diffusion through more than two different materials. *In vivo* systems are notably complex and are comprised of multiple biological polymer networks (e.g., mucus, extracellular matrix).¹¹⁶ For example, the study of oxygen permeability through contact lenses to the cornea can be represented as two interfacing hydrogels. A fluid (i.e., liquid) film interface exists between these hydrogels; this interfacial layer varies in thickness according to the topography and morphology of the gel, interfacial tension, interface potential, adsorption, partitioning, and chemistry of the gel.¹¹⁹ Fluid films between hydrogels and human tissues, such as the cornea, can range from nanometers to tens of microns.^{120–124} Characterizing fluid film thickness between sandwiched hydrogels is necessary to understand molecular transport at the interface of hydrogels.

Compartmentalization of cells in hydrogels has emerged as a useful approach for studying cellular processes. Hydrogel droplets encapsulating cells have facilitated biochemical analyses of individual cells.^{125,126} Similarly, encapsulation of cells in microwells allows researchers to scrutinize individual cells to study, in two examples, secreted proteins and nucleotides.^{127,128} In microwell-based studies, macromolecules diffuse through from a cell and through free solution to react with antibody probes immobilized along the walls or the lid of the microwell,^{129–132} and the spatial positioning of the macromolecules (e.g., proteins) relative to the antibodies in the microwell can influence the detected signal strength.¹³³

In our own research group, we have explored single-cell resolution protein electrophoresis using thin PA gels as the molecular sieving matrix. Our approach, called electrophoretic cytometry, isolates single cells in individual microwells. Cells are then chemically lysed in individual microwells, and the intracellular contents are subjected to electrophoresis in the hydrogel surrounding the microwell.^{3,7,19} To mitigate single-cell lysate diffusion out of the “open” microwell and electrophoresis gel, researchers have used a glass slide as a “lid” on the hydrogel structures. Capping with a glass lid improved lysate retention in the hydrogel.¹³⁴ This particular study demonstrated that partitioning and materials permeability can be modulated to maintain high concentration of solute in a detection area.¹³⁰ We have also demonstrated patterning chemistries onto the thin microwell-containing PA gel by applying a high density “lid” impregnated with the source chemistry, which concurrently mitigates diffusion of the single-cell lysate out of open microwells.^{19,135} Thus, understanding how time-dependent mass transport of proteins depends on operational parameters such as K_{eq} , system geometries, and D provides a framework for design of bioanalytical tools, such as electrophoretic cytometry (single-cell lysate analysis with polyacrylamide gel electrophoresis), with appreciable analytical sensitivity.

Here, we seek to understand the role of a lid layer in closing an open microwell used in electrophoretic cytometry, be that layer liquid, high-density PA gel, or glass. We have demonstrated patterning chemistries onto a thin layer of PA gel by applying a high-density lid impregnated with the source chemistry. We have also explored lid gels to

mitigate diffusion of single-cell lysate out of open microwells.^{19,135} To understand the importance of each material and the role of thin fluid (i.e., liquid) layers that form between sandwiched hydrogels, we first characterize the thickness of fluid film layers that form between hydro- gels of different densities. We then use our knowledge of fluid film thicknesses to create an experimentally validated numerical model that predicts the dependence of the microwell-encapsulated protein concentration on the fluid film thickness, partition coefficient of the hydrogels, and protein diffusivity in the lid gel for model proteins Green Fluorescent Protein (GFP) and Protein G. Understanding diffusion-driven transport of intracellular proteins in hydrogels and free solution ultimately aids selection of hydrogel properties in multi- material systems, which should be useful for applications ranging from drug delivery to high-sensitivity diagnostics.

5.2 Materials and Methods

Reagents

Acrylamide/bis-acrylamide 30% (w/w) solution, ammonium persulfate (APS), N,N,N',N'-tetramethylethylenediamine (TEMED), imidazole, sodium phosphate, sodium chloride, sodium hydroxide, sodium deoxycholate, sodium dodecyl sulfate, and Triton X-100 were obtained from Sigma-Aldrich. 10× Tris-glycine was obtained from Bio-Rad. Tris-HCl, pH 6.8 buffer was obtained from Teknova. PureProteome nickel magnetic microparticles, 10 μm, were obtained from Millipore-Sigma. TBS-T was obtained from Cell Signaling Technologies. Methacryloxyethyl thiocarbamoyl rhodamine B was obtained from Polysciences. VA-086 was obtained from Wako. N-[3-[(3-benzoylphenyl)formamido]propyl]methacrylamide (BPMA) was obtained from Pharm-Agra Laboratories. Silicon wafers were obtained from WaferNet. SU-8 developer and photoresist (SU-8 3050) were obtained from Microchem. Recombinant Protein G with His Tag were obtained from Abcam and labeled in-house with Alexa Fluor 647 NHS ester (Life Technologies). 0.5 μm rhodamine-microbeads (FluoSpheres) were obtained from Life Technologies. Gel-Slick was obtained from Lonza.

Fabrication of Rhodamine-Labeled PA Gels

“Bottom” gels (6%T, 3.3%C) PA gels were synthesized containing 5 mM BPMA and 0.005% (w/v) methacryloxyethyl thiocarbamoyl rhodamine B. The precursor solution was degassed and pipetted between an acrylate-silanized microscope slide or the No. 1 coverslip and a Gel-Slick treated silicon wafer patterned with 40 μm SU-8 features, as previously described.⁷ PA gels were crosslinked using 0.08% (w/v) APS as the initiator and 0.08% (v/v) TEMED as the catalyst. After 20 min of polymerization, the gels were peeled off the wafer, rinsed in deionized water, and gently dried under a nitrogen stream or stored in 1× TBS-T solution. 15%T, 3.3%C lid gels containing 0.005% (w/v) methacryloxyethyl thiocarbamoyl rhodamine B were fabricated using photopolymerization, as previously described.¹⁹ The 500 μm thickness of the high density 15%T gels was obtained by patterning the gel between two glass plates separated by a 500 μm thick spacer (CBS Scientific).

Image Acquisition

Confocal imaging experiments were conducted on an inverted Zeiss LSM 710 AxioObserver (Zeiss, Oberkochen, Germany). Images were acquired at room temperature using a 40× water objective (LD C-Apochromat 40× / 1.1 NA W Corr M27, Zeiss) with the correction collar set for a No. 1 coverslip. Rhodamine-labeled PA gels were fabricated on No. 1 coverslips and imaged using a DPSS-561 laser at 0.25% power, using the MBS488/561/633 beam splitter and the Zen 2010 software (Zeiss). Z-stack images were acquired with 0.42 μm step size with line scanning at x=y=z=0.42 μm pixel size.

Widefield epifluorescence images for microparticle imaging were obtained on an Olympus IX-71 inverted microscope with an Olympus LCPlanFI 40× / 0.6 NA objectives and an EMCCD Camera iXon2 (Andor). For microparticle imaging, brightfield microscopy was first utilized to find the field of view including a microparticle in a microwell. Microparticles were then imaged with 50 ms exposure times using a Cy5 filter cube (Chroma, 49009) using a time series feature in MetaMorph (Molecular Devices). Images were collected every 1 s. For particle tracking, microparticles were imaged using an Olympus UPlanFI 10× / 0.3 NA objective at 500 ms exposure and an EMCCD Camera iXon2 (Andor).

Numerical Simulations

Mass transport of proteins during cell lysis were simulated in COMSOL Multiphysics 5.3. Input parameters were obtained from literature or were experimentally determined. Partition coefficients for GFP were 0.51, 0.24, and 0.10 for 6% T PA gel to free solution, 15% T PA gel to free solution, and 6% T PA gel to 15% T PA gel, respectively.¹⁹ The gel lid was 500 μm in height, the bottom gel was 30 μm in height, and the microwell was 30 μm in height and width. To model an infinitely extending bottom gel, the width of the bottom layer, fluid layer, and top layer were 10,000 μm. These geometries were inputted into a 2D axisymmetric model. The maximum and minimum mesh element sizes were 30 and 0.3 μm, respectively. Initial conditions were modeled in the Transport of Dilute Species module as a uniform starting concentration of GFP in a 28-μm diameter spherical cell, comprising mostly of liquid (free solution). The partition and diffusion coefficients of GFP in the cell were thus assumed to be those of liquid ($K_{eq,L} = 1$ and $D_L = 1.691 \times 10^{-10}$). The diffusivity of GFP was $4.2 \times 10^{-12} \text{ m}^2 \text{ s}^{-1}$, $3.13 \times 10^{-11} \text{ m}^2 \text{ s}^{-1}$, and $1.691 \times 10^{-10} \text{ m}^2 \text{ s}^{-1}$ in 15% T gel, 6% T gel, and free solution, respectively.¹⁹ The time steps for lysis was 1 s. C_t/C_0 was estimated by taking a volume integral of the microwell at each 1 s interval and dividing by the volume integral of the microwell at $t = 0$ s.

For microparticle simulations, the same parameters as above were used. To simulate what would be measured via widefield microscopy, we included a 30-μm wide rectangle directly above the microwell to include the fluid film and lid gel. For the microparticle, we first modeled the species of Protein G released from the microparticle and free to diffuse. We assumed that background-subtracted fluorescence intensity was equivalent to the number of fluorescent particles. The background-subtracted fluorescence intensity of the microparticle fits the function:

$$y(t) = 1135.8 \exp(-0.037t) \quad (3)$$

This fluorescence as a function of time was assumed to be the amount of protein “bound” to the microparticle. For the free species, the fluorescence was calculated as the difference between C_0 and C_t . The flux, which represents the amount of free protein leaving the microparticle over the surface area per unit time, of the microparticle was calculated using the equation:

$$N_{free}(t) = \frac{d(y(0)-y(t))}{dt} \times \frac{1}{4\pi r^2} \quad (4)$$

An exponential was fit to $N(t)$, yielding:

$$N(t) = 44.425 \exp(-0.037t) \quad (5)$$

The final concentration was determined by taking a volume integral of the free species over the surface of the microwell, including the column directly above the microwell encompassing the fluid layer and lid gel, and summing to the measured fluorescence ($y(t)$) of the microparticle. The summed values were then normalized to the initial summed value.

Concentration profiles for the XZ and XY planes were obtained using the linear projection operator in COMSOL. To simulate the region surrounding a microwell, a rectangle of $100 \mu\text{m} \times 70 \mu\text{m}$ was utilized. For the contour plot, simulations were run with a $500 \mu\text{m}$ thickness lid layer using partition coefficients for GFP in glass, lid gel (15% T PA gel), and the bottom gel (6% T PA gel). For each partition coefficient, the simulation was run with three different diffusion coefficients for GFP (liquid, the bottom gel, and free solution), for a total of nine combinations. The protein solute concentration in the microwell was then obtained at $t = 15 \text{ s}$ and normalized to the initial concentration ($t = 0 \text{ s}$). These values were inputted into a contour plot in MATLAB (R2017a) using the function *contour*.

Bead Tracking in Convective Flow

Bead tracking was performed as previously described.^{3,136} Briefly, $0.5 \mu\text{m}$ fluorescent beads (FluoSpheres) were diluted 1:50,000 in phosphate buffered saline (PBS). Beads were then pipetted onto hydrated bottom gels (6% T PA gels conjugated to glass slides). A lid gel (15% T PA gel) was then interfaced to the bottom gel while imaging at 500 ms exposure time with an image acquisition rate of six frames per second. The velocity of the bead was quantified by measuring the length of the streak lines caused by the movement of the microspheres over the exposure period, as described previously.³ These values were compared to a negative control (no advection, lid, or pouring), which resulted in non-detectable velocities (no streaks). The Péclet number was calculated as:

$$Pe = L \frac{u}{D} \quad (6)$$

where $L = 30 \mu\text{m}$, u is the average measured velocity of the bead, $285 \mu\text{m/s}$ for lid gel or $13,000 \mu\text{m/s}$ for pouring,³ and $D = 1.691 \times 10^{-10} \text{ m}^2 \text{ s}^{-1}$, the diffusion coefficient of GFP in free solution.¹⁹

Image Processing and Analysis

Fluid film thicknesses were determined from confocal images in a method described by Kuypers et al.¹³⁷ Briefly, the fluorescence intensity of the XZ profiles were first background subtracted. The thickness of the fluid film was obtained by determining the “half shoulder” points, i.e., finding the local minima and maxima and determining the halfway point. The thickness was calculated as the difference in the Z-position of the half shoulder points.

Microparticle Fluorescence Quantification

Microparticle fluorescence was quantified using an in-house MATLAB script for segmentation of the microparticle. We used a Canny edge detection approach for segmentation of the microparticle. After determining the microparticle boundaries and generating a binary mask, the mask was applied to all images in the time sequence that were first background-subtracted. The fluorescence was measured as the sum of all intensity values in the mask region. For microwell quantitation, a brightfield image was first taken to determine a region of interest (ROI) encompassing the microwell. The ROI was then used to measure background-subtracted fluorescence for each image in the time series.

Statistical Analysis

Statistical analysis for two-sample Kolmogorov-Smirnov test was performed using the *kstest2* function in MATLAB. The experimental group was a vector of the mean of four separate trials, and the simulation group was a vector containing the simulation data. The null hypothesis is that the data in each vector are from the same continuous distribution.

5.3 Results and Discussion

Model of Diffusion of GFP Through Heterogeneous Materials

We first sought to understand how protein lysate losses from the closed electrophoretic cytometry device are impacted by K_{eq} and D . Lysate losses occur over time via diffusion and partitioning between the varying material and solution phases. Analytically, it is challenging to identify and quantify losses of lysate in varying geometries (domains) that comprise different material properties (and thus, varying partitioning and diffusion coefficients). Thus, we created and studied a 2D axisymmetric model (COMSOL) of a three-layer device (**Figure 5-1A**) composed of: (1) a bottom gel, which is a 30- μm thick, 6% T PA gel conjugated onto a conventional microscope slide and which houses the 30- μm diameter microwell; (2) a fluid film that arises at the interface of hydrated hydrogels and has a thickness H ; and (3) a lid, which is 500 μm thick and is composed of either a high-density (15% T) PA hydrogel or glass. Material properties are provided

in **Table 5-1**, with D and K_{eq} values obtained from the literature.¹⁹ The protein source was modeled as a 28- μm diameter sphere. Upon release from the spherical source, the concentration of the protein solute in the microwell fluid volume (C_t) decreases with time due to diffusion and chemical partitioning between the different material phases. With a large fluid reservoir, C_t approaches C_{liquid} over time. We thus calculated GFP concentration distributions as a function of time. For demonstration purposes, the figures are labeled as Cartesian (x, y, z) coordinates rather than in cylindrical (r, θ, z) coordinates.

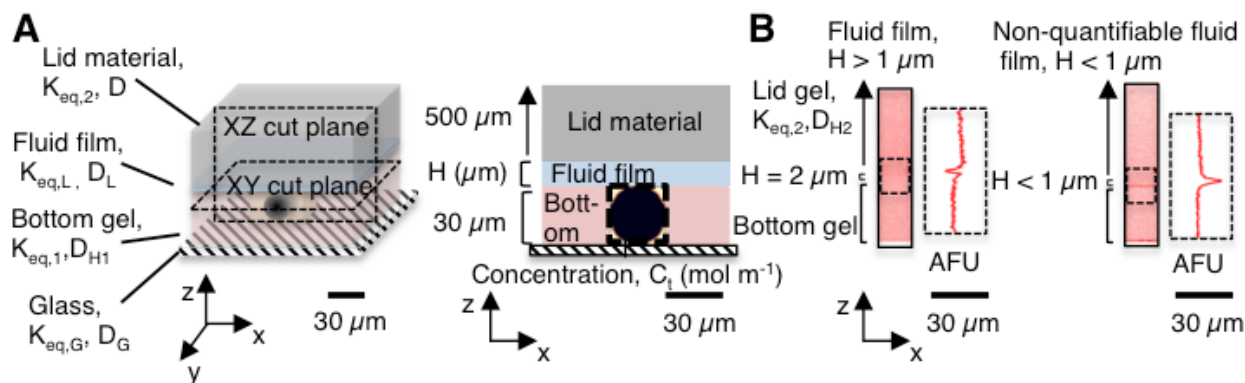


Figure 5-1. The fluid film is created by capping the bottom gel with a lid layer.

(A) Schematic of the bottom gel ($K_{eq,1}$), lid layer (Glass, $K_{eq,G}$ or lid gel, $K_{eq,2}$), interfacial fluid film (thickness, H), and microwell housing a spherical protein source. The 30- μm thick bottom gel houses a microwell (black dotted line) containing a spherical source of protein having an initial concentration, C_0 . Cut planes show side and top planes of the layered device, with protein source material diffusing from the microwell and into surrounding materials over time. Over time, the diffusion coefficient (D) of protein in each surrounding material and K_{eq} of each material determines diffusive losses of protein from microwell into respective material. (B) Confocal fluorescence micrographs (inverted, false color) of the fluid film created between the bottom gel and lid gel. The median measurable fluid film thickness was 1.7 μm ($n = 9$), excluding fluid films lacking a quantifiable thickness ($n = 8$). PA, polyacrylamide. K_{eq} , equilibrium partition coefficient. D , diffusion coefficient of GFP in each material.

Table 5-1. Partition and diffusion coefficient values for GFP in the range of layer materials characterized in this study.

Material name	Material composition	K_{eq}	D ($\text{m}^2 \text{s}^{-1}$)
Glass lid	Glass	$K_{eq,G} = 0$ (liquid, glass)	$D_G = 0$
Bottom gel (Hydrogel 1)	6% T, 3.3% C PA	$K_{eq,1} = 0.51$ (liquid, bottom gel)	$D_{H1} = 3.13 \times 10^{-11}$
Lid gel (Hydrogel 2)	15% T, 3.3% C PA	$K_{eq,2} = 0.24$ (liquid, lid gel)	$D_{H2} = 4.2 \times 10^{-12}$
Liquid layer	Liquid	$K_{eq,L} = 1$ (liquid, liquid)	$D_L = 1.691 \times 10^{-10}$

To measure the fluid film thickness in a layered hydrogel device, we incorporated rhodamine methacrylamide into the bottom gel and the lid gel (a 15%T, 3.3%C PA gel, where %T is the total amount of acrylamide and %C is the ratio of cross-linker mass to total monomer mass in the gel), incubated the sandwiched layers in a buffer solution (TBS-T) overnight, and then imaged the interface between the sandwiched hydrogels using confocal microscopy. We measured the thickness of the void between the bottom gel and the lid gel (**Figure 5-1B**) using a method similar to that employed by Kuypers et al.¹³⁷ Of the 17 total samples, 8 samples had no resolvable decrease in fluorescence in the void, and thus the fluid film thickness was not quantifiable. We attribute the lack of a signal decrease to the possibility that these samples had fluid film thicknesses smaller than our z-axis resolution of 0.42 μm , a resolution that is dictated by the pinhole diameter. Given the geometries of our system (tens to hundreds of micrometers), we considered the resolution acceptable. Of the quantifiable samples, the range of measured fluid layer thicknesses spanned from 1.3 to 1.9 μm with a median fluid layer thickness of 1.7 μm ($n = 9$). Our fluid layer thickness values are larger than the 300-600 nm fluid layer thickness values previously reported for permeable hydrogels;¹³⁸ however, those reported values were for hydrogels with elastic moduli 3 orders of magnitude larger and much lower (44%) water content than the hydrogels considered here.¹³⁹ Given that interfacial fluid films vary in thickness according to the topography, morphology, interfacial tension, interface potential, adsorption, partitioning, permeability, and chemistry of the gel,^{119,140,141} we anticipate a wide range of possible fluid film thicknesses, depending on the specific configuration of the hydrogel system under study. Our fluid layer thickness values fall in the range of fluid films thicknesses measured for layers that form between hydrogels and human tissues, such as the cornea.^{120–124}

Protein Losses from Closed and Open Microwells

For a microwell capped with a lid (i.e., closed), we sought to characterize how K_{eq} and D of GFP in the lid would affect protein concentration in that microwell over time. Protein losses from the microwell occur as proteins diffuse and partition between the different media comprising the microwell (i.e., gel, liquid, and glass). We performed numerical simulations to determine the degree of protein retention in the microwell fluid volume, as a function of the lid material (**Figure 5-2A**). We opted to scrutinize three lid materials, based on our empirical systems; hence, the lid material was simulated as glass (assumed to be impermeable, $K_{eq,G} = 0$, $D_G = 0 \text{ m}^2 \text{ s}^{-1}$), liquid (i.e. free solution), or lid gel (dense gel). For each case, we determined the concentration of GFP in the microwell at every 1 s, and normalized to the initial concentration (C_i/C_0 , **Figure 5-2B**).

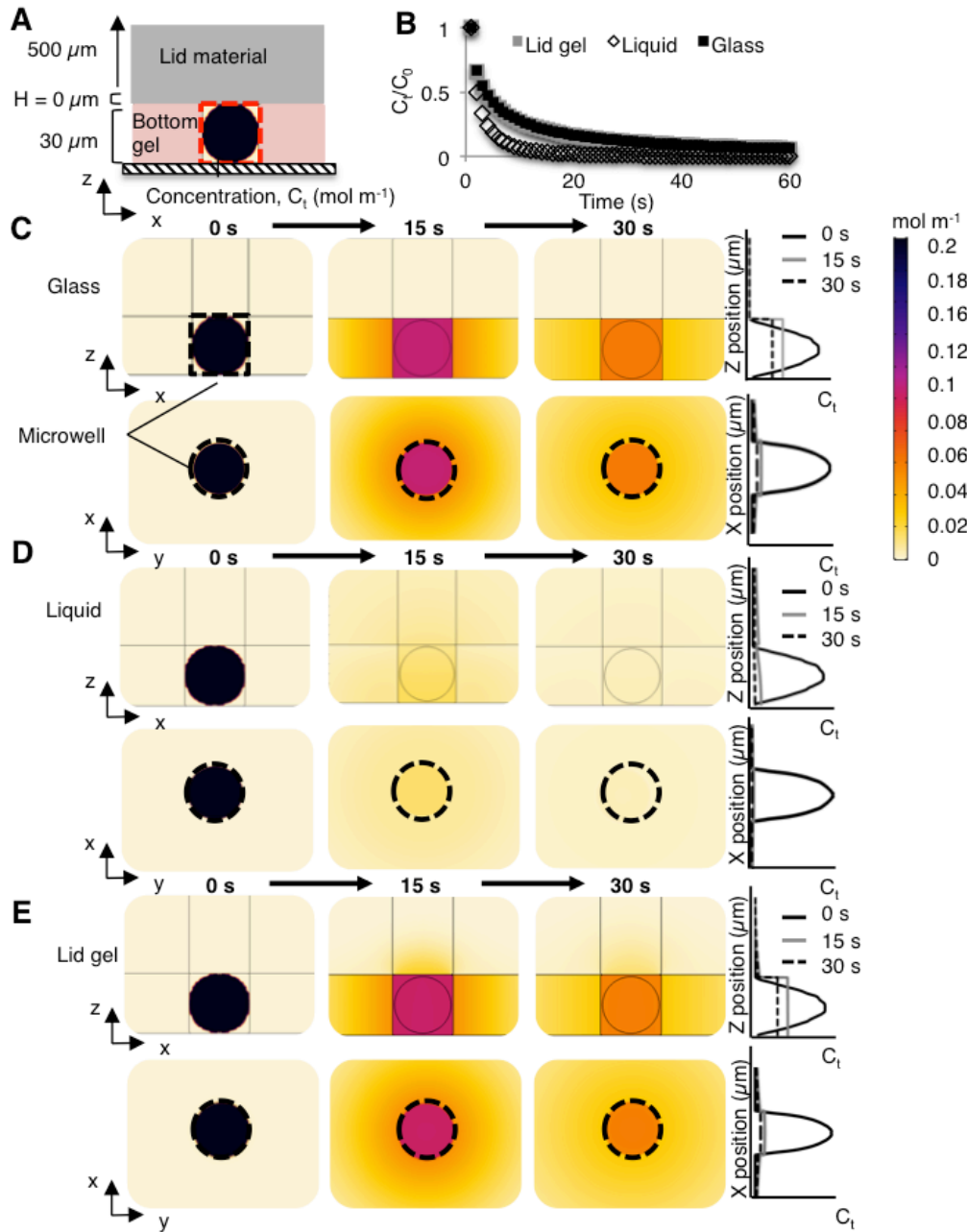


Figure 5-2. In the absence of a fluid layer, numerical simulations indicate that the lid material determines the concentration distribution of the protein source material diffusing out of the microwell. (A) Side-view schematic of 2D-axisymmetric diffusion model for a range of lid materials (glass, liquid, or lid gel). (B) Comparison of the protein solute concentration in the microwell as a function of time, normalized to the initial protein solute concentration in the microwell, as a function of different lid materials. At time $t = 15\ \text{s}$, the normalized protein solute concentration in the microwell, C_t/C_0 , decreases to 0.20 when glass or a lid gel is used, compared to 0.03 in the liquid system. (C) A glass lid layer reduces diffusion in the z-axis. (D) A liquid lid layer (open microwell) leads to rapid diffusion-based dilution of the protein source material. (E) A lid gel mitigates diffusive losses as compared to the open configuration with the same thickness ($H = 500\ \mu\text{m}$) shown in (D). The microwell is outlined in a dotted black line.

With a closed microwell, C_t/C_0 increases compared to an open microwell (liquid bath as upper boundary condition) configuration. At time $t = 15$ s, a time point pertinent to cell lysis and protein solubilization in microwells,⁵ an open microwell configuration yields $C_t/C_0 = 0.03$, whereas the presence of either a glass or lid gel yields $C_t/C_0 = 0.20$ (**Figure 5-2B**). Application of a glass lid reduces diffusion of solute out of the microwell, since protein cannot partition into the lid, and the local solute concentration in the microwell fluid volume decreases with time owing to (i) dilution throughout the microwell volume and (ii) diffusion out of the microwell into the surrounding bottom gel (**Figure 5-2C**). We first estimated a characteristic diffusion time (L^2/D) of ~ 29 s for GFP to diffuse from the microwell into the bottom gel layer in the quiescent, closed microwell configuration (where L is the microwell diameter; D is the diffusion coefficient of GFP in the bottom gel). Using numerical simulation, we then assessed the protein concentration profiles at $t = 0$ s, 15 s, and 30 s, matching the time scales of cell lysis, protein solubilization, and the expected diffusion time scale.³ From the simulations, within 1 s, the GFP within the microwell becomes uniform. The concentration of GFP along the x -axis remains uniform at $t = 15$ s. The GFP concentration remains highest in the microwell fluid volume, since partitioning inhibits protein from entering the surrounding medium (bottom gel) and there is no transport into the impermeable glass lid.

In the configuration where the microwell is open to a reservoir of fluid, we modeled the free solution with $K_{eq,L} = 1$ and $D_L = 1.691 \times 10^{-10} \text{ m}^2 \text{ s}^{-1}$ (**Figure 5-2D**). The 500 μm fluid layer thickness approximates a free solution bath, given the time scales of GFP diffusion.¹⁹ In our model, placing a glass lid 500 μm away from the solute-containing microwell did not change the concentration distribution of protein in the microwell fluid volume, as compared to the 500- μm free solution bath alone (data not shown). In contrast to the glass lid configuration, the protein concentration in the microwell fluid volume diminishes quickly for an open microwell ($C_t/C_0 = 0.03$ at $t = 15$ s), as expected. At $t = 15$ s, the protein concentration is highest at the bottom of the microwell, since no flux occurs below the microwell into the glass support. C_t/C_0 diminishes to 0.01 by $t = 30$ s.

Next, we considered a hydrogel material as the lid layer. We investigated C_t/C_0 in the microwell fluid volume when a lid gel was applied (**Figure 5-2E**). In electrophoretic cytometry, high-density lid gels have been employed for diffusive delivery of reagents to the bottom gel and to mitigate out-of-plane diffusive losses from the microwell.^{5,19,21,135} Interestingly, C_t/C_0 was similar to that of the glass lid configuration (**Figure 5-2B and Figure 5-2E**). We also investigated the solute concentration across the span of the bottom gel (i.e., the microwell and the entire bottom gel). C_t/C_0 of the bottom gel at $t = 15$ s was 0.96 when a lid gel was used, similar to the $C_t/C_0 = 1.0$ calculated for the glass lid configuration.

Overall, the application of a lid layer (glass or high-density gel) that inhibits diffusion of protein solute into the lid layer is effective at maintaining high concentrations of solute in the microwell fluid volume. Future studies seek to understand how other physico-chemical properties may also be modulated to further improve solute retention in the

microwell. For example, inclusion into the lid layer of interacting particles (e.g., via charge¹¹⁶ or hydrophilicity¹⁴²) that bind to or obstruct proteins could further decrease the mass of solute that can enter the lid layer and preserve high solute concentrations in the microwell.

Experimental Validation of the Model

To experimentally validate our computational model of the electrophoretic cytometry device, we used a microparticle-based chemistry for rapid release of proteins from a spherical source in a microwell (**Figure 5-3A**). Microparticles (10- μm diameter) conjugated with a Ni surface chemistry were coated with His-tagged proteins. Introduction of imidazole releases the protein from the particle surface, owing to competition between His and imidazole for the Ni. We have developed the microparticles as a means to deliver protein size markers to each microwell in electrophoretic cytometry.¹⁴³ Imidazole can be delivered using a lid gel, as previously described in single-cell electrophoretic assays.^{5,19,135} The Ni-His-imidazole release scheme gives short “switching” periods (seconds as compared to minutes to hours), appreciable release efficiency, and adequate spatial control for delivery to microwells, as compared to protein-PA conjugations^{144–146} photo-labile polymers,^{147–149} caged particles,¹⁵⁰ photo-activatable probes,¹⁵¹ drug-releasing nanogels,¹⁵² photo-assembly and photo-cleavable microcapsules,¹⁵³ photo-controlled release micelles,¹⁵⁴ protein-protein conjugations, and click chemistry. We use a median measured fluid film thickness of 2 μm (**Figure 5-1B**).

The kinetics of protein release from the microparticle source must be considered in constructing the simulations. To determine release kinetics, we first characterized the imidazole-triggered release of Alexa Fluor 647-labeled His-tagged Protein G (26 kDa) from microparticles. His-tagged Protein G is commercially available and has the same molecular mass as GFP. A magnet was used to actively settle Protein G-coated microparticles into microwells; excess microparticles were washed off the gel surface. The lid gel was incubated overnight in a 1 M imidazole solution. At $t = 0$ s, the lid layer was seated atop the bottom gel and the microparticle-laden microwells to initiate imidazole diffusion into the bottom gel and Protein G release from the microparticles. Epifluorescence microscopy was used to monitor the fluorescence intensity in the microwell fluid volume (**Figure 5-4**), thus allowing normalization of fluorescence signal to the initial fluorescence intensity of the microparticle. For the fluorescence signal of the microparticles, we observed an exponential decay in fluorescence that matched the signal observed in our previously observed model of imidazole delivery using a convective delivery (pouring) system [$y = 1.2789\exp(-0.035x)$], $R^2 = 0.98$, comparable to the $y = 1.18\exp(-0.04x) + 0.08$ that was previously reported.¹⁴³

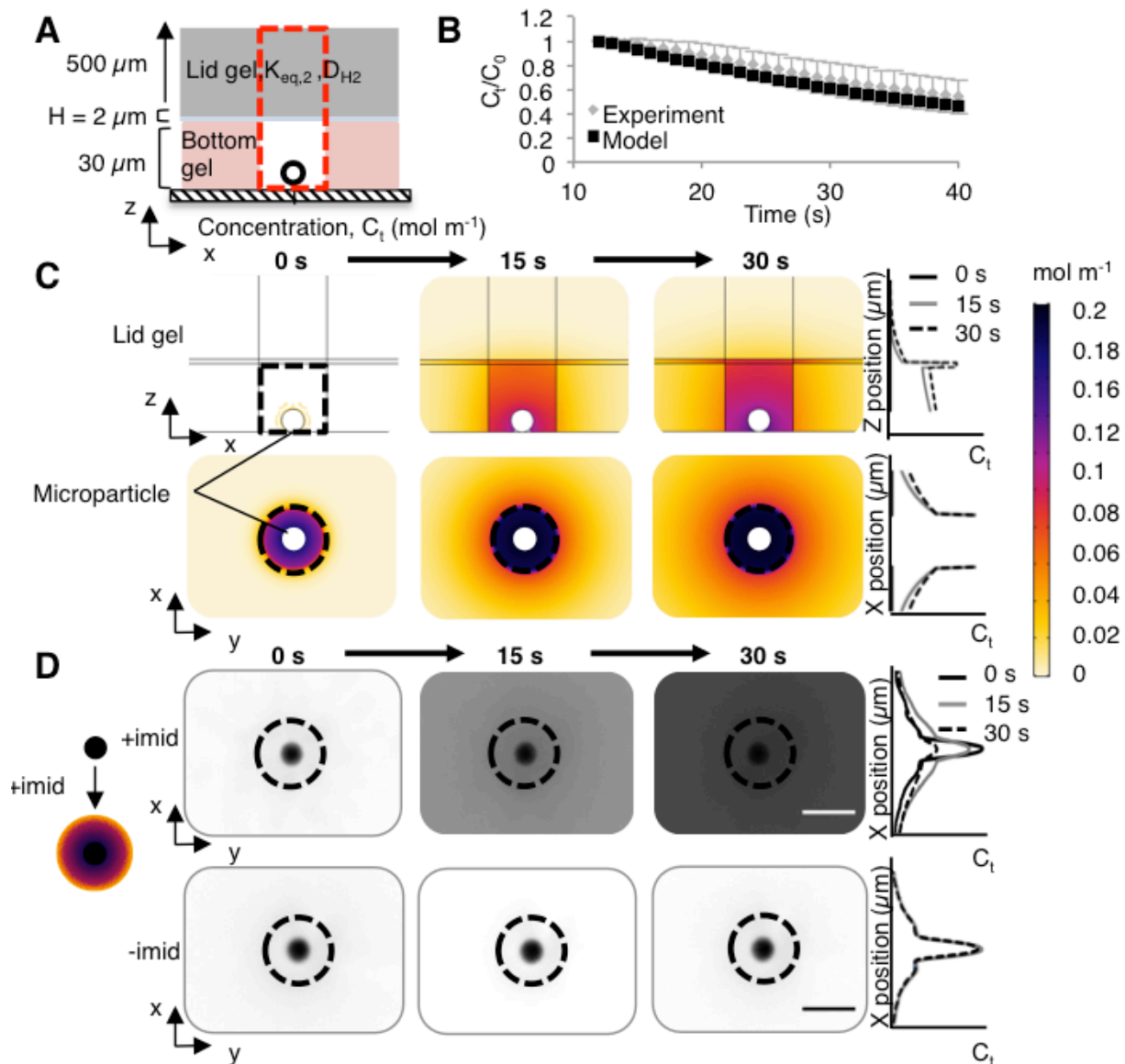


Figure 5-3. Experimental validation of protein release from a spherical source located in a hydrogel microwell. (A) Side-view schematic of the model and experiment, with 10- μm diameter microparticle coated with fluorescently labeled Protein G as the protein source (black circle). $H = 2 \mu\text{m}$. (B) Comparison of simulations (model) and experiment report similar ($p > 0.05$, Kolmogorov-Smirnov test) trends in normalized microwell fluorescence loss over time. For the simulations, an integral of the protein mass in the column extending from the microwell through the lid gel (red rectangle in A) was obtained to represent the mass of protein that is observed via wide-field microscopy (experiment). Error bars represent the standard deviation ($n = 4$). (C) Time series of simulation results show release of Protein G from a microparticle within a microwell (black dotted line). Protein G released per unit area was calculated using the number of molecules released per unit time, divided by the surface area of the microparticle. The number of Protein G molecules released per unit time was employed as a flux boundary condition in the simulations. (D) Time series of experiment results show inverted fluorescence micrographs of fluorescently labeled Protein G release at $t = 0, 15,$ and 30 s after the addition of imidazole (“+imid”), delivered by incubating the lid gel in a 1 M imidazole buffer solution. The negative control uses 0 M imidazole (“-imid”). The fluid layer thickness H is unknown in these experiments.

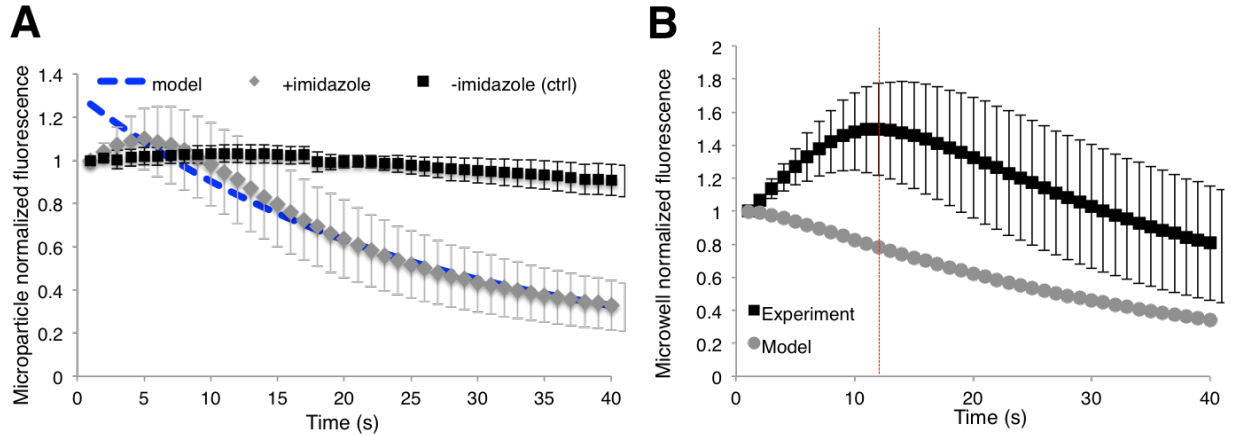


Figure 5-4. His-tagged protein release from Ni surface functionalized magnetic microparticles.

(A) Time series of fluorescence of the microparticle, normalized to the initial microparticle fluorescence. Fluorescence of the microparticle drops exponentially upon addition of imidazole ($n = 4$). The fluorescence fit an exponential $y = 1.18 \exp(-0.04x) + 0.08$. We calculated the flux of protein molecules out of the bead using the equation: Protein mass released per unit time = $\frac{d(y(0)-y(t))}{dt}$. We then obtained an equation for flux by dividing by the surface area of the microparticle. $\text{Flux}(t) = 44.425 \exp(-0.037t) / (4\pi(5 * 10^{-6} m)^2)$. (B) Microwell fluorescence as measured by widefield microscopy (experiment) and through the volume extending from the microwell through the lid gel. In the experiment, an initial increase of fluorescence was observed. In the main text, the fluorescence was normalized to the maximum of the experiment ($t = 12$ s). The model plot in the main text was also normalized to the $t = 12$ s time point.

Monitoring the fluorescence signal of the microparticle during Protein G release from the surface allowed us to establish a flux boundary condition for our simulations. First, we assumed the raw fluorescence intensity after background subtraction was equivalent to the number of fluorescent molecules or proteins. Since we ultimately normalize the final fluorescence signal to the initial signal, absolute quantification of fluorescent molecules is not necessary. Next, we defined a flux boundary condition for microparticle protein source $N(t)$ as:

$$N(t) = \frac{d(\text{Number molecules}(t=0) - \text{Number molecules}(t))}{dt} \times \frac{1}{4\pi r^2 s} \quad (2)$$

where r is the microparticle radius (5×10^{-6} m). We assume that the K_{eq} and D are similar for Protein G and GFP in the bottom gel, the liquid in the microwell fluid volume, and the lid gel, given the similarity in molecular mass. Advection from the lid gel placement was assumed to be negligible, as the Péclet number ($Pe = uL/D$, where $L = 30 \mu\text{m}$, u is the average measured velocity of the bead, $285 \mu\text{m/s}$) was measured to be two orders of magnitude lower than with delivery of lysis buffer by pouring ($n = 9$ from 3 separate trials, **Figure 5-5**). Moreover, we assumed that the microparticle was impermeable and that protein is conjugated only to the microparticle surface.

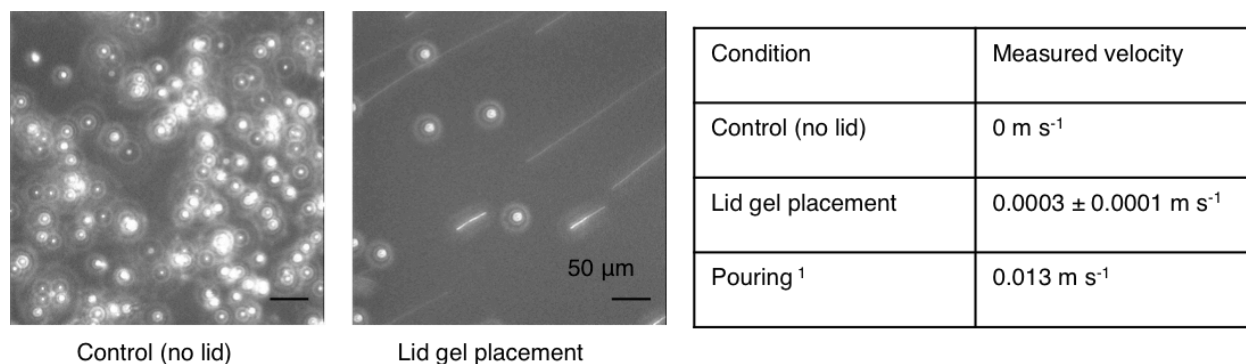


Figure 5-5. Fluorescent bead tracking reveals advection introduced by lid gel placement.

Advection during buffer delivery using a hydrogel lid application system was two orders of magnitude lower than advection generated by pouring the buffer onto the hydrogel. (mean \pm standard deviation, $n = 9$).

Comparison of experimental observations and simulations of the Protein G concentration in the microwell fluid volume showed reasonable agreement ($p > 0.05$, Kolmogorov-Smirnov test, **Figure 5-3B**). In our simulations, we measured the volume integral of Protein G mass in the column above the microwell to simulate observations via epifluorescence microscopy (**Figure 5-3A**, red dotted line). Interestingly, in our experiments, we observed an initial increase of fluorescence signal in the microwell fluid volume with a maximum measured fluorescence at $t = 12$ s ($n = 4$; **Figure 5-4B**). The increase in fluorescence is likely caused by self-quenching of the fluorescently-labeled protein while bound to the microparticle; at higher concentrations, fluorescent dyes can aggregate, causing quenching of up to 90% of fluorescence signal until the dye molecules are spaced sufficiently far apart.¹⁵⁵ We hypothesize that protein released from the microparticle surface is sufficiently diluted within the microwell such that self-quenching no longer occurs. For our simulations and our experiments, we thus normalized the concentration values to the maximum signal (i.e., at the 12 s time point).

In addition to the microwell volume, we also scrutinized the concentration distribution in the surrounding bottom gel, in the fluid film, and in the lid gel (**Figure 5-3C**). As expected, the highest concentration of Protein G ($t = 15$ s) was localized to the fluid film, which is a material that sees no partitioning-based exclusion of Protein G from microwell fluid volume and which affords Protein G a high D as compared to within the hydrogels. Because D and K_{eq} for Protein G are highest in the fluid film, the fluid volume rapidly accumulates protein. At the hydrogel walls of the microwell, we observe a Protein G concentration that drops off sharply, attributable to preferential partitioning of solute into the microwell fluid volume and D that is higher in the microwell fluid volume than in the surrounding hydrogel.

Both the simulation results and the experimental observations of solute signal released from microparticles indicated release of protein solute into the microwell fluid volume, with lower concentrations of protein solute in the surrounding hydrogel material (**Figure 5-3D**). While useful for illustrative purposes, two major caveats preclude direct quantitative comparison of the simulations and the experimental approximation. First,

the observed concentration of the released solute is expected to be lower than in the XY plane of the simulations, as the XY plane in the simulations is taken through the center of the microwell (i.e., a cross-section), where the concentration of protein is maximal. In contrast, in the experiment, the entire volume of the microwell, including through the lid, is imaged. Second, the thickness of the fluid film was not measurable, as the temporal resolution of confocal microscopy exceeds the 0–30 s window of microparticle release. Nonetheless, the agreement observed between the experiment and simulations in the microwell volume (**Figure 5-3B**) indicates that the simulations may be used to accurately predict protein concentrations within the microwell fluid volume for multiple materials, given D and K_{eq} of a given protein into the lid material.

Protein Loss from Microwells is Dependent on H , K_{eq} , and D .

Given the simulation results indicating high local concentration of proteins in the fluid film, we next sought to assess how H , K_{eq} , and D affect protein concentration in the microwell fluid volume (**Figure 5-6A**). We first varied the thickness of the fluid film (5, 10, 20, 50, and 500 μm) and observed that, as the fluid film thickness increases, C_t/C_0 decreases from 0.20 to 0.09, 0.06, 0.04, 0.03, respectively at $t = 15$ s (**Figure 5-6B**).

We noted a critical fluid film thickness, with regards to protein concentration in the fluid film. At $H = 20$ μm , $C_t/C_0 = 0.03$ and increasing the H beyond 20 μm has a muted effect on further reduction in C_t/C_0 . In this geometry, we surmise that the fluid film begins to behave as a semi-infinite medium at $H > 20$ μm . This effect can be further seen when regarding the concentration profile from the XZ plane (**Figure 5-6C**). For $H = 20$ μm , the highest concentration of protein at $t = 15$ s is in the fluid film, whereas for $H = 0$ μm , the highest concentration of protein is in the microwell fluid volume. Within the microwell fluid volume, the maximum observed concentration of protein for $H = 20$ μm is 61% lower than that for $H = 0$ μm .

Comparatively, for $H = 500$ μm , the concentration of protein within the microwell fluid volume is 74% lower than that for $H = 0$ μm . We conclude that the solute concentration in the microwell fluid volume and in the bulk of the bottom gel are sensitive to the fluid film thickness, especially when that thickness is smaller than 20 μm for the configurations studied here (**Figure 5-1B**). Consequently, design strategies to minimize the fluid film thickness are critical in applications where maintaining a high concentration of solute in the microwell fluid volume is necessary.

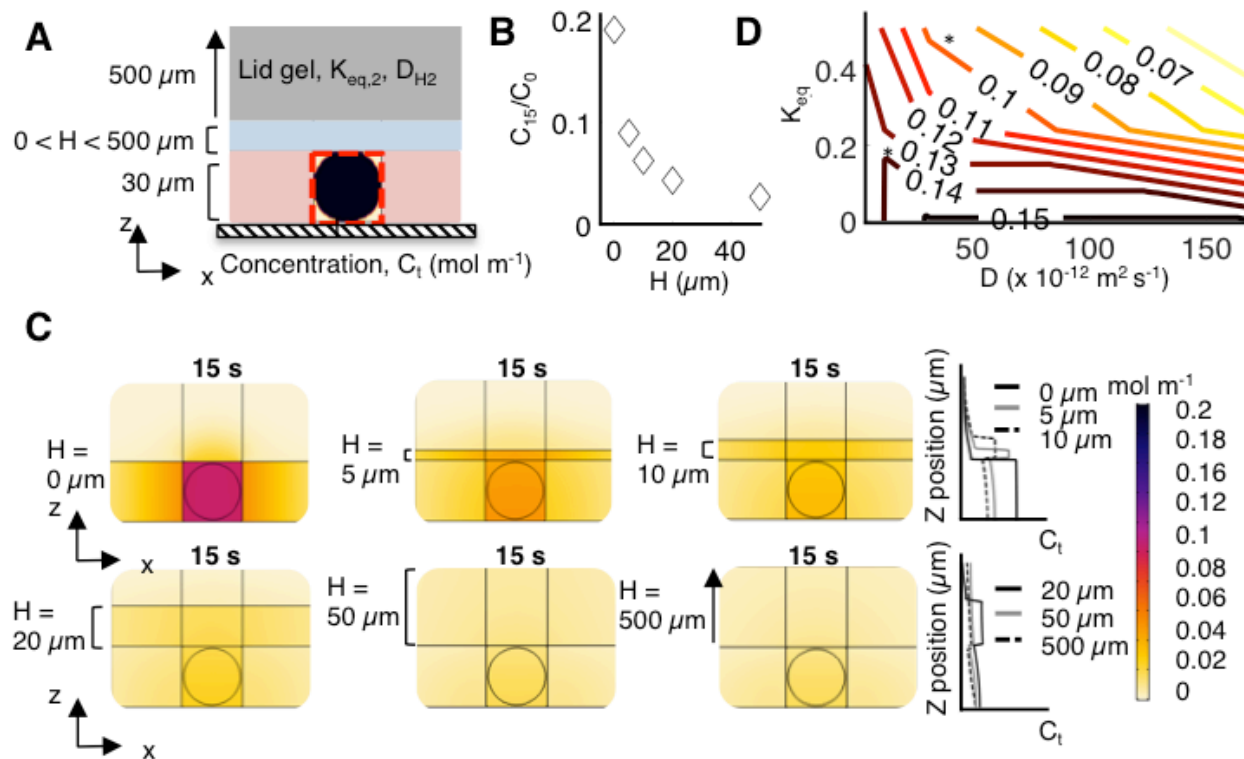


Figure 5-6. The protein solute concentration in the microwell depends on H , K_{eq} , and D for GFP in various materials, as determined by numerical simulations. (A) Side-view schematic of the model for a range of H values with a lid gel. H was varied from 0 to 500 μm . (B) Sensitivity analysis of the protein solute concentration in the microwell at time $t = 15$ s as a function of H , maintaining constant D and K_{eq} values. As H increases, C_t/C_0 decreases from 0.20 to 0.09, 0.06, 0.04, 0.03, for $H = 0, 5, 10, 20,$ and 50 μm , respectively. At $H = 20$ μm , the change in C_t/C_0 as a function of H decreases to 0.03, indicating the fluid film begins to act as a semi-infinite medium. (C) Simulation results show rapid dilution and diffusive losses of GFP with increasing H . (D) Contour plot of C_t/C_0 at time $t = 15$ s as a function of K_{eq} and D for GFP given $H = 2$ μm . The asterisk indicates conditions where D and K_{eq} for GFP are consistent with the material.

Next, we sought to understand if C_t/C_0 is more sensitive to the partitioning effect of the lid or to the change in D of the GFP in the lid material. Previous studies point to the hydrogel composition (%T, total acrylamide concentration) having a greater influence on K_{eq} than on D for proteins bovine serum albumin (BSA) and RNAse.⁹² We simulated K_{eq} and D for GFP in different materials: liquid, the bottom gel, the lid gel, and glass. We assumed a 2- μm fluid film thickness (**Figure 5-1B**). We calculated C_t/C_0 ($t = 15$ s) in the microwell fluid volume for each combination of K_{eq} and D . The simulation data reveal that C_t/C_0 is sensitive to both K_{eq} and D , albeit with a different degree of sensitivity in different regimes. For low K_{eq} , C_t/C_0 is relatively insensitive to D , since the protein cannot partition into the lid gel. However, as K_{eq} increases, C_t/C_0 ($t = 15$ s) drops rapidly. To maintain a constant value of C_t/C_0 with increasing K_{eq} , D must correspondingly decrease. Similarly, as D in the lid material increases, the K_{eq} must decrease to maintain high C_t/C_0 . Overall, the use of a lid composed of a dense gel is effective for high protein retention to the microwell fluid volume (asterisk on **Figure**

5-6D). Nonetheless, we can imagine further engineering material properties, such as decreasing both D and K_{eq} via surface treatments,¹⁵⁶ and/or decreasing the effective PA pore size to decrease D of the protein in the lid material.⁹²

5.4 Conclusions

Molecular transport through hydrogels has implications in cell and tissue engineering, drug delivery, and single-cell assays. Here, we used numerical simulations to determine how the fluid film thickness, partition coefficient, and diffusion coefficient of GFP in multiple materials (liquid, dense hydrogel, and glass) dictate the GFP concentration in microwells. We first measured the fluid film thickness between two hydrogels of different densities (%T). We found that the application of a low-permeability or impermeable lid layer mitigates diffusive losses of proteins from microwells. Further, we find that the microwell protein concentration is dependent on the fluid film thickness, the partition coefficient, and the diffusion coefficient. Overall, we generated a model that provides a framework for how time-dependent protein diffusion depends on operational parameters.

From our simulations, we determined that the protein concentration in microwells is sensitive to the fluid film thickness; thus, design strategies to minimize or eliminate fluid films could result in higher retention of protein in microwells. To minimize the fluid film thickness, hydrogel properties such as surface roughness, permeability, or elastic modulus could be manipulated.¹⁵⁷ Elastic modulus of gels can be tuned by changing crosslinking density;¹⁵⁸ however, consideration of how modulating this parameter affects other properties of the gel, such as molecular sieving, is necessary.

In addition to minimizing the fluid film, material properties of the lid hydrogel may be modulated to reduce the diffusion coefficient and/or partition coefficient of the species of interest in the lid. For example, modulating protein interactions with the lid layer by altering the charge¹¹⁶ or hydrophilicity¹⁴² present strategies to tune the partition coefficient. In-gel diffusivity can be tuned by incorporating other polymeric materials such as poly(ethylene glycol) diacrylate (PEGDA) to form interpenetrating networks that decrease solute diffusivity.¹⁵⁹ Overall, tuning of the hydrogel free volume, obstructions (i.e., rigid or mobile polymer chains), and interactions with proteins could potentially provide solutions to maintaining high protein concentrations in microwells, or make molecular transport more favorable for the desired application.

Chapter 6: Towards the Development of 3D Projection Electrophoresis for High-Throughput Single-Cell Isoelectric Focusing

This work was performed in collaboration with Dr. Samantha M. Grist.

6.1 Introduction

Protein expression, post-translational modifications, localization, and activity are essential to characterize cell state and function.¹⁶⁰ Proteomic measurements of cellular populations, especially for understanding dysfunction in cancerous cells, necessitates single-cell or low-cell resolution to accommodate cell-to-cell heterogeneity. As a brief case study: 15-20% of invasive breast cancers involve increased expression of the HER2 (also called ERBB2) protein. Several truncated HER2 isoforms lack the extracellular domain for canonical drug treatment; therefore, quantitative assessment of the expression of these truncated isoforms provides valuable information on breast cancer type and therapeutic options.^{161–165} Recent characterization of a model breast cancer cell line in the single-cell Western blotting assay reported that 7.4% of cells had an quantifiable truncated isoform, with significant heterogeneity of expression of this truncated isoform.⁴ Interrogation of HER2 isoform expression therefore necessitates the development of high-throughput proteomic assays at single cell resolution capable of distinguishing these isoforms. Proteomic separations via capillary IEF with and without subsequent immunoblot^{13,35} has been demonstrated for the lysate equivalent of 25 cells. Single-cell mass spectrometry has recently been demonstrated for high-expression protein targets.^{17,18} We posit that the ultrathin scIEF assay with subsequent immunoblot^{19–21} can complement these and other proteomic assays to assessing the expression of biologically relevant proteins.

In order to interrogate the proteomic expression of rare or low-abundance sub-populations of cancer cells, the throughput of the ultrathin scIEF assay with subsequent immunoblot^{19–21} must be expanded to accommodate 1000+ cells per experiment (currently 9-50 cells). Thus, we propose a significant modification to the assay itself, developing 3D projection electrophoresis for the high-throughput isoelectric focusing (HTP IEF) assay.

6.2 Materials and Methods

Materials

Silicon wafers (University Wafer 1156), SU8 3050 photoresist (MicroChem), titanium diisopropoxide bis(acetylacetonate) (Sigma 325252), anhydrous isopropanol (Sigma 278475), a custom in-house-designed mask (CAD/ART Services), GelSlick® (Lonza 50640), standard glass slides (VWR), dichlorodimethyl silane (Sigma 440272), 3-(trimethoxysilyl)propyl methacrylate (Sigma 440159), methanol (Sigma 179337), glacial acetic acid (Sigma 8817-46), 30%T 29:1 acrylamide/bis-acrylamide solution (Sigma A3574), N-[3-[(3-benzoylphenyl)formamido]propyl] methacrylamide (BPMA, custom synthesized by PharmAgra Labs), Rhinohide™ (ThermoFisher R33400), ammonium persulfate (APS, Sigma A3678), N,N,N',N'-tetramethylethylenediamine (TEMED, Sigma

T9281), UV photoinitiator 2,2'-Azobis[2-methyl-N-(2-hydroxyethyl)propionamide] (VA086, Wako Chemicals 61551), borosilicate glass plates (McMaster-Carr 8476K62), 4-well plates (ThermoFisher 267061), parafilm (Bemis PM-999), and permanent lab markers (VWR 52877-310) were used to fabricate materials in this study.

Slab IEF was conducted using the Novex IEF buffer set (Invitrogen LC5377), Novex IEF gels (Invitrogen EC66452BOX), IEF standard (BioRad 161-0310), proteomics-grade Ponceau S stain (Amresco K793, lot 18J0156137), Invitrolon PVDF membrane sandwich, 0.45 μm pore size (Invitrogen LC2005), and Western blotting filter paper, 7 cm \times 8.4 cm (Fisher A322).

High-throughput IEF was conducted using the immobilines pKa 3.6, pKa 7.0, and pKa 9.3 acrylamido buffers (Sigma 01716, 01729, 01738), SinuLyte® pH 4-7 ampholytes (Sigma 05087, lot BCBJ7449V), Novex Zoom® pH 4-7 ampholytes (Invitrogen ZM0022, lot 813224A), a 3D projection electrophoresis device designed and printed in-house (shown in **Figure 6-3A**),¹⁶⁶ electrode plates, standard circular magnets, 0.5 mm, 1 mm, 1.5 mm, and 2 mm gel spacers (CBS Scientific MVS0510-R, MVS1010-R, MVS1510-R, MVS2010-R), TritonX-100 detergent (Sigma X100), urea (Sigma U5378), thiourea (Sigma T8656), CHAPS (SAFC RES1300C), 1x RIPA buffer (Pierce 89900), and HALT protease / phosphatase inhibitor cocktail (ThermoFisher 78444). Tris-buffered saline with Tween-20 (TBS-T, CST 9997S) was used for gel incubation and wash steps.

The proteins and molecules used in this study were bovine serum albumin (Sigma A7030, abbreviated "**BSA**"), purified recombinant turboGFP (Evrogen FP522, lot 55201240718, a variant of the GFP with increased fluorescence, MW 27 kDa, abbreviated "**tGFP**"), myoglobin (Sigma M9267, abbreviated "**MYO**"), trypsin inhibitor (Sigma T1021, abbreviated "**TI**"), carbonic anhydrase isozyme II (Sigma C3666, abbreviated "**CA**"), and c-phycoerythrin (Sigma 52468).

The reagents used in this study for protein labeling were Cyanine 488NS, 555NS, and 647NS (Biotium 90117, 90118, 90119, abbreviated "**CFTM-488**," "**CFTM-555**," and "**CFTM-647**," respectively), 1 M pH 8.3 sodium bicarbonate solution (Biotium 99954), 10K MWCO and 3K MWCO ultrafiltration vials (Biotium 99956, 22018), Slide-A-Lyzer® MINI Dialysis units, 3500 MWCO (Pierce 69552), and 2x reaction and storage vials (Biotium 99957, 99958).

Protein Labeling

Proteins were rehydrated in MilliQ water with 0.1 M sodium bicarbonate, following manufacturer instructions. The glycine from the protein solutions was removed either by ultracentrifugation with the Allegra 21R Centrifuge (Beckman Coulter) and rehydration in 1 \times PBS (initial attempt), or by dialysis using the Slide-A-Lyzer® dialysis membranes for 72 hours in PBS with agitation and buffer exchanges every 24 hours (second attempt). Protein labeling was conducted following the Biotium CFTM dye protocol, with a molar ratio of 6, for 1 hour at room temperature, protected from light. To remove unconjugated dye, the ultracentrifugation vials with a 3 kDa molecular weight cutoff were used, and proteins were resuspended in 1 \times PBS. Proteins were dialyzed in MilliQ water with

agitation and multiple buffer exchanges (second attempt) to remove additional unconjugated dye.

Slab IEF

Slab IEF was conducted following the Novex pre-cast gel electrophoresis guide (Invitrogen, IM-1002) using the XCell SureLock Mini-Cell (Invitrogen IM-9003). The proteins from the slab IEF gels were immediately transferred to PVDF membranes using the pre-set Mixed Range Molecular Weight (25-150 kDa) transfer setting on the Pierce Power Blotter (ThermoFisher), following manufacturer instructions. The membranes were stored long-term at 4°C in MilliQ water.

The membranes were imaged on an Olympus IX-71 inverted microscope with an Olympus UPlanFi 4× (NA 0.13) objective and an EMCCD Camera iXon2 (Andor), with imaging settings loaded into MetaMorph software (7.10.1.161, Molecular Devices). The membranes were imaged using a GFP filter cube (XF100-3, Omega Optical), a Cy5 filter cube (Chroma 49009), and a TRITC filter cube (SNARF-585 emission, ET550/20× T570lpxr ET585/20m) for fluorescently-labeled protein targets. The membranes were stained with the Ponceau S stain, and imaged using a Molecular Imager ChemiDoc XRS+ with Image Lab Software (BioRad) for naturally-colored protein targets, the IEF standard, and the total protein stain. Further details are included in **Appendix 6**.

Separation Gel Fabrication

For this study, we use the canonical notation of %T as the total acrylamide monomer concentration (w/v) in solution, and %C as the ratio of bis-acrylamide crosslinker concentration to the total acrylamide monomer concentration.⁴⁷

SU8 fabrication on a silicon wafer was conducted following a standard protocol.³ Briefly, a custom mask with rails spaced 22 mm apart, and microposts of diameter 32 μm, spaced at X = Y = 400 μm in square array blocks of X = Y = 16 mm (**Figure 6-3C**), was used to fabricate features of 40 μm in height (confirmed by optical profilometry) in SU8 on the wafer, which was then silanized with dichlorodimethyl silane.

After wafer treatment with GelSlick®, PA gels were fabricated on the wafer and polymerized onto silanized half glass slides. **Table 4-1** lists the critical components of each gel condition, using 10 kDa PEG as the preformed hydrophilic polymer and leveraging porogen gel fabrication conditions developed by Righetti and colleagues.⁷⁰ Photopolymerization was implemented using VA-086 or LAP as the initiator and polymerized for 4 or 1 minutes, respectively, at 20 mW/cm² light intensity using a 390 nm UV long-pass filter (Edmund Optics) on an OAI Model 30 Collimated UV light source. See **Appendix 1** for further details.

Separation gels of dimensions X = 18 mm, Y = 18 mm, Z = 1 mm (or X = 9 mm, Y = 9 mm, Z = 1 mm) were fabricated using 1 mm spacers (CBS Scientific). These gels were fabricated on the silanized silicon wafer with microposts of diameter 32 μm (**Figure 6-3C**, further details in **Appendix 7**), on a silanized half glass slide. Gel precursor

solutions of 6%T 3.3%C PA with 5 mM BPMA were prepared. Chemical polymerization was implemented using APS and TEMED as the initiator and catalyst, respectively, for 1 hour protected from light. After fabrication, gels were gently detached from the wafer and the glass slide using a razor blade, and incubated in a 1% TritonX-100, 2% Zoom® pH 4-7 ampholyte solution in MilliQ water in a 4-well plate overnight. The resulting separation gel contained microwells of 32 μm diameter and $Z = 40 \mu\text{m}$ height along the top surface of the gel.

Equilibrium Swelling Ratio

The equilibrium swelling ratio was conducted using Flory-Rehner theory.^{47,78–80} After fabrication of PA gels on glass slides with 500 μm spacers to define gel height, gels were weighed immediately on an Ohaus Adventurer Pro weigh station to determine the “fabrication” weight, then incubated in 1 \times TBS-T for 12 hours for PEG diffusion out of the gel. After 12 hours of DI water incubation, the equilibrated gel was weighed again for the “hydration” weight, dehydrated fully with a nitrogen gas stream, and weighed a third time for the “dehydration” weight.

Boundary Gel Fabrication

The anolyte (pH 4) and catholyte (pH 7, pH 10) boundary condition gels were fabricated individually (further details in **Appendix 8**). **Table 6-1** lists the components of each of the anolyte and catholyte boundary condition gels described in this study. Gel precursor solution was pipetted onto a GelSlick®-coated glass plate, covered with a Gel-Slick-coated standard glass slide propped on 0.5 mm spacers (CBS Scientific). Gels were polymerized for 4 minutes at 20 mW/cm^2 light intensity using a 390 nm UV long-pass filter (Edmund Optics) on an OAI Model 30 Collimated UV light source. After cutting gels to $X = 18 \text{ mm}$, $Y = 18 \text{ mm}$, $Z = 500 \mu\text{m}$ dimensions, these boundary condition gels were incubated in DI water and used promptly within 24 hours.

High-throughput IEF (HTP IEF)

The high-throughput IEF assay (further details in **Appendix 9**) was implemented after the fabrication of the separation and boundary condition gels. The in-house-designed 3D projection electrophoresis chamber (**Figure 6-3A**) was placed with both electrode plates facing up. An ice pack was placed under each electrode plate. 2 mm spacers were added on the positive electrode plate to provide stability and reduce compression on the forthcoming gel sandwich. On the positive electrode plate, the anolyte gel was placed with tweezers after gentle removal of the fluid layer by a Kimwipe. The separation gel was placed similarly on top of the anolyte gel, with microwells oriented upwards. 5 μL of protein solution was pipetted into the center of the microwell array, and spread quickly and gently across the surface of the separation gel (**Figure 6-3B and E**).

After a 30 second delay (to simulate diffusion of reagents and lysis of cells in the future single-cell variant of this assay), the catholyte gel was placed similarly and rapidly on top of the separation gel. The negative electrode plate was rapidly placed on top of this 2 mm gel sandwich, overlaid with an ice pack. IEF was conducted by applying 34 V for

the desired timeframe using the PowerPac basic power supply (BioRad). After the desired timeframe of focusing, the catholyte electrode plate and the catholyte boundary gel were rapidly removed. Protein photo-immobilization was induced by application of UV at 100% intensity for 45 seconds with the Hamamatsu LC8 (Hamamatsu Photonics K.K.), sweeping across the gel assembly above the gels.

Immediately after protein photo-immobilization, the separation gels were placed in a Petri dish and sliced manually with a razor blade to obtain a thin sliver across the diagonal of the gel. The sliver was turned on its side, so that the separation axis was oriented parallel to the Petri dish. The Petri dish was set on an Olympus IX-71 inverted microscope with an Olympus UPlanFi 4× (NA 0.13) objective and an EMCCD Camera iXon2 (Andor), with imaging settings loaded into MetaMorph software (7.10.1.161, Molecular Devices). The slivers were imaged using a GFP filter cube (XF100-3, Omega Optical), a Cy5 filter cube (Chroma 49009), a TRITC filter cube (SNARF-585 emission, ET550/20× T570lpxr ET585/20m), and brightfield. Electrode plates were cleaned thoroughly and gently with MilliQ water and Kimwipes between each experimental run.

Micrographs were processed in FIJI ImageJ to extract line plots across the separation axis. These line plots analyzed using an in-house MATLAB (R2015b, MathWorks) script^{6,48,49} adapted to HTP IEF (code in **Appendix 11**). Gaussian curve fitting to the line plots led to the extraction of the peak height, peak location, peak width, area under the curve, SNR, and other assay-specific parameters from each ROI. Validation of the Gaussian curve fits is conducted analytically ($R^2 \geq 0.7$ and signal-to-noise ratio $SNR \geq 3$) and confirmed manually. For the images taken on the Olympus microscope setup, 1 pixel corresponds to 4 μm .

Confocal imaging experiments were conducted on an upright Zeiss LSM 880 NLO AiryScan with Fast-AiryScan (Zeiss, Oberkochen, Germany). Images were acquired at room temperature using a 20× water objective (Zeiss). Separation gels were imaged using a 561 laser at 40% power, a 488 laser at 20% power, and a 633 laser at 50% power, using the MBS488/561/633 beam splitter and the Zen 2010 software (Zeiss). Z-stack images were acquired.

Table 6-1. Composition of HTP IEF anolyte and catholyte gels.

Components of the anolyte and catholyte gels used for electrophoresis in this study.

Components of individual boundary gels	pH 4 anolyte	pH 7 catholyte	pH 10 catholyte
Polyacrylamide gel	15% T 3.3% C 0.2% VA-086	15% T 3.3% C 0.2% VA-086	15% T 3.3% C 0.2% VA-086
Boundary conditions	13.5 mM pKa 3.6 immobiline 6.4 mM pKa 9.3 immobiline	6.5 mM pKa 3.6 immobiline 13.5 mM pKa 7.0 immobiline	5.6 mM pKa 3.6 immobiline 14.4 mM pKa 9.3 immobiline

Statistical Analysis

To compare the means of the gel conditions assessed in this study, we assessed statistical significance using the one-way ANOVA's with Kruskal-Wallis test. To compare specific pairs of gel conditions, we applied a post-hoc Dunn's multiple comparison test with $p < 0.05$ (*), using GraphPad Prism version 8.1.1. Linear regression fit was performed using an in-house MATLAB script.

6.3 Results and Discussion

Development of a fluorescently-labeled IEF protein ladder

In order to reliably assess the separation resolution of this platform and control for IEF-based irregularities in future biological studies, we assessed multiple methods by which to create a reliable IEF protein ladder. Canonical IEF assays like slab IEF typically use commercially-available solutions of proteins, including those produced by Bio-Rad, ThermoFisher, and Amersham,^{51,167} or fluorescently-labelled peptides.¹³ Prior research by Dr. Elaine J. Su (not included here) to develop an IEF protein ladder compatible with the ultrathin IEF assay eliminated the use of the IEF standard solution (Bio-Rad) or the IEF protein marker solutions (similar to ThermoFisher 3921201), and indicated the need for a set of fluorescently-labeled proteins rather than immunoprobings for multiple protein targets or relying on visible light detection.¹⁶⁷ Our prior investigation (not included here) indicated that the commercially-available fluorescent pI markers (Sigma 89149, 77866, 73376) are not detectable after attempted immobilization with UV-activated BPMA, eliminating these molecules as candidates for the IEF ladder. The attempt to incorporate the recently-developed protein bead system into the 2D IEF assay is discussed in **0**.

In designing an in-house IEF protein ladder, we identified the following design parameters. The ideal fluorescently-labeled IEF protein ladder should include 3+ proteins spanning the full pH gradient, for interrogation of the linearity of the pH gradient. In its final form, the ladder should be fluorescently labeled in one channel, preferably the 488 channel to overlap with the BPMA-induced fluorescence background (**Appendix 13**). The fluorescence labeling on these proteins should not disrupt the pI of the proteins, nor should it add significantly to the molecular weight of the overall protein-label conjugate. The ladder should be incorporated into either the separation gel or the solution of singularized cells at sufficiently high concentration for easy detection above the LLOD without obscuring the fluorescence of adjacent immuno-labeled proteins.

Within the IEF protein ladder, each protein should be on the lower end of molecular weights (< 100 kDa), to avoid partitioning-induced issues of in-gel concentration as well as low in-gel electrophoretic mobility far from the pI. In addition, each protein should feature few to no isoforms, few to no post-translational modifications, a known theoretical or experimental pI, and sharply focused bands at the pI. The proteins must be immobilized by UV-activated BPMA, and preferably would be targeted in an immunoblot with a high-to-medium affinity primary antibody for validation. From a practical perspective, we preferred a commercially-available purified protein solution

over the need to implement a pulldown assay from lysates of cells genetically modified to overexpress the protein in question.

From these parameters, we labeled 3 proteins individually with a different CF™ dye (listed in **Table 6-2**). The CF™ dyes were reported by the manufacturer, Biotium, to not affect the isoelectric point of the labelled proteins. Conveniently, these proteins would stack in a pH gradient in an IEF assay (pH 4 < TI < CA < MYO < pH 7) in a different order than in a Western blot assay (MYO < TI < CA). Since each protein was labeled in a different fluorescence channel, this allowed us to swiftly distinguish an IEF separation from a size-based separation.

Table 6-2. Proteins and fluorescence labels in the in-house-designed IEF protein ladder.

Protein	Abbreviation	Molecular weight (kDa)	pI (manufacturer)	Experimental pI (with fluorescent label, slab IEF) (Figure 6-1)	CF™ dye label
Myoglobin	MYO	16.7	6.8 7.2	6.75 (streak)	CF™-488
Carbonic anhydrase isozyme II	CA	30	5.4	5.54	CF™-555
Trypsin inhibitor	TI	20.1	4.6	4.45	CF™-647

For validation, we first interrogated the isoelectric point of these labeled proteins, as well as AlexaFluor-555-labeled bovine serum albumin (BSA), AlexaFluor-647-labeled ovalbumin (OVA), and the naturally-fluorescent phycocyanin. For comparison and quantitative identification of the labeled proteins' pI's, we included the commercially available IEF standard (BioRad) and used the Novex slab IEF kit for robust protein separations. After rapid transfer of the slab IEF gels to PVDF membranes, we used Ponceau S stain to visualize the IEF standard and used fluorescence widefield microscopy to visualize the fluorescently-labeled proteins (**Figure 6-3A, B**). Interestingly, the AlexaFluor labels on BSA and OVA (**Figure 6-3A**) result in protein sub-populations with a range of pI's spanning over an entire pH unit. We hypothesize that different degrees of labeling on the proteins would result in this dramatic shift.

To validate the slab IEF methodology, we assessed IEF in each material by considering the slope of each pH gradient, dpH/dx . To determine dpH/dx , each of the detectable protein bands in the commercial IEF standard were fit to a Gaussian curve. We then used a linear regression fit of the proteins to estimate the pH gradient slope. The calculated $dpH/dx=0.06 \text{ mm}^{-1}$ (**Figure 6-1C, D**) for both slab IEF's match the back-of-the-envelope estimate of $dpH/dx=0.057 \text{ mm}^{-1}$ for a pH 4-7 gradient across a gel of 7 cm length. The quantitative analysis of the IEF standard from slab IEF's are in good agreement with each other.

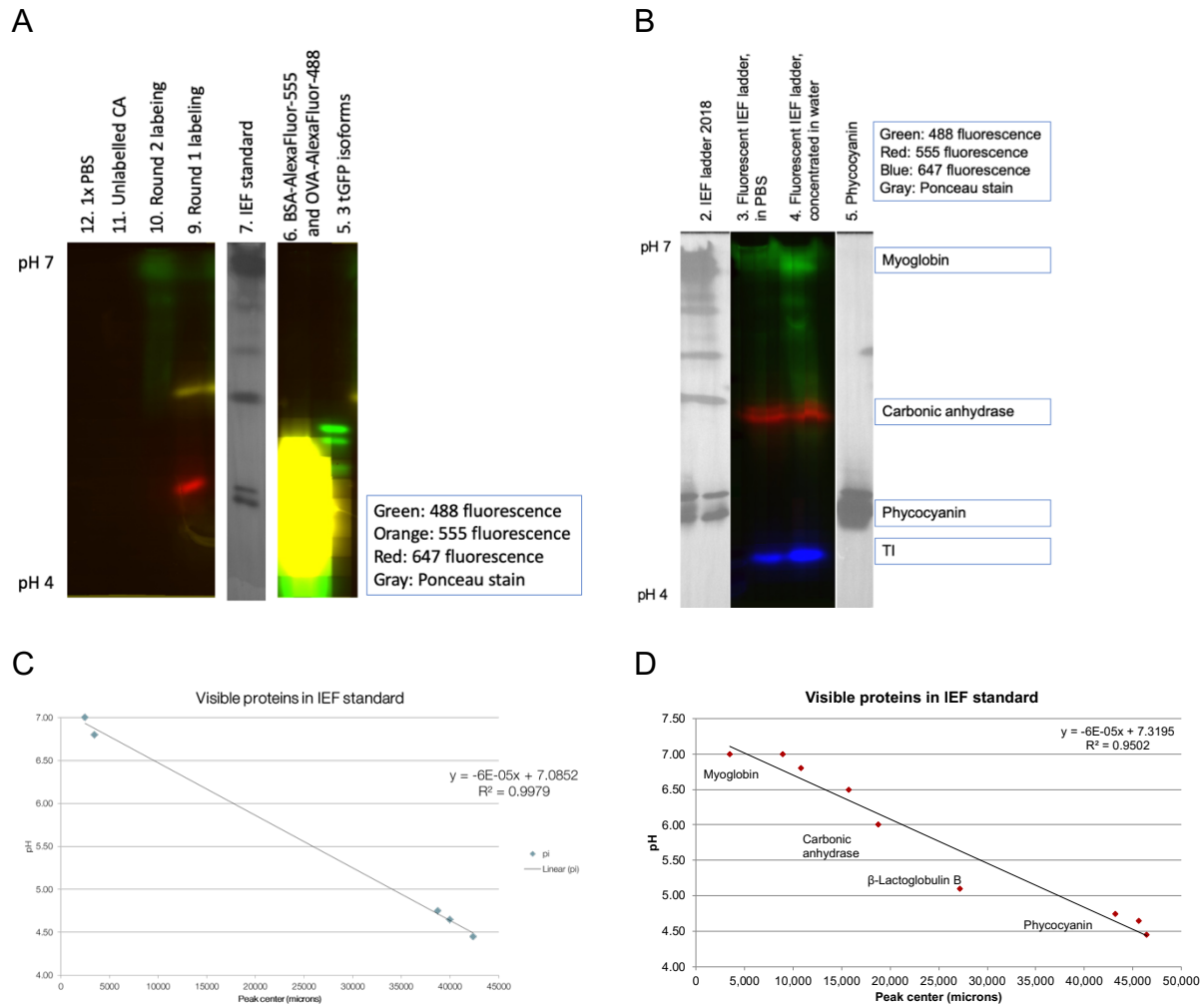


Figure 6-1. Experimental characterization of pI's of fluorescently-labeled proteins in IEF protein ladder.

(A) Slab IEF of the fluorescently-labeled IEF proteins, BSA and OVA with AlexaFluor labels, and tGFP protein. (B) Slab IEF of the fluorescently-labeled IEF proteins in PBS and concentrated in DI water, and phycocyanin. (C) Linear fit of the detectable protein peak locations and the reported protein pI's for the slab IEF reported in (A). (D) Linear fit of the detectable protein peak locations and the reported protein pI's for the slab IEF reported in (B).

We extracted the peak locations of each protein in the IEF standard (**Figure 6-3A, B**), and fit the peak locations against the reported pI's of the proteins. From the linear fit ($y = -6E-05 * x + 7.09$, with $R^2 = 0.9979$, **Figure 6-3C**), the experimental pI's of the three tGFP isoforms in **Figure 6-1A** were calculated as 4.87, 5.14, and 5.27, compared to the experimental pI's calculated from microfluidic IEF of 4.88, 5.00, and 5.19.¹⁹ From the linear fit ($y = -6E-05 * x + 7.32$, with $R^2 = 0.9502$, **Figure 6-3D**) and the peak locations of the 3 proteins in our fluorescently-labeled IEF protein ladder, we calculated the experimental pI's for each protein with the CF™ dye (**Table 6-2, Equation 6-1**). The experimental pI's for the IEF ladder are in good agreement with the manufacturer-reported pI's, confirming that the CF™ dyes do not majorly affect protein pI.

$$\Delta pI_{min} = 3 * \frac{dpH}{dx} * \sigma_{protein}$$

Equation 6-1. ΔpI_{min} quantified for proteins focused in an IEF assay.

The two rounds of labeling proteins with CF™ dyes (**Figure 6-3A**) yielded different labeling efficiencies for each protein, though researcher methodology did not vary significantly between the two rounds. Moving forward, the brighter MYO-CF™-488 from round 2 was added to the brighter CA-CF™-555 and TI-CF™-647 from round 1, to form our fluorescently-labeled IEF protein ladder. These proteins were concentrated by dialysis in water (**Figure 6-3B**) for forthcoming use. Both TI and CA focused into sharp protein bands. Resolving the two MYO isoforms proved unreliable, yielding a poorly-resolved protein band near the cathode.

Future iterations of this fluorescently-labeled IEF protein ladder should replace myoglobin with lectin (Sigma L1277, with pI's of 8.2, 8.6, 8.8), carbonic anhydrase isozyme I (Sigma C6653, pI 6.6), and/or trypsinogen (pI 9.3). Since the focused TI band is well-resolved, further development of the IEF protein ladder in the pH 4-5 range may not be required. If desired, bovine serum albumin (pI 4.6), β -lactoglobulin (pI 5.2, 5.3), and α -lactoglobulin (pI 5.0) are viable candidates. The naturally fluorescent phycocyanin (pI 4.5) overlaps with the TI band and is therefore not included in this ladder. Additional finetuning of the labeling process for accurate characterization of labeling efficiency using the NanoDrop is also required. Our attempts to characterize the labeling efficiency yielded protein peaks shifted away from the expected absorbance values. We hypothesize that this unexpected shift may be due to both a high molar excess of dye during the labeling process, and issues with ultracentrifugation both prior to the labelling (to remove glycine) and after the labeling (to remove unconjugated dye, **Figure 6-2**).



Figure 6-2. Waste products after 5 ultracentrifugation washes reveals an excess of unconjugated dye from the conjugation process.

From left to right, the first vials are excess free dye, then the waste products from 5 consecutive wash steps.

Development of the HTP IEF assay

In order to significantly increase the throughput of the ultrathin single-cell IEF with subsequent immunoblot, while maintaining the 9 mm separation length required for high IEF separation resolution, we posited an idea to leverage the Z-axis for the separation axis. Along the X- and Y-axes, we would implement an array of microwells for a 100-fold increase in throughput. It is important to note that this work was conducted in parallel with other 3D projection electrophoresis developments in this lab by Dr. Samantha Grist, among others.

Given that the immunoblot in its current form relies on passive diffusion for introduction of antibodies into the gel matrix, a 9 mm separation length in the Z-dimension would render the immunoblotting timeframes excessively long. The calculated time to equilibrium ($\tau = 36$ days) was estimated using a 3D model of diffusion ($\tau = x^2 / 6D$), where $x = 9$ mm gel height, and $D=4.3 \mu\text{m}^2/\text{s}$ for the diffusivity of IgG* in an 8%T 2.6%C PA gel.¹⁰² Over this extended timeframe, considerations of antibody degradation, antibody-antigen dissociation rates, contamination risks, and other concerns would significantly reduce immunoblotting efficiency. Therefore, as a proof-of-concept, we attempted a 1 mm separation lane (**Figure 6-3A**), while an active immunoblotting method was concurrently developed.¹⁶⁶

Thus, the high-throughput IEF assay involves three gels (**Figure 6-3B**). First, the 6%T separation gel of dimensions $X = 18$ mm, $Y = 18$ mm, and $Z = 1$ mm serves as both the anti-convective substrate for the IEF separation and the PA gel matrix to which focused proteins are immobilized using UV-activated BPMA, theoretically for the subsequent immunoblot. Second, the anolyte boundary condition gel serves as an acidic (pH 4) edge against which the ampholytes stack to form the pH gradient.^{16,19} Third, the catholyte boundary condition gel serves as the basic (pH 10) edge for the other end of the pH gradient.

For the IEF separation, we applied 34 V, for an electric field strength of 166 V/cm across the 2 mm separation axis (crossing the anolyte, separation, and catholyte gels). For comparison, the ultrathin IEF assay using the SinuLyte® ampholytes applies 690V, for an electric field strength of 139 V/cm across the 50 mm separation axis (crossing the anolyte, focusing, and catholyte components comprising the lid gel, **Chapters 2-4**).

For these large separation gels of dimensions $X = 18$ mm, $Y = 18$ mm, and $Z = 1$ mm, we considered a method to strengthen the gel without significantly increasing gel porosity (which would decrease partitioning of large molecular weight species into the gel). We investigated the effect of incorporating Rhinohide™ (a solution of high-molecular-weight linear acrylamide, by best estimate)¹⁶⁸⁻¹⁷⁰ into the gel precursor solution, on the gel porosity, using the equilibrium swelling ratio assay (**Figure 6-4**). We observed a statistically-significant difference in the equilibrium swelling ratio (Q , calculated using **Equation 6-2**) between the gels without Rhinohide™ and the ones containing 4% Rhinohide™ from a more recently purchased bottle (16.7 ± 0.26 in 6%T 3.3%C APS/TEMED gels, 18.8 ± 0.25 in gels with 4% old Rhinohide™, 19.8 ± 0.25 in gels with 4% new Rhinohide™).

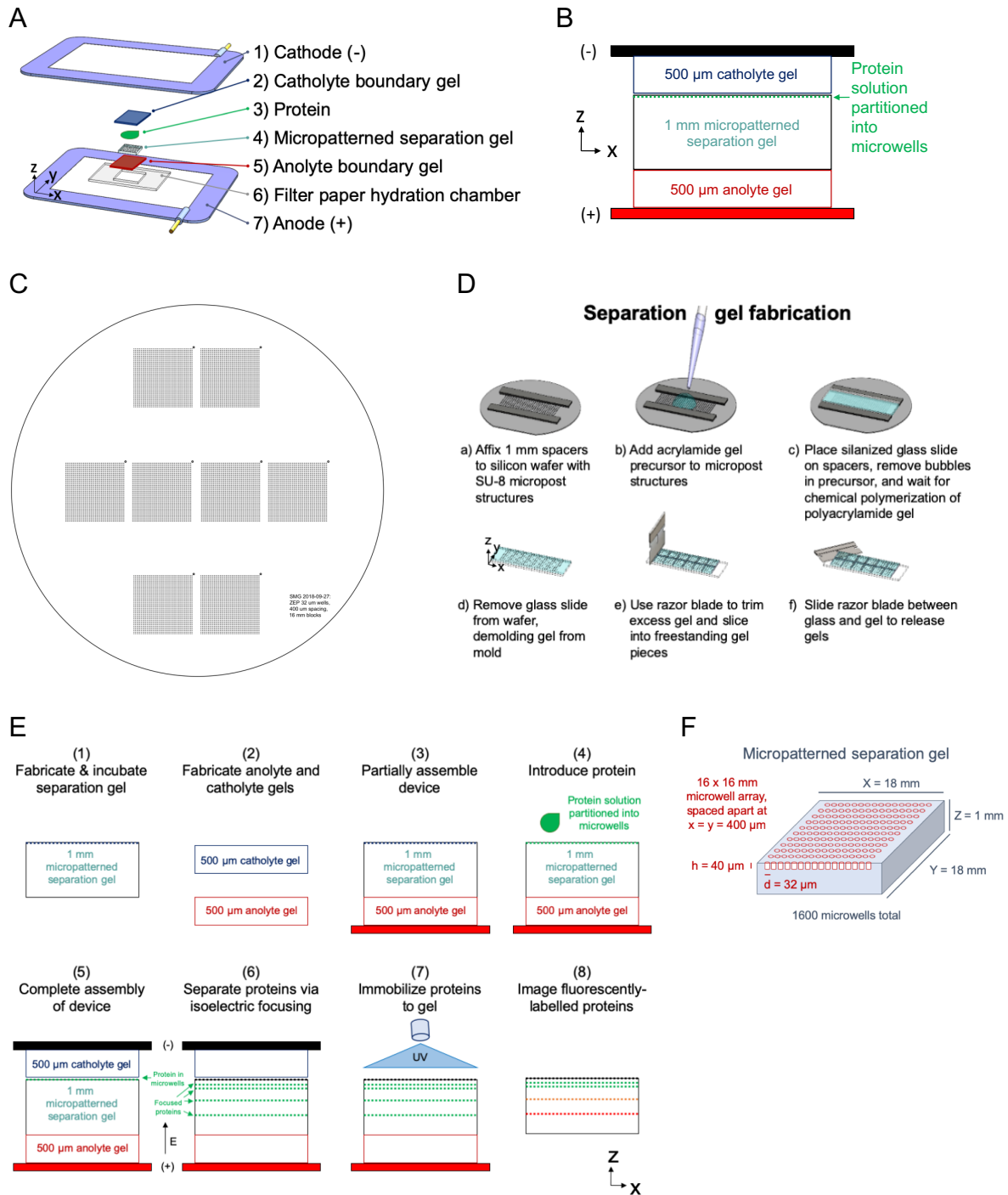


Figure 6-3. Schematic of high-throughput IEF platform using 3D projection electrophoresis.

(A) Orthogonal view of the assembly of gels within 3D projection electrophoresis chamber. (B) Side view of the assembly of gels in the HTP IEF platform. (C) Mask design for microwells of 32 μm diameter, spaced apart at $x = y = 400 \mu\text{m}$ in blocks of length $X = Y = 16 \text{ mm}$, for the fabrication of 8 $18 \times 18 \times 1 \text{ mm}$ separation gels on one wafer. (D) The workflow for fabrication of the separation gel. (E) The workflow of the HTP IEF assay, from gel fabrication and assembly through protein electrophoretic separation, immobilization, and imaging. (F) Orthogonal view of the micropatterned separation gel. Schematics are not to scale.

$$Q = \frac{\text{mass}_{hydrated\ gel}}{\text{mass}_{dehydrated\ gel}}$$

Equation 6-2. Equilibrium swelling ratio in PA gels.

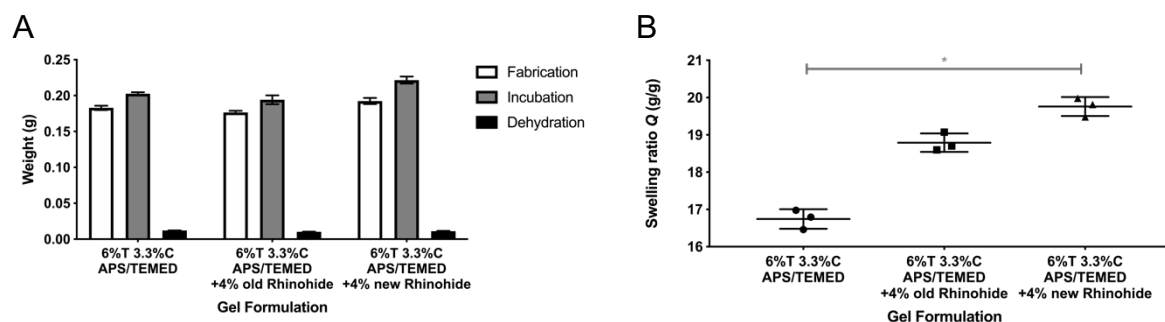


Figure 6-4. Rhinohide™ increases porosity of gels, without significant differences between Rhinohide™ lots.

(A) Gel weights measured in equilibrium swelling ratio experiment after fabrication (white); after incubation in solution to equilibrium (gray), and after dehydration (black). (B) The swelling ratio (Q) varied significantly due to the inclusion of 4% new Rhinohide™. This indirectly indicates a change in gel porosity. Mean and standard deviation marked by vertical lines for $n=3$ gels per condition. One-way ANOVA with Kruskal-Wallis test and post-test Dunn's multiple comparison test with $p<0.05$ (*).

Due to concerns about dehydration at the exposed edges of the separation gel, which might cause uneven separations across the gel, we investigated the impact of the filter paper hydration chamber. Repeated experimental runs indicated that the separation gels retained sufficient water content after 60s electrophoresis (**Figure 6-5**).

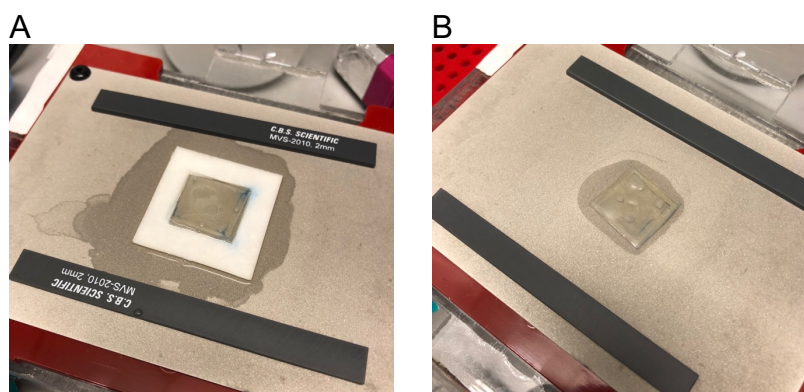


Figure 6-5. The filter paper hydration chamber is not required to maintain the hydration state of the separation gel after 60 s electrophoresis in the HTP IEF assay.

Top-down images of the post-experimentation HTP IEF separation gel and anolyte gel sandwich (clear stack in the middle of the image) (A) with the filter paper hydration chamber (white) and (B) without the filter paper on the electrode plate (beige). The 2 mm spacers are shown at the edges of the electrode plate (black). The blue-tinted edges on the separation gel are from excess TI-CF™-647.

After repeated observations of poor partitioning of the IEF protein ladder into newly-fabricated gels, we investigated the effect of methods for rendering the surface of a silicon wafer hydrophobic (dichlorodimethyl silane or GelSlick®). GelSlick® is an electrophoresis-compatible hydrophobic surface treatment, documented as an

alternative to silane-based coatings, which includes ethanol, propanol, and ethyl hydrogen sulphate.^{171,172} From the manufacturer's instructions for GelSlick®, dichlorodimethyl silane and GelSlick® are incompatible surface treatments. In addition, an excess of GelSlick® on the wafer surface transferred to the surface of the microwell-laden separation gels. After careful experimentation (not shown here) to eliminate other potential sources of error, and additional investigation by other researchers in the Herr lab, we decided to exclusively use a thin layer of GelSlick® on our silicon wafers (with extensive water rinse of the wafers prior to use) for fabrication of the separation gels.

With these modifications, we investigated the reproducibility of the IEF separations both within gels and across triplicate gels in the same experiment (**Figure 6-6A-C**). The electrical current decreased within the first 10 s for all gels, indicating the ampholytes formed a pH gradient (**Figure 6-6E**). It is important to note that the separations across the length of the gels feature several irregularities (**Figure 6-6B, C**), which indicates a need for more rigorous investigations of separation performance across the gel.

Quantitative assessment of IEF separation performance in the center of these 3 gels yielded a dpH/dx of $2.83 \pm 0.25 \text{ mm}^{-1}$ (mean \pm standard deviation for $n=3$ gels) for the Zoom® ampholytes (**Figure 6-6D**). We anticipated a dpH/dx of 3 mm^{-1} for this pH 4-7 gradient across a 1 mm separation axis. For comparison, the dpH/dx was quantified in the ultrathin IEF assay as $0.35 \pm 0.01 \text{ mm}^{-1}$ for the SinuLyte® ampholytes over a pH 4-7 gradient and a 9 mm separation axis (**Chapter 3 and Chapter 4**) and 0.40 mm^{-1} for the Polybuffer® ampholytes over a pH 4-9 gradient and a 9 mm separation axis.¹⁹ Reduction of the variability in this measurement would be necessary for a robust assay, which supports the need for the development of an immobilized pH gradient^{50,53,54} rather than a ampholyte-generated gradient.

As a measure of the linearity of the pH gradient, we measured the mean R^2 statistic of the linear regression fit as 0.95 ± 0.06 (mean \pm standard deviation for $n=3$ gels) for the Zoom® ampholytes (**Figure 6-6D**). For comparison, the R^2 statistic was quantified in the ultrathin IEF assay as 0.89 ± 0.03 for the SinuLyte® ampholytes over a pH 4-7 gradient and a 9 mm separation axis (**Chapter 3 and Chapter 4**) and 1.00 ± 0.00 for the Polybuffer® ampholytes over a pH 4-9 gradient and a 9 mm separation axis.¹⁹ The manufacturer of the Zoom ampholytes® does not provide information on the linearity of the pH gradient in IEF.

Finally, we estimated the minimum pI difference for which two neighboring protein peaks are fully resolved¹⁶ (ΔpI_{min}), using the relationship in **Equation 6-1**, where σ_{protein} is a measure of the peak quarter-width (i.e., standard deviation of the Gaussian fit to the fluorescence intensity profile when focused). When averaged over all three proteins for each gel, ΔpI_{min} was quantified as 1.14 ± 0.57 (mean \pm standard deviation for $n=3$ gels) for the Zoom® ampholytes. For comparison, ΔpI_{min} was quantified as 0.16 ± 0.02 in the ultrathin IEF assay across a 9 mm separation axis (**Chapter 3 and Chapter 4**), 0.13 ± 0.02 in the ultrathin IEF assay across a 9 mm separation axis¹⁹; and 0.11 for adherent-cell ultrathin IEF in free solution across a 9 mm separation axis²¹. Though not unexpected given the short 1 mm separation axis in the HTP IEF assay, this large ΔpI_{min}

may be remedied by careful adjustment of electric field strength and an increased separation axis length (**Chapter 2**) for improved separation performance.

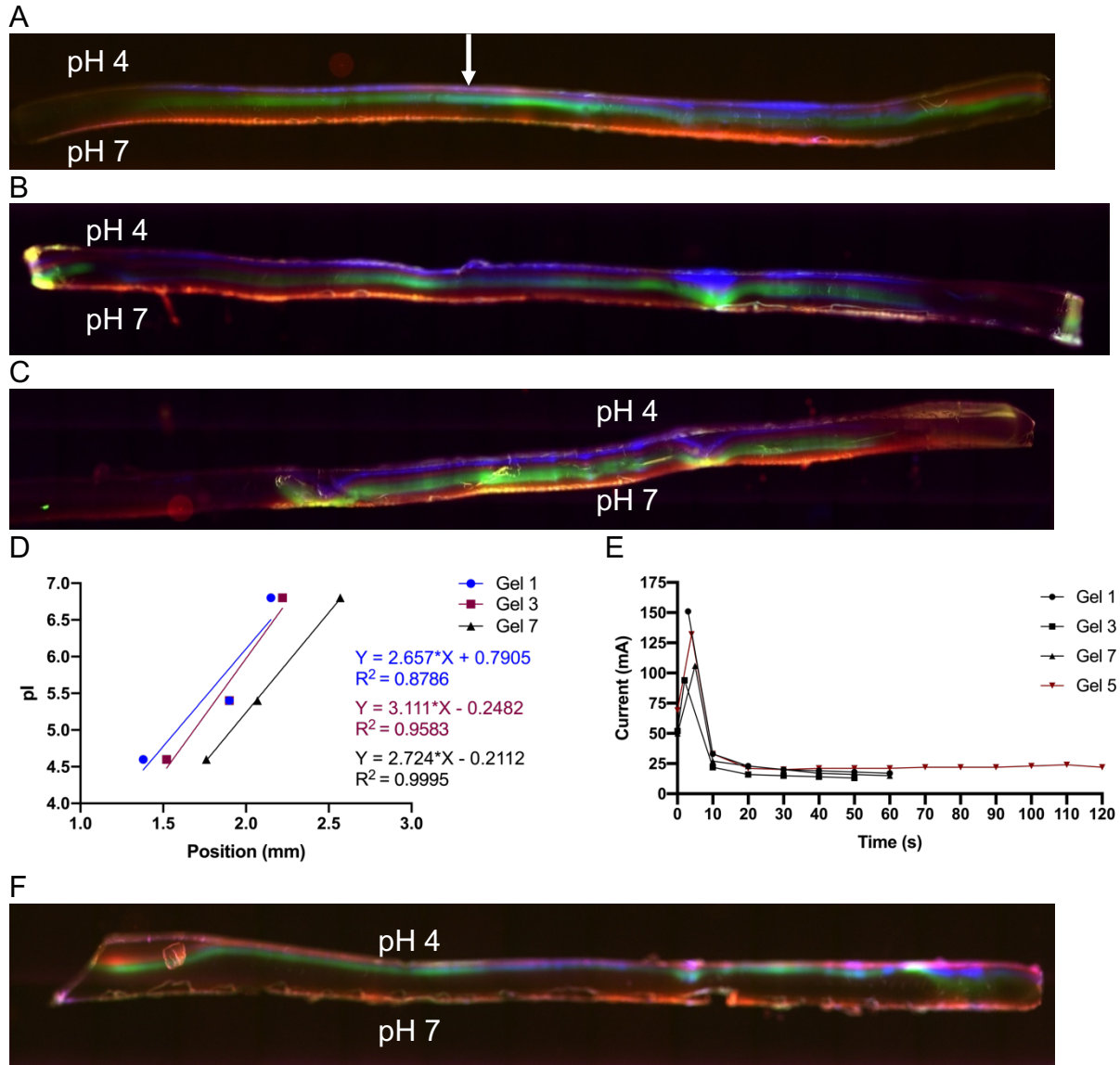


Figure 6-6. The HTP IEF assay yields reproducible separations of the fluorescently-labeled IEF protein ladder at 60 s electrophoresis.

(A-C) Widefield microscopy images of the diagonal sliver of three HTP IEF gels (named Gels 1, 3, and 7, respectively) with the fluorescently-labeled IEF protein ladder focused at 60 s electrophoresis. Myoglobin is false-colored red, carbonic anhydrase green, and trypsin inhibitor blue. Gel is oriented with the pH 4 anolyte boundary condition interface at the top of the image. White arrows indicate the approximate region at which the average fluorescence intensity was generated. (D) The peak centers of the 3 focused proteins were plotted against the protein pI's, and a linear regression fit was applied to extract IEF separation performance metrics. (E) The electrical current decreased within the first 10 s for all gels, indicating the ampholytes formed a pH gradient. (F) A HTP IEF gel in the same experiment (Gel 5) to Figure 6-8 with proteins focused at 120 s electrophoresis yielded bands collapsed at the anode.

It is particularly important to note that ΔpI_{min} is dependent on the $\sigma_{protein}$ for all 3 proteins in the IEF protein ladder. σ_{MYO} was quantified as 0.16 ± 0.14 mm, compared to $\sigma_{CA} = 0.16 \pm 0.07$ mm and $\sigma_{TI} = 0.08 \pm 0.004$ mm (mean \pm standard deviation for $n=3$ gels). The myoglobin band exhibits both a particularly diffuse band and large variation, especially as the two myoglobin isoforms were not resolved in these gels. This further supports our working conclusion to replace the myoglobin in the IEF protein ladder, as described above.

Interestingly, an $n=1$ gel in the same experiment underwent electrophoresis for 120 s (**Figure 6-6D**), yielding protein bands collapsed against the anode. It is unclear if this is an indication of anodic drift over time, or instability of the IEF pseudo-equilibrium over time, or a faulty experimental run.

An initial attempt at HTP scIEF with U251-tGFP cells (not shown here) did not yield detectable protein bands. The separation gel was incubated solely in MilliQ water for > 24 hours to maintain cell viability during the 10 min cell settling period. The anolyte and catholyte gels were the selected delivery mechanism for 2% TritonX-100 for cell lysis and 4% Zoom® ampholytes for IEF (double the standard IEF solution, for equilibration with the separation gel), incubated for > 12 hours in solution. It is unclear whether the lack of fluorescent tGFP protein bands is due to a limitation in analytical sensitivity, a requirement for immunoblotting for detection, or insufficient delivery of lysis and IEF reagents from the anolyte and catholyte gels.

6.4 Conclusions and Future Directions

In this study, we developed a fluorescently-labeled IEF protein ladder for reliable characterization of IEF immunoblots, and demonstrated a proof-of-concept HTP IEF assay using 3D projection electrophoresis. We investigated several avenues for optimization of the assay, and characterized the IEF separation performance and reproducibility of the gels.

The immediate research questions for this assay involve verification of IEF equilibrium and characterization of analytical sensitivity. In addition, it would be important to investigate if immobiline degradation upon application of an electric field might be inducing anodic drift. Modifications to the composition and/or implementation of the boundary condition gels could improve IEF stability (including the inclusion of DMAPMA⁸⁸ or Synperonic® F-108 surfactant¹⁵ in the separation gel) and better preserve *in vitro* protein state (including the inhibition of non-native disulfide bond formation¹⁷³ via hen eggwhite lysozyme). Since these separation gels are sufficiently large compared to those in ultrathin IEF assay, without the large buffer volumes typically used in slab IEF or capillary IEF assays, it would also be important to characterize the Joule heating and heat dissipation within the separation gel, especially within the center of the gel, and subsequent effects on separation resolution. Numerical simulation of diffusion-based protein distribution during lysis and electrophoresis (**Chapter 5**) would provide insight into protein losses and sufficient spacing between individual microwells for single-cell resolution.

This platform must also be integrated with developments in electrophoretic immunoblotting¹⁶⁶ and developments in the imaging workflow for 3D projection electrophoresis gels, either by confocal laser scanning microscopy, lightsheet microscopy, or other faster microscopy platforms with Z-resolution, for increased analytical sensitivity by a subsequent immunoblot. As an alternative, we posit that a modified separation gel structure, with temporary connectors in between rows of microwells, would allow the separation gel to be used as an entire unit for the IEF separation and protein immobilization. Subsequently, the temporary connectors could be disrupted and removed, rendering the 18 × 18 × 1 mm separation gel into a series of smaller 18 × 0.4 × 1 mm gel segments (one row of microwells and separation lanes contained within each gel segment), for immunoblotting and imaging via widefield epifluorescence. The reduced thickness of these gel segments would allow for standard handling of these gels with immunoblotting, thereby avoiding issues of extended immunoblotting time, concerns of antibody-antigen dissociation kinetics, etc. The N,N' - [(1-methylethylidene)bis(oxy-2,1-ethanediyl)] diacrylamide (diacrylamide ketal, DK) cross-linkers¹⁷⁴ may serve as these temporary connectors, provided modifications to reduce irregular gel swelling (as reported by Dr. Julea M. Vlassakis,¹⁷⁵ among others). One could design a sufficiently precise device to slice the separation gel with this 400 μm precision. For better microscale precision and ease of use, photopolymerization *en masse*, or via 3D printing to systematically build the multi-material separation gel, may serve this purpose well.

To reduce protein losses and subsequently improve the analytical sensitivity of this assay, the modification of the benzophenone immobilization moiety (benzophenone N-[3-[(3-benzoylphenyl)formamido]propyl] methacrylamide, BPMA) to extend the linker between the benzophenone group and the methacrylamide group incorporated into the PA gel matrix may be useful. With an extended linker, the BPMA would exhibit an increased functional radius of action, wherein the BPMA could interact with and bind to proteins during the protein immobilization step. Pairing this with tuning the BPMA concentration would preserve the maximum protein content in the IEF-focused bands, providing maximum antigen for the subsequent immunoblot, which would be especially important for low-expression protein isoforms.

With sufficient separation resolution and analytical sensitivity, this high throughput IEF platform could be used to investigate many biologically-relevant proteins. Of particular interest are the HER2 isoforms relevant in breast cancer. Recent characterization of the full-length P185 and truncated (P110) isoforms in BT474 cells in the single-cell Western blotting assay reported that 7.4% of all BT474 cells had an observable truncated isoform band (after protein immobilization and immunoblotting in this assay), with a CV of 77% in the heterogeneity of expression of this isoform and an estimated expression level of 160 femtograms of the truncated isoform.⁴ From an assessment of the feasible size-based and charge-based separations of several HER2 isoforms (**Table 6-3**), this high-throughput IEF platform may be suitable for quantitative characterization of the expression of these HER2 isoforms in breast cancer cell lines, banked breast cell lines, and primary cell or tissue samples.

Furthermore, phosphorylation of proteins is an essential mechanism for protein activation, regulating a series of signaling pathways tied to cell cycle regulation, proliferation, and activity. The ERK and Akt proteins both require multiple phosphorylations for functionality, and prior studies have indicated significant cell-to-cell heterogeneity in the activity of these proteins.^{12,176–179} Given an estimate of 1-10% phosphorylation of proteins at any time¹² and the shift in pI by a mean of 0.1 from each phosphorylation,^{180,181} it may be feasible to electrophoretically separate biologically-relevant protein isoforms in different phosphorylation states (phospho-forms) in single cells with a ΔpI of 0.1. IEF separations of ERK phospho-forms was previously demonstrated in a similar IEF platform at 25-cell resolution.¹³

The HTP IEF assay is an endpoint assay that, in its current formulation, does not convey information about the timing of protein expression. Mapping specific protein isoforms and post-translational modifications, as well as activation of specific protein pathways, to proteomic markers of the mitotic cell cycle (including cyclins, Ki67, and PCNA) would provide additional insight into the temporal aspect of protein expression and activity. The combined interrogation of HER2 isoforms, protein isoforms and phospho-forms in other pathways implicated in breast cancer, and cell cycle markers would significantly extend the combined analytical value of the HTP IEF assay towards interrogations of breast cancer, and computational identification of breast cancer cell sub-populations.

In the future, additional developments to this platform to incorporate the porogen gels as the separation gel for improved analytical sensitivity (**Chapter 3**), an immobilized pH gradient^{50,53,54} in the separation gel for improvements in ΔpI_{min} and reproducibility, and assay modifications to accommodate un-trypsinized biological samples²¹ (including novel developments by Dr. Grist and others) would create a particularly viable platform for high-selectivity, high-throughput IEF separations of proteins from single cells and relevant biological materials.

Table 6-3. The theoretical isoelectric points and molecular weights of several HER2 isoforms indicates the need for an IEF assay capable of separating proteins with a ΔpI_{min} under 0.04.^{4,161,162,164,165,182}

HER2 isoform	Length (amino acids)	Molecular weight (kDa)	Theoretical isoelectric point
P185	1255	185	5.58
$\Delta 16$	1239	~ 185	5.62
P110	645	110	5.18
P95	~608	95	5.31

Chapter 7: WAT-on-a-Chip: A Physiologically Relevant Microfluidic System Incorporating White Adipose Tissue

This work was performed in collaboration with Dr. Peter Loskill, Thiagarajan Sezhian, Dr. Kevin M. Tharp, Dr. Felipe T. Lee-Montiel, Dr. Willie Mae Reese, Dr. Peter-James H. Zushin, Dr. Andreas Stahl, and Dr. Kevin E. Healy. This work is reproduced by permission of The Royal Society of Chemistry from P Loskill, T Sezhian, K Tharp, S Jeeawoody, WM Reese, A Stahl, KE Healy. "WAT-on-a-chip: A microfluidic system incorporating physiologically relevant white adipose tissue." *Lab on a Chip*. 2017; 17:1645-54.

7.1 Introduction

Engineered tissues have emerged as a powerful tool for translational biomedical applications as well as to understand and study disease mechanisms. Although various tissue engineering approaches for regenerative medicine have been introduced,^{183,184} they typically have restricted usefulness for other applications such as drug screening due to three major limitations. First, currently they cannot recapitulate the complex circulation of humans which continuously transports nutrients, drugs, and other soluble compounds toward the tissue, and clears metabolic waste away from the tissue. Second, their macroscale requires a large number of cells preventing the parallelization and scale up for commercial applications. Third, they typically have tissue to fluid volume ratios that are not physiologic thereby altering the delicate balance of autocrine and paracrine factors on tissue function. These limitations can be overcome by integrating engineered tissue with physiologically relevant microfluidic systems to create organ-on-a-chip systems, which have evolved from a conceptual idea to a feasible new paradigm for drug screening.^{185–190} These microfluidic approaches offer significant advances including: unprecedented control of fluid flows; compatibility with high content drug screening; miniaturization of large systems for convenient operation; significant reduction of very expensive cell reagents used; physiological relevant tissue to media volumes, and potential for connection with other organ systems. Recently, a variety of promising organ-on-a-chip systems have been developed, also referred to as microphysiological systems (MPS), such as models of cardiac,³² pulmonary,¹⁹¹ hepatic,¹⁹² renal,¹⁹³ and vascular tissues.¹⁹⁴

In spite of it comprising approximately 20% body weight of healthy men and up to 25% women, and can reach more than 50% body weight in obese adults,^{195,196} adipose tissue has been frequently overlooked for MPS. Like the liver and skeletal muscle, white adipose tissue (WAT) is an insulin sensitive organ as well as a critical storage site for excess dietary energy. WAT exists in different anatomical locations and is comprised of a heterogeneous collection of cell types that are dominated by unilocular adipocytes. WAT depots not only serve as storage sites for triacylglycerol, but also have been established as a major endocrine organ secreting a variety of cytokines, termed adipokines.^{197–199} Adipokines, such as leptin and adiponectin, are known to play significant roles in a variety of human diseases and loss of all WAT, as is observed in patients with lipodystrophy, leads to severe metabolic and endocrine abnormalities.^{200–}

²⁰³ Adiponectin concentrations have, for instance, been shown to affect organs such as liver,²⁰⁴ heart,²⁰⁵ and kidney.²⁰⁶ Furthermore, the potential of adipose tissue as a direct target for pharmacotherapies is becoming recognized,²⁰⁷ especially in the context of rapidly increasing prevalence of adipose-related diseases such as obesity and type 2 diabetes. The Centers for Disease Control and Prevention, for instance, reported in 2012 that more than 35% of U.S. adults suffered from obesity.²⁰⁸ Besides the direct involvement in diseases or as a drug target, the storage character of WAT provides a further key aspect. Plasma concentrations of drug compounds and drug exposure kinetics *in vivo* are strongly affected by the “ADME” processes – absorption, distribution, metabolism, and excretion. As WAT is known to sequester hydrophobic drug compounds,^{209,210} a WAT-on-a-chip is of utmost importance in the endeavor to mimic *in vivo* ADME properties in integrated multi-organ MPS.

In recent years, a variety of engineered adipose tissue constructs have been introduced.¹⁹⁵ The majority incorporated adipocytes into three dimensional scaffolds consisting of various biomaterials,²¹¹ using for instance collagen/alginate,²¹² silk fibroin,²¹³ porous polymers,²¹⁴ decellularized extracellular matrices,²¹⁵ or bioinspired matrices.²¹⁶ While these systems have a potential as implants for regenerative medicine, their use as *in vitro* models is restricted by the limitations mentioned above. One of the limitations, the lack of circulation, was successfully addressed by incorporating the tissue constructs into macroscopic bioreactors,^{217,218} which were successfully downscaled to cm size reactors connected to microfluidic channels.²¹⁹ Initial attempts to create microscale, microfluidic systems for the culture of white adipose tissue have also been reported.^{220–222} These attempts used initially open systems, which were closed subsequent to seeding cells or inserting entire cover slides into them. While this approach elegantly circumvents the challenge of inserting fragile and buoyant adipocytes into microscale chambers, it limits the potential for further downscaling, parallelization for high content screening and integration with other systems. Additionally, although these systems succeeded in establishing a continuous flow environment, the degree of structural mimicry of the *in vivo* physiology is limited and they specifically fail in protecting the tissue from shear stresses, thereby missing a key element of the *in vivo* vasculature.

Here we present a WAT-on-a-chip system that creates a physiologically relevant microfluidic environment enabling the control of nanoliter fluid volumes and flows that are unavailable with other methods. The system consists of separate media channel and WAT chambers, which are connected *via* small micropores. Analogous to the *in vivo* blood circulation, convective transport is thereby confined to the vasculature-like channel. The WAT chamber hence provides a recapitulated native physiological niche protected from shear forces by an endothelial-like barrier in which adipocytes can be injected and supported for long term culture to produce functional adipose tissue.

7.2 Materials and Methods

Fabrication and Characterization of WAT-Chip

The multilayer WAT-chip consists of two patterned polydimethylsiloxane (PDMS, Sylgard 184) slabs sandwiching a polyethylene terephthalate (PET) membrane ($r_P = 3 \mu\text{m}$; $\rho_P = 8 \times 10^5$ pores per cm^2 ; AR Brown-US, Pittsburgh, PA). To generate the PDMS slabs, patterned master-wafers were fabricated *via* a photolithography process. Thereto, a $50 \mu\text{m}$ thick layer of SU-8 3050 photoresist (MicroChem Corp, Newton, MA) was spin coated onto silicon wafers (University Wafer, Boston, MA) and exposed to UV light through patterned transparency masks according to the manufacturer's data sheet. Wafers were developed in SU-8 developer (MicroChem Corp, Newton, MA), rinsed in isopropanol, and blow dried with N_2 . The patterned wafers were baked, and coated with trichloro-1H,1H,2H,2H-perfluorooctylsilane (FOTS, Gelest, PA, USA). The masks for both wafers were designed in AutoCAD LT (Autodesk Inc., San Rafael, CA). PDMS slabs were then replica molded using uncured PDMS in a 10:1 w/w ratio of prepolymer to curing agent. To mold the slab featuring the media channel, a total of 11 g of PDMS was poured onto the wafer and cured overnight at 60°C . Similarly, the slab featuring the cell chamber was molded using 30 g of PDMS. After peeling the molds from the wafers, inlet/outlet holes were punched in the cell chamber PDMS slab using a 0.75 mm biopsy punch (Ted Pella).

To prepare the isoporous PET membranes, they were cut to appropriate dimensions and cleaned through sonication in isopropyl alcohol for 10 min. The membranes were then exposed to oxygen plasma (Plasma Equipment Technical Services, Livermore, CA) at 60 W for 60 s. The activated membranes were incubated in a solution of 97% isopropyl alcohol, 2% bis(3-(trimethoxysilyl)propyl)amine and 1% Milli-Q water at 80°C for 20 min and subsequently rinsed with isopropyl alcohol. After drying at 80°C for 30 min, the membranes were placed in 2 mL of 70% ethanol in Milli-Q water.

To assemble the multi-layer PET/PDMS hybrid device, the unpatterned backside of the PDMS slab featuring media channels was bonded to a microscope glass slide after exposure to oxygen plasma at 60 W for 20 s. The patterned faces of both PDMS slabs were then once more exposed to oxygen plasma at 60 W for 20 s and sandwiched around the previously functionalized PET membrane, which was carefully blow dried with N_2 . To ensure a proper alignment of media channel with cell chambers, the assembly was performed under a stereomicroscope. To stabilize bonding, the devices were subsequently baked overnight at 80°C .

For the assessment of sealing and fluidic connection, both media channel and cell chambers were first prefilled with red food dye (DecACake) colored Milli-Q water followed by pumping blue colored Milli-Q water through the media channels. Color movies were taken using a Leica M80 stereomicroscope (Leica, Wetzlar, Germany) system equipped with a Leica MC170 camera.

Numerical Modeling

COMSOL Multiphysics (COMSOL, Stockholm, Sweden) was used to model fluid flow and transport of a diluted species. Treating the membrane as an array of cylindrical pores could not be achieved due to computational memory limitations. To overcome this barrier, we employed a finite element model treating the membrane as a porous media

as described previously.²²³ Briefly, the flow through the membrane was solved using the time-dependent solver with a finer physics controlled mesh. The iterative solver was employed using multigrid methods to further overcome computational limitations. The “Free and Porous Flow” module engaged the Navier–Stokes equation to solve for the free flow of the media through the cell and media channels and Darcy’s Law to solve for the flow of media through the membrane, modeled as a porous medium. The membranes used have a porosity of $\sim 5.6\%$, pore radius of $1.5 \mu\text{m}$, and a thickness or pore length of $20 \mu\text{m}$. The fluidic resistance of the pores was calculated to $R_p = 1.097 \times 10^{16} \text{Ns m}^{-6}$ by employing Dagan’s equation,²²⁴ which solves for the entrance and exit

$$R_p = \frac{\mu}{r_p^3} \left(3 + \frac{8L}{\pi r_p} \right)$$

effects through a short pore via with fluid viscosity μ , pore radius r_p , and pore length L . The hydraulic permeability K was calculated to $K = 1.45 \times 10^{-14} \text{m}^2$ using

$$K = \frac{\mu L \rho}{\pi r_p^2 R_p}$$

whereby ρ is the porosity of the membrane. Simulations are conducted with a media flow rate of $5.56 \times 10^{-12} \text{m}^3 \text{s}^{-1}$ ($20 \mu\text{L h}^{-1}$).

Additionally, the “Transport of Dilute Species” module was used to assess the ability of the membrane to allow for the diffusion of small molecules solved in the media. Therefore, the media channel is pre-filled at time point zero with “media” containing a species c in a concentration of $1 \mu\text{M}$ and constantly perfused with the same media at $20 \mu\text{L h}^{-1}$. When assuming a typical diffusion coefficient of $1 \times 10^{-9} \text{m}^2 \text{s}^{-1}$ for a biological molecule in water,²²⁵ the concentration of the species in most of the cell chamber reaches the initial concentration of $1 \mu\text{M}$ within 30 seconds.

Analytical Model

The analytical model approximates the membrane as an idealized system with pores in a hexagonally close packed arrangement with rows of pores aligned with the direction of

$$L_p = \sqrt{\frac{\pi \times r_p^2}{\sin 60 p_M}}$$

media flow and a pore-to-pore distance of with the membrane porosity p_M and the pore radius r_p . In this system, the flow in the channels can be solved using an electrical circuit analogy involving the resistance of the pores R_p , the resistances of the media and cell channel R_m and R_c respectively, and the input flow rate Q (**Figure 7-3E**).²²³ Applying this analogy to unit segments of length L_p , a generalized recurrence relation can be obtained whereby the flow rate in the n th segment of the tissue chamber

$$q_c(n) = Q \frac{R'_m}{R'_m + R'_c} (1 - \omega(n))$$

(with a total of N segments) is with

$$\omega(n) = \frac{e^{\beta n}}{e^{\beta} + e^{\beta N}} + \frac{e^{-\beta n}}{e^{-\beta} + e^{-\beta N}} \quad \text{and} \quad \beta = \cosh^{-1} \left(\frac{2R'_p + R'_m + R'_c}{2R'_p} \right).$$

The derivation of these formulas is similar to the one reported by Chung *et al.*²²³ with the difference that due to the circular structure of media and cell chamber, the width of the channel is different for each segment. Hence, all resistances R_p , R_M and R_C in

principle depend on the chamber width w and the segment index n respectively. However, as elucidated in the following these formulas can nevertheless be applied to the system by using a slight modification.

The total pore resistance of a membrane cross-section perpendicular to the media flow

consisting of multiple identical pores is $R_p(w) = \frac{R_{SP}}{N_{PW}(w)}$ with the resistance of a single

pore R_{SP} and the number of pores per cross-section $N_{PW}(w) = \frac{w}{L_p \sin 60}$.

R_{SP} can thereby be calculated using Dagan's equation, which accounts for edge effects

for flow through a short through pore, $R_{SP} = \frac{\mu}{r_p^3} \left[3 + \frac{8 h_M}{\pi r_p} \right]$ with the fluid viscosity μ and the membrane thickness (pore length) h_M . By defining projected resistances R' with

$R_p(w) = \frac{R'_p}{w}$ as well as $R_c(w) = \frac{12\mu L_p}{h_c^3 w} = \frac{R'_c}{w}$ and $R_m(w) = \frac{12\mu L_p}{h_m^3 w} = \frac{R'_m}{w}$ respectively

(Hagen–Poiseuille equation of flow in rectangular channels) and considering the fact that solely ratios of resistances occur in the formulas, we can cancel out the width dependence and replace resistances R in the equations from Chung *et al.*²²³ with

projected resistances R' . By looking at the derivative $\frac{dq_c}{dn}$ it becomes obvious that the maximum flow in the cell chamber occurs at $n = 0.5 \times N$.

Cell Culture and Differentiation

3T3-L1 fibroblasts (ATCC) were differentiated as described previously.²²⁶ Briefly, fibroblasts were cultured in DMEM medium containing 10% fetal bovine serum with 2 mM l-glutamine and 1% penicillin/streptomycin (DMEM/FBS). To induce adipogenesis, the cells were cultured in DMEM/FBS for 2 days after reaching confluence and then for 2 days in DMEM/FBS supplemented with 5 $\mu\text{g mL}^{-1}$ (0.86 μM) insulin, 0.25 μM dexamethasone, and 0.25 mM isobutylmethylxanthine. Subsequently, the medium was changed to DMEM/FBS supplemented solely with 5 $\mu\text{g mL}^{-1}$ insulin and the cells cultured for an additional 2 days. Finally, the cells were maintained in DMEM/FBS alone. Differentiated cells (at least 95% of which showed an adipocyte phenotype by accumulation of lipid droplets) were injected into the MPSs on days 6–10 after initiation of differentiation.

Cell Loading

To ensure a successful loading of the MPSs, differentiated adipocytes were singularized and maintained in suspension by treatment with 0.5% trypsin w/ EDTA for 2 min, detached from the surface, and then suspended in DMEM/FBS media. The suspension was subsequently centrifuged for 5 min at 400g and the diluted trypsin aspirated off.

After that, the cells were resuspended in fresh media such that a solution of 3–5 million cells per mL was obtained and the loading process started immediately.

To prepare the loading process, fully assembled MPSs were exposed to O₂ plasma at 180 W for 1 min thereby sterilizing and creating more hydrophilic channel surfaces. Immediately thereafter, 100–200 mL of cell solution was applied to the cell inlet ports of the MPSs, which were then stored for 15 min in the incubator to allow for sedimentation of cells resulting in a high cell density inside the inlet ports. By applying a negative pressure to the cell media inlet and outlet port using a PhD Ultra syringe pump (Harvard Apparatus) cells were loaded into the cell chamber until a densely packed cell pellet was obtained. Subsequent to the actual loading step, the MPSs were stored for 30 min in the incubator to allow cell attachment before starting the flow of media through the media channels. The media flow was achieved using a PhD Ultra syringe pump at a flow rate of 20 $\mu\text{L h}^{-1}$.

On-Chip Culture and Characterization

To assess viability of the WAT on chip, Live/Dead cytotoxicity assays were performed using a LIVE/DEAD cell imaging kit (Molecular Probes R37601) to stain viable cells with green-fluorescent calcein AM (488 nm) and dead cells with red ethidium homodimer-1 (570 nm). The live/dead imaging kit was used following the manufacturer protocol: 3T3-L1 cells in WAT chips were rinsed with 1× PBS, and 60 μL of dye was added to the devices and then incubated for 20 min. After this incubation time, images were collected using an inverted microscope Nikon TE300 with a Lumencore Spectra X light engine. Images were then processed in FIJI ImageJ. Utilizing segmentation analyses and a constant area exclusion filter counts of live or dead cells were obtained. An index of cell death was constructed from the ratio of the number of dead cell events divided by total number of cells.

For long-term culture, loaded MPSs were stored in the incubator and fed by a PhD Ultra syringe pump with continuous media flow. For visual characterization, cells were imaged daily without detachment from the syringe pump using a Nikon Eclipse TE300 microscope. To better visualize the lipid droplets, cells were stained using a nonpolar fluorophore specific for neutral lipids. Thereto, MPSs were incubated overnight at 4°C in a 4% solution of paraformaldehyde (Santa Cruz Biotechnology). Subsequently, a solution of PBS with 0.1% Tween (PBST) was flushed through the MPSs for 3 hours followed by a 2 hour flush with PBST containing 1 $\mu\text{g mL}^{-1}$ 4,4-difluoro-1,3,5,7,8-pentamethyl-4-bora-3a,4a-diaza-s-indacene (BODIPY D-3922, Molecular Probes, Eugene, OR) and 300 nM 4',6-diamidino-2-phenylindole (DAPI, Molecular Probes). After a final washing step with PBS, the MPSs were imaged with a Zeiss LSM710 laser-scanning microscope (Carl Zeiss, Jena, Germany).

To characterize the uptake functionality of the adipocytes in the MPS after two weeks in-chip culture, the cells were fed with a fluorescently-labeled fatty acid analog. DMEM/FBS media was supplemented with 4 μM 4,4-difluoro-5-methyl-4-bora-3a,4a-diaza-s-indacene-3-dodecanoic acid (BODIPY D-3823, Molecular Probes). After 12 h continuous flow feeding in the incubator, the MPSs were imaged using a Nikon Eclipse

TE300 fluorescence microscope equipped with an ORCA-Flash 4.0 CMOS Camera (Hamamatsu, Hamamatsu-city, Japan).

Confocal immunofluorescence microscopy was conducted on WAT chips that were fixed after 3 days and 9 days respectively of on-chip culture using 4% PFA for 30 min and a subsequent 1× PBS wash. Triton X-100 was used to permeabilize the cells followed by a 3% BSA blocking solution wash. After tissue fixation, 3T3-L1 cells were stained with DAPI (nuclei-blue), Phalloidin (Actin-GFP) and LipidTOX (lipid droplets-red). Confocal images were collected using a Carl Zeiss LSM 710 confocal microscope equipped with a plan-apochromat 10×/0.45 objective imaging DAPI (excitation 405 nm, emission: 410–494 nm), GFP (excitation 488 nm, emission: 493–550 nm), and LipidTOX red (excitation 595 nm, emission: 599–734 nm) channels.

For the visualization of the collagen in the ECM, picrosirius red staining (Polysciences Inc. Warrington, PA) was used following the manufacturer protocol. Briefly, WAT chips were incubated for 1 hour, followed by two washes with an acetic acid solution. Bright field images were then collected using a Zeiss Axio Imager microscope (Carl Zeiss, Jena, Germany) equipped with a QImaging MicroPublisher 5.0 color camera (Q Imaging, Surrey, BC, Canada). On the images, collagen appears red with a pale yellow background.

7.3 Results and Discussion

Concept of the Microphysiological WAT-on-a-Chip

To mimic the physiological environment of adipose tissue inside a microfluidic environment we have developed a microphysiological system that has three main elements: a media channel, circular cell chambers, and a microporous membrane in between. Analogous to the *in vivo* blood circulation, media travels through the media channel as a vasculature-like microcirculation between multiple WAT chambers and constantly transports fresh nutrients and other soluble factors (e.g. drug compounds, cytokines) to and metabolic waste and secreted factors away from the tissue (**Figure 7-1A**). The media channel and WAT chambers are connected via small micropores (diameter 3 μm) that act as a perfusion barrier (**Figure 7-1B and C**). The perfusion barrier mimics the *in vivo* endothelial barrier by allowing nutrients, drugs, and other media compounds to diffuse to the tissue while protecting the cells from shear stresses. The diffusion properties are regulated by the pore size and pore density. The circular geometry of the WAT chambers (diameter 600 μm, height 50 μm) creates a homogeneous supply with nutrients for the entire WAT tissue and enables the direct exchange of soluble factors with the media for each individual cell, which is important as *in vivo* each adipocyte is attached to at least one capillary.²²⁷ Additionally, the microfluidic concept enables the temporal and lateral control of nanoliter fluid volumes and flows. The much smaller liquid volumes compared to standard cell culture further prevents non-physiological dilution of autocrine and paracrine factors. The basic principle of a vertically adjacent configuration of separate media and tissue compartments enables a large degree of flexibility in terms of circulation architecture including in series- or in parallel-connections of multiple tissue chambers (**Figure 7-1D**)

interconnected by low dead-volume microchannels (width 40 μm , height 50 μm). Since the footprint of one tissue chamber is below 1 mm^2 , it is possible to fabricate hundreds of cell chambers on a plate with standard multi-well plate dimension and thus enable high throughput screening. Another advantage of the microfluidics-based design is that the WAT-on-a-chip is amenable for characterization of a variety of structural and functional endpoints. For example, the optical accessibility of the tissue chamber enables the flexible use of high-resolution microscopy techniques for live cell imaging and the continuous media flow allows for temporal collection of the supernatant and subsequent analysis using for instance mass spectrometry or colorimetric assays. Additionally, the underlying concept permits the integration of the system in multi-organ circulations.²²⁸

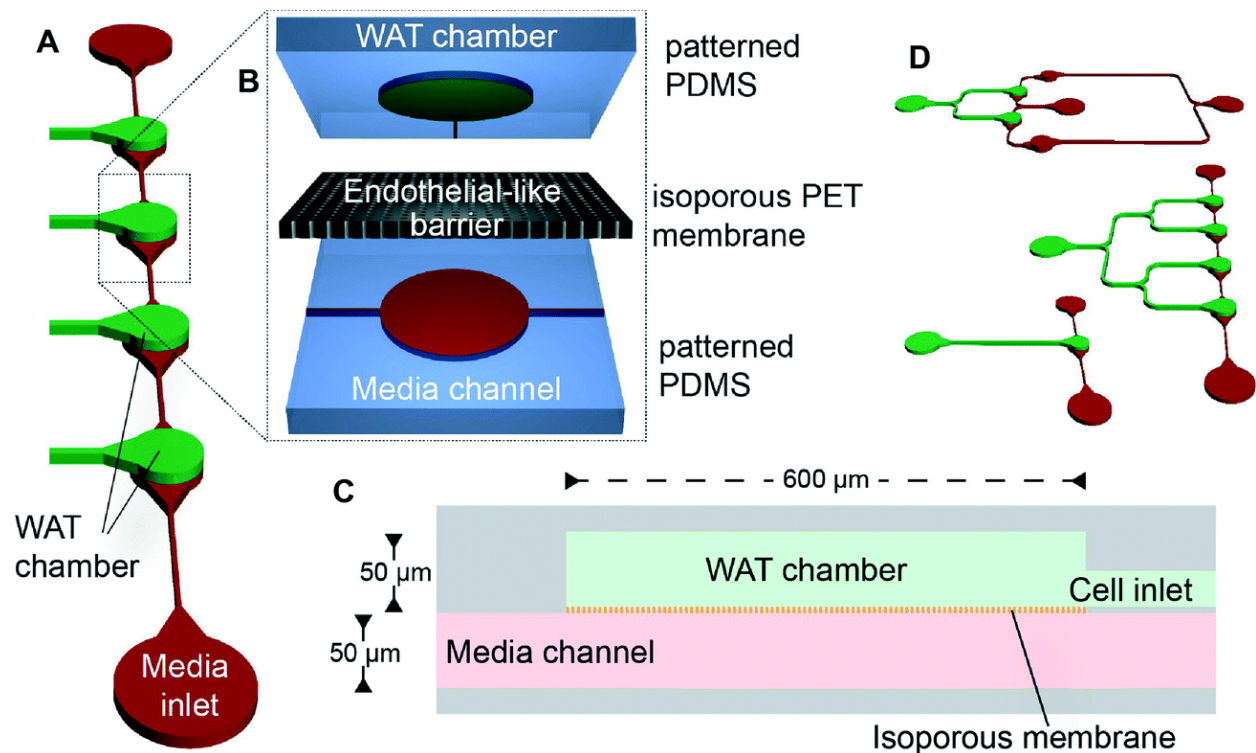


Figure 7-1. Schematic concept of the WAT-on-a-chip.

(A) Scheme demonstrating the underlying idea of separated media channel and multiple individual WAT chambers. (B) Schematic design and (C) cross section of the multilayer PDMS–PET hybrid system. The MPS is based on a sandwich structure consisting of an isoporous PET membrane in between two PDMS layers, whereby the upper one features the WAT chamber (green) and the lower one the media channel (red). (D) Examples of different circulation architecture versions connecting multiple cell chambers in series or in parallel.

Fabrication of the Multilayer Hybrid System

The media channel and the WAT chambers are patterned via UV-lithography and replica molded in two polydimethylsiloxane (PDMS) slabs, which constitute the lower and upper layers respectively of the three-layer hybrid MPS. The middle layer consists of an isoporous polyethylene terephthalate (PET) membrane. By choosing commercially available track-etched PET membranes, a variety of pore sizes and pore densities, *viz.*

diffusion properties, can be employed without restriction by aspect-ratio limitations of UV-lithography and without changes in the actual fabrication process. Important for analysis methods requiring optical transparency, the choice of membranes with controlled angles of the pores is critical. To enable long-term tissue culture and the choice of a wide variety of fluidic parameters, a strong bonding of the three components is required. To achieve a coupling between the PET membrane and the PDMS devices, we employed a bis-amino-silane modification of the membrane recently introduced by Sip and Folch²²⁹ (**Figure 7-2A-C**). Note that many commercially available PET membranes are surface treated with PVP or other hydrophilic coatings, which will interfere with the coupling process. The advantage of this silane coupling approach is that the process solely requires commercially available reagents, is uniformly applied to surfaces and thus mostly feature-independent, and is compatible with PDMS oxygen plasma bonding. The silane treated membrane is sandwiched between two PDMS slabs, which have been activated via oxygen plasma (**Figure 7-2D**). The components are then carefully aligned, brought into contact, and cured resulting in a bonded and sealed PDMS/PET hybrid system (**Figure 7-2E**).

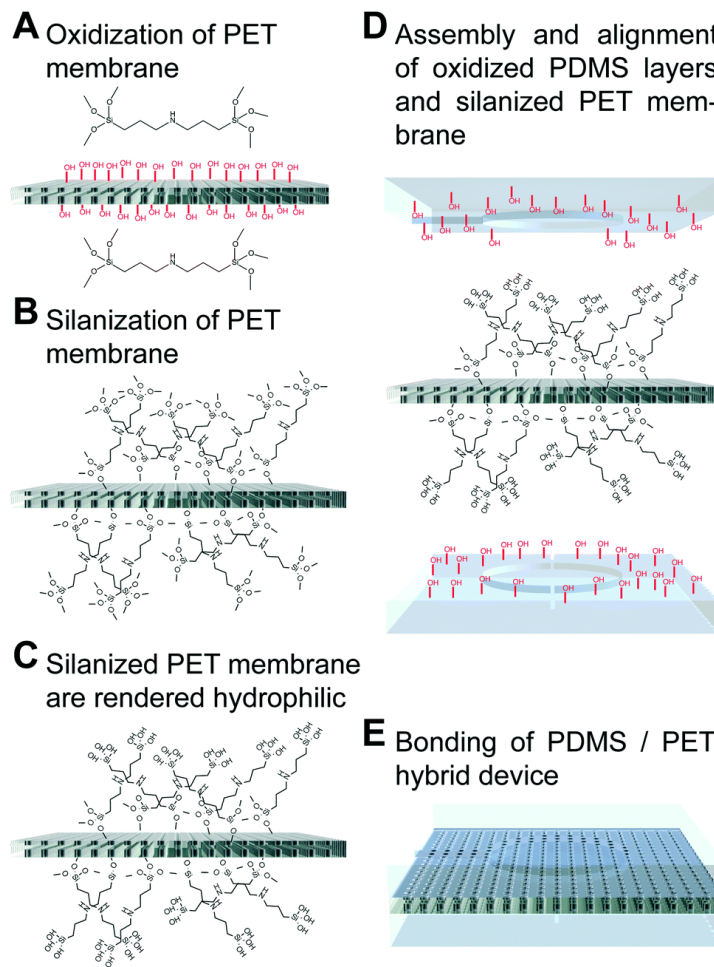


Figure 7-2. Fabrication of the multilayer PDMS–PET hybrid MPS.

(A) an isoporous PET membrane is activated using O₂ plasma and treated with a bis-amino silane solution at elevated temperature. The functionalized membrane is subsequently (B) cured to further

cross-link the silane layer and (C) hydrophilic coating *via* immersion in a 70% ethanol/water mixture. (D) The silanized membrane is sandwiched between two activated PDMS layers, which are aligned under a stereoscope (E) the PDMS/PET hybrid device is bonded, dried and baked.

Characterization of Transport Processes

One of the major elements of the MPS is the separation of transport processes. In the human body, most tissues do not experience shear forces due to convective blood flow since they are protected by the endothelial barrier. Similarly, inside the MPS, the tissue is not subject to convective flow but is supplied by diffusive transport while the transport within the media channels is predominately convective (**Figure 7-3A**). This is ensured by a narrow cross-section of the isoporous membranes with 3 μm diameter pores creating a fluidic resistance into the cell chamber significantly higher than through the media channel. The fluidic connection of cell and media channel as well as the different timescales of transport processes was shown using DI water colored with food dyes (**Figure 7-3B**). This qualitative characterization demonstrated that pumping a blue liquid into the media channels of a system entirely filled with red liquid leads to an immediate replacement of the liquid in the media channel and a subsequent color change in the cell chambers due to dye diffusion through the membrane.

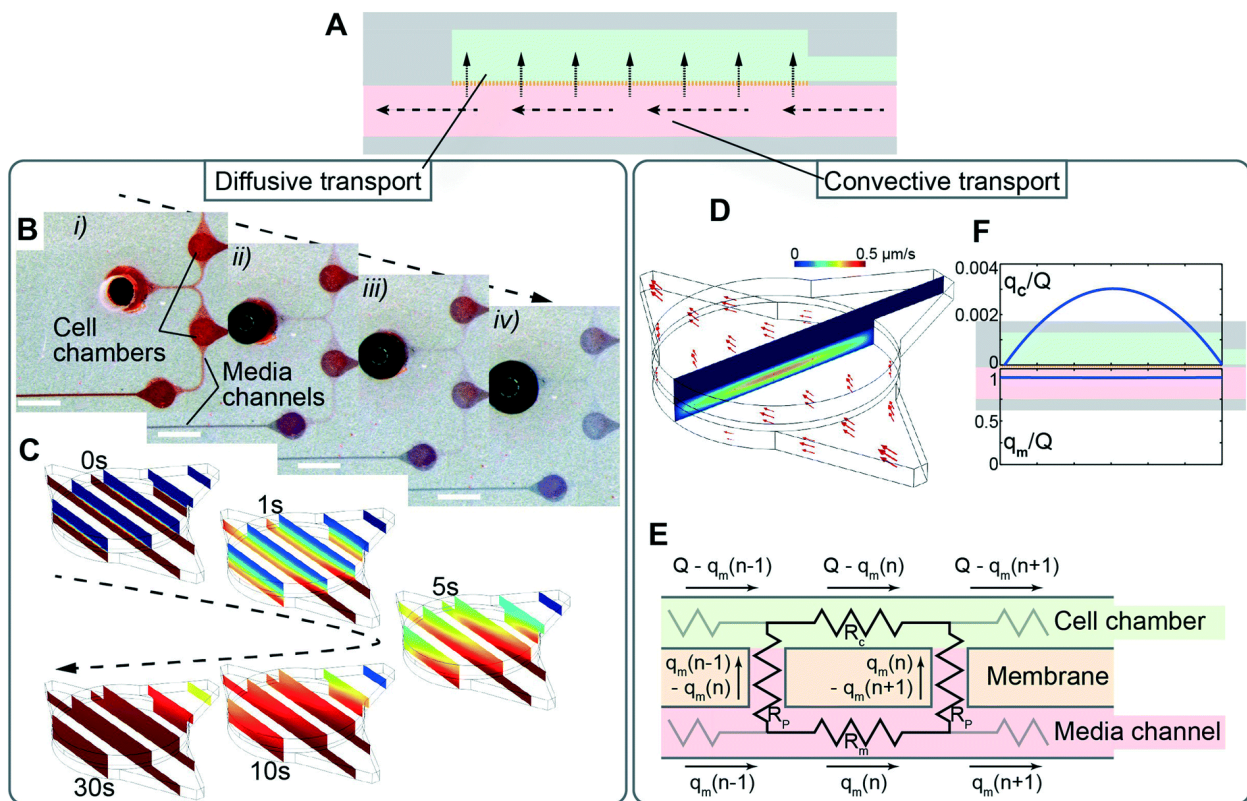


Figure 7-3. Characterization of transport processes inside the MPS.

(A) Schematic view of the MPS highlighting the two different transport processes: convective flow within the media channel and purely diffusive transport to the tissue chamber. (B) Time series of pictures at subsequent timepoints (i)–(iv) showing the replacement of red dyed water by injection of blue dyed water into the media channels. Note the subsequent change of color in the cell chambers due to diffusion through the membrane. (C) COMSOL simulation of the diffusion of small molecules from the media

channel in the z-axis to the tissue chamber on physiological timescales. Orthogonal view of flow profile across several points in the MPS. (D) Schematic representation of the electrical circuit analogy using an idealized membrane on which the analytical model is based on. Adapted from ²²³. Color bar applies for both (C) and (D). (E) Input flow rate fraction in the tissue chamber along the flow axis calculated by the analytical model. (F) Simulated velocity profile of flow in the MPS, inset shows the magnified view. Note the lack of convection within the diffusive barriers and predominant convective flow through the nutrient channels. Thus, mass transport to the tissue is exclusively diffusive.

Additionally, we employed quantitative theoretical models to demonstrate the desired transport separation effect. Using numerical analysis employing a “Transport of Diluted Species” model we assessed the concentration change in the cell chamber when pumping a liquid with a diffusive solute through the media channel. Due to the high computational costs of modeling the “small scale” membrane pores individually as well as the “large scale” channel structures, we employed a finite element model treating the membrane as a porous media. A time series of snapshots of the concentration distribution reveals a diffusive supply of media to the tissue on physiological timescales (**Figure 7-3C**). Similarly, we simulated the flow fields in both the media channel and the cell chamber revealing the successful confinement of the convective flow as target and thereby confirming that the membrane effectively shields cells from the convective flow in the media channel and the resulting shear stress (**Figure 7-3D**).

Independent of the numerical finite element model, we employed an analytical model which we developed based on a concept recently introduced by Chung *et al.*:²²³ application of the theoretical equations for our system results in a distribution of the flow rate in the cell chamber as shown in **Figure 7-3F** and a maximum flow rate of less than 1/100 of the input flow rate in the media channel. Note that this value is independent of the width of the chamber and the fluidic viscosity of the media. Furthermore, considering that the tissue in the cell chamber will significantly increase the fluidic resistance, the actual flow rate in the tissue chamber will be even lower.

Taken together, both models provide qualitatively the same results although different approximations for the character of the membrane were used. Each model verified the separation of transport processes and thereby the shear stress protective effect of the membrane. The separation of transport processes providing a shear-force protection of the tissue is a key aspect of our system and serves as a recapitulation of the *in vivo* endothelial barrier. However, while providing mechanical support and controlled passive diffusion, the system does not fully mimic active transportation processes displayed by endothelial cells. Future systems with endothelial cells on the media-channel-side of the membrane can be envisioned to incorporate those processes as well. The choice of commercially available membranes, moreover, allows for the change of pore sizes, *viz.* diffusion properties, without changes in the actual fabrication process.

Injection and Culture of Functional Adipose Tissue

To create adipose tissue in the MPS, we obtained adipocytes by differentiating murine 3T3-L1 preadipocytes. Between 6–8 days after induction of adipogenesis, cells were harvested and loaded into the cell chambers of the MPS through small tree-like loading channels (width 80 μm , height 50 μm). Due to their fragility and buoyancy, adipocytes

were more problematic than other cell types in terms of handling and compatibility with small-scale dimensions and shear stresses. Hence, an early injection time point was chosen, at which lipid droplets were clearly visible, but still small and sparsely distributed. Loaded chambers were subsequently fed using a syringe pump induced continuous flow through the media channels. Within 24 h of loading, the cells reattached and initiated the formation of a tissue.

An important prerequisite for the applicability of a WAT-on-a-chip MPS for drug screening applications is the capability to keep the tissue viable and functional over longer time periods, which we studied using a variety of approaches: as shown by Live/Dead cytotoxicity assays, (**Figure 7-4A and B**) the MPS was able to keep the injected cells viable. Confocal immunofluorescence imaging further confirmed the 3D character of the adipose tissue in the MPS (**Figure 7-4C**). To investigate the functionality of cells and the presence of cell-secreted ECM, an essential constituent of the 3D tissue, we performed picosirius red staining visualizing collagen I and III at two different time points after cell loading (**Figure 7-4D**).

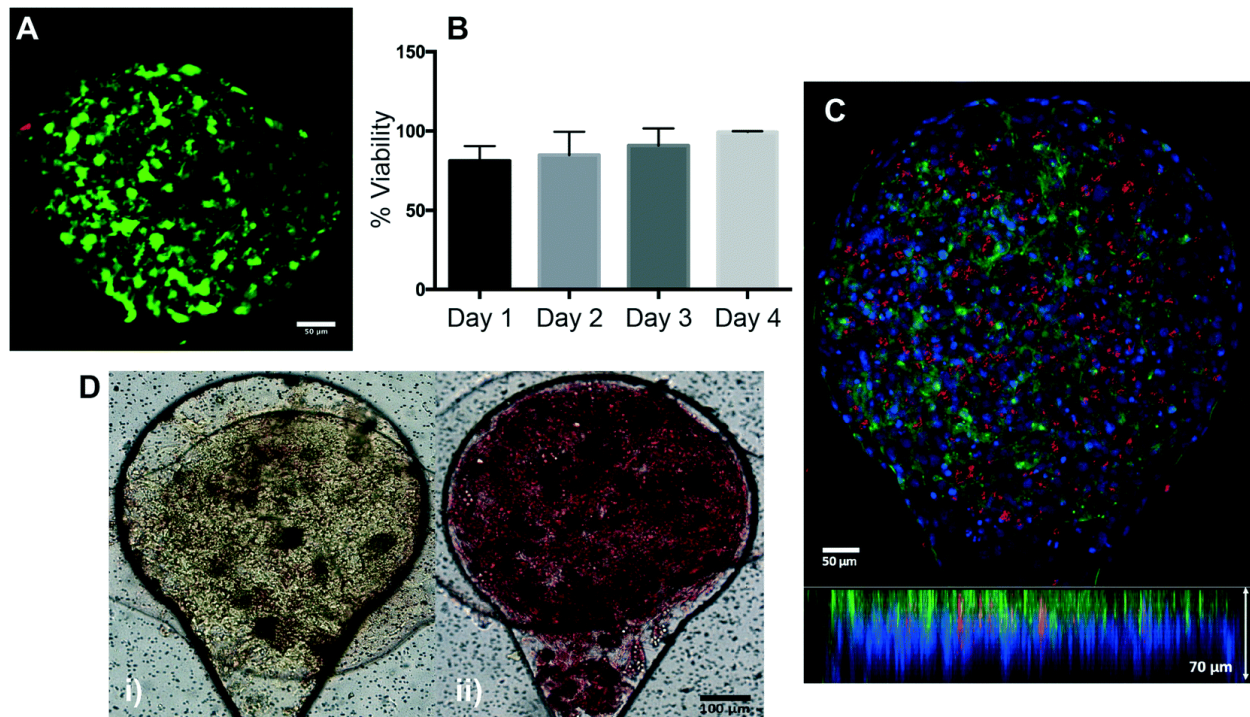


Figure 7-4. Physiologically relevant adipose tissue in the MPS.

(A) Fluorescence microscopy image of a Live/Dead cytotoxicity assay after four days of on-chip culture. (B) Quantification of the percentage of viable cells in the MPS at different time points of on-chip culture. (C) Confocal image of 3T3-L1 adipocytes after 9 days in culture in the WAT MPS revealing a 3D tissue like structure. Cells were stained with phalloidin to show part of the cytoskeleton, DAPI to visualize the nuclei and LipidTOX red for the neutral lipid droplets. (D) Bright field images of MPS's stained with picosirius red after (i) 3 days and (ii) 9 days of on-chip culture showing a functional secretion of ECM (collagen), essential for a physiological tissue structure.

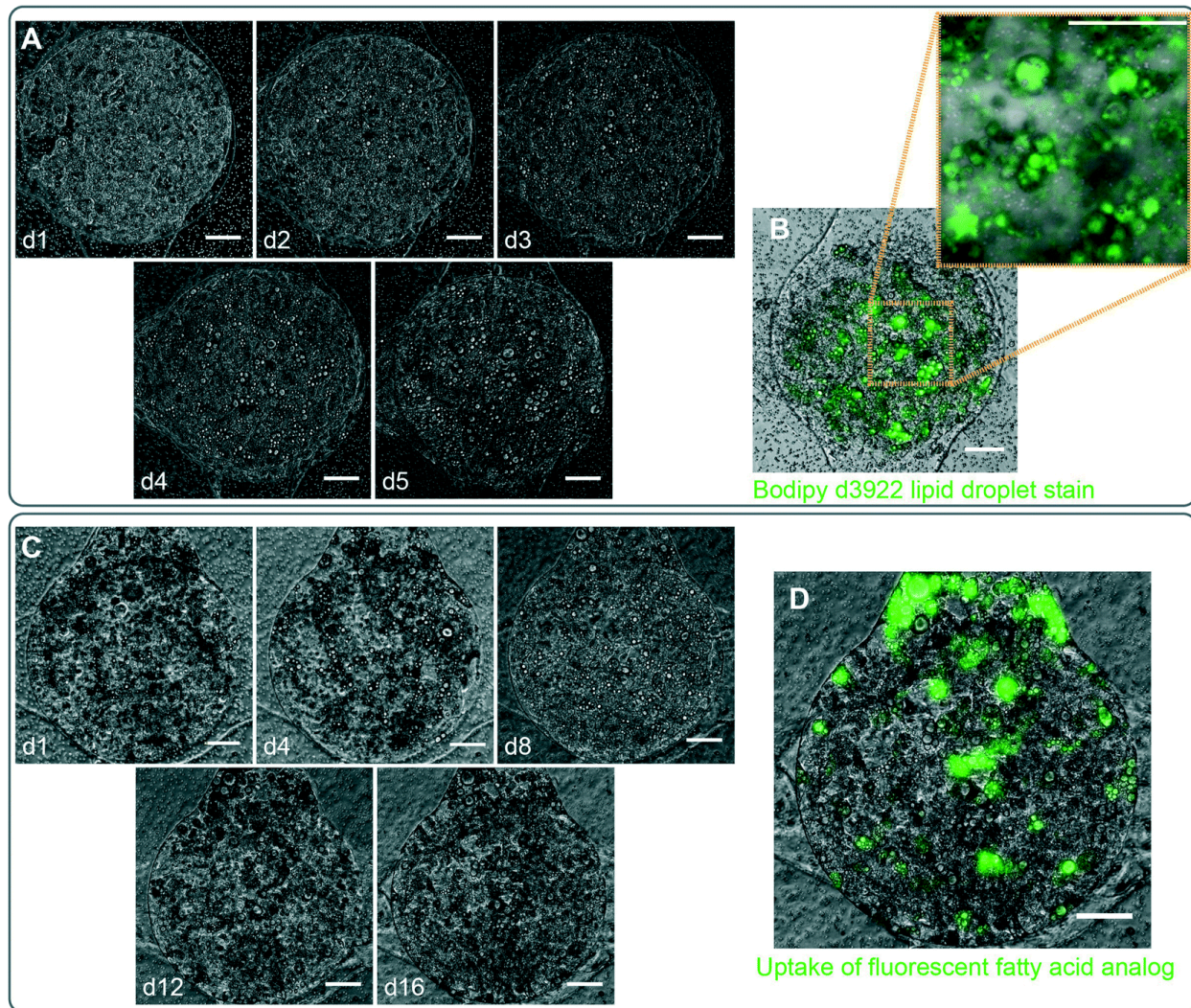


Figure 7-5. The MPS enables maintenance of viability and functionality of adipose tissue.

(A) Series of optical microscopy images of a typical WAT chamber inside the MPS taken at subsequent days reveals the formation and growth of lipid droplets indicating functional fatty acid uptake. (B) Fluorescent microscopy images inside an MPS stained six days after loading using a Bodipy D3922 dye highlights the abundance of lipid droplet. (C) Series of optical microscopy images shows formation and growth of lipid droplets for more than two weeks demonstrating the long-term culture capability of the MPS. (D) Fluorescence microscopy image subsequent to exposure to the fluorescently labeled fatty acids analog C1-Bodipy-C12 confirming the fatty acid uptake ability and functionality of the tissue after two weeks on chip culture (scalebars 100 μm).

In situ bright field microscopy characterization in 24 h intervals clearly showed the expansion of cells and growth of lipid droplets indicating fully functional lipid metabolism by the adipose tissue (**Figure 7-5A**). To visualize and confirm the lipid droplets, we employed a Bodipy 493/503 (D-3922, Molecular Probes) stain allowing us to detect the lipid droplets through standard epifluorescence and confocal microscopy (**Figure 7-5B**). Our MPS, moreover, enabled the culture of adipose tissue for more than two weeks as demonstrated by the continuous growth of lipid droplets, indicating no loss of fatty acid uptake and triacylglycerol synthesis capabilities (**Figure 7-5C**).

To directly assess relevant metabolic function, we visualized fatty acid uptake, a transporter mediated process²³⁰ by incubating the MPS with medium containing a BSA-bound fluorescently-labeled long-chain fatty acid analog, *i.e.* C1-Bodipy-C12 500/510 (D-3823, Molecular Probes). Standard epifluorescence microscopy revealed that, two weeks after loading, large numbers of cells within the MPS showed significant uptake functionality (**Figure 7-5D**). Thus, the MPS was capable of keeping adipose tissue viable and functional over longer time periods. Ultimately, our WAT MPS will enable additional physiological assays for lipids and glucose metabolism as well as insulin sensitivity and, given the small dimensions and potential for massive parallelization, our WAT MPS will allow for the rapid screening of adverse drug effects in complex metabolic systems. Down the road, the exploitation of microfabrication and microfluidic approaches provides the system with the potential for the integration with other microfluidic based organ systems. This will make the WAT MPS a powerful testbed opening a wide range of opportunities for fundamental biomedical studies as well as for translational applications in pharmaceutical industry.

7.4 Conclusions

We have developed a WAT-on-a-chip MPS that integrates adipose tissue in an environment which features crucial parts of the *in vivo* physiology such as continuous nutrient delivery and media exchange, spatially homogeneous nutrient supply, close proximity to the vasculature of each individual cell, separation of transport processes, as well as shear force protection for the tissue. Additionally, it has a low-cost character and is highly accessible for a variety of endpoint characterizations. The WAT MPS is capable of maintaining the viability and function of the tissue over multiple weeks. The highly controlled and computationally predictable character of the MPS make it a versatile tool for the study of adipose tissue properties and responses to external stimulations, as well as adipose tissue associated diseases such as obesity and type 2 diabetes.

Chapter 8: *In Vitro* Cardiac Tissue Models: Current Status and Future Prospects

This article was written in collaboration with Dr. Anurag Mathur, Dr. Zhen Ma, Dr. Peter Loskill, and Dr. Kevin E. Healy. This article was published in *Advanced Drug Delivery Reviews*, 96, A Mathur, Z Ma, P Loskill, S Jeeawoody, KE Healy, “*In vitro* cardiac tissue models: Current status and future prospects,” 203-13, Copyright Elsevier B.V., 2016, e-publication 2015.

8.1 Introduction

Drug discovery and development is a challenging road, and current methods to evaluate drug safety and efficacy are costly and inefficient. The average time between drug discovery and commercialization is 10-15 years, with median costs over \$5 billion.²³¹ During preclinical and clinical development, cardiotoxicity remains a major cause of failure, with high rates of post-approval withdrawal of medicines.²³² Furthermore, effective pre-clinical evaluation of drugs is essential for treating cardiovascular diseases affecting 17.5 million people worldwide and accounting for 31% of all global deaths in 2012.²³³ However, major barriers inhibit current research in human drug screening: experimental *in vivo* interventions have unacceptably high risks for humans enrolled in clinical trials, and non-human animal models fail to fully recapitulate human physiology. For example, the resting heart rate in mice is tenfold higher than in humans, while the mouse QT interval is one-fourth of a typical human.²³⁴ Due to inter-species differences in ion channels, biological pathways, and pharmacokinetic properties, animal models do not faithfully predict human cardiotoxicity. Thus, human *in vitro* models of cardiac tissue that are predictive of human drug response would be a significant advancement for understanding, studying, and developing new drugs and strategies for treating cardiac diseases.

An ideal *in vitro* cardiac model should accurately recapitulate the physiological or pathological conditions of the human heart, including three-dimensional (3D) anisotropic tissue structure, orientation of the extracellular matrix (ECM) network, vascularization, and circulation (**Figure 8-1**). Traditional 2D *in vitro* systems, although informative,^{24,25} cannot accurately mimic the complex 3D conditions due to their inability to recapitulate the dynamics of the biological and mechanical properties of the *in vivo* microenvironment.²⁶ The 3D models are characterized by establishment of adhesion complexes and tissue polarity, and by changes in cytoskeletal structure and cell volume that are significantly different from those found in cells cultured as monolayers. As a result, the translational results in 2D conditions are fundamentally different from those in 3D.²⁷

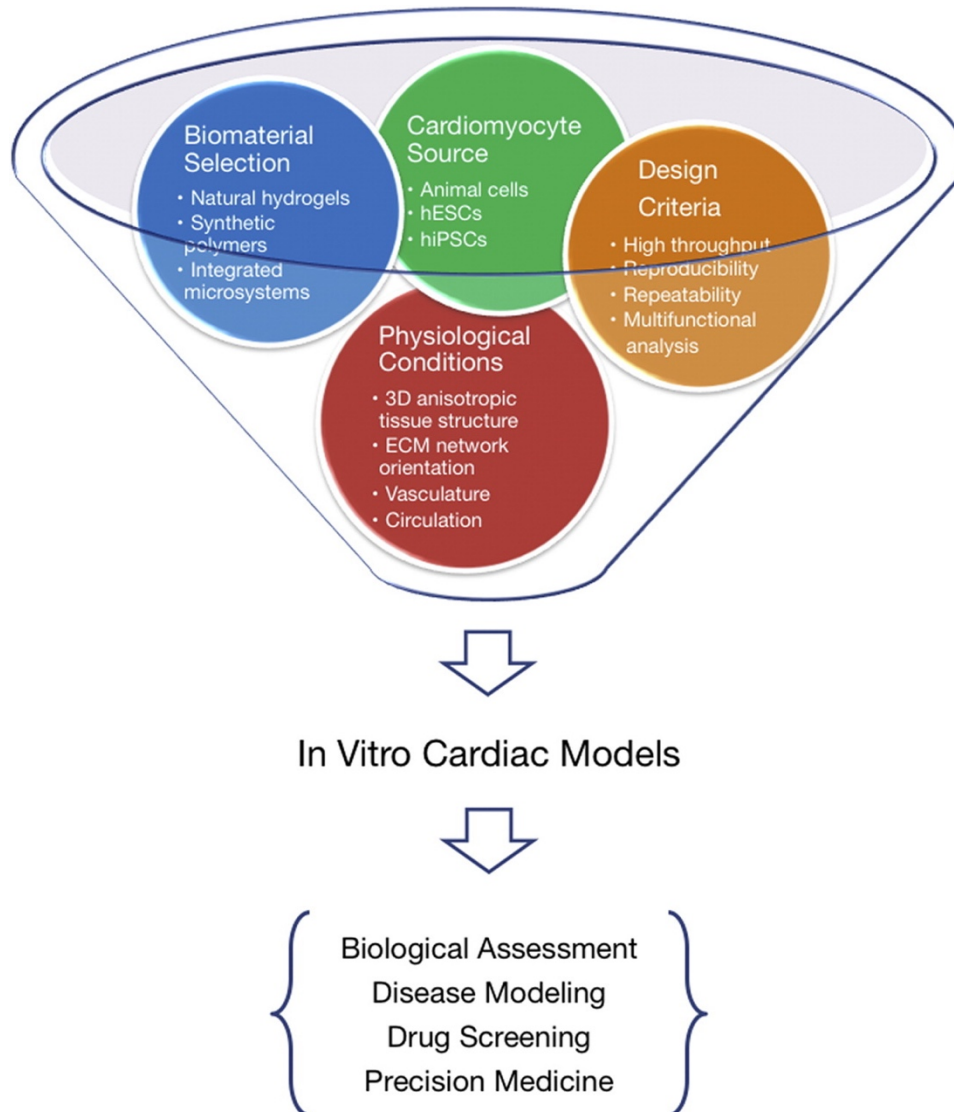


Figure 8-1. Overview of *in vitro* cardiac tissue model.

New *in vitro* biomaterial-based cardiac tissue models have the potential to be used for fundamental research and translational applications. In particular, the areas of drug discovery, disease modeling, and precision medicine could benefit immensely from these emerging technologies.

Human cardiovascular conditions *in vitro* can be achieved by developing engineered physiologically relevant 3D models, for instance by embedding cells in biomaterial matrices or microfabricated devices. For the purpose of *in vitro* modeling, biomaterials and microsystems not only serve as scaffolds for tissue formation, but also provide a highly-controllable microenvironment that incorporates key niche elements to enable precise regulation of cell fate and function.^{235–237} Specifically, the complex tissue and organ architecture of the heart is maintained by extensive 3D ECM networks, including fibrous proteins (e.g. collagen, elastin), adhesive glycoproteins (e.g. laminin, fibronectin) and proteoglycans.²³⁸ This ECM network, primarily in the form of perimysial collagen fibers, guides the anisotropic alignment of cardiomyocytes (CMs), mechanically confines the cells to connect each other, and contributes to stress-strain relationships

for the heart.²³⁹ Perimysial collagen fibers are comprised of bundles of twisted constituent fibrils (~40-50 nm in diameter), forming fibers that range from ~0.5-10 µm in diameter and ~100-200 µm in spacing, allowing several CMs to fit in-between.²⁴⁰ Furthermore, the perimysial collagen fibers are arranged parallel with the long axis of cardiac muscle and therefore are one of the most significant components of the myocardium that contributes to its non-linear passive stiffness in the direction of the cardiac muscle fibers.²⁴¹ The perimysial fibers interact with the CMs via various mechanotransduction pathways, and ultimately affect normal cardiac function. For example, the fibrillar collagen networks register sarcomere Z-line across the CM membrane, and thereby ensure equal stretching of contiguous cells and maintenance of the mechanical continuity between CMs.²⁴² Given the key role of ECM in heart development and mechanical functions, development of an *in vitro* cardiac model requires biomaterials, methods, and systems to host the cells, control the cell-cell and cell-ECM interactions, and regulate the cell fate and functions.

In this review, we focus on the important role of biomaterials and microsystems used for *in vitro* cardiac models. First, we briefly discuss the cell source used for cardiac tissue models, and emphasize human induced pluripotent stem cells (hiPSCs) as the most promising cell type for generation of human CMs. Then, we highlight key properties of different *in vitro* models, along with their advantages and limitations for applications, such as drug cardiotoxicity screening and human heart disease modeling.

8.2 Cell Sources for Cardiac Tissue Models

In the adult human heart, CMs account for roughly 75% of the heart volume, although they represent only about 33% of the total cell number.^{243,244} Therefore, identifying the optimal source of beating CMs is the first step in the development of a functioning *in vitro* cardiac model. Early cardiac tissue models depended on either immortalized human cell lines or primary cells isolated from multiple species. The immortalized human ventricular AC cell line was developed using fusion of primary ventricular CMs with a SC-40 transformed fibroblast cell line.²⁴⁵ Primary CMs isolated from embryonic chicken and neonatal mice and rats were the next most common cell sources for cardiac models,²⁴⁶⁻²⁴⁸ but increased awareness that animal cell-based models cannot truly recapitulate human physiology has led to the development of more sophisticated cells to build human-like tissue models.

The advancement of stem cell biology has spearheaded the development of *in vitro* cardiac models that employ differentiated pluripotent stem and progenitor cells.²⁴⁹ Originally, mesenchymal stem cells (MSCs) were widely used for cardiac tissue models to investigate their beneficial effects on damaged cardiac tissues, either through transdifferentiation or paracrine signaling.²⁵⁰⁻²⁵² However, MSC's suboptimal capability for cardiac differentiation has limited the use of these cells in cardiac tissue models.

For better recapitulation of human physiology and pathology, *in vitro* cardiac models now focus on human pluripotent stem cells, including human embryonic stem cells (hESCs) and hiPSCs^{253,254} (**Table 8-1**). Contracting CMs were first generated from hiPSCs through co-culture with END2 mouse endoderm-like cells, a methodology

restricted by its reliance on animal cells.²⁵⁵ hiPSCs suspended in fetal bovine serum to make 3D aggregates of embryoid bodies was later used to generate CMs. Initial protocols produced contracting embryoid bodies with only 5-15% efficiency,²⁵⁶ and subsequent optimization with timely addition of growth factors (such as Activin A, BMP4 and FGF) improved this efficiency to over 70%.²⁵⁷ Nowadays, monolayer differentiation, which involves simple, serum-free, and scalable protocols, has largely replaced embryoid body formation.^{258,259} Meanwhile, Activin A and BMP4 have been replaced by small molecules CHIR99021 and IWP4, which leads to greater reliability and higher efficiency.²⁶⁰ Recently, chemically defined method to replace Matrigel-coating with synthesized vitronectin peptide, and “B27” with l-ascorbic acid 2-phosphate and recombinant human albumin has been used to generate CMs at 85% purity, that can be enriched to 95% with sodium lactate.²⁶¹ Based on these advances, City of Hope scientists funded by California Institute of Regenerative Medicine (CIRM) are currently developing a bag-based bioreactor system for scalable and controllable production of Good Manufacturing Practices (GMP)-level hESC-CMs, which will remove a key barrier to developing regenerative medicine products, especially for cardiac repair requiring for high doses of human CMs.²⁶²

Table 8-1. Generation of cardiomyocytes from human pluripotent stem cells.

Methods	Media	Yield	Disadvantage
Feeder layer	Serum-based media Mouse END-2 cells ²⁵⁵	35%	Low yield Serum media Requirement of mouse feeder cells
Embryoid Bodies	Serum-based media ²⁵⁶	5-15%	Low yield Serum media
	RPMI + B27 supplement ActivinA + BMP4 ²⁵⁷	60%	Medium yield Requirement of EB formation Batch variability of growth factors Chemical undefined “B27”
	Bioreactor suspension culture ²⁶² RPMI + B27 supplement Small molecules	90%	Chemical undefined “B27”
Monolayer	RPMI + B27 supplement ActivinA + BMP4 ²⁵⁹	35%	Low yield Batch variability of growth factors Chemical undefined “B27”
	RPMI + B27 supplement Matrigel Sandwich ActivinA + BMP4 ²⁵⁸	90%	Batch variability of Matrigel and growth factors Chemical undefined “B27”
	RPMI + B27 supplement Small molecules ²⁶⁰	90%	Chemical undefined “B27”
	RPMI + human albumin l-ascorbic acid 2-phosphate (AA 2-P) Small molecules ²⁶¹	85%	

Exciting advances in genome-editing methods by endonuclease (ZFN or TALEN) or palindromic repeat (CRISPR) are being introduced to engineer cardiac disease-associated gene mutations into hiPSC lines with the same genetic background, which will be instrumental for generating libraries of disease-specific CMs for drug testing and disease modeling.^{263,264} To work effectively in the area of patient-specific cells and disease models, a high degree of collaboration and coordination amongst academic laboratories and industry is required. To this end, various institutions, like CIRM, Cellular Dynamics International (CDI), Coriell Institute for Medical Research, Axiogenesis, and Stanford University, are working cohesively to establish a bank of hiPSCs, which will ensure the development of standard operating procedures and practices in order to achieve efficiency, consistency, and high throughput.^{265,266} Making this hiPSC bank available to a broader base of researchers would strongly support a more thorough understanding of the nature of cardiovascular diseases, and the development of cures and stem cell therapies for said diseases.

One key area of research that needs to be addressed prior to full-scale use of iPSCs for cardiac drug screening and development is the maturity of the CMs. During heart development, cardiac muscle cells undergo a complex series of structural changes that ultimately result in their adult phenotype.²⁶⁷ CM maturation *in vivo* is also regulated by diverse factors, including topographical, electrical, mechanical, biochemical, and cellular interaction cues. However, hiPSC-CMs *in vitro* retain a relatively immature phenotype and exhibit relatively small size, reduced electrical excitability, impaired excitation-contraction coupling, and incomplete adrenergic sensitivity.²⁶⁸ This is one of the critical obstacles to the successful development of predictive drug and toxicology screens, as well as safe and efficient cardiac therapies. Currently, efforts focus on dissecting the external cues (e.g., chemical, physical, electrical), deciphering signaling pathways, and harnessing this information to accelerate the maturation process.²⁶⁹ Hereby, engineering methods will play a crucial role to stimulate the *in vitro* processing of hiPSC-CMs maturation by providing relevant environmental motifs, such as anisotropic morphology, external electrical stimulation, mechanical loading, and extracellular matrices.

8.3 Cell Micropatterning for 2D Cardiomyocyte Alignment

An optimal *in vitro* model would incorporate the aforementioned hiPSCs into an *in vivo*-like tissue structure while providing researchers with precise control over cell types, ECM composition, cell-cell interactions, and microenvironment geometry. In early studies on the effect of CM anisotropic morphology, cardiac cells were aligned on a thin collagen surface coating that was spread using a cell scraper and polymerized while slowly being poured within a slightly tilted dish.²⁷⁰ Later, microabrasion was employed to create aligned CMs with anisotropic sarcomeric structure, by unidirectional abrading polyvinyl chloride (PVC) coverslips using lapping papers with different grit sizes.²⁷¹

More recently, microfabrication-based patterning techniques (**Figure 8-2**) have been used to establish *in vitro* culture models and investigate the fundamental physiological and pathological characteristics of CMs. Cell alignment can be controlled by surface topography²⁷²⁻²⁷⁶ by micromolding with microchannels fabricated from PDMS.²⁷⁷⁻²⁷⁹

Microcontact printing ECM proteins created cell-adhesive areas of various shapes on cell-repelling surfaces, using, for instance, laminin onto polyacrylamide thin films,^{280,281} fibronectin onto alginate,²⁸² laminin onto PDMS,²⁸³ or repelling areas on adhesive surfaces using chitosan and hyaluronic acid onto PDMS and glass.^{284,285} Significant observations in calcium handling, action potentials, and conduction velocities were more similar to adult mouse myocardium in aligned CMs as compared to those grown in randomly oriented cultures.^{286,287} Monolayer of aligned neonatal rat CMs created by microcontact-printing method was found to undergo fibrosis after activation of TGF- β signaling pathway and reduce electrical conduction due to the mechanical interactions between myofibroblasts and CMs.²⁸⁸

Micropatterning hiPSC-derived CMs (hiPSC-CMs) by microcontact printing collagen onto polyacrylamide has been used to increase the maturity level of hiPSC-CMs with optimized culture media.²⁸⁹ A similar microcontact printing approach with laminin was used to generate hESC-CM microarrays for functional analysis and drug screening, assessing the effects of treatment with H₂O₂ on CM viability and contractility.²⁹⁰

Micropatterning techniques also enable precise control over the shape and size of cell colonies and are regularly used to generate uniform embryoid bodies (EBs) for studies of embryogenesis and cardiomyogenesis. Contained in poly(ethylene glycol) (PEG) hydrogel microwells, mouse ESCs formed homogeneous EBs of different sizes. The size of the EBs modulated differential expression of WNT5a and WNT11, leading to higher CM differentiation in large EBs, compared to higher endothelial differentiation in small EBs.²⁹¹ The size of 3D polyurethane microwells was also found to modulate cell-cell contact and canonical Wnt/ β -catenin signaling in human ESCs, resulting in higher CM differentiation in larger wells.^{292,293} A more extensive study of microwells in silicone rubber sheets fabricated via laser cutting revealed that cell patterning resulted in homogeneous expression of pluripotent markers in hiPSCs and improved yield and reproducibility of cardiac differentiation.²⁹⁴ Studies on the effects of patterning sizes on embryogenesis and cardiogenesis were also conducted by microcontact printing Matrigel to generate uniform EBs. Patterned EBs revealed that the ratio of Gata6 (endoderm-associated marker) to Pax6 (neural-associated marker) expression increased with decreasing colony size. Larger EBs with endoderm-biased (high Gata6/Pax6) gene expression at early stages exhibited higher mesoderm and cardiac induction.²⁹⁵ This approach was further used for high-throughput analysis of cell fate determination and endogenous signaling pathway activation and differentiation bias.²⁹⁶

Recently, researchers found that the geometric confinement from the micropatterned substrate was able to trigger self-organization of hESCs, which recapitulated spatial cell fate patterning during early embryonic development. In response to BMP4, colonies reproducibly differentiated to an outer trophoderm-like ring, an inner ectodermal circle, and a ring of mesendoderm expressing primitive-streak markers in between.²⁹⁷ Synergism of biochemical cues and geometric confinement on micropatterned hiPSCs can induce self-organizing lineage specification and creation of a 3D beating human cardiac microchamber, which resembles the developing primitive human heart. These *in vitro* cardiac microchambers were used to screen drugs likely to generate cardiac

malformations during development. For example, applying thalidomide during the cardiac differentiation not only reduced differentiation efficiency, but also significantly damaged the formation of cardiac microchambers with smaller size, lower contractility, and decreased beat rates compared to the control.²⁹⁸

Although micropatterning methods can confine colony geometry, regulate cell morphology and functions, and support high-throughput analysis, these 2D culture platforms lack the full architecture and functional properties of 3D human tissues and organs, and thus are of limited use for cardiac research. These 2D results have been seen as the first step towards engineering cardiac models, which can be used as templates for 3D tissue structure. Ongoing 2D research would focus on single-cell micropatterning and analysis, which can provide insight on cellular machinery, characterize the heterogeneity of cell population, and enable high-throughput screening for single-cell response to different environmental factors. Compared to CM alignment for mimicking heart muscle tissue, single CM micropatterning is extensively involved in exploring myofibrillogenesis and its relationship with extracellular factors. By microcontact printing ECM protein on the coverslip to shape single CM into the predefined patterns, researchers found that not only cell shape was defined but also the cytoskeleton was under reorganization into the predicted architecture.²⁹⁹ It was noticed that the spatial configuration of ECM played a key role in regulating the other three factors: cell shape,²⁴⁶ sarcomere orientation,³⁰⁰ and nuclear morphology.³⁰¹

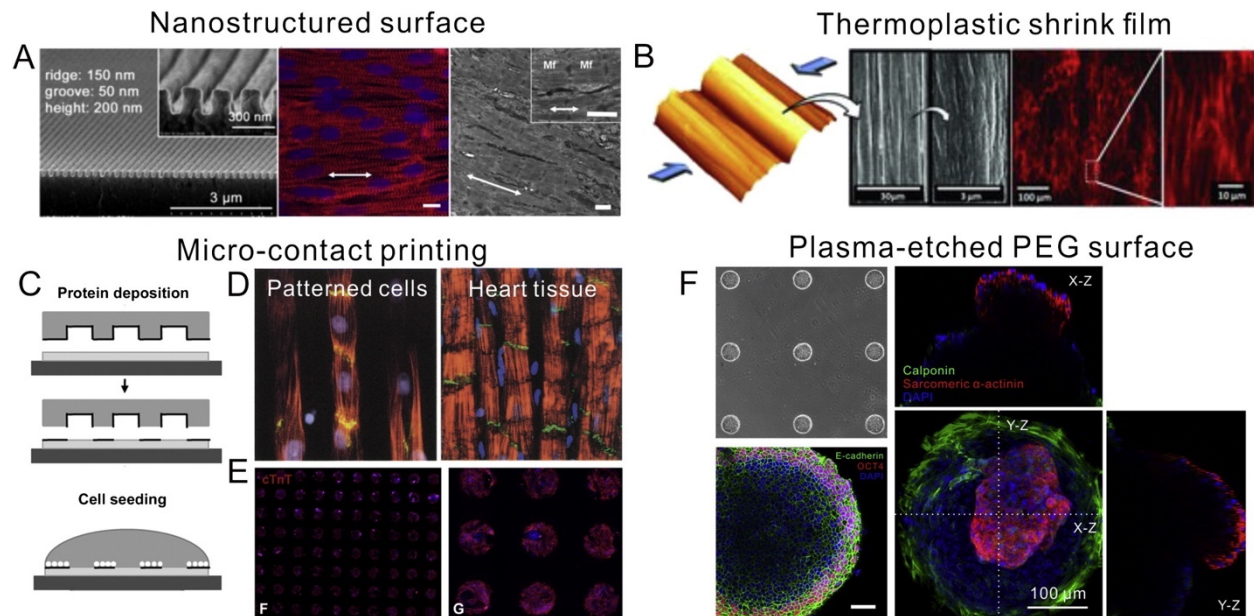


Figure 8-2. Micropatterned 2D cardiac models.

Topographical alignment of CMs with (A) Microfabricated nanostructured surface;²⁷⁶ (B) Prestressed thermoplastic shrink film with tunable multi-scaled wrinkles;²⁷⁵ and (C) Microcontact-printed patterns of pattern CMs into (D) Aligned stripes to mimic adult cardiac tissue structure²⁸¹ and (E) Circular colonies for high-throughput screening.²⁹⁰ (F) Using oxygen plasma to etch PEG surfaces under a PDMS stencil protection allows micropatterning hiPSCs and determining stem cell fate during cardiac differentiation.²⁹⁸

8.4 Biomaterials Used to Generate 3D Cardiac Models

Engineering a 3D cardiac tissue with physiologically relevant microenvironment and cell morphology presents a significant challenge for *in vitro* cardiac modeling. Biomaterials have played a major role in creating 3D tissue models, since they not only support cell attachment and alignment, but also transmit load, provide physiologically relevant stiffness, and ideally can be degraded and replaced over time by cell-secreted ECM proteins. Several representative natural and synthetic biomaterials-based engineered heart tissue (EHT) systems are shown in **Figure 8-3**. We have classified them as either hydrogel based or fibrous cardiac models, each is discussed in greater detail below.

8.4.1 Natural Hydrogel-Based Cardiac Models

Hydrogels consisting of two naturally occurring proteins, collagen and fibrin, have been widely used to generate EHT. Matrigel was often used as a supplemental material to increase cell viability and attachment due to its various growth factors and matrix components. The first EHT consisted of a 3D scaffold of collagen I with embryonic chick CMs.³⁰² Later, they were further developed into ring structures with neonatal rat CMs,³⁰³ which could be stacked and implanted for successful improvement of the function of infarcted rat heart.³⁰⁴ Currently, EHTs are primarily designed in a two-post configuration, allowing for characterization of contraction forces. Parallel EHT arrays consisting of a mixture of fibrinogen, Matrigel, thrombin, and neonatal rat CMs³⁰⁵ or hESC-CMs³⁰⁶, on a silicone post rack casted from Teflon molds, were used for preliminary drug screening. Proarrhythmic compounds chromanol and erythromycin was shown to affect EHT repolarization inhibition, and the cardiotoxic drug doxorubicin affected EHT force generation in a time- and dose-dependent manner.³⁰⁵ Isoprenaline and carbachol were found to affect the spontaneous contractile rate. Repolarization was inhibited by E-4031 (3 nM IC₅₀), procainamide (100 μM IC₅₀), sertindole (10 nM IC₅₀), quinidine (1000 nM IC₅₀), and cisapride (30 nM IC₅₀).³⁰⁶

EHTs of collagen I and fibrinogen were also generated on microfabricated devices with micron-scale standing posts, and researchers found that the matrix composition affected the dynamic and static contractility of the cardiac tissues.³⁰⁷ Using these micro-EHTs, researchers were able to model dilated cardiomyopathy caused by titin mutation, and demonstrated that 3D titin-mutant EHTs exhibited lower contraction forces compared to WT EHTs, such difference in contractile function was not possible to be detected by single-cell assays.³⁰⁸ This configuration was further employed to generate EHTs based on a mixture of collagen I, Matrigel, and hESC-CMs for preclinical drug screening and gene transfer. The 610 nM IC₅₀ value generated for verapamil in these EHTs surpassed the 160 nM IC₅₀ for traditional iPSC cells in 2D culture, indicating better recapitulation of human physiology compared to a 2D culture system. However, an insufficient response to isoproterenol suggested cardiac tissue immaturity.³⁰⁹ A multi-post configuration with collagen I and Matrigel was used to design and formulate cardiac microtissues using hiPSC-CMs, and researchers found that tissue structure and non-CM population played important roles in tissue integrity and maturation.³¹⁰ This multi-post platform was further applied to establish a tachycardiac model of arrhythmogenesis for *in vitro* patient-specific disease modeling.

The 3D cardiac tissue structure was also created using fibrin-based hydrogel matrix generated by soft lithography technique with controllable size and architecture; these EHTs demonstrated increased spontaneous beat rate and twitch amplitude upon exposure to isoproterenol, with an EC₅₀ of 95 nM falling within the reported 30-160 nM range for adult human ventricular tissue. CMs differentiated from ESCs and from cardiac progenitor cells (CPCs) were seeded into this engineered hydrogel to yield highly aligned CMs and robust intercellular coupling with rapid action potential conduction (22-25 cm/s) and significant contractile forces (up to 2 mN).^{311,312}

In all post-based *in vitro* cardiac microtissues, various natural biomaterials (e.g. collagen I, fibrin, Matrigel) served as an initial scaffold and ECM to support cell attachment, whereas the posts stabilized the developing tissue as the cells condensed and remodeled the scaffold, which had the effect of 3D alignment of the encapsulated CMs. The flexible PDMS posts additionally served as the sensor enabling the measurement of contraction force generated by the beating CMs. These contractile forces are a key output of EHTs and are coupled with CM electrophysiology and hypertrophy within EHTs; however, these forces are highly dependent on the biomaterial composition, making it difficult to compare drug responses among different EHTs developed by different research groups. A high degree of natural material variability is of major concern in efforts to establish standardized assays for drug screening with the requirements of consistency, reproducibility, and high-throughput capability. Such material variability will affect tissue formation and cellular responses, which will eventually lead to the variation of functional readout, such as contractile force measured by the posts.

8.4.2 Synthetic Fibrous Cardiac Models

Synthetic biomaterials provide an attractive alternative to natural materials, as researchers can control the entire synthesis process as well as the materials' mechanical properties, topography, and structure. A number of synthetic polymers have been used to create 3D cardiac scaffolds for either *in vitro* models or implantable patches to repair and regenerate the infarcted tissue. Key requirements for synthetic scaffolds are that they recapitulate the native 3D hierarchical fibrillar structure, possess biomimetic surface properties, and demonstrate mechanical integrity. The most frequently used synthetic polymers for cardiac tissue engineering are polyurethane, poly ϵ -caprolactone (PCL), polylactic acid (PLA), polyglycolic acid (PGA), and their copolymers. One example of synthetic material-based cardiac constructs were generated with neonatal rat CMs and poly(glycerol sebacate) (PGS) and maintained in a bioreactor with simultaneous culture medium perfusion and electrical conditioning, which led to enhanced organization and functionality of engineered cardiac tissue.³¹³

Cell alignment can be obtained with electrospun nanofiber-based scaffolds, which provide flexible matrices and topographic properties offering support and guidance for the CMs. CMs organized into anisotropic cardiac tissue on aligned PCL/gelatin composite electrospun nanofibrous scaffolds to structurally mimic the oriented ECM in myocardium.³¹⁴ The orientation and density of electrospun polymethylglutarimide (PMGI) nanofibers defined the overall architecture of the cardiac tissue, which was

optimized for best alignment with 30-50 fibers/mm and an average distance between fibers of under 30 μm .³¹⁵ An aligned fibrous mesh of electrospun polyester blend, poly(3-hydroxybutyrate-co-3-hydroxyvalerate) (PHBV), P(L-D,L)LA, and poly(glycerol sebacate) (PGS) was shown to enhance cardiomyogenic differentiation of human umbilical cord mesenchymal stem cells.³¹⁶ Similarly, rotary jet spinning was used to fabricate highly aligned nanofiber constructs from a blend of collagen, gelatin, and PCL polymer, which promoted better sarcomere formation in CMs.³¹⁷

Electrospun 3D scaffolds with aligned nanofibers using synthetic polymers successfully mimic the structure and orientation of native ECM in the myocardium and help CMs self-organize with anisotropic structure. However, the micron scale porosity of these scaffolds limits cell infiltration into the matrix and thereby the creation of a 3D tissue. As such, the scaffolds are 3D in nature, but the tissue is really a 2D structure similar to those created on micropatterned surfaces. To address this limitation, a highly defined scaffold structure was fabricated by two-photon initiated polymerization (TPIP) with unprecedented control over a wide range of matrix features. A 3D human cardiac disease model was created by seeding hiPSC-CMs, with long QT syndrome type 3 (LQT3), on the TPIP-fabricated synthetic filamentous scaffolds. Tailoring the mechanical properties of the scaffolds modulated the contractility of residing hiPSC-CMs and, more importantly, recapitulated the abnormal contractility of long QT syndrome. Treatment with caffeine increased the spontaneous contractile rate and maximum contractile velocity and high doses of caffeine and nifedipine both caused cessation of beating. In contrast, treatment with E-4031 indicated irregular beating patterns, and propranolol induced significant uncoordinated beating, suggestive of cardiac arrhythmias, in a dose-dependent manner.³¹⁸

A collagen-based cardiac tissue model, termed “biowire,” combined architectural and electrical cues to generate a microenvironment conducive to maturation of hiPSC-derived cardiac tissues.³¹⁹ The hiPSC-CMs were seeded with collagen type I into a microfabricated well and subjected to electrical stimulation with a progressive increase in frequency. Biowires submitted to electrical stimulation had markedly increased myofibril ultrastructural organization, elevated conduction velocity, and improved both electrophysiological and Ca^{2+} handling properties compared to non-stimulated controls. These changes suggested enhanced CM maturation that depended on the stimulation rate. The biowire maturation represented an intermediate phenotype as CMs undergo maturation from the embryonic state, as evidenced by low membrane conductance. The use of electrical stimulation in conjunction with stretch as a mimic of cardiac load, concurrently or sequentially, might be required to induce terminal differentiation and maturation in hiPSC-CMs.^{320,321}

These findings collectively suggest that 3D tissue engineered models with defined cellular microenvironments hold great promise for high-content drug screening and cardiotoxicity testing. The integration of biomaterials with existing iPSC-based disease models could better recapitulate disease pathology and may represent superior scalability and flexibility for creating large numbers of personalized models to meet diverse and urgent patient needs.

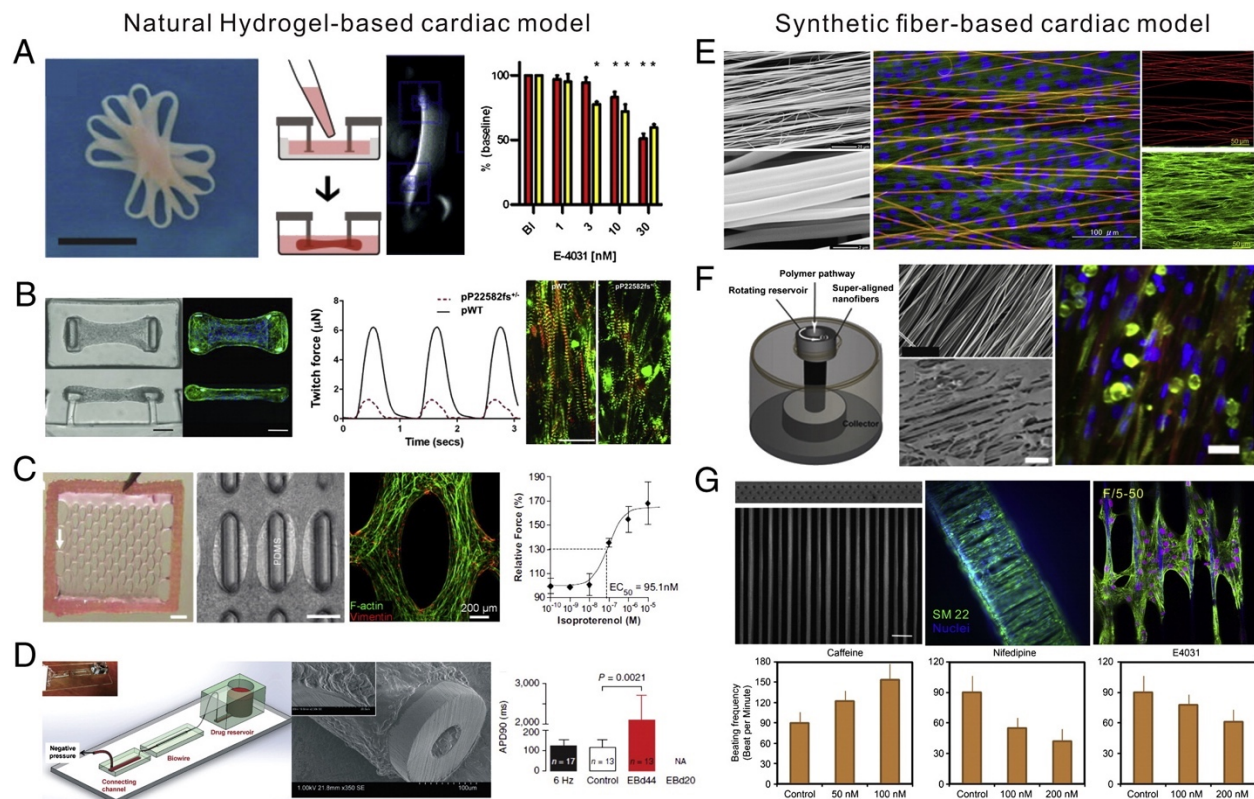


Figure 8-3. Biomaterial-based 3D cardiac models.

(A) Engineered heart mini-tissues (millimeter scale) were made from fibrin and hiPSCs for implantation³⁰⁴ and drug-screening purpose.³⁰⁵ (B) Engineered heart micro-tissues (micron scale) made from collagen were used to model the dilated cardiomyopathy caused by titin mutation.³⁰⁸ (C) Fibrin-based cardiac tissue patch was generated by soft lithography with controllable size and architecture and its drug response to isoproterenol.³¹¹ (D) A biowires platform combining architectural and electrical cues generated a microenvironment conducive to the maturation of hiPSC-derived cardiac tissues.³²¹ (E) Electrospun nanofiber scaffolds were made for creating the continuous anisotropic cardiac tissue.³¹⁵ (F) Aligned nanofiber scaffolds made by rotary jet spinning promoted better sarcomere formation in CMs.³¹⁷ (G) High-defined filamentous scaffolds made by two-photon initiated polymerization were used to create an aligned hiPSC-CMs-based cardiac model for drug screening.³¹⁸

8.5 Microdevices for 3D Cardiac Models

Moving away from scaffold-based cardiac models, highly miniaturized and integrated microphysiological systems are currently being developed as “heart-on-a-chip” technology to provide more controlled 3D microenvironments, with enhanced multiple functionalities and increased throughput. Such microphysiological systems (**Figure 8-4**) combined with hiPSC technology are expected to not only better predict on toxicity and efficacy of potential drugs in human physiologically relevant conditions, but also provide a more in-depth understanding of human cardiac disease in complex and heterogeneous microenvironments.

An engineered anisotropic ventricular myocardium was first developed by micropatterning neonatal rat CMs on poly(N-isopropylacrylamide) (PIPAAm)/PDMS-

based thin elastomeric film, which can simultaneously measure the contractile function, quantify the electrical propagation, and evaluate cytoskeletal architecture in cardiac tissues during pharmacological interventions. A dose-dependent increase in spontaneous beat rate and stress was reported in response to epinephrine.³²² This microsystem was further incorporated with fluidic control for drug washout, a heating element for temperature control, and embedded electrodes for electrical field stimulation.³²³ This system was not only used to characterize the cardiac tissue derived from various cell types (primary neonatal mouse CMs, mouse iPSC-CMs, and human iPSC-CMs),³²⁴ but also to model maladaptive cardiac hypertrophy³²⁵ and patient-specific mitochondrial cardiomyopathy, specifically, the Barth Syndrome (BTHS) – a mitochondrial disorder caused by mutation of the gene encoding tafazzin (*TAZ*).³²⁶ To study the pathophysiology underlying BTHS, the group generated hiPSC-CMs from two patients with BTHS and discovered metabolic, structural and functional abnormalities associated with *TAZ* mutation. This elegant study provided new insights into the pathogenesis of Barth syndrome, and pointed to a new treatment strategy for BTHS.

For improved modeling specific types of cardiac disease, unique platforms should be designed to mimic the pathological microenvironment occurring during the disease progression. A paper-based culture system was developed with multiple layers of paper-containing cells, suspended in hydrogels, stacked to form a layered 3D model of a cardiac tissue. Mass transport of oxygen and glucose into this 3D system was modulated to induce an ischemic environment in the bottom layers of the stack. This *in vitro* cardiac model mechanistically studied cellular motility and viability, and recapitulated the cellular interactions and gradients of molecules in the heart under ischemia. However, the cardiospheres in the stacked papers lacked the aligned structure to mimic the *in vivo* tissue structure. Moreover, this system currently makes it difficult to determine the concentration of small molecules (e.g., oxygen, glucose, or cytokines) *in situ* and to measure the contractility of CMs without complex optics.³²⁷

To allow accurate prediction of drug cardiotoxicity, a microfluidic-based microphysiological system was designed to recapitulate a minimal organoid of the human myocardium.³² Pharmacological studies on this system with verapamil (950 nM IC₅₀), isoproterenol (315 nM EC₅₀), metoprolol (244 μM IC₅₀), and E-4031 (392 nM IC₅₀) predicted a higher safety margin and had better concordance with tissue-scale values and clinical observations, compared to those in cellular-scale studies and large-scale animals. The human cardiac microphysiological system was proposed to complement animal models, and in the future may have the potential to replace animal studies, which often are expensive, unethical, and unable to accurately predict the drug's actual effect.

Since the discovery of Moore's law, the semiconductor industry has come a long way, and the development of new microfabrication techniques has equipped the bioengineering community with tools, which can be employed for basic and translational applications. Microengineered *in vitro* models with multiple readouts have a great potential to better mimic the *in vivo* physiology and provide a deeper understanding of the physiological events that characterize cardiac development and function. These

systems provide fine control over fluid flow, creating microcirculation mimicking the *in vivo* transport; massive parallelization for high content readouts; miniaturization of large systems for convenient operation and reduction of reagent use, leading to lower operational costs; and unprecedented control of system architecture and dimensions at the biological scale (nm to μm). We envision the use of microtechnologies coupled with hiPSC biology to revolutionize the areas of drug screening, disease modeling, and personalized medicine.

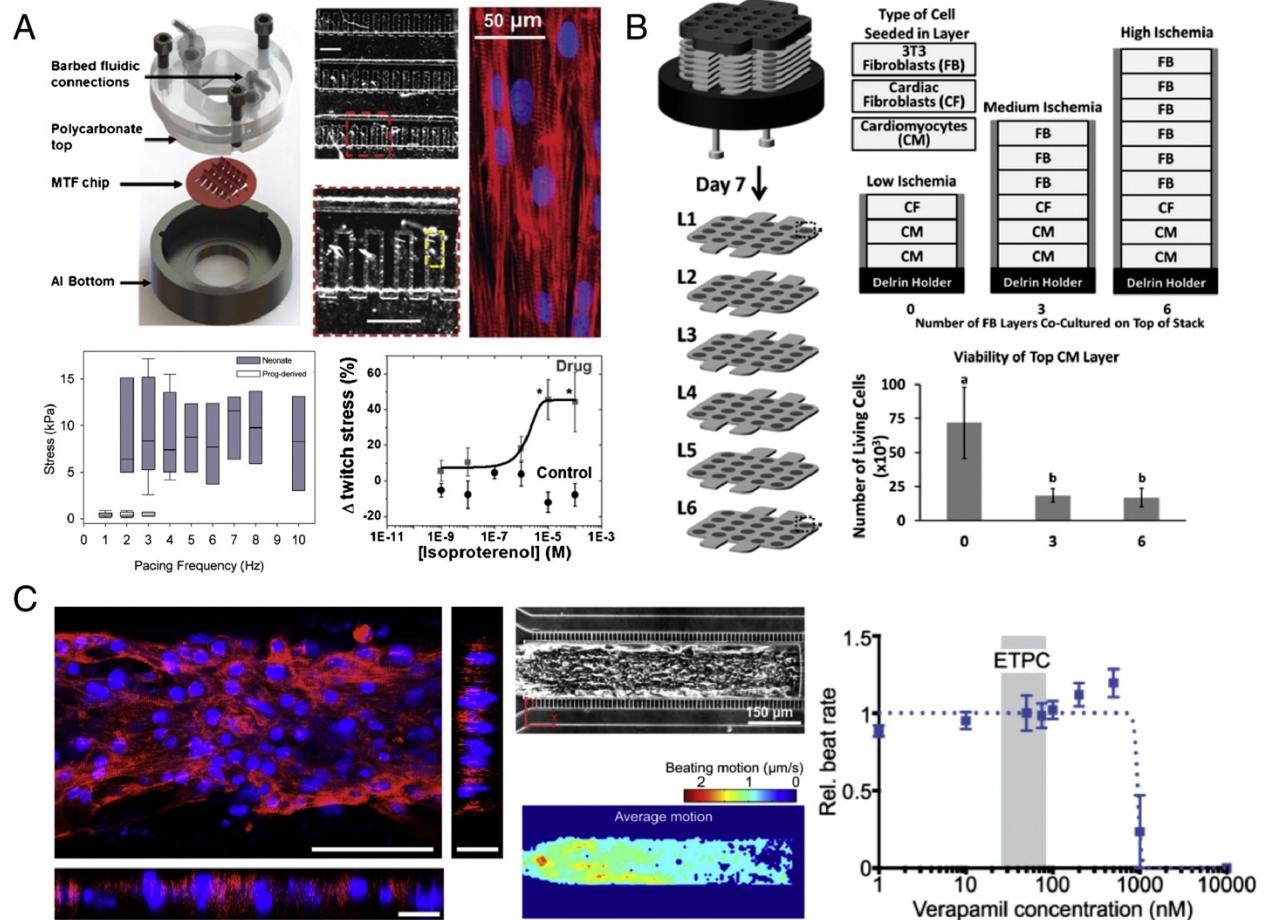


Figure 8-4. Microdevice-based 3D cardiac models.

(A) PIPAAm-based “heart-on-chip” microsystem³²³ can measure the deformation of the elastomeric thin film to characterize the contractility of cardiac tissue derived from various cell types and assess the drug response to isoproterenol.³²⁴ (B) A stacked-paper culture system containing CMs was used to mimic the pathological microenvironment occurring during cardiac ischemia.³²⁷ (C) A microfluidic-based microphysiological system was designed to recapitulate a minimal organoid of the human myocardium with highly aligned tissue architecture and anisotropic beating behavior, allowing for accurate prediction of drug cardiotoxicity.³²

8.6 Perspective and Conclusions

The heart is a powerful, complex organ that has intrigued both artists and scientists for millennia. *In vitro* cardiac tissue models present great opportunities for regenerative medicine, drug screening, and disease modeling. The opportunities, however, coincide

with enormous challenges due to the complexity of cardiac structure and function. A standardized, reproducible, and scalable process for differentiating hiPSCs to CMs is required for consistent cell quality. Recent developments in the cardiogenic differentiation open the possibility of obtaining such human CMs in the laboratory.^{260,261}

The immaturity of hiPSC-CMs complicates the cells' adoption as a reliable readout for translational applications. Such immature embryonic or neonatal-like CMs cannot compare morphologically with large and stiff ventricular CMs in the adult human heart.³²⁸ Thus, cardiac tissues constructed from hiPSC-CMs have significantly lower field potentials and contraction forces than adult ventricular tissue, so at this point cannot be considered an exact *in vitro* model of mature myocardium. It has been suggested that tissue-engineering methods would necessitate the maturation of hiPSC-CMs in a physiologically mimicked microenvironment.^{289,312,319} This suggests that genetic and environmental factors interact and lead to CM maturation, though the mechanism and process is not fully understood.

We summarize the current *in vitro* cardiac tissue models, along with their advantages and limitations for applications, such as drug cardiotoxicity screening and human heart disease modeling (**Table 8-2**). An ideal *in vitro* cardiac tissue model should be physiologically relevant with multiple biological, mechanical, and electrical readouts, ensuring different functional endpoints for a particular application. Appropriate biomaterials used for the cardiac tissue models need to be chosen carefully according to the specific applications. For example, microsystems with conventional PDMS as a substrate result in drug stability problems and unpredictable device performance, due to its absorption and retention of highly hydrophobic compounds.^{329,330} Acceptance of these models will require automation, robustness, and easy integration into the workflow at pharmaceutical companies. Specifically for drug development and testing, the microfluidic-based system with standardized fabrication and process holds great promise on high-content screening with electrical and mechanical measurement and integration with multiple organs to achieve “human on a chip.”

A more futuristic application is envisioned in the area of precision medicine, an emerging approach for disease treatment and prevention that takes into account individual variability in genes, environment, and lifestyle for each person.^{331,332} The promise of precision medicine for cancer therapeutics is already being realized with the recent introduction of several targeted therapies, some with companion diagnostic tests that identify patients most likely to benefit from treatment.³³³ Moving forward, we hope to see physiologically functional *in vitro* cardiac models of individual- and disease-specific hiPSCs on chips, which can be termed as “patient on a chip.” This approach will help to diagnose and design better treatment strategy for individual patients. Success, however, will depend on how effectively and how efficiently engineering and biology can be integrated to create such systems.

Table 8-2. Analysis of *in vitro* cardiac tissue models and the corresponding mechanical, electrophysiological, and biological outcomes.

Characteristics				Outcomes			
Platform		Cell Type	Materials	Coating	Mechanical	Beat rate (bpm)	Biological
Micro-patterning	Surface topography	nrCM	PVC cover slips	Fibronectin ²⁷¹		☆	+
		nrCM	PDMS	Laminin ²⁷²		☆	++
		nrCM	Polyurethane, polystyrene	²⁷³		15-50	+
		nmCM	PDMS	Fibronectin, laminin, collagen I ²⁷⁴		☆	++
	Microcontact printing	nrCM	Polyacrylamide	Laminin, Matrigel ²⁸⁰	Young's modulus 5-35 kPa	☆	++
		nrCM	Alginate	Fibronectin ²⁸²	Young's modulus 57 kPa	60-240 (pacing)	++
		nrCM	PDMS, Stretch device	Collagen ²⁸³		☆	+
		nrCM	Polystyrene	Chitosan ²⁸⁴		☆	++
		nrCM	PDMS	Hyaluronic acid, fibronectin ²⁸⁵		60-100	+
		nmCM	Glass, polyresist	²⁸⁶		☆	++
		hESC-CM, hiPSC-CM	Polyacrylamide	Gelatin ²⁸⁹	Contractile stress 0.2-0.5 mN/mm ²	60-180 (pacing)	++
	hESC-CM	Polyacrylamide	Laminin ²⁹⁰	Elastic modulus 15-35 kPa	50	++	
	Micro-fabrication	Microposts	hESC-CM, nrCM	Silicone post racks	Fibrin, Matrigel ³⁰⁶	Contractile force 100-300 μN	300
nrCM, hiPSC-CM			PDMS	Collagen, fibrinogen ^{307,308}	Contractile force 2-6 μN	33-60	++
hESC-CM			PDMS posts	Collagen, Matrigel ³⁰⁹	Contractile force 0.3 mN	70	++
hESC-CM, nrCM			PDMS posts	Collagen, Matrigel ³¹⁰		☆	++
hESC-CM			PDMS posts	Fibrin ³¹¹	Contractile force 2 mN	☆	++
hESC-CM			PDMS posts, patch	Fibrin, Matrigel ³¹²	Contractile force 3 mN	60-180 (pacing)	++
Perfusion bioreactor		nrCM	Poly(glycerol sebacate), channels	Laminin ³¹³	Elastic modulus 34.55 ± 1.26 kPa, Pore size 75–150 μm	180 (pacing)	++
Biowires		hESC-CM	PDMS	Collagen ^{319,320}	Conduction velocity 11–16 cm/s, Young's modulus 1–6 kPa	60–360 (pacing)	++
Two-photon polymerization		hiPSC-CM, Long QT3 syndrome	Filamentous matrix	Fibronectin ³¹⁸	Maximal contraction velocity 15–25 μm/s	90	++
MPS systems		nrCM, hESC-CM, hiPSC-CM, Barth syndrome	PDMS, PIPAAm	Fibronectin Gelatin ^{322,323,325,326}	Young's modulus 1.52 MPa, Systolic stress 15–20 kPa, Diastolic stress 8.0 kPa	120 (pacing)	++
		hiPSC-CM	PDMS	Fibronectin ³²	Average contraction velocity 3 μm/s	55-80	++

Abbreviations in Table 2

CM	Cardiomyocytes
nrCM	Neonatal rat cardiomyocytes
nmCM	Neonatal mouse cardiomyocytes
hESC-CM	Human embryonic stem cell-derived CMs
hiPSC-CM	Human induced pluripotent stem cell-derived CMs
Beat rate	Beat per minute (BPM)
☆	Spontaneous contractions reported without beat rate
+	Indications of CMs are limited to: cell alignment and elongation, morphological assessment, genetic assessment
++	Indications of CMs include: sarcomeres, functional gap junctions, appropriate responses to drug treatments, as well as indications from '+'

Chapter 9: Conclusions and Future Directions

In this dissertation, we sought to develop high-selectivity, high-throughput proteomic analytical tools at single- to low-cell resolution. We characterized the contribution of ampholytes on IEF separation resolution, and leveraged IEF separation theory to optimize assay performance. We investigated the performance of highly-porous polyacrylamide hydrogel matrices in the ultrathin IEF assay with subsequent immunoblot. To further understand analytical sensitivity limitations in ultrathin electrophoretic cytometry assays, we modeled protein diffusion in multi-material substrates. Finally, we demonstrated a proof-of-concept variant of the single cell IEF assay with increased throughput for interrogation of proteomic expression from arrays of single cells. The expansion of these proteomic assays towards high sensitivity, high selectivity, and high throughput platforms interrogating single cell function expands the biological toolkit with which one can quantify and understand the biological functions of cells and tissues at the micro scale. Building databases of proteomic function and dysfunction, in line with the Human Protein Atlas,³³⁴ provides a roadmap for the design of therapeutic interventions.

In addition, we sought to develop *in vitro* microscale tissue models better recapitulating human physiology for drug screening. We developed and characterized the adipose *in vitro* model “WAT-on-a-chip” for drug screening applications. We also reviewed the *in vitro* cardiac model space. It is particularly intriguing to envision the further development of *in vitro* organ models, with complex mechanical and biological microarchitectures characteristic of *in vivo* organs. Recreating the *in vivo* niche for multiple cell types acting in synergy would provide valuable information on organ function at the micro- to mesoscale as well as modeling tissue response to drugs.^{32,189} Furthermore, linking²²⁸ these organ models into a facsimile of the human body, with multiple quantitative, non-terminal assessment modalities integrated throughout the linked model system, provides a more wholistic view of human drug response not currently available in the *in vitro* setting.

References

- (1) Newman, J. R. S.; Ghaemmaghami, S.; Ihmels, J.; Breslow, D. K.; Noble, M.; DeRisi, J. L.; Weissman, J. S. Single-Cell Proteomic Analysis of *S. Cerevisiae* Reveals the Architecture of Biological Noise. *Nature* **2006**, *441* (7095), 840–846. <https://doi.org/10.1038/nature04785>.
- (2) Chen, G.; Gharib, T. G.; Huang, C.-C.; Taylor, J. M. G.; Misek, D. E.; Kardia, S. L. R.; Giordano, T. J.; Iannettoni, M. D.; Orringer, M. B.; Hanash, S. M.; et al. Discordant Protein and mRNA Expression in Lung Adenocarcinomas. *Mol. Cell. Proteomics* **2002**, *1* (4), 304 LP – 313. <https://doi.org/10.1074/mcp.M200008-MCP200>.
- (3) Hughes, A. J.; Spelke, D. P.; Xu, Z.; Kang, C.-C.; Schaffer, D. V.; Herr, A. E. Single-Cell Western Blotting. *Nat. Methods* **2014**, *11* (7), 749–755.
- (4) Kang, C.-C.; Ward, T. M.; Bockhorn, J.; Schiffman, C.; Huang, H.; Pegram, M. D.; Herr, A. E. Electrophoretic Cytopathology Resolves ERBB2 Forms with Single-Cell Resolution. *npj Precis. Oncol.* **2018**, *2* (1), 10. <https://doi.org/10.1038/s41698-018-0052-3>.
- (5) Yamauchi, K. A.; Herr, A. E. Subcellular Western Blotting of Single Cells. *Microsystems Nanoeng.* **2017**, *3*, 16079. <https://doi.org/10.1038/micronano.2016.79>.
- (6) Sinkala, E.; Sollier-Christen, E.; Renier, C.; Rosàs-Canyelles, E.; Che, J.; Heirich, K.; Duncombe, T. A.; Vlassakis, J.; Yamauchi, K. A.; Huang, H.; et al. Profiling Protein Expression in Circulating Tumour Cells Using Microfluidic Western Blotting. *Nat. Commun.* **2017**, *8*, 14622.
- (7) Kang, C.-C.; Yamauchi, K. A.; Vlassakis, J.; Sinkala, E.; Duncombe, T. A.; Herr, A. E. Single Cell-Resolution Western Blotting. *Nat. Protoc.* **2016**, *11* (8), 1508–1530. <https://doi.org/10.1038/nprot.2016.089>.
- (8) Toriello, N. M.; Douglas, E. S.; Thaitrong, N.; Hsiao, S. C.; Francis, M. B.; Bertozzi, C. R.; Mathies, R. A. Integrated Microfluidic Bioprocessor for Single-Cell Gene Expression Analysis. *Proc. Natl. Acad. Sci.* **2008**, *105* (51), 20173 LP – 20178. <https://doi.org/10.1073/pnas.0806355106>.
- (9) Altschuler, S. J.; Wu, L. F. Cellular Heterogeneity: Do Differences Make a Difference? *Cell* **2010**, *141* (4), 559–563. <https://doi.org/10.1016/j.cell.2010.04.033>.
- (10) Loroch, S.; Zahedi, R. P.; Sickmann, A. Highly Sensitive Phosphoproteomics by Tailoring Solid-Phase Extraction to Electrostatic Repulsion-Hydrophilic Interaction Chromatography. *Anal. Chem.* **2015**, *87* (3), 1596–1604. <https://doi.org/10.1021/ac502708m>.
- (11) Brumbaugh, K.; Johnson, W.; Liao, W.-C.; Lin, M.-S.; Houchins, J. P.; Cooper, J.; Stoesz, S.; Campos-Gonzalez, R. Overview of the Generation, Validation, and Application of Phosphosite-Specific Antibodies. In *Signal Transduction Immunohistochemistry: Methods and Protocols*; Kalyuzhny, A. E., Ed.; Springer, 2011; Vol. 717, pp 3–43. <https://doi.org/10.1007/978-1-61779-024-9>.
- (12) Atrih, A.; Turnock, D.; Sellar, G.; Thompson, A.; Feuerstein, G.; Ferguson, M. A. J.; Huang, J. T. J. Stoichiometric Quantification of Akt Phosphorylation Using LC-MS/MS. *J. Proteome Res.* **2010**, *9* (2), 743–751. <https://doi.org/10.1021/pr900572h>.
- (13) O'Neill, R. A.; Bhamidipati, A.; Bi, X.; Deb-Basu, D.; Cahill, L.; Ferrante, J.; Gentalen, E.; Glazer, M.; Gossett, J.; Hacker, K.; et al. Isoelectric Focusing Technology Quantifies Protein Signaling in 25 Cells. *Proc. Natl. Acad. Sci.* **2006**, *103* (44), 16153–16158.
- (14) Anderson, J. C.; Peck, S. C. A Simple and Rapid Technique for Detecting Protein Phosphorylation Using One-Dimensional Isoelectric Focusing Gels and Immunoblot Analysis. *Plant J.* **2008**, *55* (5), 881–885. <https://doi.org/10.1111/j.1365-313X.2008.03550.x>.
- (15) Wang, Z.; Ivory, C.; Minerick, A. R. Surface Isoelectric Focusing (SIEF) with Carrier Ampholyte PH Gradient. *Electrophoresis* **2017**, *38* (20), 2565–2575. <https://doi.org/10.1002/elps.201600565>.
- (16) Righetti, P. G. *Isoelectric Focusing: Theory, Methodology and Application*; Work, T. S., Work, E., Eds.; Elsevier Biomedical, 1983.
- (17) Budnik, B.; Levy, E.; Harmange, G.; Slavov, N. SCoPE-MS: Mass Spectrometry of Single Mammalian Cells Quantifies Proteome Heterogeneity during Cell Differentiation. *Genome Biol.* **2018**, *19* (1), 161. <https://doi.org/10.1186/s13059-018-1547-5>.
- (18) Zhu, Y.; Clair, G.; Chrisler, W. B.; Shen, Y.; Zhao, R.; Shukla, A. K.; Moore, R. J.; Misra, R. S.; Pryhuber, G. S.; Smith, R. D.; et al. Proteomic Analysis of Single Mammalian Cells Enabled by Microfluidic Nanodroplet Sample Preparation and Ultrasensitive NanoLC-MS. *Angew. Chemie Int. Ed.* **2018**, *57* (38), 12370–12374. <https://doi.org/10.1002/anie.201802843>.

- (19) Tentori, A. M.; Yamauchi, K. A.; Herr, A. E. Detection of Isoforms Differing by a Single Charge Unit in Individual. *Angew. Chemie Int. Ed.* **2016**, *55*, 1–6.
- (20) Yamauchi, K. A.; Tentori, A. M.; Herr, A. E. Arrayed Isoelectric Focusing Using Photopatterned Multi-Domain Hydrogels. *Electrophoresis* **2018**, *39* (8), 1040–1047.
- (21) Su, E. J.; Herr, A. E. Electrophoretic Cytometry of Adherent Cells. *Lab Chip* **2017**, *17* (24), 4312–4323.
- (22) Takahashi, K.; Tanabe, K.; Ohnuki, M.; Narita, M.; Ichisaka, T.; Tomoda, K.; Yamanaka, S. Induction of Pluripotent Stem Cells from Adult Human Fibroblasts by Defined Factors. *Cell* **2007**, *131* (5), 861–872. <https://doi.org/10.1016/j.cell.2007.11.019>.
- (23) Yu, J.; Vodyanik, M. A.; Smuga-Otto, K.; Antosiewicz-Bourget, J.; Frane, J. L.; Tian, S.; Nie, J.; Jonsdottir, G. A.; Ruotti, V.; Stewart, R.; et al. Induced Pluripotent Stem Cell Lines Derived from Human Somatic Cells. *Science (80-.)*. **2007**, *318* (5858), 1917–1920. <https://doi.org/10.1126/science.1151526>.
- (24) Singhvi, R.; Kumar, A.; Lopez, G. P.; Stephanopoulos, G. N.; Wang, D. I.; Whitesides, G. M.; Ingber, D. E. Engineering Cell Shape and Function. *Science (80-.)*. **1994**, *264* (5159), 696–698. <https://doi.org/10.1126/science.8171320>.
- (25) Chen, C. S.; Mrksich, M.; Huang, S.; Whitesides, G. M.; Ingber, D. E. Geometric Control of Cell Life and Death. *Science (80-.)*. **1997**, *276* (5317), 1425–1428. <https://doi.org/10.1126/science.276.5317.1425>.
- (26) Shao, Y.; Sang, J.; Fu, J. On Human Pluripotent Stem Cell Control: The Rise of 3D Bioengineering and Mechanobiology. *Biomaterials* **2015**, *52*, 26–43. <https://doi.org/https://doi.org/10.1016/j.biomaterials.2015.01.078>.
- (27) Weaver, V. M.; Fischer, A. H.; Peterson, O. W.; Bissell, M. J. The Importance of the Microenvironment in Breast Cancer Progression: Recapitulation of Mammary Tumorigenesis Using a Unique Human Mammary Epithelial Cell Model and a Three-Dimensional Culture Assay. *Biochem. Cell Biol.* **1996**, *74* (6), 833–851. <https://doi.org/10.1139/o96-089>.
- (28) Shuler. Organ-, Body- and Disease-on-a-Chip Systems. *Lab Chip* **2017**, *17*, 2345–2346. <https://doi.org/10.1039/C7LC90068F>.
- (29) Abaci, H. E.; Shuler, M. L. Human-on-a-Chip Design Strategies and Principles for Physiologically Based Pharmacokinetics/Pharmacodynamics Modeling. *Integr. Biol.* **2015**, *7* (4), 383–391. <https://doi.org/10.1039/C4IB00292J>.
- (30) Zhang, B.; Radisic, M. Organ-on-a-Chip Devices Advance to Market. *Lab Chip* **2017**, *17*, 2395–2420. <https://doi.org/10.1039/C6LC01554A>.
- (31) Zhang, B.; Korolj, A.; Lai, B. F. L.; Radisic, M. Advances in Organ-on-a-Chip Engineering. *Nat. Rev. Mater.* **2018**, *3* (8), 257–278. <https://doi.org/10.1038/s41578-018-0034-7>.
- (32) Mathur, A.; Loskill, P.; Shao, K.; Huebsch, N.; Hong, S.; Marcus, S. G.; Marks, N. C.; Mandegar, M. A.; Conklin, B. R.; Lee, L. P.; et al. Human iPSC-Based Cardiac Microphysiological System for Drug Screening Applications. *Sci. Rep.* **2015**, *5* (8883), 1–7. <https://doi.org/10.1038/srep08883>.
- (33) Stoyanov, A. IEF-Based Multidimensional Applications in Proteomics: Toward Higher Resolution. *Electrophoresis* **2012**, *33* (22), 3281–3290. <https://doi.org/10.1002/elps.201200221>.
- (34) Drysdale, J. W.; Righetti, P.; Bunn, H. F. The Separation of Human and Animal Hemoglobins by Isoelectric Focusing in Polyacrylamide Gel. *Biochim. Biophys. Acta - Protein Struct.* **1971**, *229* (1), 42–50. [https://doi.org/https://doi.org/10.1016/0005-2795\(71\)90315-1](https://doi.org/https://doi.org/10.1016/0005-2795(71)90315-1).
- (35) Stoyanov, A. V.; Das, C.; Fredrickson, C. K.; Hugh Fan, Z. Conductivity Properties of Carrier Ampholyte PH Gradients in Isoelectric Focusing. *Electrophoresis* **2005**, *26* (2), 473–479.
- (36) Tentori, A. M.; Hughes, A. J.; Herr, A. E. Microchamber Integration Unifies Distinct Separation Modes for Two-Dimensional Electrophoresis. *Anal. Chem.* **2013**, *85* (9), 4538–4545.
- (37) GE Healthcare. *Chromatofocusing with Polybuffer and Polybuffer Exchangers. Instructions 52-1586-00 AL.*; 2006.
- (38) Sinus Biochemistry and Electrophoresis GmbH. Sinulyte Carrier Ampholytes. 2013.
- (39) Invitrogen Corporation. Zoom Carrier Ampholytes. Technical Information. 2003, pp 1–2.
- (40) Davies, H. Some Physical and Chemical Properties of the Ampholine Chemicals. *Protides Biol. Fluids* **1970**, *17*, 389–396. <https://doi.org/10.1016/B978-0-08-015566-1.50066-6>.
- (41) Righetti, P. G.; Simó, C.; Sebastiano, R.; Citterio, A. Carrier Ampholytes for IEF, on Their Fortieth Anniversary (1967–2007), Brought to Trial in Court: The Verdict. *Electrophoresis* **2007**, *28* (21), 3799–3810. <https://doi.org/10.1002/elps.200700232>.

- (42) Sebastiano, R.; Simó, C.; Mendieta, M. E.; Antonioli, P.; Citterio, A.; Cifuentes, A.; Peltre, G.; Righetti, P. G. Mass Distribution and Focusing Properties of Carrier Ampholytes for Isoelectric Focusing: I. Novel and Unexpected Results. *Electrophoresis* **2006**, *27* (20), 3919–3934. <https://doi.org/10.1002/elps.200600170>.
- (43) Rabilloud, T.; Barzaghi, B.; Righetti, P. G. Use of Polybuffer as Carrier Ampholytes in Mixed-Bed Immobilized Gels for Isoelectric Focusing. *J. Biochem. Biophys. Methods* **1988**, *16* (2), 237–241. [https://doi.org/https://doi.org/10.1016/0165-022X\(88\)90034-6](https://doi.org/https://doi.org/10.1016/0165-022X(88)90034-6).
- (44) Hruška, V.; Jaroš, M.; Gaš, B. Simul 5 - Free Dynamic Simulator of Electrophoresis. *Electrophoresis* **2006**, *27* (5–6), 984–991. <https://doi.org/10.1002/elps.200500756>.
- (45) Kozłowski, L. P. Proteome-PI: Proteome Isoelectric Point Database. *Nucleic Acids Res.* **2016**, *45* (D1), D1112–D1116. <https://doi.org/10.1093/nar/gkw978>.
- (46) Gianazza, E.; Righetti, P. G. Size and Charge Distribution of Macromolecules in Living Systems. *J. Chromatogr. A* **1980**, *193* (1), 1–8. [https://doi.org/https://doi.org/10.1016/S0021-9673\(00\)81438-7](https://doi.org/https://doi.org/10.1016/S0021-9673(00)81438-7).
- (47) Baker, J. P.; Stephens, D. R.; Blanch, H. W.; Prausnitz, J. M. Swelling Equilibria for Acrylamide-Based Polyampholyte Hydrogels. *Macromolecules* **1992**, *25* (7), 1955–1958.
- (48) Kang, C.-C.; Yamauchi, K. A.; Vlassakis, J. M.; Sinkala, E.; Duncombe, T. A.; Herr, A. E. Single Cell – Resolution Western Blotting. *Nat. Protoc.* **2016**, *11* (8), 1508–1530. <https://doi.org/10.1038/nprot.2016.089>.
- (49) Vlassakis, J. M.; Yamauchi, K. A.; Herr, A. E. Automated Image Analysis Algorithms for High-Throughput Western Blotting. *SLAS Technol.* **2019**, in preparation.
- (50) Righetti, P. G. *Immobilized PH Gradients: Theory and Methodology*; Burdon, R. H., van Knippenberg, P. H., Eds.; Elsevier, 1990.
- (51) Macounová, K.; Cabrera, C. R.; Holl, M. R.; Yager, P. Generation of Natural PH Gradients in Microfluidic Channels for Use in Isoelectric Focusing. *Anal. Chem.* **2000**, *72* (16), 3745–3751. <https://doi.org/10.1021/ac000237d>.
- (52) Huang, T.; Pawliszyn, J. Microfabrication of a Tapered Channel for Isoelectric Focusing with Thermally Generated PH Gradient. *Electrophoresis* **2002**, *23* (20), 3504–3510. [https://doi.org/10.1002/1522-2683\(200210\)23:20<3504::AID-ELPS3504>3.0.CO;2-X](https://doi.org/10.1002/1522-2683(200210)23:20<3504::AID-ELPS3504>3.0.CO;2-X).
- (53) Bjellqvist, B.; Ek, K.; Righetti, P. G.; Gianazza, E.; Görg, A.; Westermeier, R.; Postel, W. Isoelectric Focusing in Immobilized PH Gradients: Principle, Methodology and Some Applications. *J. Biochem. Biophys. Methods* **1982**, *6*, 317–339. [https://doi.org/10.1016/0165-022X\(82\)90013-6](https://doi.org/10.1016/0165-022X(82)90013-6).
- (54) Sommer, G. J.; Singh, A. K.; Hatch, A. V. On-Chip Isoelectric Focusing Using Photopolymerized Immobilized PH Gradients. *Anal. Chem.* **2008**, *80* (9), 3327–3333. <https://doi.org/10.1021/ac702523g>.
- (55) Raymond, S.; Weintraub, L. Acrylamide Gel as a Supporting Medium for Zone Electrophoresis. *Science (80-)*. **1959**, *130* (3377), 711. <https://doi.org/10.1126/science.130.3377.711>.
- (56) Ornstein, L. Disc Electrophoresis - I Background and Theory. *Ann. N. Y. Acad. Sci.* **1964**, *121* (2), 321–349. <https://doi.org/10.1111/j.1749-6632.1964.tb14207.x>.
- (57) Davis, B. J. Disc Electrophoresis - II Method and Application to Human Serum Proteins. *Ann. N. Y. Acad. Sci.* **1964**, *121* (2), 404–427. <https://doi.org/10.1111/j.1749-6632.1964.tb14213.x>.
- (58) Chung, M.; Kim, D.; Herr, A. E. Polymer Sieving Matrices in Microanalytical Electrophoresis. *Analyst* **2014**, *139* (22), 5635–5654.
- (59) Huynh, M.-L.; Russell, P.; Walsh, B. Tryptic Digestion of In-Gel Proteins for Mass Spectrometry Analysis. In *Two-dimensional Electrophoresis Protocols*; Tyther, R., Sheehan, D., Eds.; Humana Press, 2009; pp 507–513. https://doi.org/10.1007/978-1-59745-281-6_34.
- (60) Renart, J.; Reiser, J.; Stark, G. R. Transfer of Proteins from Gels to Diazobenzoyloxymethyl-Paper and Detection with Antisera: A Method for Studying Antibody Specificity and Antigen Structure. *Proc. Natl. Acad. Sci.* **1979**, *76* (7), 3116–3120. <https://doi.org/10.1073/pnas.76.7.3116>.
- (61) Towbin, H.; Staehelin, T.; Gordon, J. Electrophoretic Transfer of Proteins from Polyacrylamide Gels to Nitrocellulose Sheets: Procedure and Some Applications. *Proc. Natl. Acad. Sci.* **1979**, *76* (9), 4350–4354. <https://doi.org/10.1073/pnas.76.9.4350>.
- (62) Burnette, W. N. “Western Blotting”: Electrophoretic Transfer of Proteins from Sodium Dodecyl Sulfate-Polyacrylamide Gels to Unmodified Nitrocellulose and Radiographic Detection with Antibody and Radioiodinated Protein A. *Anal. Biochem.* **1981**, *112* (2), 195–203. [https://doi.org/https://doi.org/10.1016/0003-2697\(81\)90281-5](https://doi.org/https://doi.org/10.1016/0003-2697(81)90281-5).
- (63) Görg, A.; Postel, W.; Westermeier, R. Ultrathin-Layer Isoelectric Focusing in Polyacrylamide Gels

- on Cellophane. *Anal. Biochem.* **1978**, *89* (1), 60–70.
- (64) Frey, M. D.; Kinzkofer, A.; Bassim Atta, M.; Radola, B. J. Preparation of Rehydratable Polyacrylamide Gels and Their Application in Ultrathin-Layer Isoelectric Focusing. *Electrophoresis* **1986**, *7* (1), 28–40.
- (65) Fan, A. C.; Deb-basu, D.; Orban, M. W.; Gotlib, J. R.; Natkunam, Y.; O'Neill, R. A.; Padua, R.; Xu, L.; Taketa, D.; Shirer, A. E.; et al. Nanofluidic Proteomic Assay for Serial Analysis of Oncoprotein Activation in Clinical Specimens. *Nat. Med.* **2009**, *15* (5), 566–571. <https://doi.org/10.1038/nm.1903>.
- (66) Hughes, A. J.; Lin, R.; Peehl, D. M.; Herr, A. E. Microfluidic Integration for Automated Targeted Proteomic Assays. *PNAS* **2012**, *109* (16), 5972–5977.
- (67) Hughes, A. J.; Tentori, A. M.; Herr, A. E. Bistable Isoelectric Point Photoswitching in Green Fluorescent Proteins Observed by Dynamic Immunoprobed Isoelectric Focusing. *J. Am. Chem. Soc.* **2012**, *134*, 17582–17591.
- (68) Su, A.; Smith, B.; Herr, A. E. In Situ Measurement of Thermodynamic Partitioning in Open Hydrogels. *Anal. Chem.* **2019**. <https://doi.org/10.1021/acs.analchem.9b03582>.
- (69) Vlassakis, J. M.; Herr, A. E. Effect of Polymer Hydration State on In-Gel Immunoassays. *Anal. Chem.* **2015**, *87* (21), 11030–11038.
- (70) Righetti, P. G.; Caglio, S.; Saracchi, M.; Quaroni, S. Laterally Aggregated Polyacrylamide Gels for Electrophoresis. *Electrophoresis* **1992**, *13*, 587–595.
- (71) Holmes, D. L.; Stellwagen, N. C. Estimation of Polyacrylamide Gel Pore Size from Ferguson Plots of Linear DNA Fragments II. Comparison of Gels with Different Crosslinker Concentrations, Added Agarose and Added Linear Polyacrylamide. *Electrophoresis* **1991**, *12*, 612–619.
- (72) Lee, A. G.; Arena, C. P.; Beebe, D. J.; Palecek, S. P. Development of Macroporous Poly(Ethylene Glycol) Hydrogel Arrays within Microfluidic Channels. *Biomacromolecules* **2010**, *11* (12), 3316–3324.
- (73) Asnaghi, D.; Giglio, M.; Bossi, A.; Righetti, P. G. Large-Scale Microsegregation in Polyacrylamide Gels (Spinodal Gels). *J. Chem. Phys.* **1995**, *102* (24), 9736–9742.
- (74) Wensch, E.; de Besi, P.; Righetti, P. G. Conventional Isoelectric Focusing and Immobilized PH Gradients in “macroporous” Polyacrylamide Gels. *Electrophoresis* **1993**, *14*, 583–590.
- (75) Menter, P. *Acrylamide Polymerization - A Practical Approach. BioRad Technical Note 1156*.
- (76) Gelfi, C.; Righetti, P. G. Polymerization Kinetics of Polyacrylamide Gels I. Effect of Different Cross-linkers. *Electrophoresis* **1981**, *2* (4), 213–219.
- (77) Gehrke, S. H.; Fisher, J. P.; Palasis, M.; Lund, M. E. Factors Determining Hydrogel Permeability. *Ann. N. Y. Acad. Sci.* **1997**, 179–184.
- (78) Sperling, L. *Introduction to Physical Polymer Science*, 4th ed.; Wiley & Sons Inc: Hoboken, New Jersey, 2006.
- (79) Peters, A.; Candau, S. J. Kinetics of Swelling of Polyacrylamide Gels. *Macromolecules* **1986**, *19* (7), 1952–1955.
- (80) Flory, P. J.; Rehner, J. Statistical Mechanics of Cross-Linked Polymer Networks II Swelling. *J. Chem. Phys.* **1943**, *11* (11), 521–526.
- (81) Neira, H. D.; Herr, A. E. Kinetic Analysis of Enzymes Immobilized in Porous Film Arrays. *Anal. Chem.* **2017**, *89* (19), 10311–10320.
- (82) Gopal, A.; Herr, A. E. Multiplexed In-Gel Microfluidic Immunoassays: Characterizing Protein Target Loss during Reprobing of Benzophenone-Modified Hydrogels. *Sci. Rep.* **2019**, *9*, 15389. <https://doi.org/10.1038/s41598-019-51849-8>.
- (83) Lira, L. M.; Martins, K. A.; Cordoba de Torresi, S. I. Structural Parameters of Polyacrylamide Hydrogels Obtained by the Equilibrium Swelling Theory. *Eur. Polym. J.* **2009**, *45* (4), 1232–1238.
- (84) Rilbe, H. Historical and Theoretical Aspects of Isoelectric Focusing. *Ann. N. Y. Acad. Sci.* **1973**, *209* (1), 11–22.
- (85) Rilbe, H. Stable PH Gradients - a Key Problem in Isoelectric Focusing. In *Proceedings of the International Symposium*; Radola, B. J., Graesslin, D., Eds.; Walter de Gruyter, 1977; pp 35–50.
- (86) Gelfi, C.; Boss, M. L.; Righetti, P. G. Diffusion Coefficients of Proteins in Carrier Ampholytes versus Immobiline Gels. *J. Chromatogr.* **1987**, *390*, 225–236.
- (87) Guttman, A. Capillary Sodium Dodecyl Sulfate-Gel Electrophoresis of Proteins. *Electrophoresis* **1996**, *17*, 1333–1341.
- (88) Righetti, P. G.; Macelloni, C. New Polyacrylamide Matrices for Drift-Free Isoelectric Focusing. *J.*

- Biochem. Biophys. Methods* **1982**, 6 (1), 1–15.
- (89) Silvertand, L.; Torano, J. S.; van Bennekom, W.; de Jong, G. Recent Developments in Capillary Isoelectric Focusing. *J. Chromatogr. A* **2008**, 1204 (2), 157–170.
- (90) Dorman, G.; Nakamura, H.; Pulsipher, A.; Prestwich, G. D. The Life of Pi Star: Exploring the Exciting and Forbidden Worlds of the Benzophenone Photophore. *Chem. Rev.* **2016**, 116 (24), 15284–15398.
- (91) Royal Society of Chemistry. Benzophenone, CSID=2991 <http://www.chemspider.com/Chemical-Structure.2991.html> (accessed Jan 31, 2019).
- (92) Tong, J.; Anderson, J. L. Partitioning and Diffusion of Proteins and Linear Polymers in Polyacrylamide Gels. *Biophys. J.* **1996**, 70 (3), 1505–1513.
- (93) Liu, L.; Li, P.; Asher, S. A. Entropic Trapping of Macromolecules by Mesoscopic Periodic Voids in a Polymer Hydrogel. *Nature* **1999**, 397 (6715), 141–144.
- (94) Righetti, P. G.; Brost, B. C. W.; Snyder, R. S. On the Limiting Pore Size of Hydrophilic Gels for Electrophoresis and Isoelectric Focusing. *J. Biochem. Biophys. Methods* **1981**, 4 (5–6), 347–363.
- (95) Rüchel, R.; Steere, R. L.; Erbe, E. F. Transmission-Electron Microscopic Observations of Freeze-Etched Polyacrylamide Gels. *J. Chromatogr. A* **1978**, 166 (2), 563–575.
- (96) Denisin, A. K.; Pruitt, B. L. Tuning the Range of Polyacrylamide Gel Stiffness for Mechanobiology Applications. *ACS Appl. Mater. Interfaces* **2016**, 8 (34), 21893–21902.
- (97) Tong, H.; Zhang, L.; Kaspar, A.; Rames, M. J.; Huang, L.; Woodnutt, G.; Ren, G. Peptide-Conjugation Induced Conformational Changes in Human IgG1 Observed by Optimized Negative-Staining and Individual-Particle Electron Tomography. *Sci. Rep.* **2013**, 3, 1–9.
- (98) Armstrong, J.; Wenby, R.; Meiselman, H.; Fisher, T. The Hydrodynamic Radii of Macromolecules and Their Effect on Red Blood Cell Aggregation. *Biophys. J.* **2004**, 87 (6), 4259–4270.
- (99) Occhetta, P.; Sadr, N.; Piraino, F.; Redaelli, A.; Moretti, M.; Rasponi, M. Fabrication of 3D Cell-Laden Hydrogel Microstructures through Photo-Mold Patterning. *Biofabrication* **2013**, 5 (3), 35002. <https://doi.org/10.1088/1758-5082/5/3/035002>.
- (100) Wang, Z.; Jin, X.; Dai, R.; Holzman, J. F.; Kim, K. An Ultrafast Hydrogel Photocrosslinking Method for Direct Laser Bioprinting. *RSC Adv.* **2016**, 6 (25), 21099–21104. <https://doi.org/10.1039/C5RA24910D>.
- (101) Fairbanks, B. D.; Schwartz, M. P.; Bowman, C. N.; Anseth, K. S. Photoinitiated Polymerization of PEG-Diacrylate with Lithium Phenyl-2,4,6-Trimethylbenzoylphosphinate: Polymerization Rate and Cytocompatibility. *Biomaterials* **2009**, 30 (35), 6702–6707. <https://doi.org/10.1016/j.biomaterials.2009.08.055>.
- (102) Hughes, A. J.; Herr, A. E. Microfluidic Western Blotting. *PNAS* **2012**, 109 (52), 21450–21455.
- (103) Righetti, P. G.; Chiari, M.; Nesi, M.; Caglio, S. Towards New Formulations for Polyacrylamide Matrices, as Investigated by Capillary Zone Electrophoresis. *J. Chromatogr. A* **1993**, 638 (2), 165–178. [https://doi.org/10.1016/0021-9673\(93\)83425-R](https://doi.org/10.1016/0021-9673(93)83425-R).
- (104) Righetti, P. G. Macroporous Gels: Facts and Misfacts. *J. Chromatogr. A* **1995**, 698 (1–2), 3–17.
- (105) Giddings, J. C. *Unified Separation Science*; 1991. <https://doi.org/10.4103/0301-4738.58471>.
- (106) Ogston, A. G. The Spaces in a Uniform Random Suspension of Fibres. *Trans. Faraday Soc.* **1958**, 54 (0), 1754. <https://doi.org/10.1039/tf9585401754>.
- (107) Shekaran, A.; García, J. R.; Clark, A. Y.; Kavanaugh, T. E.; Lin, A. S.; Guldborg, R. E.; García, A. J. Bone Regeneration Using an Alpha 2 Beta 1 Integrin-Specific Hydrogel as a BMP-2 Delivery Vehicle. *Biomaterials* **2014**, 35 (21), 5453–5461. <https://doi.org/10.1016/j.biomaterials.2014.03.055>.
- (108) Boerckel, J. D.; Kolambkar, Y. M.; Dupont, K. M.; Uhrig, B. A.; Phelps, E. A.; Stevens, H. Y.; García, A. J.; Guldborg, R. E. Effects of Protein Dose and Delivery System on BMP-Mediated Bone Regeneration. *Biomaterials* **2011**, 32 (22), 5241–5251. <https://doi.org/10.1016/J.BIOMATERIALS.2011.03.063>.
- (109) Dembczynski, R.; Jankowski, T. Characterisation of Small Molecules Diffusion in Hydrogel-Membrane Liquid-Core Capsules. *Biochem. Eng. J.* **2000**, 6 (1), 41–44. [https://doi.org/10.1016/S1369-703X\(00\)00070-X](https://doi.org/10.1016/S1369-703X(00)00070-X).
- (110) Amsden, B. Solute Diffusion within Hydrogels. Mechanisms and Models. *Macromolecules* **1998**, 31 (23), 8382–8395. <https://doi.org/10.1021/MA980765F>.
- (111) Westrin, B. A.; Axelsson, A.; Zacchi, G. Diffusion Measurement in Gels. *J. Control. Release* **1994**, 30 (3), 189–199. [https://doi.org/10.1016/0168-3659\(94\)90025-6](https://doi.org/10.1016/0168-3659(94)90025-6).

- (112) Schulz, R.; Yamamoto, K.; Klossek, A.; Flesch, R.; Hönzke, S.; Rancan, F.; Vogt, A.; Blume-Peytavi, U.; Hedtrich, S.; Schäfer-Korting, M.; et al. Data-Based Modeling of Drug Penetration Relates Human Skin Barrier Function to the Interplay of Diffusivity and Free-Energy Profiles Designed the Model; *And. Proc. Natl. Acad. Sci.* **2017**, *114* (14), 3631–3636. <https://doi.org/10.1073/pnas.1620636114>.
- (113) Schwarzl, R.; Du, F.; Haag, R.; Netz, R. R. General Method for the Quantification of Drug Loading and Release Kinetics of Nanocarriers. *Eur. J. Pharm. Biopharm.* **2017**, *116*, 131–137. <https://doi.org/10.1016/J.EJPB.2016.12.015>.
- (114) Hettiaratchi, M. H.; Schudel, A.; Rouse, T.; García, A. J.; Thomas, S. N.; Guldberg, R. E.; McDevitt, T. C. A Rapid Method for Determining Protein Diffusion through Hydrogels for Regenerative Medicine Applications. *APL Bioeng.* **2018**, *2* (2), 026110. <https://doi.org/10.1063/1.4999925>.
- (115) Siepmann, J.; Rathbone, M. J.; Siegel, R. A. *Fundamentals and Applications of Controlled Release Drug Delivery*; New York, 2012. <https://doi.org/10.1007/978-1-4614-0881-9>.
- (116) Zhang, X.; Hansing, J.; Netz, R. R.; DeRouchey, J. E. Particle Transport through Hydrogels Is Charge Asymmetric. *Biophys. J.* **2015**, *108* (3), 530–539. <https://doi.org/10.1016/j.bpj.2014.12.009>.
- (117) Hansing, J.; Netz, R. R. Particle Trapping Mechanisms Are Different in Spatially Ordered and Disordered Interacting Gels. *Biophys. J.* **2018**, *114* (11), 2653–2664. <https://doi.org/10.1016/j.bpj.2018.04.041>.
- (118) Jang, S. S.; Goddard, W. A.; Kalani, M. Y. S. Mechanical and Transport Properties of the Poly(Ethylene Oxide)–Poly(Acrylic Acid) Double Network Hydrogel from Molecular Dynamic Simulations. *J. Phys. Chem. B* **2007**, *111* (7), 1729–1737. <https://doi.org/10.1021/jp0656330>.
- (119) Andrade, J. D.; King, R. N.; Gregonis, D. E. Probing the Hydrogel/Water Interface. In *Hydrogels for Medical and Related Applications*; 1976; pp 206–224. <https://doi.org/10.1021/bk-1976-0031.ch016>.
- (120) Larrea, X.; Büchler, P. A Transient Diffusion Model of the Cornea for the Assessment of Oxygen Diffusivity and Consumption. *Investig. Ophthalmology Vis. Sci.* **2009**, *50* (3), 1076. <https://doi.org/10.1167/iovs.08-2479>.
- (121) Orsborn, G. N.; Zantos, S. G. Corneal Desiccation Staining with Thin High Water Content Contact Lenses. *CLAO J.* **1988**, *14* (2), 81–85.
- (122) Nichols, J. J.; King-Smith, P. E. Thickness of the Pre- and Post-Contact Lens Tear Film Measured In Vivo by Interferometry. *Investig. Ophthalmology Vis. Sci.* **2003**, *44* (1), 68. <https://doi.org/10.1167/iovs.02-0377>.
- (123) Sapra, K. T.; Bayley, H. Lipid-Coated Hydrogel Shapes as Components of Electrical Circuits and Mechanical Devices. *Sci. Rep.* **2012**, *2* (1), 848. <https://doi.org/10.1038/srep00848>.
- (124) Nichols, J. J.; King-Smith, P. E. The Impact of Hydrogel Lens Settling on the Thickness of the Tears and Contact Lens. *Investig. Ophthalmology Vis. Sci.* **2004**, *45* (8), 2549. <https://doi.org/10.1167/iovs.04-0149>.
- (125) Klein, A. M.; Mazutis, L.; Akartuna, I.; Tallapragada, N.; Veres, A.; Li, V.; Peshkin, L.; Weitz, D. A.; Kirschner, M. W. Droplet Barcoding for Single-Cell Transcriptomics Applied to Embryonic Stem Cells. *Cell* **2015**, *161* (5), 1187–1201. <https://doi.org/10.1016/j.cell.2015.04.044>.
- (126) Rotem, A.; Ram, O.; Shores, N.; Sperling, R. A.; Goren, A.; Weitz, D. A.; Bernstein, B. E. Single-Cell ChIP-Seq Reveals Cell Subpopulations Defined by Chromatin State. *Nat. Biotechnol.* **2015**, *33* (11), 1165–1172. <https://doi.org/10.1038/nbt.3383>.
- (127) Love, J. C.; Ronan, J. L.; Grotenbreg, G. M.; van der Veen, A. G.; Ploegh, H. L. A Microengraving Method for Rapid Selection of Single Cells Producing Antigen-Specific Antibodies. *Nat. Biotechnol.* **2006**, *24* (6), 703–707. <https://doi.org/10.1038/nbt1210>.
- (128) Gierahn, T. M.; Wadsworth, M. H.; Hughes, T. K.; Bryson, B. D.; Butler, A.; Satija, R.; Fortune, S.; Love, J. C.; Shalek, A. K. Seq-Well: Portable, Low-Cost RNA Sequencing of Single Cells at High Throughput. *Nat. Methods* **2017**, *14* (4), 395–398. <https://doi.org/10.1038/nmeth.4179>.
- (129) Lu, Y.; Chen, J. J.; Mu, L.; Xue, Q.; Wu, Y.; Wu, P.-H.; Li, J.; Vortmeyer, A. O.; Miller-Jensen, K.; Wirtz, D.; et al. High-Throughput Secretomic Analysis of Single Cells to Assess Functional Cellular Heterogeneity. *Anal. Chem.* **2013**, *85* (4), 2548–2556. <https://doi.org/10.1021/ac400082e>.
- (130) Torres, A. J.; Hill, A. S.; Love, J. C. Nanowell-Based Immunoassays for Measuring Single-Cell Secretion: Characterization of Transport and Surface Binding. *Anal. Chem.* **2014**, *86* (23), 11562–

11569. <https://doi.org/10.1021/ac4030297>.
- (131) Song, Q.; Han, Q.; Bradshaw, E. M.; Kent, S. C.; Raddassi, K.; Nilsson, B.; Nepom, G. T.; Hafler, D. A.; Love, J. C. On-Chip Activation and Subsequent Detection of Individual Antigen-Specific T Cells. *Anal. Chem.* **2010**, *82* (2), 473–477. <https://doi.org/10.1021/ac9024363>.
- (132) Zhu, H.; Stybayeva, G.; Macal, M.; Ramanculov, E.; George, M. D.; Dandekar, S.; Revzin, A. A Microdevice for Multiplexed Detection of T-Cell-Secreted Cytokines. *Lab Chip* **2008**, *8* (12), 2197. <https://doi.org/10.1039/b810244a>.
- (133) Shi, Q.; Qin, L.; Wei, W.; Geng, F.; Fan, R.; Shin, Y. S.; Guo, D.; Hood, L.; Mischel, P. S.; Heath, J. R. Single-Cell Proteomic Chip for Profiling Intracellular Signaling Pathways in Single Tumor Cells. *Proc. Natl. Acad. Sci. U. S. A.* **2012**, *109* (2), 419–424. <https://doi.org/10.1073/pnas.1110865109>.
- (134) Kang, C.-C.; Lin, J.-M. G.; Xu, Z.; Kumar, S.; Herr, A. E. Single-Cell Western Blotting after Whole-Cell Imaging to Assess Cancer Chemotherapeutic Response. *Anal. Chem.* **2014**, *86*, 10429–10436.
- (135) Vlassakis, J.; Herr, A. E. Joule Heating-Induced Dispersion in Open Microfluidic Electrophoretic Cytometry. *Anal. Chem.* **2017**, *89* (23), 12787–12796. <https://doi.org/10.1021/acs.analchem.7b03096>.
- (136) Duncombe, T. A.; Herr, A. E. Photopatterned Free-Standing Polyacrylamide Gels for Microfluidic Protein Electrophoresis. *Lab Chip* **2013**, *13* (11), 2115–2123. <https://doi.org/10.1039/c3lc50269d>.
- (137) Kuypers, L. C.; Decraemer, W. F.; Dirckx, J. J.; Timmermans, J.-P. A Procedure to Determine the Correct Thickness of an Object with Confocal Microscopy in Case of Refractive Index Mismatch. *J. Microsc.* **2005**, *218*, 68–78.
- (138) McClure, G.; Jin, Z. M.; Fisher, J.; Tighe, B. J. Determination of Lubricating Film Thickness for Permeable Hydrogel and Non-Permeable Polyurethane Layers Bonded to a Rigid Substrate with Articular Reference to Cushion Form Hip Joint Replacements. *Proc. Inst. Mech. Eng. Part H J. Eng. Med.* **1996**, *210* (2), 89–93. https://doi.org/10.1243/PIME_PROC_1996_210_397_02.
- (139) Engler, A. J.; Sen, S.; Sweeney, H. L.; Discher, D. E. Matrix Elasticity Directs Stem Cell Lineage Specification. *Cell* **2006**, *126* (4), 677–689. <https://doi.org/10.1016/j.cell.2006.06.044>.
- (140) Ting, L. L. Engagement Behavior of Lubricated Porous Annular Disks. Part I: Squeeze Film Phase — Surface Roughness and Elastic Deformation Effects. *Wear* **1975**, *34* (2), 159–172. [https://doi.org/10.1016/0043-1648\(75\)90062-9](https://doi.org/10.1016/0043-1648(75)90062-9).
- (141) Bujurke, N. M.; Patil, H. P. The Effects of Variable Permeability and Roughness of Porous Bearings. *Int. J. Mech. Sci.* **1992**, *34* (5), 355–362. [https://doi.org/10.1016/0020-7403\(92\)90023-A](https://doi.org/10.1016/0020-7403(92)90023-A).
- (142) Cevc, G. Partition Coefficient vs. Binding Constant: How Best to Assess Molecular Lipophilicity. *Eur. J. Pharm. Biopharm.* **2015**, *92*, 204–215. <https://doi.org/10.1016/J.EJPB.2015.03.008>.
- (143) Kim, J. J.; Chan, P. P. Y.; Vlassakis, J.; Geldert, A.; Herr, A. E. Microparticle Delivery of Protein Markers for Single-Cell Western Blotting from Microwells. *Small* **2018**, 1802865. <https://doi.org/10.1002/smll.201802865>.
- (144) Voit, B.; Braun, F.; Gernert, M.; Sieczkowska, B.; Millaruelo, M.; Messerschmidt, M.; Mertig, M.; Opitz, J. Photolabile and Thermally Labile Polymers as Templates and for Surface Patterning. *Polym. Adv. Technol.* **2006**, *17* (9–10), 691–693.
- (145) Braun, F.; Eng, L.; Trogisch, S.; Voit, B. Novel Labile Protected Amine Terpolymers for the Preparation of Patterned Functionalized Surfaces: Synthesis and Characterization. *Macromol. Chem. Phys.* **2003**, *204* (12), 1486–1496. <https://doi.org/10.1002/macp.200350015>.
- (146) Braun, F.; Eng, L.; Loppacher, C.; Trogisch, S.; Voit, B. Novel Diazosulfonate Terpolymers for the Preparation of Structured Functionalized Surfaces: Synthesis and Characterization. *Macromol. Chem. Phys.* **2002**, *203* (12), 1781–1789.
- (147) Wu, Y.; Zhang, L.; Zhang, M.; Liu, Z.; Zhu, W.; Zhang, K. Bottlebrush Polymers with Self-Immolative Side Chains. *Polym. Chem.* **2018**, *9* (14), 1799–1806. <https://doi.org/10.1039/C8PY00182K>.
- (148) De Alwis Watuthantrige, N.; Kurek, P. N.; Konkolewicz, D. Photolabile Protecting Groups: A Strategy for Making Primary Amine Polymers by RAFT. *Polym. Chem.* **2018**, *9* (13), 1557–1561. <https://doi.org/10.1039/C7PY01398A>.
- (149) Shi, D.; Matsusaki, M.; Akashi, M. Photo-Tunable Protein Release from Biodegradable Nanoparticles Composed of Cinnamic Acid Derivatives. *J. Control. Release* **2011**, *149* (2), 182–189. <https://doi.org/10.1016/J.JCONREL.2010.08.009>.

- (150) Jin, Q.; Mitschang, F.; Agarwal, S. Biocompatible Drug Delivery System for Photo-Triggered Controlled Release of 5-Fluorouracil. *Biomacromolecules* **2011**, *12* (10), 3684–3691. <https://doi.org/10.1021/bm2009125>.
- (151) Schuster, B. S.; Allan, D. B.; Kays, J. C.; Hanes, J.; Leheny, R. L. Photoactivatable Fluorescent Probes Reveal Heterogeneous Nanoparticle Permeation through Biological Gels at Multiple Scales. *J. Control. Release* **2017**, *260*, 124–133. <https://doi.org/10.1016/J.JCONREL.2017.05.035>.
- (152) Kabanov, A. V.; Vinogradov, S. V. Nanogels as Pharmaceutical Carriers: Finite Networks of Infinite Capabilities. *Angew. Chemie Int. Ed.* **2009**, *48* (30), 5418–5429. <https://doi.org/10.1002/anie.200900441>.
- (153) Yuan, X.; Fischer, K.; Schä, W. Photocleavable Microcapsules Built from Photoreactive Nanospheres. *Langmuir* **2005**. <https://doi.org/10.1021/la051491+>.
- (154) Jiang, J.; Tong, X.; Morris, D.; Zhao, Y. Toward Photocontrolled Release Using Light-Dissociable Block Copolymer Micelles. *Macromolecules* **2006**, *39* (13), 4633–4640. <https://doi.org/10.1021/ma060142z>.
- (155) Swati R. Mujumdar; Ratnakar B. Mujumdar; Charsetta M. Grant, A.; Waggoner, A. S. Cyanine-Labeling Reagents: Sulfobenzindocyanine Succinimidyl Esters. *Bioconjug. Chem.* **1996**, *7* (3), 356–362. <https://doi.org/10.1021/BC960021B>.
- (156) Seu, K. J.; Pandey, A. P.; Haque, F.; Proctor, E. A.; Ribbe, A. E.; Hovis, J. S. Effect of Surface Treatment on Diffusion and Domain Formation in Supported Lipid Bilayers. *Biophys. J.* **2007**, *92* (7), 2445–2450. <https://doi.org/10.1529/biophysj.106.099721>.
- (157) Dunn, A. C.; Sawyer, W. G.; Angelini, T. E. Gemini Interfaces in Aqueous Lubrication with Hydrogels. *Tribol. Lett.* **2014**, *54* (1), 59–66. <https://doi.org/10.1007/s11249-014-0308-1>.
- (158) Tse, J. R.; Engler, A. J. Preparation of Hydrogel Substrates with Tunable Mechanical Properties. *Curr. Protoc. Cell Biol.* **2010**, *47* (1), 10.16.1-10.16.16. <https://doi.org/10.1002/0471143030.cb1016s47>.
- (159) Fu, Y.; Kao, W. J. Drug Release Kinetics and Transport Mechanisms from Semi-Interpenetrating Networks of Gelatin and Poly(Ethylene Glycol) Diacrylate. *Pharm. Res.* **2009**, *26* (9), 2115–2124. <https://doi.org/10.1007/s11095-009-9923-1>.
- (160) Vogel, C.; de Sousa Abreu, R.; Ko, D.; Le, S.-Y.; Shapiro, B. A.; Burns, S. C.; Sandhu, D.; Boutz, D. R.; Marcotte, E. M.; Penalva, L. O. Sequence Signatures and mRNA Concentration Can Explain Two-Thirds of Protein Abundance Variation in a Human Cell Line. *Mol. Syst. Biol.* **2010**, *6* (1), 400. <https://doi.org/10.1038/msb.2010.59>.
- (161) Ward, A.; Balwierz, A.; Zhang, J. D.; Küblbeck, M.; Pawitan, Y.; Hielscher, T.; Wiemann, S.; Sahin, Ö. Re-Expression of MicroRNA-375 Reverses Both Tamoxifen Resistance and Accompanying EMT-like Properties in Breast Cancer. *Oncogene* **2013**, *32* (9), 1173–1182. <https://doi.org/10.1038/onc.2012.128>.
- (162) Inoue, K.; Fry, E. A. Aberrant Splicing of Estrogen Receptor, HER2, and CD44 Genes in Breast Cancer. *Genet. Epigenet.* **2015**, *7*, GEG.S35500. <https://doi.org/10.4137/GEG.S35500>.
- (163) UniProt Consortium. UniprotKB - P04626 ERBB2\HUMAN.
- (164) Pedersen, K.; Angelini, P.-D.; Laos, S.; Bach-Faig, A.; Cunningham, M. P.; Ferrer-Ramón, C.; Luque-García, A.; García-Castillo, J.; Parra-Palau, J. L.; Scaltriti, M.; et al. A Naturally Occurring HER2 Carboxy-Terminal Fragment Promotes Mammary Tumor Growth and Metastasis. *Mol. Cell. Biol.* **2009**, *29* (12), 3319–3331. <https://doi.org/10.1128/MCB.01803-08>.
- (165) Sasso, M.; Bianchi, F.; Ciravolo, V.; Tagliabue, E.; Campiglio, M. HER2 Splice Variants and Their Relevance in Breast Cancer. *J. Nucleic Acids Investig.* **2011**, *2* (1), e9. <https://doi.org/10.4081/jnai.2011.2454>.
- (166) Grist, S. M.; Mourdoukoutas, A. P.; Herr, A. E. 3D Projection Electrophoresis for Single-Cell Immunoblotting. *bioRxiv* **2019**, 805770. <https://doi.org/10.1101/805770>.
- (167) Hu, R.-M.; Chiang, K.-H.; Chang, Y.-C.; Yang, T.-C. Characterization of the Charge Variants of L2 β -Lactamase in *Stenotrophomonas Maltophilia*. *J. Med. Microbiol.* **2009**, *58* (3), 318–321. <https://doi.org/https://doi.org/10.1099/jmm.0.000380-0>.
- (168) Life Technologies. Safety Data Sheet: Rhinohide Polyacrylamide Gel Strengthener Concentrate. R33400. 2019, pp 1–7.
- (169) Schulenberg, B.; Arnold, B.; Patton, W. F. An Improved Mechanically Durable Electrophoresis Gel Matrix That Is Fully Compatible with Fluorescence-Based Protein Detection Technologies. *Proteomics* **2003**, *3* (7), 1196–1205. <https://doi.org/10.1002/pmic.200300440>.

- (170) Updyke, T.; Beardslee, T. US 9,057,694 B2. Compositions And Methods For Improving Resolution Of Biomolecules Separated On Polyacrylamide Gels., 2015.
- (171) Westermeier, R. *Electrophoresis in Practice: A Guide to Methods and Applications of DNA and Protein Separations*; John Wiley & Sons, Ltd, 2016.
- (172) Lonza. Safety Data Sheet: GelSlick Solution. Ref. 49611.4 / 000000012961. 2019, pp 1–14.
- (173) Correia, J. J.; Welch, M. K.; Williams, R. C. Evidence for the Spontaneous Formation of Disulfide Crosslinked Aggregates of Tubulin during Nondenaturing Electrophoresis. *Arch. Biochem. Biophys.* **1987**, *255* (2), 244–253. [https://doi.org/https://doi.org/10.1016/0003-9861\(87\)90391-2](https://doi.org/https://doi.org/10.1016/0003-9861(87)90391-2).
- (174) Duncombe, T. A.; Kang, C. C.; Maity, S.; Ward, T. M.; Pegram, M. D.; Murthy, N.; Herr, A. E. Hydrogel Pore-Size Modulation for Enhanced Single-Cell Western Blotting. *Adv. Mater.* **2016**, *28* (2), 327–334. <https://doi.org/10.1002/adma.201503939>.
- (175) Vlassakis, J. M. Integrated Electrophoretic Cytometry Separations and Immunoassays for Proteins and Their Complexes, University of California, Berkeley, and University of California, San Francisco, 2018.
- (176) Yang, S. X.; Costantino, J. P.; Kim, C.; Mamounas, E. P.; Nguyen, D.; Jeong, J. H.; Wolmark, N.; Kidwell, K.; Paik, S.; Swain, S. M. Akt Phosphorylation at Ser473 Predicts Benefit of Paclitaxel Chemotherapy in Node-Positive Breast Cancer. *J. Clin. Oncol.* **2010**, *28* (18), 2974–2981. <https://doi.org/10.1200/JCO.2009.26.1602>.
- (177) Umemura, S.; Yoshida, S.; Ohta, Y.; Naito, K.; Osamura, R. Y.; Tokuda, Y. Increased Phosphorylation of Akt in Triple-Negative Breast Cancers. *Cancer Sci.* **2007**, *98* (12), 1889–1892. <https://doi.org/10.1111/j.1349-7006.2007.00622.x>.
- (178) Yang, Z.-Y.; Di, M.-Y.; Yuan, J.-Q.; Shen, W.-X.; Zheng, D.-Y.; Chen, J.-Z.; Mao, C.; Tang, J.-L. The Prognostic Value of Phosphorylated Akt in Breast Cancer: A Systematic Review. *Sci. Rep.* **2015**, *5*, 7758. <https://doi.org/10.1038/srep07758>.
- (179) Filippi, S.; Barnes, C. P.; Kirk, P. D. W. W.; Kudo, T.; Kunida, K.; McMahon, S. S.; Tsuchiya, T.; Wada, T.; Kuroda, S.; Stumpf, M. P. H. H. Robustness of MEK-ERK Dynamics and Origins of Cell-to-Cell Variability in MAPK Signaling. *Cell Rep.* **2016**, *15* (11), 2524–2535. <https://doi.org/10.1016/j.celrep.2016.05.024>.
- (180) Cell Signalling Technology. PhosphoSite: Akt1 <https://www.phosphosite.org/proteinAction?id=570>.
- (181) Zhu, K.; Zhao, J.; Lubman, D. M.; Miller, F. R.; Barder, T. J. Protein PI Shifts Due to Posttranslational Modifications in the Separation and Characterization of Proteins. *Anal. Chem.* **2005**, *77* (9), 2745–2755.
- (182) Gasteiger, E.; Gattiker, A.; Hoogland, C.; Ivanyi, I.; Appel, R. D.; Bairoch, A. ExpASY: The Proteomics Server for in-Depth Protein Knowledge and Analysis. *Nucleic Acids Res.* **2003**, *31* (13), 3784–3788. <https://doi.org/10.1093/nar/gkg563>.
- (183) Mikos, A. G.; Herring, S. W.; Ochareon, P.; Elisseeff, J.; Lu, H. H.; Kandel, R.; Schoen, F. J.; Toner, M.; Mooney, D.; Atala, A.; et al. Engineering Complex Tissues. *Tissue Eng.* **2006**, *12* (12), 3007–3039.
- (184) Berthiaume, F.; Maguire, T. J.; Yarmush, M. L. Tissue Engineering and Regenerative Medicine: History, Progress, and Challenges. *Annu. Rev. Chem. Biomol. Eng.* **2011**, *2*, 403–430.
- (185) Scannell, J. W.; Blanckley, A.; Boldon, H.; Warrington, B. Diagnosing the Decline in Pharmaceutical R&D Efficiency. *Nat. Rev. Drug Discov.* **2012**, *11* (3), 191–200.
- (186) Marx, U.; Sandig, V. *Drug Testing In Vitro: Breakthroughs and Trends in Cell Culture Technology*; Wiley-VCH: Weinheim, 2007.
- (187) Baker, M. A Living System on a Chip. *Nature* **2011**, *471*, 661–665.
- (188) Huh, D.; Torisawa, Y.; Hamilton, G. A.; Kim, H. J.; Ingber, D. E. Microengineered Physiological Biomimicry: Organs-on-Chips. *Lab Chip* **2012**, No. 12, 2156–2164.
- (189) Mathur, A.; Loskill, P.; Hong, S.; Lee, J.; Marcus, S. G.; Dumont, L.; Conklin, B. R.; Willenbring, H.; Lee, L. P.; Healy, K. E. Human Induced Pluripotent Stem Cell-Based Microphysiological Tissue Models of Myocardium and Liver for Drug Development. *Stem Cell Res. Ther.* **2013**, *4*, S14.
- (190) Bhatia, S. N.; Ingber, D. E. Microfluidic Organs-on-Chips. *Nat. Biotechnol.* **2014**, *32* (8), 760–772.
- (191) Huh, D.; Matthews, B. D.; Mammoto, A.; Montoya-zavala, M.; Hsin, H. Y.; Ingber, D. E. Reconstituting Organ-Level Lung Functions on a Chip. *Science (80-.)*. **2010**, *328* (5986), 1662–1668.
- (192) Lee, P. J.; Hung, P. J.; Lee, L. P. An Artificial Liver Sinusoid with a Microfluidic Endothelial-like Barrier for Primary Hepatocyte Culture. *Biotechnol. Bioeng.* **2007**, *97* (5), 1340–1346.

- (193) Jang, K.-J.; Suh, K.-Y. A Multi-Layer Microfluidic Device for Efficient Culture and Analysis of Renal Tubular Cells. *Lab Chip* **2010**, *10*, 36–42.
- (194) Hsu, Y.; Moya, M. L.; Hughes, C. C. W.; George, S. C.; Lee, A. P. A Microfluidic Platform for Generating Large-Scale Nearly Identical Human Microphysiological Vascularized Tissue Arrays. *Lab Chip* **2013**, *13* (15), 2990–2998.
- (195) Tanzi, M. C.; Fare, S. Adipose Tissue Engineering: State of the Art, Recent Advances and Innovative Approaches. *Expert Rev. Med. Devices* **2009**, No. 5, 533–551.
- (196) Young, B.; Woodford, P.; O'Dowd, G. *Wheater's Functional Histology*; Elsevier Health Sciences, 2013.
- (197) Trayhurn, P.; Beattie, J. H. Physiological Role of Adipose Tissue: White Adipose Tissue as an Endocrine and Secretory Organ. *Proc. Nutr. Soc.* **2001**, *60* (3), 329–339.
- (198) Scherer, P. Adipose Tissue: From Lipid Storage Compartment to Endocrine Organ. *Diabetes* **2006**, *55* (6), 1537–1545.
- (199) Kim, S.; Moutsaid-Moussa, N. Secretory, Endocrine and Autocrine/Paracrine Function of the Adipocyte. *J. Nutr.* **2000**, *130* (12), 3110S–3115S.
- (200) Shehzad, A.; Iqbal, W.; Shehzad, O.; Lee, Y. S. Adiponectin: Regulation of Its Production and Its Role in Human Diseases. *Hormones* **2012**, *11* (1), 8–20.
- (201) Tilg, H.; Moschen, A. R. Adipocytokines: Mediators Linking Adipose Tissue, Inflammation and Immunity. *Nat. Rev. Immunol.* **2006**, *6*, 772–783.
- (202) Rega-Kaun, G.; Kaun, C.; Wojta, J. More than a Simple Storage Organ: Adipose Tissue as a Source of Adipokines Involved in Cardiovascular Disease. *Thromb. Haemost.* **2013**, *110* (04), 641–650.
- (203) Bluher, M.; Mantzoros, C. S. From Leptin to Other Adipokines in Health and Disease: Facts and Expectations at the Beginning of the 21st Century. *Metabolism*. **2015**, *64* (1), 131–145.
- (204) Buechler, C.; Wanninger, J.; Neumeier, M. Adiponectin, a Key Adipokine in Obesity Related Liver Diseases. *World J. Gastroenterol.* **2011**, *17* (23), 2801–2811.
- (205) Han, S. H.; Quon, M. J.; Kim, J.; Koh, K. K. Adiponectin and Cardiovascular Disease: Response to Therapeutic Interventions. *J. Am. Coll. Cardiol.* **2007**, *49* (5), 531–538.
- (206) Jia, T.; Carrero, J. J.; Lindholm, B.; Stenvinkel, P. The Complex Role of Adiponectin in Chronic Kidney Disease. *Biochimie* **2012**, *94* (10), 2150–2156.
- (207) Nawrocki, A. R.; Scherer, P. Keynote Review: The Adipocyte as a Drug Discovery Target. *Drug Discov. Today* **2005**, *10* (18), 1219–1230.
- (208) Ogden, C. L.; Carroll, M. D.; Kit, B. K.; Flegal, K. M. Prevalence of Obesity in the United States, 2009–2010. *NCHS Data Brief* **2012**, *82*, 108.
- (209) Lafuente-Lafuente, C.; Alvarez, J.-C.; Leenhardt, A.; Mouly, S.; Extramiana, F.; Caulin, C.; Funck-Bretano, C.; Bergmann, J.-F. Amiodarone Concentrations in Plasma and Fat Tissue during Chronic Treatment and Related Toxicity. *Br. J. Clin. Pharmacol.* **2009**, *67* (5), 511–519.
- (210) Poulin, P.; Schoenlein, K.; Theil, F.-P. Prediction of Adipose Tissue: Plasma Partition Coefficients for Structurally Unrelated Drugs. *J. Pharm. Sci.* **2000**, *90* (4), 436–447.
- (211) Choi, J. H.; Gimble, J. M.; Lee, K.; Marra, K. G.; Rubin, J. P.; Yoo, J. J.; Vunjak-Novakovic, G.; Kaplan, D. L. Adipose Tissue Engineering for Soft Tissue Regeneration. *Tissue Eng. Part B Rev.* **2010**, *16* (4), 413–426.
- (212) Yao, R.; Du, Y.; Zhang, R.; Lin, F.; Luan, J. A Biomimetic Physiological Model for Human Adipose Tissue by Adipocytes and Endothelial Cell Cocultures with Spatially Controlled Distribution. *Biomed. Mater.* **2013**, *8* (4).
- (213) Mauney, J. R.; Nguyen, T.; Gillen, K.; Kirker-Head, C.; Gimble, J. M.; Kaplan, D. L. Engineering Adipose-like Tissue in Vitro and in Vivo Utilizing Human Bone Marrow and Adipose-Derived Mesenchymal Stem Cells with Silk Fibroin 3D Scaffolds. *Biomaterials* **2007**, *28* (35), 5280–5290.
- (214) Wiggerhauser, P. S.; Muller, D. F.; Melchels, F. P. W.; Egana, J. T.; Storck, K.; Mayer, H.; Leuthner, P.; Skodacek, D.; Hopfner, U.; Machens, H. G.; et al. Engineering of Vascularized Adipose Constructs. *Cell Tissue Res.* **2012**, *347* (3), 747–757.
- (215) Wang, L.; Johnson, J. A.; Zhang, Q.; Beahm, E. K. Combining Decellularized Human Adipose Tissue Extracellular Matrix and Adipose-Derived Stem Cells for Adipose Tissue Engineering. *Acta Biomater.* **2013**, *9* (11), 8921–8931.
- (216) Tharp, K. M.; Jha, A. K.; Kraiczky, J.; Yesian, A.; Karateev, G.; Sinisi, R.; Dubikovskaya, E.; Healy, K. E.; Stahl, A. Matrix-Assisted Transplantation of Functional Beige Adipose Tissue. *Diabetes*

- 2015**, 64 (11), 3713–3724.
- (217) Frye, C. A.; Patrick Jr, C. W. Three-Dimensional Adipose Tissue Model Using Low Shear Bioreactors. *Vitr. Cell. Dev. Biol. - Anim.* **2006**, 42 (5–6), 109–114.
- (218) Guzzardi, M. A.; Domenici, C.; Ahluwalia, A. Metabolic Control Through Hepatocyte and Adipose Tissue Cross-Talk in a Multicompartmental Modular Bioreactor. *Tissue Eng. Part A* **2011**, 17 (11–12), 1635–1642.
- (219) Godwin, L. A.; Brooks, J. C.; Hoepfner, L. D.; Wanders, W.; Judd, R. L.; Easley, C. J. A Microfluidic Interface for the Culture and Sampling of Adiponectin from Primary Adipocytes. *Analyst* **2015**, 140 (4), 1019–1025.
- (220) Viravaidya, K.; Shuler, M. L. Incorporation of 3T3-L1 Cells To Mimic Bioaccumulation in a Microscale Cell Culture Analog Device for Toxicity Studies. *Biotechnol. Prog.* **2008**, 20 (2), 590–597.
- (221) Clark, A. K.; Sousa, K. M.; Chisolm, C. N.; MacDougald, O. A.; Kennedy, R. T. Reversibly Sealed Multilayer Microfluidic Device for Integrated Cell Perfusion and On-Line Chemical Analysis of Cultured Adipocyte Secretions. *Anal. Bioanal. Chem.* **2010**, 397 (7), 2939–2947.
- (222) Dugan, C. E.; Kennedy, R. T. Measurement of Lipolysis Products Secreted by 3T3-L1 Adipocytes Using Microfluidics. *Methods Enzymol.* **2014**, 538, 195–209.
- (223) Chung, H. H.; Chan, C. K.; Khire, T. S.; Marsh, G. A.; Clark, A.; Waugh, R. E.; McGrath, J. L. Highly Permeable Silicon Membranes for Shear Free Chemotaxis and Rapid Cell Labeling. *Lab Chip* **2014**, 14 (14), 2456–2468. <https://doi.org/10.1039/C4LC00326H>.
- (224) Dagan, Z.; Weinbaum, S.; Pfeffer, R. Theory and Experiment on the Three-Dimensional Motion of a Freely Suspended Spherical Particle at the Entrance to a Pore at Low Reynolds Number. *Chem. Eng. Sci.* **1983**, 38 (4), 583–596. [https://doi.org/https://doi.org/10.1016/0009-2509\(83\)80118-3](https://doi.org/https://doi.org/10.1016/0009-2509(83)80118-3).
- (225) Hazel, J. R.; Sidell, B. D. A Method for the Determination of Diffusion Coefficients for Small Molecules in Aqueous Solution. *Anal. Biochem.* **1987**, 166 (2), 335–341. [https://doi.org/https://doi.org/10.1016/0003-2697\(87\)90582-3](https://doi.org/https://doi.org/10.1016/0003-2697(87)90582-3).
- (226) Liao, J.; Sportsman, R.; Harris, J.; Stahl, A. Real-Time Quantification of Fatty Acid Uptake Using a Novel Fluorescence Assay. *J. Lipid Res.* **2005**, 46 (3), 597–602. <https://doi.org/10.1194/jlr.D400023-JLR200>.
- (227) Patrick Jr, C. W. Adipose Tissue Engineering: The Future of Breast and Soft Tissue Reconstruction Following Tumor Resection. *Semin. Surg. Oncol.* **2000**, 19 (3), 302–311.
- (228) Loskill, P.; Marcus, S. G.; Mathur, A.; Reese, W. M.; Healy, K. E. MORGANO: A Lego®-Like Plug & Play System for Modular Multi-Organ-Chips. *PLoS One* **2015**, 10 (10), e0139587. <https://doi.org/10.1371/journal.pone.0139587>.
- (229) Sip, C. G.; Folch, A. Stable Chemical Bonding of Porous Membranes and Poly(Dimethylsiloxane) Devices for Long-Term Cell Culture. *Biomicrofluidics* **2014**, 8 (3), 36504. <https://doi.org/10.1063/1.4883075>.
- (230) Anderson, C. M.; Stahl, A. SLC27 Fatty Acid Transport Proteins. *Mol. Aspects Med.* **2013**, 34 (2), 516–528. <https://doi.org/https://doi.org/10.1016/j.mam.2012.07.010>.
- (231) Herper, M. The Cost Of Creating A New Drug Now \$5 Billion, Pushing Big Pharma To Change. *Forbes*. August 2013, pp 6–11.
- (232) Ferri, N.; Siegl, P.; Corsini, A.; Herrmann, J.; Lerman, A.; Benghozi, R. Drug Attrition during Pre-Clinical and Clinical Development: Understanding and Managing Drug-Induced Cardiotoxicity. *Pharmacol. Ther.* **2013**, 138 (3), 470–484. <https://doi.org/10.1016/j.pharmthera.2013.03.005>.
- (233) Go, A. S.; Mozaffarian, D.; Roger, V. L.; Benjamin, E. J.; Berry, J. D.; Blaha, M. J.; Dai, S.; Ford, E. S.; Fox, C. S.; Franco, S.; et al. Heart Disease and Stroke Statistics — 2014 Update. *Circulation* **2014**, 129 (3), 1–268. <https://doi.org/10.1161/01.cir.0000441139.02102.80>.
- (234) Passier, R.; van Laake, L. W.; Mummery, C. L. Stem-Cell-Based Therapy and Lessons from the Heart. *Nature* **2008**, 453 (7193), 322–329. <https://doi.org/10.1038/nature07040>.
- (235) Bouten, C. V. C.; Dankers, P. Y. W.; Driessen-Mol, A.; Pedron, S.; Brizard, A. M. A.; Baaijens, F. P. T. Substrates for Cardiovascular Tissue Engineering. *Adv. Drug Deliv. Rev.* **2011**, 63 (4), 221–241. <https://doi.org/https://doi.org/10.1016/j.addr.2011.01.007>.
- (236) Hirt, M. N.; Hansen, A.; Eschenhagen, T. Cardiac Tissue Engineering. *Circ. Res.* **2014**, 114 (2), 354–367. <https://doi.org/10.1161/CIRCRESAHA.114.300522>.
- (237) Zhao, Y.; Feric, N. T.; Thavandiran, N.; Nunes, S. S.; Radisic, M. The Role of Tissue Engineering and Biomaterials in Cardiac Regenerative Medicine. *Can. J. Cardiol.* **2014**, 30 (11), 1307–1322.

- <https://doi.org/https://doi.org/10.1016/j.cjca.2014.08.027>.
- (238) Parker, K. K.; Ingber, D. E. Extracellular Matrix, Mechanotransduction and Structural Hierarchies in Heart Tissue Engineering. *Philos. Trans. R. Soc. Lond. B. Biol. Sci.* **2007**, *362* (1484), 1267–1279. <https://doi.org/10.1098/rstb.2007.2114>.
- (239) Robinson, T. F.; Geraci, M. A.; Sonnenblick, E. H.; Factor, S. M. Coiled Perimysial Fibers of Papillary Muscle in Rat Heart: Morphology, Distribution, and Changes in Configuration. *Circ. Res.* **1988**, *63* (3), 577–592. <https://doi.org/10.1161/01.RES.63.3.577>.
- (240) Kanzaki, Y.; Terasaki, F.; Okabe, M.; Fujita, S.; Katashima, T.; Otsuka, K.; Ishizaka, N. Three-Dimensional Architecture of Cardiomyocytes and Connective Tissue in Human Heart Revealed by Scanning Electron Microscopy. *Circulation* **2010**, *122* (19), 1973–1974. <https://doi.org/10.1161/CIRCULATIONAHA.110.979815>.
- (241) MacKenna, D. A.; Vaplon, S. M.; McCulloch, A. D. Microstructural Model of Perimysial Collagen Fibers for Resting Myocardial Mechanics during Ventricular Filling. *Am. J. Physiol. Circ. Physiol.* **1997**, *273* (3), H1576–H1586. <https://doi.org/10.1152/ajpheart.1997.273.3.H1576>.
- (242) Baicu, C. F.; Stroud, J. D.; Livesay, V. A.; Hapke, E.; Holder, J.; Spinale, F. G.; Zile, M. R. Changes in Extracellular Collagen Matrix Alter Myocardial Systolic Performance. *Am. J. Physiol. Circ. Physiol.* **2003**, *284* (1), H122–H132. <https://doi.org/10.1152/ajpheart.00233.2002>.
- (243) Borg, T. K.; Ranson, W. F.; Moslehy, F. A.; Caulfield, J. B. Structural Basis of Ventricular Stiffness. *Lab. Invest.* **1981**, *44* (1), 49–54.
- (244) Caulfield, J. B.; Borg, T. K. The Collagen Network of the Heart. *Lab. Invest.* **1979**, *40* (3), 364–372.
- (245) Davidson, M. M.; Nesti, C.; Palenzuela, L.; Walker, W. F.; Hernandez, E.; Protas, L.; Hirano, M.; Isaac, N. D. Novel Cell Lines Derived from Adult Human Ventricular Cardiomyocytes. *J. Mol. Cell. Cardiol.* **2005**, *39* (1), 133–147. <https://doi.org/https://doi.org/10.1016/j.yjmcc.2005.03.003>.
- (246) Parker, K. K.; Tan, J.; Chen, C. S.; Tung, L. Myofibrillar Architecture in Engineered Cardiac Myocytes. *Circ. Res.* **2008**, *103* (4), 340–342. <https://doi.org/10.1161/CIRCRESAHA.108.182469>.
- (247) Badie, N.; Bursac, N. Novel Micropatterned Cardiac Cell Cultures with Realistic Ventricular Microstructure. *Biophys. J.* **2009**, *96* (9), 3873–3885. <https://doi.org/https://doi.org/10.1016/j.bpj.2009.02.019>.
- (248) Kaneko, T.; Kojima, K.; Yasuda, K. An On-Chip Cardiomyocyte Cell Network Assay for Stable Drug Screening Regarding Community Effect of Cell Network Size. *Analyst* **2007**, *132* (9), 892–898. <https://doi.org/10.1039/B704961G>.
- (249) Burridge, P. W.; Keller, G.; Gold, J.; Wu, J. C. Production of De Novo Cardiomyocytes: Human Pluripotent Stem Cell Differentiation and Direct Reprogramming. *Cell Stem Cell* **2012**, *10* (1), 16–28. <https://doi.org/10.1016/j.stem.2011.12.013>.
- (250) Figeac, F.; Lesault, P.-F.; Le Coz, O.; Damy, T.; Souktani, R.; Trébeau, C.; Schmitt, A.; Ribot, J.; Mounier, R.; Guguin, A.; et al. Nanotubular Crosstalk with Distressed Cardiomyocytes Stimulates the Paracrine Repair Function of Mesenchymal Stem Cells. *Stem Cells* **2014**, *32* (1), 216–230. <https://doi.org/10.1002/stem.1560>.
- (251) Haneef, K.; Naeem, N.; Khan, I.; Iqbal, H.; Kabir, N.; Jamall, S.; Zahid, M.; Salim, A. Conditioned Medium Enhances the Fusion Capability of Rat Bone Marrow Mesenchymal Stem Cells and Cardiomyocytes. *Mol. Biol. Rep.* **2014**, *41* (5), 3099–3122.
- (252) Citro, L.; Naidu, S.; Hassan, F.; Kuppusamy, M. L.; Kuppusamy, P.; Angelos, M. G.; Khan, M. Comparison of Human Induced Pluripotent Stem-Cell Derived Cardiomyocytes with Human Mesenchymal Stem Cells Following Acute Myocardial Infarction. *PLoS One* **2015**, *9* (12), 1–16. <https://doi.org/10.1371/journal.pone.0116281>.
- (253) Dell’Era, P.; Benzoni, P.; Crescini, E.; Valle, M.; Xia, E.; Consiglio, A.; Memo, M. Cardiac Disease Modeling Using Induced Pluripotent Stem Cell-Derived Human Cardiomyocytes. *World J. Stem Cells* **2015**, *7* (2), 329–342. <https://doi.org/10.4252/wjsc.v7.i2.329>.
- (254) Hartman, M. E.; Dai, D.-F.; Laflamme, M. A. Human Pluripotent Stem Cells: Prospects and Challenges as a Source of Cardiomyocytes for in Vitro Modeling and Cell-Based Cardiac Repair. *Adv. Drug Deliv. Rev.* **2016**, *96*, 3–17. <https://doi.org/https://doi.org/10.1016/j.addr.2015.05.004>.
- (255) Mummery, C.; Ward-van Oostwaard, D.; Doevendans, P.; Spijker, R.; van den Brink, S.; Hassink, R.; van der Heyden, M.; Ophof, T.; Pera, M.; de la Riviere, A. B.; et al. Differentiation of Human Embryonic Stem Cells to Cardiomyocytes. *Circulation* **2003**, *107* (21), 2733–2740. <https://doi.org/10.1161/01.CIR.0000068356.38592.68>.

- (256) Kehat, I.; Kenyagin-Karsenti, D.; Snir, M.; Segev, H.; Amit, M.; Gepstein, A.; Livne, E.; Binah, O.; Itskovitz-Eldor, J.; Gepstein, L. Human Embryonic Stem Cells Can Differentiate into Myocytes with Structural and Functional Properties of Cardiomyocytes. *J. Clin. Invest.* **2001**, *108* (3), 407–414. <https://doi.org/10.1172/JCI12131>.
- (257) Kattman, S. J.; Witty, A. D.; Gagliardi, M.; Dubois, N. C.; Niapour, M.; Hotta, A.; Ellis, J.; Keller, G. Stage-Specific Optimization of Activin/Nodal and BMP Signaling Promotes Cardiac Differentiation of Mouse and Human Pluripotent Stem Cell Lines. *Cell Stem Cell* **2011**, *8* (2), 228–240. <https://doi.org/https://doi.org/10.1016/j.stem.2010.12.008>.
- (258) Zhang, J.; Klos, M.; Wilson, G. F.; Herman, A. M.; Lian, X.; Raval, K. K.; Barron, M. R.; Hou, L.; Soerens, A. G.; Yu, J.; et al. Extracellular Matrix Promotes Highly Efficient Cardiac Differentiation of Human Pluripotent Stem Cells: The Matrix Sandwich Method. *Circ. Res.* **2012**, *111* (9), 1125–1136. <https://doi.org/10.1161/CIRCRESAHA.112.273144>.
- (259) Laflamme, M. A.; Chen, K. Y.; Naumova, A. V.; Muskheli, V.; Fugate, J. A.; Dupras, S. K.; Reinecke, H.; Xu, C.; Hassanipour, M.; Police, S.; et al. Cardiomyocytes Derived from Human Embryonic Stem Cells in Pro-Survival Factors Enhance Function of Infarcted Rat Hearts. *Nat. Biotechnol.* **2007**, *25* (9), 1015–1024. <https://doi.org/10.1038/nbt1327>.
- (260) Lian, X.; Zhang, J.; Azarin, S. M.; Zhu, K.; Hazeltine, L. B.; Bao, X.; Hsiao, C.; Kamp, T. J.; Palecek, S. P. Directed Cardiomyocyte Differentiation from Human Pluripotent Stem Cells by Modulating Wnt / b -Catenin Signaling under Fully Defined Conditions. *Nat. Protoc.* **2013**, *8* (1), 162–175. <https://doi.org/10.1038/nprot.2012.150>.
- (261) Burridge, P. W.; Matsa, E.; Shukla, P.; Lin, Z. C.; Churko, J. M.; Ebert, A. D.; Lan, F.; Diecke, S.; Huber, B.; Mordwinkin, N. M.; et al. Chemically Defined Generation of Human Cardiomyocytes. *Nat. Methods* **2014**, *11* (8), 855–860. <https://doi.org/10.1038/nmeth.2999>.
- (262) Chen, V. C.; Couture, S. M.; Ye, J.; Lin, Z.; Hua, G.; Huang, H. P.; Wu, J.; Hsu, D.; Carpenter, M. K.; Couture, L. A. Scalable GMP Compliant Suspension Culture System for Human ES Cells. *Stem Cell Res.* **2012**, *8* (3), 388–402. <https://doi.org/10.1016/j.scr.2012.02.001>.
- (263) Miyaoka, Y.; Chan, A. H.; Judge, L. M.; Yoo, J. C.; Huang, M.; Nguyen, T. D.; Lizarraga, P.; So, P.-L.; Conklin, B. R. Isolation of Single-Base Genome-Edited Human IPS Cells without Antibiotic Selection. *Nat. Methods* **2014**, *11* (3), 291–293. <https://doi.org/10.1038/nmeth.2840>.
- (264) Wang, Y.; Zhang, W. Y.; Hu, S.; Lan, F.; Lee, A. S.; Huber, B.; Lisowski, L.; Liang, P.; Huang, M.; De Almeida, P. E.; et al. Genome Editing of Human Embryonic Stem Cells and Induced Pluripotent Stem Cells with Zinc Finger Nucleases for Cellular Imaging. *Circ. Res.* **2012**, *111* (12), 1494–1503. <https://doi.org/10.1161/CIRCRESAHA.112.274969>.
- (265) Taylor, C. J.; Bolton, E. M.; Pocock, S.; Sharples, L. D.; Pedersen, R. A.; Bradley, J. A. Banking on Human Embryonic Stem Cells: Estimating the Number of Donor Cell Lines Needed for HLA Matching. *Lancet* **2005**, *366* (9502), 2019–2025. [https://doi.org/https://doi.org/10.1016/S0140-6736\(05\)67813-0](https://doi.org/https://doi.org/10.1016/S0140-6736(05)67813-0).
- (266) Stacey, G. N.; Crook, J. M.; Hei, D.; Ludwig, T. Banking Human Induced Pluripotent Stem Cells: Lessons Learned from Embryonic Stem Cells? *Cell Stem Cell* **2013**, *13* (4), 385–388. <https://doi.org/10.1016/j.stem.2013.09.007>.
- (267) Laflamme, M. A.; Murry, C. E. Heart Regeneration. *Nature* **2011**, *473*, 326.
- (268) Robertson, C.; Tran, D.; George, S. Concise Review: Maturation Phases of Human Pluripotent Stem Cell-Derived Cardiomyocytes. *Stem Cells* **2013**, *31* (5), 1–17. <https://doi.org/10.1002/stem.1331.Concise>.
- (269) Yang, X.; Pabon, L.; Murry, C. E. Engineering Adolescence: Maturation of Human Pluripotent Stem Cell-Derived Cardiomyocytes. *Circ. Res.* **2014**, *114* (3), 511–523. <https://doi.org/10.1161/CIRCRESAHA.114.300558>.
- (270) Simpson, D. G.; Terracio, L.; Terracio, M.; Price, R. L.; Turner, D. C.; Borg, T. K. Modulation of Cardiac Myocyte Phenotype In-Vitro by the Composition and Orientation of the Extracellular-Matrix. *J. Cell. Physiol.* **1994**, *161* (1), 89–105.
- (271) Bursac, N.; Parker, K. K.; Iravanian, S.; Tung, L. Cardiomyocyte Cultures with Controlled Macroscopic Anisotropy: A Model for Functional Electrophysiological Studies of Cardiac Muscle. *Circ. Res.* **2002**, *91* (12), e45–e54. <https://doi.org/10.1161/01.RES.0000047530.88338.EB>.
- (272) Motlagh, D.; Hartman, T. J.; Desai, T. A.; Russell, B. Microfabricated Grooves Recapitulate Neonatal Myocyte Connexin43 and N-Cadherin Expression and Localization. *J. Biomed. Mater. Res. Part A* **2003**, *67A* (1), 148–157. <https://doi.org/10.1002/jbm.a.10083>.

- (273) Wang, P. Y.; Yu, J.; Lin, J. H.; Tsai, W. B. Modulation of Alignment, Elongation and Contraction of Cardiomyocytes through a Combination of Nanotopography and Rigidity of Substrates. *Acta Biomater.* **2011**, *7* (9), 3285–3293. <https://doi.org/10.1016/j.actbio.2011.05.021>.
- (274) Luna, J. I.; Ciriza, J.; Garcia-Ojeda, M. E.; Kong, M.; Herren, A.; Lieu, D. K.; Li, R. A.; Fowlkes, C. C.; Khine, M.; McCloskey, K. E. Multiscale Biomimetic Topography for the Alignment of Neonatal and Embryonic Stem Cell-Derived Heart Cells. *Tissue Eng. Part C Methods* **2011**, *17* (5), 579–588. <https://doi.org/10.1089/ten.tec.2010.0410>.
- (275) Chen, A.; Lieu, D. K.; Freschauf, L.; Lew, V.; Sharma, H.; Wang, J.; Nguyen, D.; Karakikes, I.; Hajjar, R. J.; Gopinathan, A.; et al. Shrink-Film Configurable Multiscale Wrinkles for Functional Alignment of Human Embryonic Stem Cells and Their Cardiac Derivatives. *Adv. Mater.* **2011**, *23* (48), 5785–5791. <https://doi.org/10.1002/adma.201103463>.
- (276) Kim, D.-H.; Lipke, E. A.; Kim, P.; Cheong, R.; Thompson, S.; Delannoy, M.; Suh, K.-Y.; Tung, L.; Levchenko, A. Nanoscale Cues Regulate the Structure and Function of Macroscopic Cardiac Tissue Constructs. *Proc. Natl. Acad. Sci.* **2010**, *107* (2), 565–570. <https://doi.org/10.1073/pnas.0906504107>.
- (277) Ma, Z.; Liu, Q.; Liu, H.; Yang, H.; Yun, J. X.; Eisenberg, C. A.; Borg, T. K.; Xu, M.; Gao, B. Z. Laser-Patterned Stem Cell Bridges in a Cardiac Muscle Model for on-Chip Electrical Conductivity Analyses. *Lab Chip* **2012**, *29* (6), 997–1003. <https://doi.org/10.1016/j.biotechadv.2011.08.021>. Secreted.
- (278) Ma, Z.; Liu, Q.; Yang, H.; Runyan, R. B.; Eisenberg, C. A.; Xu, M.; Borg, T. K.; Markwald, R.; Wang, Y.; Gao, B. Z. Laser Patterning for the Study of MSC Cardiogenic Differentiation at the Single-Cell Level. *Light Sci. Appl.* **2013**, *2*, e68. <https://doi.org/10.1038/lsa.2013.24>.
- (279) Annabi, N.; Selimovic, S.; Cox, J. P. A.; Ribas, J.; Bakooshli, M. A.; Heintze, D.; Weiss, A. S.; Cropek, D.; Khademhosseini, A. Hydrogel-Coated Microfluidic Channels for Cardiomyocyte Culture. *Lab Chip* **2012**, *29* (6), 997–1003. <https://doi.org/10.1016/j.biotechadv.2011.08.021>. Secreted.
- (280) Cimetta, E.; Pizzato, S.; Bollini, S.; Serena, E.; De Coppi, P.; Elvassore, N. Production of Arrays of Cardiac and Skeletal Muscle Myofibers by Micropatterning Techniques on a Soft Substrate. *Biomed. Microdevices* **2009**, *11* (2), 389–400. <https://doi.org/10.1007/s10544-008-9245-9>.
- (281) McDevitt, T. C.; Angello, J. C.; Whitney, M. L.; Reinecke, H.; Hauschka, S. D.; Murry, C. E.; Stayton, P. S. In Vitro Generation of Differentiated Cardiac Myofibers on Micropatterned Laminin Surfaces. *J. Biomed. Mater. Res.* **2002**, *60* (3), 472–479. <https://doi.org/10.1002/jbm.1292>.
- (282) Agarwal, A.; Farouz, Y.; Nesmith, A. P.; Deravi, L. F.; McCain, M. L.; Parker, K. K. Micropatterning Alginate Substrates for in Vitro Cardiovascular Muscle on a Chip. *Adv. Funct. Mater.* **2013**, *23* (30), 3738–3746. <https://doi.org/10.1002/adfm.201203319>.
- (283) Camelliti, P.; Gallagher, J. O.; Kohl, P.; McCulloch, A. D. Micropatterned Cell Cultures on Elastic Membranes as an in Vitro Model of Myocardium. *Nat. Protoc.* **2006**, *1* (3), 1379–1391. <https://doi.org/10.1038/nprot.2006.203>.
- (284) Karp, J. M.; Yeo, Y.; Geng, W.; Cannizarro, C.; Yan, K.; Kohane, D. S.; Vunjak-Novakovic, G.; Langer, R. S.; Radisic, M. A Photolithographic Method to Create Cellular Micropatterns. *Biomaterials* **2006**, *27* (27), 4755–4764. <https://doi.org/10.1016/j.biomaterials.2006.04.028>.
- (285) Khademhosseini, A.; Eng, G.; Yeh, J.; Kucharczyk, P. a.; Langer, R. S.; Vunjak-Novakovic, G.; Radisic, M. Microfluidic Patterning for Fabrication of Contractile Cardiac Organoids. *Biomed. Microdevices* **2007**, *9* (2), 149–157. <https://doi.org/10.1007/s10544-006-9013-7>.
- (286) Thomas, S. P.; Bircher-Lehmann, L.; Thomas, S. A.; Zhuang, J.; Saffitz, J. E.; Kleber, A. G. Synthetic Strands of Neonatal Mouse Cardiac Myocytes: Structural and Electrophysiological Properties. *Circ. Res.* **2000**, *87* (6), 467–473.
- (287) Pong, T.; Adams, W. J.; Bray, M.-A.; Feinberg, A. W.; Sheehy, S. P.; Werdich, A. A.; Parker, K. K. Hierarchical Architecture Influences Calcium Dynamics in Engineered Cardiac Muscle. *Exp. Biol. Med.* **2011**, *236* (3), 366–373. <https://doi.org/10.1258/ebm.2010.010239>.
- (288) Thompson, S. A.; Copeland, C. R.; Reich, D. H.; Tung, L. Mechanical Coupling Between Myofibroblasts and Cardiomyocytes Slows Electric Conduction in Fibrotic Cell Monolayers. *Circulation* **2011**, *123* (19), 2083–2093. <https://doi.org/10.1161/CIRCULATIONAHA.110.015057>.
- (289) Ribeiro, M. C.; Tertoolen, L. G.; Guadix, J. a.; Bellin, M.; Kosmidis, G.; D’Aniello, C.; Monshouwer-Kloots, J.; Goumans, M.-J.; Wang, Y.; Feinberg, A. W.; et al. Functional Maturation of Human Pluripotent Stem Cell Derived Cardiomyocytes in Vitro – Correlation between Contraction Force

- and Electrophysiology. *Biomaterials* **2015**, *51*, 138–150.
<https://doi.org/10.1016/j.biomaterials.2015.01.067>.
- (290) Serena, E.; Cimetta, E.; Zatti, S.; Zaglia, T.; Zagallo, M.; Keller, G.; Elvassore, N. Micro-Arrayed Human Embryonic Stem Cells-Derived Cardiomyocytes for In Vitro Functional Assay. *PLoS One* **2012**, *7* (11), 1–10. <https://doi.org/10.1371/journal.pone.0048483>.
- (291) Hwang, Y.-S.; Chung, B. G.; Ortmann, D.; Hattori, N.; Moeller, H.-C.; Khademhosseini, A. Microwell-Mediated Control of Embryoid Body Size Regulates Embryonic Stem Cell Fate via Differential Expression of WNT5a and WNT11. *PNAS* **2009**, *106* (40), 16978–16983.
<https://doi.org/10.1073/pnas.0905550106>.
- (292) Mohr, J. C.; Zhang, J.; Azarin, S. M.; Soerens, A. G.; de Pablo, J. J.; Thomson, J. A.; Lyons, G. E.; Palecek, S. P.; Kamp, T. J. The Microwell Control of Embryoid Body Size in Order to Regulate Cardiac Differentiation of Human Embryonic Stem Cells. *Biomaterials* **2010**, *31* (7), 1885–1893.
<https://doi.org/10.1016/j.biomaterials.2009.11.033>.
- (293) Azarin, S. M.; Lian, X.; Larson, E. A.; Popelka, H. M.; de Pablo, J. J.; Palecek, S. P. Modulation of Wnt/ β -Catenin Signaling in Human Embryonic Stem Cells Using a 3-D Microwell Array. *Biomaterials* **2012**, *33* (7), 2041–2049.
<https://doi.org/https://doi.org/10.1016/j.biomaterials.2011.11.070>.
- (294) Myers, F. B.; Silver, J. S.; Zhuge, Y.; Beygui, R. E.; Zarins, C. K.; Lee, L. P.; Abilez, O. J. Robust Pluripotent Stem Cell Expansion and Cardiomyocyte Differentiation via Geometric Patterning. *Integr. Biol.* **2013**, *5* (12), 1495–1506. <https://doi.org/10.1039/c2ib20191g>.
- (295) Bauwens, C. L.; Peerani, R.; Niebruegge, S.; Woodhouse, K. A.; Kumacheva, E.; Husain, M.; Zandstra, P. W. Control of Human Embryonic Stem Cell Colony and Aggregate Size Heterogeneity Influences Differentiation Trajectories. *Stem Cells* **2008**, *26* (9), 2300–2310.
<https://doi.org/10.1634/stemcells.2008-0183>.
- (296) Nazareth, E. J. P.; Ostblom, J. E. E.; Lückner, P. B.; Shukla, S.; Alvarez, M. M.; Oh, S. K. W.; Yin, T.; Zandstra, P. W. High-Throughput Fingerprinting of Human Pluripotent Stem Cell Fate Responses and Lineage Bias. *Nat. Methods* **2013**, *10*, 1225.
- (297) Warmflash, A.; Sorre, B.; Etoc, F.; Siggia, E. D.; Brivanlou, A. H. A Method to Recapitulate Early Embryonic Spatial Patterning in Human Embryonic Stem Cells. *Nat. Methods* **2014**, *11*, 847.
- (298) Ma, Z.; Wang, J.; Loskill, P.; Huebsch, N.; Koo, S.; Svedlund, F. L.; Marks, N. C.; Hua, E. W.; Grigoropoulos, C. P.; Conklin, B. R.; et al. Self-Organizing Human Cardiac Microchambers Mediated by Geometric Confinement. *Nat. Commun.* **2015**, *6*, 7413.
<https://doi.org/10.1038/ncomms8413>.
- (299) Geisse, N. A.; Sheehy, S. P.; Parker, K. K. Control of Myocyte Remodeling in Vitro with Engineered Substrates. *Vitr. Cell. Dev. Biol. - Anim.* **2009**, *45* (7), 343–350.
- (300) Bray, M.-A.; Sheehy, S. P.; Parker, K. K. Sarcomere Alignment Is Regulated by Myocyte Shape. *Cell Motil.* **2008**, *65* (8), 641–651. <https://doi.org/10.1002/cm.20290>.
- (301) Bray, M.-A. P.; Adams, W. J.; Geisse, N. A.; Feinberg, A. W.; Sheehy, S. P.; Parker, K. K. Nuclear Morphology and Deformation in Engineered Cardiac Myocytes and Tissues. *Biomaterials* **2010**, *31* (19), 5143–5150. <https://doi.org/https://doi.org/10.1016/j.biomaterials.2010.03.028>.
- (302) Eschenhagen, T.; Fink, C.; Remmers, U.; Scholz, H.; Wattchow, J.; Weil, J.; Zimmermann, W.; Dohmen, H. H.; Schäfer, H.; Bishopric, N.; et al. Three-Dimensional Reconstitution of Embryonic Cardiomyocytes in a Collagen Matrix: A New Heart Muscle Model System. *FASEB J.* **1997**, *11* (8), 683–694. <https://doi.org/10.1096/fasebj.11.8.9240969>.
- (303) Zimmermann, W. H.; Fink, C.; Kralisch, D.; Remmers, U.; Weil, J.; Eschenhagen, T. Three-Dimensional Engineered Heart Tissue from Neonatal Rat Cardiac Myocytes. *Biotechnol. Bioeng.* **2000**, *68* (1), 106–114.
- (304) Zimmermann, W.-H.; Melnychenko, I.; Wasmeier, G.; Didié, M.; Naito, H.; Nixdorff, U.; Hess, A.; Budinsky, L.; Brune, K.; Michaelis, B.; et al. Engineered Heart Tissue Grafts Improve Systolic and Diastolic Function in Infarcted Rat Hearts. *Nat. Med.* **2006**, *12* (4), 452–458.
<https://doi.org/10.1038/nm1394>.
- (305) Hansen, A.; Eder, A.; Bönstrup, M.; Flato, M.; Mewe, M.; Schaaf, S.; Aksehirlioglu, B.; Schwörer, A.; Uebeler, J.; Eschenhagen, T. Development of a Drug Screening Platform Based on Engineered Heart Tissue. *Circ. Res.* **2010**, *107* (1), 35–44.
<https://doi.org/10.1161/CIRCRESAHA.109.211458>.
- (306) Schaaf, S.; Shibamiya, A.; Mewe, M.; Eder, A.; Stöhr, A.; Hirt, M. N.; Rau, T.; Zimmermann, W.-H.;

- Conradi, L.; Eschenhagen, T.; et al. Human Engineered Heart Tissue as a Versatile Tool in Basic Research and Preclinical Toxicology. *PLoS One* **2011**, *6* (10), 1–11. <https://doi.org/10.1371/journal.pone.0026397>.
- (307) Boudou, T.; Legant, W. R.; Mu, A.; Borochin, M. A.; Thavandiran, N.; Radisic, M.; Zandstra, P. W.; Epstein, J. A.; Margulies, K. B.; Chen, C. S. A Microfabricated Platform to Measure and Manipulate the Mechanics of Engineered Cardiac Microtissues. *Tissue Eng. Part A* **2012**, *18* (9–10), 910–919. <https://doi.org/10.1089/ten.tea.2011.0341>.
- (308) Hinson, J. T.; Chopra, A.; Nafissi, N.; Polacheck, W. J.; Benson, C. C.; Swist, S.; Gorham, J.; Yang, L.; Schafer, S.; Sheng, C. C.; et al. Titin Mutations in IPS Cells Define Sarcomere Insufficiency as a Cause of Dilated Cardiomyopathy. *Science* (80-.). **2015**, *349* (6251), 982–986. <https://doi.org/10.1126/science.aaa5458>.
- (309) Turnbull, I. C.; Karakikes, I.; Serrao, G. W.; Backeris, P.; Lee, J. J.; Xie, C.; Senyei, G.; Gordon, R. E.; Li, R. a.; Akar, F. G.; et al. Advancing Functional Engineered Cardiac Tissues toward a Preclinical Model of Human Myocardium. *FASEB J.* **2014**, *28* (2), 644–654. <https://doi.org/10.1096/fj.13-228007>.
- (310) Thavandiran, N.; Dubois, N.; Mikryukov, A.; Massé, S.; Beca, B.; Simmons, C. A.; Deshpande, V. S.; McGarry, J. P.; Chen, C. S.; Nanthakumar, K.; et al. Design and Formulation of Functional Pluripotent Stem Cell-Derived Cardiac Microtissues. *Proc. Natl. Acad. Sci.* **2013**, *110* (49), E4698–E4707. <https://doi.org/10.1073/pnas.1311120110>.
- (311) Liao, B.; Christoforou, N.; Leong, K. W.; Bursac, N. Pluripotent Stem Cell-Derived Cardiac Tissue Patch with Advanced Structure and Function. *Biomaterials* **2011**, *32* (35), 9180–9187. <https://doi.org/10.1016/j.biomaterials.2011.08.050>.
- (312) Zhang, D.; Shadrin, I. Y.; Lam, J.; Xian, H.-Q.; Snodgrass, H. R.; Bursac, N. Tissue-Engineered Cardiac Patch for Advanced Functional Maturation of Human ESC-Derived Cardiomyocytes. *Biomaterials* **2013**, *34* (23), 5813–5820. <https://doi.org/10.1016/j.biomaterials.2013.04.026>.
- (313) Maidhof, R.; Tandon, N.; Lee, E. J.; Luo, J.; Duan, Y.; Yeager, K.; Konofagou, E.; Vunjak-Novakovic, G. Biomimetic Perfusion and Electrical Stimulation Applied in Concert Improved the Assembly of Engineered Cardiac Tissue. *J. Tissue Eng. Regen. Med.* **2012**, *6* (10), e12–e23. <https://doi.org/10.1002/term.525>.
- (314) Kai, D.; Prabhakaran, M. P.; Jin, G.; Ramakrishna, S. Guided Orientation of Cardiomyocytes on Electrospun Aligned Nanofibers for Cardiac Tissue Engineering. *J. Biomed. Mater. Res. Part B Appl. Biomater.* **2011**, *98B* (2), 379–386. <https://doi.org/10.1002/jbm.b.31862>.
- (315) Orlova, Y.; Magome, N.; Liu, L.; Chen, Y.; Agladze, K. Electrospun Nanofibers as a Tool for Architecture Control in Engineered Cardiac Tissue. *Biomaterials* **2011**, *32* (24), 5615–5624. <https://doi.org/https://doi.org/10.1016/j.biomaterials.2011.04.042>.
- (316) Kenar, H.; Kose, G. T.; Toner, M.; Kaplan, D. L.; Hasirci, V. A 3D Aligned Microfibrous Myocardial Tissue Construct Cultured under Transient Perfusion. *Biomaterials* **2011**, *32* (23), 5320–5329. <https://doi.org/https://doi.org/10.1016/j.biomaterials.2011.04.025>.
- (317) Badrossamay, M. R.; Balachandran, K.; Capulli, A. K.; Golecki, H. M.; Agarwal, A.; Goss, J. A.; Kim, H.; Shin, K.; Parker, K. K. Engineering Hybrid Polymer-Protein Super-Aligned Nanofibers via Rotary Jet Spinning. *Biomaterials* **2014**, *35* (10), 3188–3197. <https://doi.org/https://doi.org/10.1016/j.biomaterials.2013.12.072>.
- (318) Ma, Z.; Koo, S.; Finnegan, M.; Loskill, P.; Huebsch, N.; Marks, N. C.; Conklin, B. R.; Grigoropoulos, C. P.; Healy, K. E. Three-Dimensional Filamentous Human Diseased Cardiac Tissue Model. *Biomaterials* **2014**, *35* (5), 1367–1377. <https://doi.org/10.1016/j.biomaterials.2013.10.052>.
- (319) Nunes, S. S.; Miklas, J. W.; Liu, J.; Aschar-Sobbi, R.; Xiao, Y.; Zhang, B.; Jiang, J.; Massé, S.; Gagliardi, M.; Hsieh, A.; et al. Biowire: A Platform for Maturation of Human Pluripotent Stem Cell-Derived Cardiomyocytes. *Nat. Methods* **2013**, *10*, 781.
- (320) Miklas, J. W.; Nunes, S. S.; Sofia, A.; Reis, L. A.; Pahnke, A.; Xiao, Y.; Laschinger, C.; Radisic, M. Bioreactor for Modulation of Cardiac Microtissue Phenotype by Combined Static Stretch and Electrical Stimulation. *Biofabrication* **2014**, *6* (2). <https://doi.org/10.1088/1758-5082/6/2/024113>.
- (321) Xiao, Y.; Zhang, B.; Liu, H.; Miklas, J. W.; Gagliardi, M.; Pahnke, A.; Thavandiran, N.; Sun, Y.; Simmons, C.; Keller, G.; et al. Microfabricated Perfusible Cardiac Biowire: A Platform That Mimics Native Cardiac Bundle. *Lab Chip* **2014**, *14*, 869–882. <https://doi.org/10.1039/C3LC51123E>.
- (322) Grosberg, A.; Alford, P. W.; McCain, M. L.; Parker, K. K. Ensembles of Engineered Cardiac

- Tissues for Physiological and Pharmacological Study: Heart on a Chip. *Lab on a Chip*. 2011, p 4165. <https://doi.org/10.1039/c1lc20557a>.
- (323) Agarwal, A.; Goss, J. A.; Cho, A.; McCain, M. L.; Parker, K. K. Microfluidic Heart on a Chip for Higher Throughput Pharmacological Studies. *Lab Chip* **2013**, *13*, 3599–3608. <https://doi.org/10.1039/C3LC50350J>.
- (324) Feinberg, A. W.; Ripplinger, C. M.; van der Meer, P.; Sheehy, S. P.; Domian, I.; Chien, K. R.; Parker, K. K. Functional Differences in Engineered Myocardium from Embryonic Stem Cell-Derived versus Neonatal Cardiomyocytes. *Stem Cell Reports* **2013**, *1* (5), 387–396. <https://doi.org/https://doi.org/10.1016/j.stemcr.2013.10.004>.
- (325) McCain, M. L.; Sheehy, S. P.; Grosberg, A.; Goss, J. A.; Parker, K. K. Recapitulating Maladaptive, Multiscale Remodeling of Failing Myocardium on a Chip. *Proc. Natl. Acad. Sci.* **2013**, *24*, 9770–9775. <https://doi.org/10.1073/pnas.1304913110>.
- (326) Wang, G.; McCain, M. L.; Yang, L.; He, A.; Pasqualini, F. S.; Agarwal, A.; Yuan, H.; Jiang, D.; Zhang, D.; Zangi, L.; et al. Modeling the Mitochondrial Cardiomyopathy of Barth Syndrome with Induced Pluripotent Stem Cell and Heart-on-Chip Technologies. *Nat. Med.* **2014**, *20*, 616.
- (327) Mosadegh, B.; Dabiri, B. E.; Lockett, M. R.; Derda, R.; Campbell, P.; Parker, K. K.; Whitesides, G. M. Three-Dimensional Paper-Based Model for Cardiac Ischemia. *Adv. Healthc. Mater.* **2014**, *3* (7), 1036–1043. <https://doi.org/10.1002/adhm.201300575>.
- (328) Lundy, S. D.; Zhu, W.-Z.; Regnier, M.; Laflamme, M. A. Structural and Functional Maturation of Cardiomyocytes Derived from Human Pluripotent Stem Cells. *Stem Cells Dev.* **2013**, *22* (14), 1991–2002. <https://doi.org/10.1089/scd.2012.0490>.
- (329) Abate, A. R.; Lee, D.; Do, T.; Holtze, C.; Weitz, D. A. Glass Coating for PDMS Microfluidic Channels by Sol–Gel Methods. *Lab Chip* **2008**, *8*, 516–518. <https://doi.org/10.1039/B800001H>.
- (330) Sun, L.; Luo, Y.; Gao, Z.; Zhao, W.; Lin, B. Easy-to-Fabricate Thin-Film Coating on PDMS Substrate with Super Hydrophilicity and Stability. *Electrophoresis* **2015**, *36* (6), 889–892. <https://doi.org/10.1002/elps.201400366>.
- (331) Collins, F. S.; Varmus, H. A New Initiative on Precision Medicine. *N. Engl. J. Med.* **2015**, *372* (9), 793–795. <https://doi.org/10.1056/NEJMp1415160>.
- (332) Ashley, E. A. The Precision Medicine Initiative: A New National Effort. *JAMA* **2015**, *313* (21), 2119–2120. <https://doi.org/10.1001/jama.2015.3595>.
- (333) Tsimberidou, A. M.; Eggermont, A. M. M.; Schilsky, R. L. Precision Cancer Medicine: The Future Is Now, Only Better. *Am. Soc. Clin. Oncol. Educ. B.* **2014**, 61–69. https://doi.org/10.14694/edbook_am.2014.34.61.
- (334) Omenn, G. S.; Lane, L.; Lundberg, E. K.; Beavis, R. C.; Overall, C. M.; Deutsch, E. W. Metrics for the Human Proteome Project 2016: Progress on Identifying and Characterizing the Human Proteome, Including Post-Translational Modifications. *J. Proteome Res.* **2016**, *15* (11), 3951–3960. <https://doi.org/10.1021/acs.jproteome.6b00511>.
- (335) Sun, Y. P.; Sears, D. F.; Saltiel, J. Resolution of Benzophenone Delayed Fluorescence and Phosphorescence Spectra. Evidence of Vibrationally Unrelaxed Prompt Benzophenone Fluorescence. *J. Am. Chem. Soc.* **1989**, *111* (2), 706–711.

Appendices

Appendix 1: Protocol: fabrication of porogen separation gels

Materials:

For all materials except BPMA, I used a single bottle for this research work as much as possible. Lot numbers are noted in lab notebooks. For BPMA, I used the same lot throughout this research, prepared by various lab members in DMSO to create 100 mM stock vials.

- 30% 3.3%C acrylamide stock solution:
 - o Personal stocks at 4°C, brown plastic bottles, dated 2016 and 2019
- 20%T 8%C acrylamide stock solution:
 - o Personal stock at 4°C, labeled glass bottle with orange top + foil. Previously made from 40% acrylamide solution + bisacrylamide powder.
- 5% PEG stock solution:
 - o Personal stock at RT, labeled glass bottle with orange top. Vortex extensively and let bubbles settle out.
- TrisHCl stock solution:
 - o Shared stock bottle. No dilution.
- APS:
 - o Shared bottle in flammables cabinet, dated 2016. Weigh out into Eppendorf tube, and make a 10% solution in MilliQ water.
- TEMED:
 - o Shared bottle on shared materials shelf in the 4°C fridge (with the TBS-T, antibodies, and shared IEF materials), dated 2016. Use 100% solution (no dilution).
- VA-086:
 - o Shared bottle, covered with aluminum foil, at 4°C. Make 2% stock solution.
- LAP (from startup company Allevi, formerly named Biobots):
 - o Shared bottle, covered with aluminum foil, in clear box, at -20°C (in door). Make 1% stock solution.
- BPMA:
 - o Most recent aliquot from shared stock at -20°C. Make sure the vial has not been previously thawed. No dilution. Thaw at RT under foil, and triturate.

Precursor solutions with APS/TEMED

6%T 3.3%C APS/TEMED PA gel -- negative control			
50	100	160	30%T 3.3%C 29:1 acrylamide solution
12.5	25	40	TrisHCl pH 8.8 (1.5 mM)
12.5	25	40	BPMA
172.8	345.6	553	MilliQ water
0.2	0.4	0.64	TEMED 100%
2	4	6.4	APS 10% in MilliQ water
250	500	800	total

Note: different acrylamide solution for all gels below! Use 20% 8%C stock solution.

PEG 0%		6%T 8%C APS/TEMED PA gel + 0.0% PEG				
Total Volume [μL]			250	800	1000	
Reagent	Stock conc.	Final Conc.	Vol. [μL]	Vol. [μL]	Vol. [μL]	
Acrylamide soln [%T]	20	6	75	240	300	
PEG [%]	5	0	0	0	0	
Tris-HCl pH 8.8 [mM]	1.5	0.075	12.5	40	50	
BPMA [mM]	100	5	12.5	40	50	
APS [%]	10	0.08	2	6.4	8	
TEMED [%]	100	0.08	0.2	0.64	0.8	
Water (MilliQ)	-		147.8	472.96	591.2	

PEG 0.5%		6%T 8%C APS/TEMED PA gel + 0.5% PEG				
Total Volume [μL]			250	800	1000	
Reagent	Stock conc.	Final Conc.	Vol. [μL]	Vol. [μL]	Vol. [μL]	
Acrylamide soln [%T]	20	6	75	240	300	
PEG [%]	5	0.5	25	80	100	
Tris-HCl pH 8.8 [mM]	1.5	0.075	12.5	40	50	
BPMA [mM]	100	5	12.5	40	50	
APS [%]	10	0.08	2	6.4	8	
TEMED [%]	100	0.08	0.2	0.64	0.8	
Water	-		122.8	392.96	491.2	

PEG 1.0%		6%T 8%C APS/TEMED PA gel + 1.0% PEG				
Total Volume [μL]			250	800	1000	
Reagent	Stock conc.	Final Conc.	Vol. [μL]	Vol. [μL]	Vol. [μL]	
Acrylamide soln [%T]	20	6	75	240	300	
PEG [%]	5	1	50	160	200	
Tris-HCl pH 8.8 [mM]	1.5	0.075	12.5	40	50	
BPMA [mM]	100	5	12.5	40	50	
APS [%]	10	0.08	2	6.4	8	
TEMED [%]	100	0.08	0.2	0.64	0.8	
Water	-		97.8	312.96	391.2	

PEG 1.5%		6%T 8%C APS/TEMED PA gel + 1.5% PEG				
Total Volume [μL]			250	800	1000	
Reagent	Stock conc.	Final Conc.	Vol. [μL]	Vol. [μL]	Vol. [μL]	
Acrylamide soln [%T]	20	6	75	240	300	
PEG [%]	5	1.5	75	240	300	
Tris-HCl pH 8.8 [mM]	1.5	0.075	12.5	40	50	
BPMA [mM]	100	5	12.5	40	50	
APS [%]	10	0.08	2	6.4	8	
TEMED [%]	100	0.08	0.2	0.64	0.8	
Water	-		72.8	232.96	291.2	

PEG 2.0%		6%T 8%C APS/TEMED PA gel + 2.0% PEG				
Total Volume [μL]			250	800	1000	
Reagent	Stock conc.	Final Conc.	Vol. [μL]	Vol. [μL]	Vol. [μL]	
Acrylamide soln [%T]	20	6	75	240	300	
PEG [%]	5	2	100	320	400	
Tris-HCl pH 8.8 [mM]	1.5	0.075	12.5	40	50	
BPMA [mM]	100	5	12.5	40	50	
APS [%]	10	0.08	2	6.4	8	
TEMED [%]	100	0.08	0.2	0.64	0.8	
Water	-		47.8	152.96	191.2	

Precursor solutions with VA-086

PEG 0%		6%T 8%C VA-086 PA gel + 0.0% PEG				
Total Volume [μL]			250	800	1000	
Reagent	Stock conc.	Final Conc.	Vol. [μL]	Vol. [μL]	Vol. [μL]	
Acrylamide soln [%T]	20	6	75	240	300	
PEG [%]	5	0	0	0	0	
Tris-HCl pH 8.8 [mM]	1.5	0.075	12.5	40	50	
BPMA [mM]	100	5	12.5	40	50	
VA-086 [%]	2	0.2	25	80	100	
Water (MilliQ)	-		125	400	500	

PEG 0.5%		6%T 8%C VA-086 PA gel + 0.5% PEG				
Total Volume [μL]			250	800	1000	
Reagent	Stock conc.	Final Conc.	Vol. [μL]	Vol. [μL]	Vol. [μL]	
Acrylamide soln [%T]	20	6	75	240	300	
PEG [%]	5	0.5	25	80	100	
Tris-HCl pH 8.8 [mM]	1.5	0.075	12.5	40	50	
BPMA [mM]	100	5	12.5	40	50	
VA-086 [%]	2	0.2	25	80	100	
Water (MilliQ)	-		100	320	400	

PEG 1.0%		6%T 8%C VA-086 PA gel + 1.0% PEG				
Total Volume [μL]			250	800	1000	
Reagent	Stock conc.	Final Conc.	Vol. [μL]	Vol. [μL]	Vol. [μL]	
Acrylamide soln [%T]	20	6	75	240	300	
PEG [%]	5	1	50	160	200	
Tris-HCl pH 8.8 [mM]	1.5	0.075	12.5	40	50	
BPMA [mM]	100	5	12.5	40	50	
VA-086 [%]	2	0.2	25	80	100	
Water (MilliQ)	-		75	240	300	

PEG 1.5%		6%T 8%C VA-086 PA gel + 1.5% PEG				
Total Volume [μL]			250	800	1000	
Reagent	Stock conc.	Final Conc.	Vol. [μL]	Vol. [μL]	Vol. [μL]	
Acrylamide soln [%T]	20	6	75	240	300	
PEG [%]	5	1.5	75	240	300	
Tris-HCl pH 8.8 [mM]	1.5	0.075	12.5	40	50	
BPMA [mM]	100	5	12.5	40	50	
VA-086 [%]	2	0.2	25	80	100	
Water (MilliQ)	-		50	160	200	

PEG 2.0%		6%T 8%C VA-086 PA gel + 2.0% PEG				
Total Volume [μL]			250	800	1000	
Reagent	Stock conc.	Final Conc.	Vol. [μL]	Vol. [μL]	Vol. [μL]	
Acrylamide soln [%T]	20	6	75	240	300	
PEG [%]	5	2	100	320	400	
Tris-HCl pH 8.8 [mM]	1.5	0.075	12.5	40	50	
BPMA [mM]	100	5	12.5	40	50	
VA-086 [%]	2	0.2	25	80	100	
Water (MilliQ)	-		25	80	100	

Precursor solutions with LAP

PEG 0%		6%T 8%C LAP PA gel + 0.0% PEG				
Total Volume [μL]			250	800	1000	
Reagent	Stock conc.	Final Conc.	Vol. [μL]	Vol. [μL]	Vol. [μL]	
Acrylamide soln [%T]	20	6	75	240	300	
PEG [%]	5	0	0	0	0	
Tris-HCl pH 8.8 [mM]	1.5	0.075	12.5	40	50	
BPMA [mM]	100	5	12.5	40	50	
LAP [%]	1	0.2	50	160	200	
Water (MilliQ)	-		100	320	400	

PEG 0.5%		6%T 8%C LAP PA gel + 0.5% PEG				
Total Volume [μL]			250	800	1000	
Reagent	Stock conc.	Final Conc.	Vol. [μL]	Vol. [μL]	Vol. [μL]	
Acrylamide soln [%T]	20	6	75	240	300	
PEG [%]	5	0.5	25	80	100	
Tris-HCl pH 8.8 [mM]	1.5	0.075	12.5	40	50	
BPMA [mM]	100	5	12.5	40	50	
LAP [%]	1	0.2	50	160	200	
Water (MilliQ)	-		75	240	300	

PEG 1.0%		6%T 8%C LAP PA gel + 1.0% PEG				
Total Volume [μL]			250	800	1000	
Reagent	Stock conc.	Final Conc.	Vol. [μL]	Vol. [μL]	Vol. [μL]	
Acrylamide soln [%T]	20	6	75	240	300	
PEG [%]	5	1	50	160	200	
Tris-HCl pH 8.8 [mM]	1.5	0.075	12.5	40	50	
BPMA [mM]	100	5	12.5	40	50	
LAP [%]	1	0.2	50	160	200	
Water (MilliQ)	-		50	160	200	

PEG 1.5%		6%T 8%C LAP PA gel + 1.5% PEG				
Total Volume [μL]			250	800	1000	
Reagent	Stock conc.	Final Conc.	Vol. [μL]	Vol. [μL]	Vol. [μL]	
Acrylamide soln [%T]	20	6	75	240	300	
PEG [%]	5	1.5	75	240	300	
Tris-HCl pH 8.8 [mM]	1.5	0.075	12.5	40	50	
BPMA [mM]	100	5	12.5	40	50	
LAP [%]	1	0.2	50	160	200	
Water (MilliQ)	-		25	80	100	

PEG 2.0%		6%T 8%C LAP PA gel + 2.0% PEG				
Total Volume [μL]			250	800	1000	
Reagent	Stock conc.	Final Conc.	Vol. [μL]	Vol. [μL]	Vol. [μL]	
Acrylamide soln [%T]	20	6	75	240	300	
PEG [%]	5	2	100	320	400	
Tris-HCl pH 8.8 [mM]	1.5	0.075	12.5	40	50	
BPMA [mM]	100	5	12.5	40	50	
LAP [%]	1	0.2	50	160	200	
Water (MilliQ)	-		0	0	0	

Fabrication steps

250 μL is sufficient for a full glass slide (25 \times 75 mm) of PA gel of height 40 μm .

1. Add all components to the precursor solution (include LAP or VA-086, do not include APS/TEMED), and make sure solution is at RT (to avoid gas entrapment within cold solution).
2. Vortex 30 s (to make sure PEG is well-mixed into precursor solution).
3. Degas 5 min. Use immediately.
4. (APS/TEMED: chemical polymerization)
 - a. Add TEMED with P1 pipette. Triturate \sim 10 times.
 - b. Add APS with P10 pipette.
 - c. Switch to P200 pipette. Triturate extensively for \sim 20-30 s (to mix PEG in solution).
 - d. Pipet immediately into polymerization setup (wafer, glass slide, etc.).
 - e. Immediately cover with foil-covered plastic dish, with a wet Kimwipe (to avoid dehydration).
 - f. (APS/TEMED) Polymerize for 20 min.
5. (LAP or VA-086: photo-polymerization)
 - a. Triturate extensively for \sim 20-30 s (to mix PEG in solution).
 - b. Pipet immediately into polymerization setup (wafer, glass slide, etc.).
 - c. Polymerize on the OAI for 4 minutes (VA-086) or 1 minute (LAP).
6. Note: All 8%C gels should look distinctly white rather than clear. Distinct opacity difference.
7. Use water to rehydrate gel for 1-2 min, then lift off of polymerization setup.
 - a. Gels should lift off cleanly.
8. Rinse in TBS-T (16-24 hours, note time, to allow for PEG diffusion out of gel). Exchange solution every \sim 8 hours.
 - a. If gels are polymerized on glass slides, place in 4-well dish, with at least 10 mL TBS-T per well (to create a sink).
9. Rinse in TBS-T briefly.
10. Rinse in DI water for 30 min before use (to remove TBS-T).

Appendix 2: Ultrathin IEF training bootcamp

Literature

To read first:

- Righetti textbook 1983 "Isoelectric focusing: theory, methodology, and applications"
- Herr dissertation, Chapter 1
- Yamauchi dissertation, Chapter 1
- Tentori, Yamauchi, Herr 2016 Angew Chemie (scIEF)
- Yamauchi, Tentori, Herr 2018 Electrophoresis (back to back pH gradient)
- Su, Herr 2018 Lab on a Chip (adherent cell IEF)
- O'Neill et al 2006 (25-cell IEF)
- Giddings textbook "Unified Separation Science"

- Kirby textbook
- Glantz textbook “Primer of Biostatistics”

To read promptly (non-exhaustive list):

- Herr, Molho, 2003 Analytical Chemistry (microfluidic IEF + free solution EP)
- Tia, Herr 2009 Lab on a Chip (review paper)
- Tia, Brown, Chen, Herr 2013 (microfluidic IEF)
- Hughes, Lin, Peehl, Herr 2012 PNAS (microfluidic IEF)
- Hughes, Tentori, Herr 2013 JACS (IEF and GFP)
- Tentori, Hughes, Herr 2013 Analytical Chemistry (2DE)
- Silvertand et al 2008 (cIEF review paper)
- Zhu et al 2005 Analytical Chemistry
- Johlfs et al 2015 PLOS One
- Hruska et al 2006 Electrophoresis (Simul5 software)
- Wang et al 2007 Electrophoresis
- Macounova et al 2000 Analytical Chemistry
- Macounova et al 2001 Analytical Chemistry
- Anderson 2008 Plant Journal
- the Righetti body of literature

Other researchers in the IEF space (non-exhaustive list)

- Rilbe/Svensson
- Gelfi
- Thormann
- Gorg
- Stoyanov
- Ivory
- Minerick
- Pawliszyn

On immobilized pH gradients (IPG) (non-exhaustive list)

- Righetti textbook 1990 “immobilized pH gradients: theory and methodology”
- Bjellqvist et al, 1982 IPG
- Sommer 2008

Superuser trainings

- Safety tour
- BNC
- BNC wafer fabrication
- Tissue culture
- OAI
- Onyx microscope
- Hamamatsu
- HVPS

- GenePix
- scWB training (potentially through Cold Spring Harbor Labs preparation in the summer)

Critical lab processes

- Wafer fabrication
- Well gel fabrication
- Lid gel fabrication
- scIEF
- scIEF worksheet and protocol
- MATLAB analysis script
- Immunoprobing

Bootcamp

1. scIEF with pl markers
 - a. Run 1: mentor runs, mentee observes
 - b. MATLAB analysis training
 - c. Run 2: mentee runs with mentor
 - d. Run 3: mentee runs, mentor observes
 - e. Run 4: mentee runs independently
 - f. MATLAB analysis comparison
 - g. Independent replicate runs by mentee to reach n=3 replicates matching mentor's data
 - i. Use EJS bootcamp results_summary pptx file as guideline
 - ii. Experiment type
 - iii. Assay parameters
 - iv. Key changes from previous experiments
 - v. Results
 - vi. Comments and main findings
2. scIEF with purified protein ladder
3. scIEF with U251-tGFP or MCF7-GFP + immunoblot for tGFP or GFP
4. slab IEF

Metrics for success

- Comfort with scIEF workflow
- Knowledge of IEF literature
- Knowledge of IEF metrics
- Validate MATLAB analysis: same metrics extracted from mentor's data sets
- Validate IEF training: reproducible replicates
- Validate IEF training: mentee's data with quantitative metrics matching those from mentor's data

Appendix 3: Protocol: Ultrathin IEF assay with pI markers and tGFP protein (native lysis)

sciEF + pI Markers + tGFP protein Runs # _____

Date: _____ Time: _____

SJ

(Separation) Well Gel (6% T)		
Slide design =		
Gelslick wafer & rinse		
Cut silanized glass slide to size (1/2 length)		
GEL TYPE =		
Fab gel		
(porogen) rinse in TBS-T at 4°C for 16-24 hours ()		
Rinse in DI H ₂ O for 30 minutes		
Cut to focusing region pre-solution		
Draw imaging zone on glass slide		
	DI H ₂ O	32.5 µL
1:100	pH 4.5 marker (12/16)	2.5 µL
1:100	pH 5.5 marker (12/16)	2.5 µL
1:100	pH 6.6 marker (12/16)	2.5 µL
	tGFP-488 protein	µL
Incubate in 30 µL solution for 30 minutes		
Do not dehydrate; use immediately		

OAI		
Turn on		
Warm up for >10 minutes		
20 mW/cm ² , longpass filter, 240 seconds		

(Analyte pH 4) Acid Lid Gel (15% T)		
GelSlick glass board		
Cut glass slide to size (3/4 length)		
GelSlick glass slide		
Uncoated spacer		
Assemble & tape		
Test with DI H ₂ O <input type="checkbox"/> no leak		
A3574	30% T	500.0 µL
13.5 mM	pKa 3.6 Immobiline	68.0 µL
6.4 mM	pKa 9.3 Immobiline	32.0 µL
	DI H ₂ O	300.0 µL
Fresh (2%)	VA-086	100.0 µL
20 mg/ml		
Degas 5 minutes (Σ = 1000 µL)		
Cast gel		
UV 240 seconds, longpass filter		
Aspirate out remaining liquid <input type="checkbox"/> gel		
Test with DI H ₂ O <input type="checkbox"/> no leak		

Order of operations:
Well gel in solution → base gel → acid gel → focusing gel

Slides =

TIMING MATTERS! This protocol makes sufficient quantities of reagents for two consecutive runs.

Test the pH of all 3 lid gel precursor solutions before use.

(Catholyte pH 10) Base Lid Gel (15% T)		
A3574	30% T	500.0 µL
5.6 mM	pKa 3.6 Immobiline	28.0 µL
14.4 mM	pKa 9.3 Immobiline	72.0 µL
	DI H ₂ O	300.0 µL
Fresh (2%)	VA-086	100.0 µL
20 mg/ml		
Degas 5 minutes (Σ = 1000 µL)		
Cast gel		
UV 240 seconds, longpass filter		
Aspirate out remaining liquid <input type="checkbox"/> gel		
Remove spacer & tape <input type="checkbox"/> no leak		
Rinse with DI H ₂ O		
Remove any remaining gel from center area		
Maintain in DI H ₂ O min		

ONYX MICROSCOPE

Microscope Room: Metamorph, HVPS		
Purple sciEF container	Tweezers	Razor
Well gel on wafer	Timer	Pen
Calibration slide	Tape	Doc
Lid gels on glass slide	Box	Onyx 16
Cooling block	TBS-T	HVPS
Turn on microscope		
Warm up for > 10 minutes		
Hours =		
Set up & tape down sciEF container onto microscope		
Set up & tape down HVPS electrodes		
Metamorph		
Calibrate (4x mag, 2x bin, ___ exp, ___ gain, UV-LP)		
Calibrate (4x mag, 2x bin, ___ exp, ___ gain, GFP)		
Calibrate (___ exp, ___ gain, Brightfield)		
Set up scan slide		
Set up folder for saving images		
Turn on Hamamatsu LC8 + warm for > 10 minutes		

Focusing Lid Gel (15% T)		
A3574	30% T	250.00 µL
18%	Triton X-100	27.75 µL
1:100	Sinulyte pH 4-7 CA	5.00 µL
	DI H ₂ O	167.25 µL
Fresh (2%)	VA-086	50.00 µL
20 mg/ml		
Degas 5 minutes (Σ = 1000 µL)		
Cast gel		
UV 240 seconds, longpass filter		
Aspirate out remaining liquid <input type="checkbox"/> gel		

Microscope		
Lights OFF		
Place well gel on sciEF chamber		
Lid gel -- CAREFULLY		
Glass slide on top		
Electrodes + 30 sec "lysis" and diffusive loading		
Turn on HVPS → manual, 690 V, constant voltage		
Scan slide 0 minutes		
Voltage on		

+ 30 sec "lysis"

Run A

Time	Voltage	Current	Power	Bands	Observations	Imaging Notes
0 sec	690 V					0.0 min UV-LP
10 sec						
20 sec						
30 sec						
40 sec						
50 sec						
1 min						1.0 min UV-LP
1.5 min						
2 min						
2.5 min						2.5 min UV-LP
3						
3.5						3.5 min GFP
4						
4.5						
5 min						5.0 min UV-LP
5.5						
6						6.0 min GFP
6.5						
7						Set up for Hamamatsu use
7.5 min						7.5 min UV-LP
8						
8.5						8.5 min GFP
9						
9.5						Set up for Hamamatsu use
10 min						10.0 min UV-LP
10.5						
11						11.0 min GFP
11.5						
12						
<p>Draw:</p> <ol style="list-style-type: none"> precisely where the imaging region is on the slide (for post-TBS-T imaging) alignment of focusing region to the top edge of the separation gel 						<p>Stop electric field at 12 minutes Close shutter UV 100% intensity / 45 s Open shutter</p>
						<p>Image immediately, if desired</p>
						<p>Post-UV GFP Post-UV UV-LP Post-UV Brightfield</p>
						<p>Remove glass slide Post-UV Brightfield</p>
						<p>Rinse in TBS-T 30 min</p> <p>Find ROI Image again (post-immobilization) Post-TBST GFP Post-TBST Brightfield</p>
<p>DI water on shaker for 5 minutes Dehydrate completely with nitrogen stream</p> <p>Genepix: tGFP native fluorescence (488)</p> <p>Immunoprobing for tGFP:</p> <p>Store in slide-holder in the dark at RT</p>						

Appendix 4: Protocol: Ultrathin scIEF assay with cells (native lysis)

Native scIEF + _____ cells Runs # _____ Date: _____ Time: _____ SJ

Well Gel (6% T)			
Slide design =			
Silanize wafer			
Rinse			
Cut silanized glass slide to size (1/2 length)			
Draw imaging zone on glass slide			
A3574	30% T	50.0 μ L	
1.5 M	TrisHCl	12.5 μ L	
	BPMA-C	12.5 μ L	
	DI H ₂ O	172.8 μ L	
Degas 10 minutes (Σ = 250 μ L)			
fresh	TEMED	0.2 μ L	
fresh 10%	APS	2 μ L	
Cast gel			
Silanized slide			
Wet kimwipe			
Foil			
Time =			min
Cut well gel to imaging zone			
Dehydrate gel completely & store in dark			

OAI			
Turn on			
Warm up for > 10 minutes			
Check 20 mW/cm ²			
Add longpass filter			
Time = 240 seconds			

Acid Lid Gel (15% T)			
GelSlick glass board			
Cut glass slide to size (3/4 length)			
GelSlick glass slide			
Uncoated spacer			
Assemble & tape			
Test with DI H ₂ O <input type="checkbox"/> no leak <input type="checkbox"/>			
A3574	30% T	500.0 μ L	
13.5 mM	pKa 3.6	68.0 μ L	
	Immobiline		
6.4 mM	pKa 9.3	32.0 μ L	
	Immobiline		
	DI H ₂ O	300.0 μ L	
20 mg/mL	VA-086	100.0 μ L	
stock			
Degas 5 minutes (Σ = 1000 μ L)			
Cast gel			
UV 240 seconds, longpass filter			
Aspirate out remaining liquid <input type="checkbox"/> gel <input type="checkbox"/>			
Test with DI H ₂ O <input type="checkbox"/> no leak <input type="checkbox"/>			

Slides =

Base Lid Gel (15% T)			
A3574	30% T	500.0 μ L	
5.6 mM	pKa 3.6 Immobiline	28.0 μ L	
14.4 mM	pKa 9.3 Immobiline	72.0 μ L	
	DI H ₂ O	300.0 μ L	
20 mg/mL	VA-086	100.0 μ L	
stock			
Degas 5 minutes (Σ = 1000 μ L)			
Cast gel			
UV 240 seconds, longpass filter			
Aspirate out remaining liquid <input type="checkbox"/> gel <input type="checkbox"/>			
Remove spacer & tape <input type="checkbox"/> no leak <input type="checkbox"/>			
Rinse with DI H ₂ O			
Remove any remaining gel from center area			
Maintain in DI H ₂ O / min			

Microscope Room: Hamamatsu, HVPS			
Purple scIEF container	Tweezers	Razor	
Dehydrated well gels	Timer	Pen	
10 mL 1:100 CA : H ₂ O	30 ml PBS	Doc	
60mm, 4-well dishes	Foil	Tape	
Cooling block	TBS-T	Onyx 16	
Lid gels on glass slide	Ice	HVPS	
Turn on Hamamatsu LC8 (2 steps)			
Warm up for > 5 minutes			
Hours =			
Setting = 100% intensity			
Setting = 45 seconds			
Set up & tape down scIEF container			
Set up & tape down HVPS electrodes			

Order of operations

Well gel → base gel → settle cells → acid gel → focusing gel
→ rehydrate → rinse → CA → lysis → EP → UV

Native scIEF

1% Sinulyte 1:100, base pH 10, 9 mm, 690 V

TIMING MATTERS! This protocol supports two consecutive runs.

Cells	
Dissociate cells	
Cell type =	
Passage =	
Resuspend _____ M/mL, 100 µL/well gel + cell strainer	
Store on ice	
Place 10 µL cell drop onto microwell line on well gel	
Place on cooling block for 10 MIN	

Focusing Lid Gel (15% T)		
A3574	30% T	500.0 µL
18% stock	Triton X-100	55.5 µL
1:100	Sinulyte pH 4-7 CA	10.0 µL
	DI H ₂ O	154.5 µL
20% w/v stock	CHAPS	180.0 µL (40 mg)
20 mg/mL stock	VA-086	100.0 µL
Degas 5 minutes (Σ = 1000 µL)		
Cast gel		
UV 240 seconds, longpass filter		
Aspirate out remaining liquid □ gel □		
Maintain alone / min		

Microscope Room	
Check under scope for cells	
Wick off fluid	
Rinse with PBS (5 mL)	
Rehydrate in PBS (10 mL)	for 5 MIN
Recheck under scope for cells	
Rinse with PBS (5 mL)	
Wipe off excess liquid from edges	
Place well gel in C.A. solution (5 mL) for 30 S	
Wipe off excess liquid from edges	
Well gel onto scIEF container	
Lid gel – CAREFULLY	for 30 S
Glass slide on top	
Electrodes	
Turn on HVPS → manual, 690 V , constant voltage	
Voltage on	for 6 MIN
Voltage off	
Select tape-covered button	
UV photocapture (sweep)	for 45 S
TBS-T on shaker	for 30 MIN
DI water on shaker	for 5 MIN
Dehydrate → Genepix → store at RT (long-term) + foil	

Cleanup	
Cooling block back to fridge / freezer	
All liquids and containers → bleach → biohazard	
All cells → bleach → biohazard	
Wipe down all surfaces with bleach → ethanol → dry	
No cycling Hamamatsu → on for use within 4 hours	
No cycling OAI → on all day	



Run A			Run B		
mA @	min	sec	mA @	min	sec
mA @	min	sec	mA @	min	sec
mA @	min	sec	mA @	min	sec
mA @	min	sec	mA @	min	sec
mA @	min	sec	mA @	min	sec
mA @	min	sec	mA @	min	sec
mA @	min	sec	mA @	min	sec
mA @	min	sec	mA @	min	sec
mA @	min	sec	mA @	min	sec
mA @	min	sec	mA @	min	sec
mA @	min	sec	mA @	min	sec
mA @	min	sec	mA @	min	sec
mA @	min	sec	mA @	min	sec
mA @	min	sec	mA @	min	sec
mA @	min	sec	mA @	min	sec
mA @	min	sec	mA @	min	sec

Appendix 5: Protocol: Ultrathin scIEF assay with cells (denaturing lysis)

Denaturing scIEF + _____ cells Runs # _____ Date: _____ Time: _____ SJ

Well Gel (6% T)		
Slide design =		
Silanize wafer		
Rinse		
Cut silanized glass slide to size (1/2 length)		
Draw imaging zone on glass slide		
A3574	30% T	50.0 μ L
1.5 M	TrisHCl	12.5 μ L
	BPMA-C	12.5 μ L
	DI H ₂ O	172.8 μ L
Degas 10 minutes (Σ = 250 μ L)		
fresh	TEMED	0.2 μ L
fresh 10%	APS	2 μ L
Cast gel		
Silanized slide		
Wet kimwipe		
Foil		
Time =		min
Cut well gel to imaging zone		
Dehydrate gel completely & store in dark		

OAI	
Turn on	
Warm up for > 10 minutes	
Setting = 20 mW/cm ²	
Setting = longpass filter	
Setting = 240 seconds	

Acid Lid Gel (15% T)		
GelSlick glass board		
Cut glass slide to size (3/4 length)		
GelSlick glass slide		
Uncoated spacer		
Assemble & tape		
Test with DI H ₂ O		<input type="checkbox"/> no leak <input type="checkbox"/>
A3574	30% T	500.0 μ L
13.5 mM	pKa 3.6	68.0 μ L
	Immobiline	
6.4 mM	pKa 9.3	32.0 μ L
	Immobiline	
	DI H ₂ O	300.0 μ L
Fresh (2%)	VA-086	100.0 μ L
20 mg/ml		
Degas 5 minutes (Σ = 1000 μ L)		
Cast gel		
UV 240 seconds, longpass filter		
Aspirate out remaining liquid		<input type="checkbox"/> gel <input type="checkbox"/>
Test with DI H ₂ O		<input type="checkbox"/> no leak <input type="checkbox"/>

Slides =

Base Lid Gel (15% T)		
A3574	30% T	500.0 μ L
5.6 mM	pKa 3.6 Immobiline	28.0 μ L
14.4 mM	pKa 9.3 Immobiline	72.0 μ L
	DI H ₂ O	300.0 μ L
Fresh (2%)	VA-086	100.0 μ L
20 mg/ml		
Degas 5 minutes (Σ = 1000 μ L)		
Cast gelAQ		
UV 240 seconds, longpass filter		
Aspirate out remaining liquid		<input type="checkbox"/> gel <input type="checkbox"/>
Remove spacer & tape		<input type="checkbox"/> no leak <input type="checkbox"/>
Rinse with DI H ₂ O		
Remove any remaining gel from center area		
Maintain in DI H ₂ O		/ min

Microscope Room: Hamamatsu, HVPS		
Purple scIEF container	Tweezers	Razor
Dehydrated well gels	Timer	Pen
20 mL 1:100 CA : H ₂ O	30 ml PBS	Doc
60mm, 4-well dishes	Foil	Tape
Cooling block	TBS-T	Onyx 16
Lid gels on glass slide	Ice	HVPS
Turn on LC8 (2 steps)		
Warm up for > 5 minutes		
Hours =		
Setting = 100% intensity		
Setting = 45 seconds		
Set up & tape down scIEF container		
Set up & tape down HVPS electrodes		

15 minutes to weigh detergents

Order of operations:

Well gel \rightarrow base gel \rightarrow settle cells \rightarrow acid gel \rightarrow focusing gel
 \rightarrow rehydrate \rightarrow rinse \rightarrow CA \rightarrow lysis \rightarrow EP \rightarrow UV

TIMING MATTERS! This protocol can be used for two consecutive experimental runs.

Denaturing scIEF

Cells	
Dissociate cells	
Cell type =	
Passage =	
Resuspend _____ M/mL, 100 µL/well gel + cell strainer	
Store on ice	
Place 10 µL cell drops onto microwell line on well gel	
Place on cooling block for 10 MIN	

Focusing Lid Gel (15% T)		
A7802	40% T	375.0 µL
18%	Triton X-100	55.5 µL
1:100	Sinulyte pH 4-7 CA	10.0 µL
	DI H ₂ O	559.5 µL
Fresh, solid	CHAPS	40 mg
Fresh, solid	Urea	420 mg
Fresh, solid	Thiourea	152 mg
Fresh, solid	VA-086	2 mg
Dissolve all chaotropes and detergents thoroughly		
Degas 5 minutes ($\Sigma = 1000 \mu\text{L}$)		
Cast gel		
UV 240 seconds, longpass filter		
Aspirate out remaining liquid □ gel □		
Maintain alone / min		

Microscope Room	
Check under scope for cells	
Wick off fluid	
Rinse with PBS (5 mL)	
Rehydrate in PBS (10 mL)	for 5 MIN
Recheck under scope for cells	
Rinse with PBS (5 mL)	
Wipe off excess liquid from edges	
Place well gel in C.A. solution (5 mL) for 30 S	
Wipe off excess liquid from edges	
Well gel onto scIEF container	
Lid gel – CAREFULLY	for 30 S
Glass slide on top	
Electrodes	
Turn on HVPS → manual, 690 V , constant voltage	
Voltage on	for 6 MIN
Voltage off	
Select tape-covered button	
UV photocapture (sweep)	for 45 SEC
TBS-T on shaker	for 30 MIN
DI water on shaker	for 5 MIN
Dehydrate → Genepix → store at RT (long-term) + foil	

Cleanup	
Cooling block back to fridge / freezer	
All liquids and containers → bleach → biohazard	
All cells → bleach → biohazard	
Wipe down all surfaces with bleach → ethanol → dry	
No cycling Hamamatsu → on for use within 4 hours	
No cycling OAI → on all day	



Run A			Run B		
mA @	min	sec	mA @	min	sec
mA @	min	sec	mA @	min	sec
mA @	min	sec	mA @	min	sec
mA @	min	sec	mA @	min	sec
mA @	min	sec	mA @	min	sec
mA @	min	sec	mA @	min	sec
mA @	min	sec	mA @	min	sec
mA @	min	sec	mA @	min	sec
mA @	min	sec	mA @	min	sec
mA @	min	sec	mA @	min	sec

Appendix 6: Protocol: slab IEF with purified protein ladder

Protocol adapted from ThermoFisher: https://assets.thermofisher.com/TFS-Assets/LSG/manuals/electrophoresisguide_man.pdf, Invitrogen Novex pre-case gel electrophoresis guide, IM-1002, revised 07 Oct 2010

Refer to XCell SureLock™ Mini-Cell manual (IM-9003) for device instructions.

Purchase IEF materials

- Novex IEF buffer set (Invitrogen LC5377)
 - o Novex IEF anode buffer
 - o Novex IEF cathode buffer
 - o Novex IEF sample buffer
- Novex IEF gels (Invitrogen EC66452BOX for pH 3-7)
 - o 5%T 2.6%C polyacrylamide gel + 2% Novex ampholytes
 - o The 5 gels in this order are viable for 2 months from date of receipt. Plan experiments accordingly.
 - o Store at 4°C
- IEF standard, pH range 4.45-9.6 (BioRad 161-0310)
- XCell SureLock Mini-Cell (Invitrogen IM-9003, also used for slab Western blot in the Herr lab)
- (if transfer is desired) Rapid transfer system, PVDF membrane, filter paper, methanol
- (if fixation is desired) Fixative
- (if total protein stain is desired) Ponceau or Coomassie total protein stain
- (if immunoblot is desired) selected primary antibody, selected secondary antibody conjugated with HRP, Western Lightning solution, BSA, TBS-T
- Before proceeding, check lab stocks of all other materials.

Prepare cell lysate

1. Trypsinize cells, spin down, resuspend in 1× PBS, count.
2. Wash 2x in 1× PBS
3. Make IEF buffer of choice.
 - a. Native IEF buffer (1% TritonX-100, 3.6% CHAPS, 1% HALT inhibitor, in DI water, 20 mL)
 - i. 1.111 mL of stock 18% TritonX-100 solution
 - ii. 40 mg of CHAPS powder
 - iii. 18.689 mL of DI water
 - iv. 200 µL of HALT protease/phosphatase inhibitor (1:100 dilution final)
 - b. Denaturing IEF buffer with DTT (7M urea, 2M thiourea, 1% TritonX-100, 3.6% CHAPS, 20 mM DTT solution, 1% HALT inhibitor, in 20 mL DI water)
 - i. 1.111 mL of stock 18% TritonX-100 solution (1% final)
 - ii. 40 mg of CHAPS powder (3.6% final)
 - iii. 8400 mg of urea (7M final)
 - iv. 3040 mg of thiourea (2M final)

- v. 18.689 mL of DI water
- vi. 61.7 mg of DTT powder (20 mM final)
 - 1. 154.253 g/mol
 - 2. from Wang et al Proteomics 2004 – not stable in water. Make fresh and use promptly.
- vii. 200 µL of HALT protease/phosphatase inhibitor (1:100 dilution final)
- 4. Spin down, resuspend cells in IEF buffer of choice.
 - a. Use biohazard-compatible centrifuge.
 - b. Make sure to orient all Eppendorf tubes the same way, in case cell pellet is difficult to visually identify.
 - c. Make sure to close Eppendorf tubes completely.
- 5. Allow cells to lyse for 60 minutes, vortexing every 5-10 min.
- 6. Centrifuge 14,000 g, 15 min, 4°C.
- 7. Claim supernatant.
 - a. Store viscous remaining solution at -20°C until final results are collected.
- 8. Freeze -20°C overnight if needed.
- 9. * Consider desalting protocol for IEF.
- 10. Thaw on ice.
- 11. Dilute 1:1 with appropriate sample buffer (below). Load into slab IEF gel (below).
- 12. Store remaining lysate in -20°C freezer.

Prepare anode buffer

Prepare 1× IEF Anode Buffer using Novex® IEF Anode Buffer (50X).

- 1. Prepare 1000 mL of IEF Anode Buffer as follows:

Reagent	Amount
Novex IEF Anode Buffer (50×)	20 mL
MilliQ water	980 mL
Total Volume	1000 mL

- 2. Mix thoroughly. Use this buffer to fill the Lower Buffer Chamber of the XCell SureLock™ Mini-Cell for electrophoresis.

Prepare cathode buffer

Prepare 1× IEF Cathode Buffer using the appropriate Novex® IEF Cathode Buffer pH 3–10 (10×) or pH 3–7 (10×)

- 1. Prepare 200 mL of IEF Cathode Buffer as follows:

Reagent	Amount
Novex IEF Cathode Buffer (10×)	20 mL
MilliQ water	180 mL
Total Volume	200 mL

- 2. Mix thoroughly. Use this buffer to fill the Upper Buffer Chamber of the XCell SureLock™ Mini-Cell for electrophoresis.

Prepare samples

Samples for IEF Gels are prepared without SDS to avoid affecting the pI of the protein. Reducing agents are also **not recommended** for the same reason.

1. Prepare samples for IEF Gels as described below (on ice):

Reagent	Amount
Sample	5 μ L
Novex IEF Sample Buffer pH 3–7 (2 \times)	5 μ L
Total	10 μ L

2. Load the sample immediately. **Do not heat samples for IEF Gels.**

Sample order

For ease of subsequent analysis, fill at least 2 lanes with undiluted IEF standard, and stagger these lanes such that the gel orientation is not reversible.

Lane	Sample
1	
2	
3	IEF standard
4	
5	
6	
7	IEF standard
8	
9	
10	
11	
12	

Slab protocol

Wear gloves and safety glasses when handling gels. XCell *SureLock*TM Mini-Cell requires 200 mL for the Upper Buffer Chamber and 600 mL for the Lower Buffer Chamber.

1. Before starting, make sure HVPS has slab IEF electrophoresis settings loaded.
2. Remove the Novex® Pre-Cast Gel from the pouch.
3. Rinse the gel cassette with deionized water. Peel off the tape from the bottom of the cassette.
4. Gently pull the comb out of the cassette in one smooth motion.
5. Rinse the sample wells with the appropriate 1 \times Running Buffer (**Cathode Buffer**). Invert the gel and shake the gel to remove the buffer. Repeat two more times.
6. Orient the two gels in the Mini-Cell such that the notched “well” side of the cassette faces inwards toward the Buffer Core. Seat the gels on the bottom of the Mini-Cell and lock into place with the Gel Tension Wedge. Refer to the XCell *SureLock*TM Mini-Cell manual (IM-9003) for detailed instructions.
 1. **Note:** If you are running just one gel, use the plastic Buffer Dam in place of the second gel cassette to form the Upper Buffer Chamber.

7. Fill the Upper Buffer Chamber with a small amount of the Running Buffer to check for tightness of seal. If you detect a leak from Upper to the Lower Buffer Chamber, discard the buffer, reseal the chamber, and check the seal again.
 1. **Cathode buffer**
8. Once the seal is tight, fill the Upper Buffer Chamber (Inner) with the appropriate 1× Running Buffer. The buffer level must exceed the level of the wells.
9. Load an appropriate volume of sample at the desired protein concentration onto the gel (see page 8 of IM-1002 manual for recommended loading volumes).
10. Load IEF protein standard.
11. Fill the Lower Buffer Chamber with 600 mL of the appropriate 1× Running Buffer.
 1. **Anode buffer**
12. Place the XCell *SureLock*[™] Mini-Cell lid on the Buffer Core. With the power on the power supply turned off, connect the electrode cords to the power supply [red to (+) jack, black to (-) jack].
 1. **Use new lid, connected to HVPS electrodes, connected to HVPS**

Electrophoresis conditions

Before starting to assemble the slab IEF, make sure to add the following steps as a method to the HVPS.

HVPS >> IEF >> slab IEF method

- 100 V constant for 1 hour
- 200 V constant for 1 hour
- 500 V constant for 30 minutes

Note start time.

Start to prepare for rapid transfer > 10 minutes before the 500 V IEF step ends (once the electric field is turned off, the proteins will diffuse out of their focused bands. Any extraneous time before transfer results in losses in separation resolution).

Transfer

Use rapid transfer system! ***Prepare membranes/filter papers during 500V stage.***

1. Follow instructions on system
2. Here, we used PVDF membrane and 4 pieces filter paper (2 pieces around PVDF in package, 2 extra)
3. During 500V stage
 - Place 4 pieces of filter paper in Ziploc container to equilibrate.
 - Place PVDF membrane in pipette tip lid and cover in cold MeOH (in fridge) for 1 min. Then pour back and add transfer buffer. Use tweezers to handle membrane.
 - Pry open gel holder
 - Cut off comb region and thicker region at bottom
 - Rinse in transfer buffer
4. After 500V stage

- Disassemble IEF gel from Mini-Cell and from containment.
- Place 2 pieces of wetted filter paper on bottom electrode
- Place membrane over filter paper (place down slowly from one corner to avoid introducing bubbles)
- Peel gel off of edge while gel is under transfer buffer. Place directly on membrane
- Add more buffer, ensure no bubbles (can press on gel with gloves)
- Add 2 pieces of filter paper on top and use roller to ensure no bubbles
- Start transfer (mixed MW program is typically sufficient)
- Prepare small plastic box for membrane (available from Stanley Stockroom)

Imaging pre-stain

1. Take pictures of the membrane and the gel to gauge color
2. Image the membrane using white light epi on the Chemidoc.
3. Image the membrane (UV-longpass for pI markers, fluorescence for purified IEF protein ladder) on Onyx.

Ponceau stain

1. Use Amresco Ponceau S stain.
2. 1x solution in square dish
3. Stain for 2-**10 minutes** (longer = more intense stain).
4. Stop stain by rinsing in DI water.

Imaging post-stain

1. Image the membrane using white light epi on the Chemidoc, and take pictures.

Blot and probe

Following immunoprobng protocol from slab Western blot

1. Rinse out Ponceau stain extensively (multiple solution exchanges until the DI water is clear).
2. Block in 5% BSA in TBS-T
3. Primary antibody probing in small plastic box, 10 mL of 0.5% BSA/TBS-T solution with set of antibodies, 4°C overnight
4. Save primary antibody solution for future use
5. Rinse 3x in TBS-T for 10 min each on shaker
6. Sequential secondary antibody probing
 - a. Secondary antibody probing in small plastic box, 10 mL of 0.5% BSA/TBS-T solution with single antibody type, 1h on shaker
 - b. Save secondary antibody solution for future use
 - c. Rinse 3x in TBS-T for 10 min each on shaker
 - d. Set up Chemidoc
 - i. Turn on system and camera

- ii. Open ImageLab software
- iii. Create new protocol
- iv. Choose Application → Blots → Chemi
- v. Could also create custom application
- vi. If doing UV, can add Xciteblue conversion screen
- vii. Usually set to Bio-Rad ready gel, which has similar size to membrane
- viii. Usually set exposure time to 10-30s
- e. Chemiluminescence on Chemidoc
 - i. Mix 2 components of Western Lightning solution 1:1, 8 mL
 - ii. Go to Chemidoc, wait ~90s
 - iii. Wipe plate with Kimwipe
 - iv. Use tweezers to place membrane (centered) on plate
 - v. Use 'position gel' to show brightfield and move the membrane until it's in field
 - vi. Take images at different exposures (10s, 30s, 1 min, 5 min)
 - vii. Take white light epi image to see ladder for positioning
 - viii. If signal degrades too much, can place membrane back into detection reagent and image again
 - ix. Remove membrane, place in dish, clean tray with Kimwipe and water
 - x. Export TIFs and save files
- f. Wash membrane in DI water
- g. Wash membrane in TBS-T 1h
- h. Repeat secondary immunoprobng and imaging for remaining antibodies

Storage

Store membrane short-term in 1× TBS-T, parafilm, aluminum foil, 4°C

Appendix 7: Protocol: HTP scIEF fabrication of separation gels

Use HTP IEF wafer (silanized, no GelSlick®) with 32- μ m-diameter, 40- μ m-height microposts at 400x400 μ m spacing in 16x16 mm blocks

Typically, 8 microwell gels of 18x18 mm size is sufficient for an experiment.

Materials:

- 30% acrylamide stock solution
- APS
 - o Weigh out into Eppendorf tube, and make a 10% solution in MilliQ water.
- TEMED
 - o Use 100% solution (no dilution).
- BPMA:
 - o Most recent aliquot from shared stock at -20°C. Make sure the vial has not been previously thawed. No dilution. Thaw at RT under foil, and triturate.
- Novex Zoom® ampholytes pH 4-7
- Rhinohide™
- 18% TritonX-100 stock solution
 - o Make 5+ mL of 18% stock solution. First, pipet requisite MilliQ water into 15 mL Falcon tube. Cut end 1000 mL pipet tip for a wider opening. Slowly (avoid bubbles or damage to pipette) pipet requisite 100% TritonX-100 from stock bottle into Falcon tube. Leave pipet tip in Falcon tube. Heat in a water bath at 55°C for an hour. Pipet gently to mix.
 - o Store at RT under foil for <1 month
- 1 mm spacers
- Silanized glass slide
- Z-projection IEF wafer
- Razor blade (NEW! Make sure this is sharp)
- 4-well plate

Precursor solutions

6%T 3.3%C PA gel + 10% new Rhinohide™							
200	30%T 3.3%C 29:1 polyacrylamide						
50	BPMA						
641.2	DI water						
100	10% Rhinohide™ final (new)						
0.8	TEMED 100%						
8	APS 10%						
1000	total						

Fabrication steps

1000 μ L is sufficient for a single 18x18x1 mm gel (X-Y-Z).

1. Add all components to the precursor solution except APS and TEMED, and make sure solution is at RT (to avoid gas entrapment within cold solution).
2. Set up wafer + 1 mm spacers. Tape down spacers at the edges.
3. Mix well. Degas 5 min. Use immediately.
4. Add TEMED with P1 pipette. Triturate ~10 times.
5. Add APS with P10 pipette.
6. Switch to P200 pipette. Pipet immediately onto wafer. Overlay silanized glass slide.
7. Immediately cover with foil-covered plastic dish, with a wet Kimwipe (to avoid dehydration).
8. Polymerize for 1 hour. At 30 min mark, check hydration of Kimwipe.
9. Use water to rehydrate gel for 1-2 min, then lift off of polymerization setup.
 - a. Gels should lift off cleanly, without damaging microposts.
10. Cut gels to desired dimensions and gently remove from glass slide.
 - a. 18 \times 18 mm in X-Y
 - b. 9 \times 9 mm in X-Y
11. Place free-standing separation gels well-up in 4-well plate. Place multiple gels into a single well, without stacking. Minimize well usage.
12. Rinse in MilliQ water.
13. Create IEF solution (7 mL per well of 4-well plate)
 - a. 2% Zoom[®] ampholyte pH 4-7 solution
 - b. 1% TritonX-100 (from 18% stock solution)
 - c. In MilliQ water
14. Incubate gels in 7 mL solution for each well of a 4-well plate; aluminum foil; 4[°]C overnight
 - a. IEF solution should diffuse into gel to equilibrium.
15. Use promptly the next day.

Appendix 8: Protocol: HTP scIEF fabrication of anolyte and catholyte gels

The anolyte and catholyte boundary gels for the HTP IEF assay are featureless 18 \times 18 \times 0.5 mm or 9 \times 9 \times 0.5 mm PA gels with immobilines incorporated into the hydrogel matrix for embedded pH.

Materials:

- 30% T acrylamide solution
- pKa 3.6 immobiline
- pKa 9.3 immobiline
- pKa 7.0 immobiline
- VA-086
- DI water + squirt bottle

- Glass plate
- Silanized glass slide
- 0.5 mm spacers
- Schematic of 18×18 and 9×9 gel dimensions
- Razor blade (NEW! Make sure this is sharp)
- 4-well plate

Precursor solutions

Anolyte Gel (6% T) pH 4			
A3574	30% T Acrylamide solution	500.00	
13.5 mM	pKa 3.6 Immobiline	68.00	
6.4 mM	pKa 9.3 Immobiline	32.00	
	DI H ₂ O	300.00	
Fresh (2%) 20mg/mL	VA-086	100.00	
Degas 5 minutes ($\Sigma = 1000 \mu\text{L}$)			
Catholyte Gel (6% T) pH 7			
A3574	30% T Acrylamide solution	500.00	
6.5 mM	pKa 3.6 Immobiline	32.50	
13.5 mM	pKa 7.0 Immobiline	67.50	
	DI H ₂ O	300.00	
Fresh (2%) 20mg/mL	VA-086	100.00	
Degas 5 minutes ($\Sigma = 1000 \mu\text{L}$)			
Catholyte Gel (6% T) pH 10			
A3574	30% T Acrylamide solution	500.00	
5.6 mM	pKa 3.6 Immobiline	28.00	
14.4 mM	pKa 9.3 Immobiline	72.00	
	DI H ₂ O	300.00	
Fresh (2%) 20mg/mL	VA-086	100.00	
Degas 5 minutes ($\Sigma = 1000 \mu\text{L}$)			

Fabrication steps

Remember to make a set of anolyte gels (pH 4) and a set of catholyte gels (pH 10 or pH 7). It is recommended to briefly set up a work station at a bench next to the OAI.

1. GelSlick® glass plate and glass slide.
2. Place the glass slide on top of the glass plate, propped up on the 0.5 mm spacers. Tape down the edges of the spacers, but make sure the tape does not interfere with the 0.5 mm height of this assembly. Check that the spacers are maximally spaced apart to maximize the number of gels obtained from each round of polymerization.
3. Add all components to the precursor solution, and make sure solution is at RT (to avoid gas entrapment within cold solution). Mix thoroughly.
4. Use pH strips to test pH of each solution.
5. Degas solution for 5 minutes.

6. Pipet the degassed PA solution between the glass slide and glass plate. Make sure there are no air bubbles.
7. After polymerization, remove from OAI. Place glass plate over the 18x18 or 9x9 gel schematic. Gently remove glass slide without disrupting gel. Add a small amount of DI water to maintain hydrated state of gel.
8. Hold the razor blade perpendicular to the glass slide. Slide through the gel to remove edges, then to cut gel to desired dimensions (18×18×0.5 or 9×9×0.5 mm), using the schematic underneath as a guide.
9. Place gels in DI water in the 4-well plate.
10. Use pH strips to test pH of each gel (dry gently with edge of Kimwipe to remove fluid layer).
11. Rinse glass plate thoroughly before reuse or storage. Use fresh silanized glass slides for each round of gel polymerization.
12. Use promptly that day.

Appendix 9: Protocol: HTP scIEF with purified protein ladder (native lysis)

Last updated 11-06-2018

Experimental Goal on 11-06-2018

Investigate ability to focus proteins in the ZEP system with our semi-validated IEF protein ladder. Investigate source of unusual focusing in HTP scIEF gels.

- Test catholyte gel → **4/7 vs 4/10**
- Test separation time → **45, 60, 90, 120 sec**

Learning moments from previous experiments:

- Use anolyte/catholyte shield gels to form the boundary conditions.
- This time, use larger (18×18 mm) gels to reduce edge effects.
- Choose a 6%T gel for focusing, and use Zoom® ampholyte buffers in thick separation gel.
- Leave gels in ampholyte buffer overnight to allow any unpolymerized acrylamide/Rhinohide™/BPMA to diffuse away.
- Attempt to focus new labeled ladder of TI, CA, and MYO in native conditions at 34 V/cm (pending current limitations).
- Aim for a field of 166 V/cm (34V for BCs) (scIEF uses 139 V/cm).
- Remember to place the spacers on the (+) electrode plate.
- The filter paper hydration chamber is not required.

Stack: benchtop << **(+) electrode plate** << 500 μm anolyte gel << 1 mm separation gel << protein solution << 500 μm catholyte gel << **(-) electrode plate**

Experimental groups = 6%T 10% Rhinohide™ in MilliQ water, 60s electrophoresis, ladder, no filter paper (8 gels)

Reagents and Equipment

- IEF buffer, from **Appendix 8**
 - MilliQ water
 - 18% Triton X-100 solution
 - Zoom® pH 4-7 ampholytes
- 2 mm spacers
- Labeled protein solutions in 1× PBS
 - Myoglobin from 7/3/18 labeling round
 - TI and CA from 6/28/18 labeling round
- Naturally fluorescent proteins
 - Phycocyanin
 - tGFP
- 18×18 mm separation gels fabricated, with IEF buffer diffused into gel overnight at 4°C, from **Appendix 7**
- Anolyte and catholyte gels, freshly fabricated, from **Appendix 8**
 - pH 4 anolyte
 - pH 7 catholyte
 - pH 10 catholyte
- New electrode system with magnetic closures (for projection electrophoresis)
- Hamamatsu

Expectations:

1. All gels: We will see spots of protein in the gel corresponding to the microwells.
2. HTP IEF gels: If we are focusing, the protein bands should approach a pseudo-equilibrium position, that is not disrupted by extended time.

Testing after experiment:

1. Rinse the gels in DI water before placing in 2 mL 1× TBS-T.
2. Leave gel in 1× TBS-T overnight to rinse away any non-photocaptured protein, and image using Onyx and ScanSlide after this incubation.
3. Use a razor blade to slice the gel to image cross-sections.
 - a. Characterize slope of pH gradient, linearity of pH gradient, separation resolution between each fluorescent protein, and ΔpI_{min} .
4. Next steps: Image the gel with confocal. Confirm reproducibility of this result. Characterize IEF stability with timelapse experiment.

Preparation of purified protein solutions

For 40 μ L mixed IEF protein ladder solution, mix:

- 13.33 μ L TI-647 (2018-06-28)
- 13.33 μ L MYO-488 (2018-07-03)
- 13.33 μ L CA-555 (2018-06-28)

Electrophoresis

1. Make sure Hamamatsu is turned on and cap is off
2. Stack:
 - a. Anolyte gel (in DI water)
 - b. Separation well gel
 - i. Partly dry (Kimwipe)
 - ii. Add 5 μ L protein solution to each gel. Spread with flat edge of 10 μ L pipette tip.
 - c. Catholyte gel (in DI water)
3. Stack on bottom electrode and assemble electrode system
4. Run electrophoresis at **34 V (BCs)**.
5. Quickly open the electrodes, remove the filter paper, and photocapture 45s using the Hamamatsu. Record the time to photocapture start, and gel orientation with respect to the electrodes.

Imaging

1. Cut the gel through wells, creating a slice to image with widefield fluorescence.
2. Image the gel using fluorescence microscopy (multi-dimensional imaging on Onyx) and ScanSlide.
3. If Onyx images look good, image the gel with confocal microscopy to more quantitatively measure the protein migration properties.

Notes during experiment

Trial	Conditions	IEF & Photocapture	Observations
1	10% Rhinohide™ 60s electrophoresis, ladder, no filter paper pH 4 acid BC pH 7 base BC	0s 10s 20s 30s 40s 50s 60s $t_{\text{photocapture}}$ Direction	
2	10% Rhinohide™ 60s electrophoresis, ladder, no filter paper pH 4 acid BC pH 10 base BC	0s 10s 20s 30s 40s 50s 60s $t_{\text{photocapture}}$ Direction	
3	10% Rhinohide™ 90s electrophoresis, ladder, no filter paper pH 4 acid BC pH 7 base BC	0s 10s 20s 30s 40s 50s 60s 70s 80s 90s $t_{\text{photocapture}}$ Direction	

4	10% Rhinohide™ 90s electrophoresis, ladder, no filter paper pH 4 acid BC pH 10 base BC	0s 10s 20s 30s 40s 50s 60s 70s 80s 90s t _{photocapture} Direction	
5	10% Rhinohide™ 120s electrophoresis, ladder, no filter paper pH 4 acid BC pH 7 base BC	0s 10s 20s 30s 40s 50s 60s 70s 80s 90s 100s 110s 120s t _{photocapture} Direction	
6	10% Rhinohide™ 120s electrophoresis, ladder, no filter paper pH 4 acid BC pH 10 base BC	0s 10s 20s 30s 40s 50s 60s 70s 80s 90s 100s 110s 120s t _{photocapture} Direction	
7	10% Rhinohide™ 45s electrophoresis, ladder, no filter paper pH 4 acid BC pH 7 base BC	0s 10s 20s 30s 40s 45s t _{photocapture} Direction	
8	10% Rhinohide™ 45s electrophoresis, ladder, no filter paper pH 4 acid BC pH 10 base BC	0s 10s 20s 30s 40s 45s t _{photocapture} Direction	

Appendix 10: Protocol: desalted IEF cell lysate

Last updated in November 2016

Cell Lysate

Source (with modifications): 2D Gel Sample Preparation using Amersham kit, protocol provided online by Rutgers New Jersey Medical School

One may also refer to the cell lysate protocol in **Appendix 6**.

Estimated Time: 1 hour (not including pre-procedure cell singularization).

Materials:

- Denaturing lysis buffer (5 mL), thoroughly mixed and dissolved
 - o 2100 mg urea
 - o 760 mg thiourea
 - o 200 mg CHAPS
 - o 277.5 μ L of 18% v/v TritonX-100 (final 1%)
 - o 4.7225 mL of DI water
 - o * Note that these are the same concentrations as in the denaturing focusing gel!
 - o * Incorporate phosphatase/kinase/protease inhibitors as needed (1:100 HALT).
 - o * Do not freeze this buffer! Chaotropes degrade over time when hydrated.
- RIPA buffer (5 mL)
 - o Pierce RIPA buffer, catalog #89900
 - o * Incorporate phosphatase/kinase/protease inhibitors as needed.
- Dissociated cells
- Vortex
- Centrifuge
- Eppendorf tubes (1.5 mL) blocked with 5% BSA in TBS-T

Steps:

1. (during cell dissociation) Turn on Beckman Coulter Allegra 21R Centrifuge. Set to 4°C. Close and allow to cool to goal temperature.
2. (recommended) Block 4+ Eppendorf tubes (1.5 mL) with 5% BSA in TBS-T for 1 hour. Use these tubes for all procedures.
 - a. This should inhibit protein adsorption.
3. Transfer appropriate quantity of cells to 2 1.5 mL Eppendorf tubes.
 - a. 1 M / mL is effective (SJ Oct 2016).
 - b. **Vial #1** = denaturing lysis buffer condition
 - c. **Vial #2** = RIPA buffer condition
4. Pellet cells.
5. Resuspend cell pellets in the respective lysis buffer.
 - a. You need the RIPA buffer sample for BCA assay. All of the chaotropes and detergents in the denaturing lysis buffer affect the readout of the BCA assay.
 - b. Note: you will need at least 1.5 mL of each lysis solution for the upcoming desalting and BCA assay procedures. I recommend freezing down all excess lysis solution with your lysates in -20°C.
6. Sonicate for 3 rounds of 5 seconds.
7. Move Eppendorf tubes to centrifuge. Spin down at 14,000 g for 30 min at 4°C.
 - a. DNA should collect at the bottom of the tube (semi-transparent viscous material). Be careful when moving Eppendorf tubes.
8. Transfer supernatant to clean Eppendorf tubes **Vials #3 and #4**.
9. <<PAUSE>> Store at -20°C.

Desalting

Source (with modifications): ReadyPrep 2-D Cleanup Kit Instruction Manual, Bio-Rad

Estimated Time: 1.5 hours (not including pre-procedure preparation).
Numerous short incubation steps!

Materials:

- ReadyPrep 2-D Cleanup Kit, catalog #163-2130, Bio-Rad
- Centrifuge and vortex

Note: there are other mechanisms by which to desalt a lysate. Bio-Rad's Bio-Spin Columns with Bio-Gel P-30 is also effective (see Tentori, Yamauchi, Herr *Angew Chem* 2016,¹⁹ supplement page 9, section entitled "Cell Lysate Microfluidic IEF").

Steps:

1. (at least 1 hour before) Put the large Wash Reagent 2 bottle in the -20°C freezer. Failure to do so will drastically affect protein yield.
2. (recommended) Block 2+ Eppendorf tubes (1.5 mL) with 5% BSA in TBS-T for 1 hour. Use these tubes for all procedures.
 - a. This should inhibit protein adsorption.
3. (30 minutes prior) Turn on Beckman Coulter Allegra 21R Centrifuge. Set to 4°C. Close and allow to cool to goal temperature.
4. Thaw lysate solutions. Mix thoroughly.
5. Transfer 100 µL of cell lysate (in denaturing lysis buffer, **Vial #3**) to a new Eppendorf tube (**Vial #5**).
6. Transfer 100 µL of cell lysate (in RIPA buffer, **Vial #4**) to a new Eppendorf tube (**Vial #6**).
 - a. Goal concentration = 1 – 500 µg protein in 100 µL lysate solution.
 - b. Use BCA assay to quantify.
7. Use **Vials #5 and #6**.
8. Follow **steps 2-14** (pages 5-8 of the ReadyPrep manual).
9. Post-desalting, you should have **Vials #5 and #6** for the desalted cell IEF lysate in denaturing lysis buffer and RIPA buffer, respectively.
10. <<PAUSE>> Store at -20°C. Make sure to vortex extensively before use.

BCA Assay

Source (with modifications): Hector Neira (July 2015) and Pierce BCA Protein Assay instruction manual

Estimated Time: 1 hour

Materials:

- Pierce BCA Protein Assay Kit (catalog #23225)
- 96-well plate, clear flat bottom

- Microplate covers (Titer-Tops pre-cut, adhesive-backed polyethylene film, catalog #9188-6775)
- Warm room (328 Stanley) and plate reader

Steps:

- (recommended) Block 10+ Eppendorf tubes (0.65 mL) with 5% BSA in TBS-T for 1 hour. Use these tubes for all procedures.
 - Protein adsorption of standard curve solutions will affect your readings.
- Prepare layout of samples in 96-well plate.

	1	2	3	4	5	6	7	8	9	10	11	12
A												
B	Standard #1	Standard #2	Standard #3	Standard #4	Standard #5	Standard #6	Standard #7	Pre-desalt 1:10	Pre-desalt 1:20	Post-desalt 1:10	Post-desalt 1:20	
C												
D												

- Prepare standard curve solutions. Start with 200 μ L of 2 mg/mL BSA (glass vial from kit).

Standard #	BSA (μ L)	RIPA Buffer (μ L)	Final Volume	Final Concentration (μ g/mL)
1	100	0	100 μ L	2000
2	50	50	100 μ L	1000
3	25	75	100 μ L	500
4	12.5	87.5	100 μ L	250
5	6.25	93.75	100 μ L	125
6	3.12	96.88	100 μ L	62.5
7	0	100	100 μ L	0

- If you're working with phosphatase / kinase / protease inhibitors, add them in LAST to the standard.
 - If you mix them into the RIPA buffer before, you will end up with different inhibitor concentrations in your final standard solutions, which WILL affect your BCA results.
- Thaw **Vial #4** (IEF cell lysate in RIPA buffer) **and Vial #6** (desalted IEF cell lysate in RIPA buffer).
 - Denaturing lysis buffer produces a colorimetric change stronger than the highest standard.
- Mix thoroughly.
- Prepare 1:10 and 1:20 dilutions of both samples.
- Freeze down the stock sample solutions again at -20°C .

9. Prepare BCA Working Reagent.
 - a. $(7 \text{ standards} + 4 \text{ unknowns}) * (3 \text{ replicates}) * (200 \mu\text{L per well}) = 6.6 \text{ mL}$
 - b. 7 mL of BCA working reagent = 6.86 mL BCA reagent A + 140 μL BCA reagent B.
10. Add 200 μL of BCA working reagent to each well.
 - a. The microchannel pipette introduces error (imperfect volume handling). It is preferable to do this with an individual pipette.
11. Seal plate with microplate cover to minimize evaporation.
12. Quickly add 25 μL of standard or diluted sample to each well.
 - a. Minimize bubbles! Speed is important.
13. Seal the plate with the same microplate cover. Place it in the warm room for 30 minutes.
14. Meanwhile, set up for absorbance read at 562 nm.
15. Read absorbance at 30 and 35 minutes.
 - a. Export data as Excel file.
 - b. At this point, you can either save this plate (for future use of unused wells) or dispose of it, depending on the layout of your samples.
16. Fit linear regression to the data & calculate protein concentrations.

Note: the plate reader reads each lane horizontally, then travels in an S-format across the rest of the plate. Put your samples in the same row as the standards for most accurate measurements (minimal time delay).

Note: triplicates!

Expected Yield: 50% losses from desalting protocol (SJ Nov 2016)

Use of Desalted IEF Cell Lysate

Optimal = use in scIEF, similarly to pI markers or purified protein solution

- Dehydrate well gel completely.
- Prepare solution of desalted IEF cell lysate with ampholytes.
- Rehydrate in lysate-ampholyte solution (40 μL / 9 mm well gel) over ~30 minutes on cooling block with aluminum foil cover and hydrated Kimwipe.
- Use immediately in scIEF platform. No rinsing!

Alternate = incorporate desalted IEF cell lysate into well gel precursor solution.

- Note: may affect gel polymerization (SJ Oct 2016).

Alternate = pipet desalted IEF cell lysate on top of hydrated well gel, over ~30 minutes on cooling block with aluminum cover.

- Note: 10 minutes is insufficient (SJ Oct 2016). Resulting protein concentration both in well gel and in fluidic layer between well gel and lid gel may affect IEF results.

Appendix 11: MATLAB script for ultrathin IEF assay with pI markers and purified proteins

These MATLAB scripts were modified from the scWB analysis scripts written and provided by Dr. Julea M. Vlassakis and Dr. Kevin A. Yamauchi. Modifications within each script are typically annotated with a descriptive note preceded by “ %TODO ”.

Commands

```
% Shaheen Jeeawoody
% Last updated March 7, 2019
% scWB analysis script, modified for scIEF, modified for pI markers

% TODO change all instances of "filename"

diary filename % record all actions

struct = scIEF_roiGeneration_pl('filename.tif', 100, 3000, 0);
% modifications: no rotation, no microwells

num_peaks = 1; snr_threshold = 0.7; r2_threshold = 0.7;
backgroundWidth = 0; struct = intProf_pl(struct, backgroundWidth);
% modifications: manual background subtraction, manual pixel conversion
% TODO remember to background subtract!
% TODO remember to check the pixel conversion in intProf_pl

close all

% pI marker 4.5
struct = fitPeaks (struct, num_peaks, snr_threshold); struct.R2
struct = goodProfiles(struct, r2_threshold);
% modifications: plot the Gaussian fits overlaid on the line-plots
% modifications: fit one peak at a time

% pI marker 5.5
struct2 = fitPeaks (struct, num_peaks, snr_threshold); struct2.R2
struct2 = goodProfiles(struct2, r2_threshold);

% pI marker 6.6
struct3 = fitPeaks (struct, num_peaks, snr_threshold); struct3.R2
struct3 = goodProfiles(struct3, r2_threshold);

% POST-ANALYSIS: characterize pH gradient linearity dpH/dx and R^2 of linear regression fit

% extract peak centers
pI45=struct.fit_coefficients(:,1); pI55=struct2.fit_coefficients(:,1); pI66=struct3.fit_coefficients(:,1);
b(1) = pI45(2); b(2) = pI55(2); b(3) = pI66(2); b=b/1000; % convert from microns to millimeters
pI=[4.5 5.5 6.6];

% plot linearity
figure(5);hold on; pH=pI(1:3); gssb=b(1:3); plot(gssb, pH, 'bd-')
xlabel('Position (mm)'); ylabel('pI marker'); title('Linearity of pH gradient at X minutes - filename');
lin=polyfit(gssb,pH,1);
slope=lin(1) % print slope of linear regression fit
yintercept=lin(2) % print y intercept of linear regression fit
```

```

yfit=polyval(lin,gssb); plot(gssb,yfit,'r')
yresid=pH-yfit;
rsq=1-(sum(yresid.^2)/((length(pH)-1)*var(pH))) % print R^2 of linear regression fit
text(gssb(1)+0.1,pH(2)-0.1, strcat(['dpH/dx = ' num2str(lin(1))]);
text(gssb(1)+0.1,pH(2)-0.2, strcat(['R^2 = ' num2str(rsq)]));
hold off
% TODO remember to save figure as .tif and .fig

% print all relevant values
struct.fit_coefficients
struct2.fit_coefficients
struct3.fit_coefficients
% remember, sigma = c / sqrt(2)

save AllVariables_filename.mat % save all variables for future use
diary off % turn off diary

```

scIEF_roiGeneration_pl

```

function [struct] = scIEF2_roiGeneration_pl(filename,horzspacing,vertspacing, vert_offset)
% This function rotates/aligns the raw image and segments the image into ROIs
% Outputs:
% Struct [structure]: A data structure containing objects (3D matrix
% with each ROI contained in a different z, and coordinates of the ROIs)
% Inputs:
% filename [string]: A string containing the name of the fluorescence image to be processed
% horzspacing [num]: Well-to-well spacing (horizontal)
% vertspacing [num]: Well-to-well spacing (vertical)
% vert_offset [num]: Offset from the well center to the end of the separation (vertical)

%% versions
% 0.1-Created April, 2016
% 0.2 (5.15.16): Updated to apply same transform for ROI generation if user
% inputs a struct with the fields "angle" and "rotate".
% 0.3 (5.20.16): Added "rows" and "wells per row" fields to structure.
% 0.4 (2017): Modified for pl markers (no rotation)

% TODO deleted option for inputting script

% TODO suppress warning on resizing image
warning('off','images:initSize:adjustingMag')

%TODO set protein target
str=char('pl');
struct.name=str;

%Load the image file in Matlab
img=imread(filename);
%Display more contrasted img in window
contrasted_img=histeq(img);
imshow(contrasted_img);

% TODO no rotation
imgrotated=img;
size(img)

```

```

% TODO
%size(img)

test=1;
% TODO modified to accommodate only 1 row of microwells
% TODO no rotation
    x_upperleftwell=1+horzspacing/2;
    y_upperleftwell=1;
    x_upperrightwell=size(img,2)-1;
    y_upperrightwell=1; % TODO FIX

%store the coordinates of the direction vector that extends from the upper left well to the right most point
of the array
dir_vector1=[x_upperrightwell,y_upperleftwell]-[x_upperleftwell,y_upperleftwell];
%store the coordinates of the direction vector that extends from the upper left well to the upper right well
dir_vector2=[x_upperrightwell,y_upperrightwell]-[x_upperleftwell,y_upperleftwell];
%Find angle between the two direction vectors [angle in degrees]
cosangle=dot(dir_vector1,dir_vector2)/(norm(dir_vector1)*norm(dir_vector2));
angle=acosd(cosangle);
    if (y_upperrightwell<y_upperleftwell)
        angle=-angle;
    end

%Rotate the image so the array is aligned
b=imrotate(imgrotated,angle,'nearest','crop');
b_contrasted=histeq(b);
imshow(b_contrasted); % TODO changed for ease of visibility from % imshow(b);
hold on
sz=size(b)/2;
rotation_matrix=[cosd(-angle),-sind(-angle);sind(-angle),cosd(-angle)];
new_upper_left=rotation_matrix*[x_upperleftwell-(sz(2))];(y_upperleftwell-sz(1));
new_upper_right=rotation_matrix*[x_upperrightwell-sz(2)];(y_upperrightwell-sz(1));

x_new_upper_left=new_upper_left(1)+sz(2);
y_new_upper_left=new_upper_left(2)+sz(1) - vert_offset;
x_new_upper_right=new_upper_right(1)+sz(2);
y_new_upper_right=new_upper_right(2)+sz(1) - vert_offset;

%generate matrix to store ROIs
%Determine number of wells per row
wells_per_row=round((x_new_upper_right-x_new_upper_left)/horzspacing)
% TODO

%Determine number of rows
rows=1;

%Determine total number of wells
total_wells=wells_per_row*rows;
b=imgrotated;
%for loop to fill in the 3D matrix with ROIs from the image (proceeds row by row of the microwell array
from left to right)
mat=zeros(vertspacing,horzspacing,total_wells);
for i=1:rows
    for j=1:wells_per_row
        z=(wells_per_row)*(i-1)+j;

```

```

row_start=(round(x_new_upper_left)-horzspacing/2)+((j-1)*horzspacing);
row_end=row_start+horzspacing;
col_start=(round(y_new_upper_left)+((i-1)*vertspacing));
col_end=col_start+vertspacing;
x=row_start:1:(row_end-1);
y=repmat(col_start,1,length(x));
y2=col_start:1:(col_end-1);
x2=repmat((row_end-1),1,length(y2));
mat(:,z)=b(col_start:(col_end-1),row_start:(row_end-1));

    plot(x',y','Color','w','LineStyle','-');
    plot(x',y','Color','k','LineStyle',':');
    plot(x2',y2','Color','w','LineStyle','-');
    plot(x2',y2','Color','k','LineStyle',':');

    % TODO label lane
    text(row_start,col_start,num2str(j));
end
    % TODO label pixel values (start, 1/3, 1/2, 2/3, end)
text(row_end,col_start,num2str(col_start));
col_t13 = (col_end - col_start) / 3 * 1 + col_start;
text(row_end,col_t13,num2str(col_t13));
col_t12 = (col_end - col_start) / 2 * 1 + col_start;
text(row_end,col_t12,num2str(col_t12));
col_t23 = (col_end - col_start) / 3 * 2 + col_start;
text(row_end,col_t23,num2str(col_t23));
text(row_end,col_end,num2str(col_end));
end

struct.rois=mat;
struct.vert_offset = vert_offset;

% TODO save image, using protein target name & filename, assuming .tif
fn = strsplit(filename, '.tif');
struct.filename = strjoin(strcat(fn(1), '_', str));
imgname = strjoin(strcat(fn(1), '_', str, '_roiGeneration'));
print(ffigure(1),imgname, '-dtiffn');

end

```

intProf_pl

```

function [struct] = intProf_pl(struct,subtract)
%Generate intensity profiles from the ROI stacks in the output of roiGeneration
% and perform background subtraction on the profiles
% Outputs
%Struct [structure]: A data structure containing objects (Intensity profiles for each ROI, 3D matrix
% with each ROI contained in a different z, and coordinates of the ROIs)
% Inputs
%Struct [structure]: The data structure from roiGeneration containing the ROIs for each lane
mat=struct.rois;
[x_dim,y_dim,z_dim]=size(mat);
int_profiles=zeros(x_dim,2,z_dim);

%pix_conversion is the number of microns per pixel
pix_conversion=4; % ONYX 4X objective with 2x binning, confirmed SJ

```

```

%pix_conversion=1.6; % ONYX 10X objective with 2x binning, confirmed SJ

% for loop to generate the intensity profiles for each ROI in the z-stack of the matrix Mat.
% The intensity profile is an average of the pixel intensities across the short-axis of the ROI.
figure
for i=1:z_dim
    lane=mat(:,i);
    dist=(0:pix_conversion:pix_conversion*(x_dim-1));
    int=sum(lane,2);
    avg_int=int/(y_dim);
    bsub_int=avg_int-subtract; % TODO changed for pl markers: manual background subtraction
    lane_profile=[dist',bsub_int];
    int_profiles(:,i)=lane_profile;
    plot(dist',bsub_int);
    hold on
end
struct.int_prof=int_profiles;
end

```

fitPeaks

```

%% Header
% Inputs: data_struct: data structure containing the data set with the following fields:
% - int_prof: matrix containing the intensity profiles
% - num_peaks (optional): number of expected peaks can be 1, 2, or 3. Default is 1
% - snr_threshold(optional): Threshold value of signal-to-noise ratio (SNR). Lanes with at least 1 peak
%   with an estimated SNR greater than the threshold value will be curve fit. Typical threshold value is 3.

% Outputs: data_struct: data structure containing the data set with the following fields:
% - int_prof: matrix containing the intensity profiles (unchanged)
% - good_devices: boolean vector indicating the good devices
% - fit_coefficients: m x 3 x p matrix containing the gaussian fit coefficients. m is the number of peaks
%   and p is the number of good devices (good_devices)
% - R2: m x 1 matrix containing the R^2 values of the Gaussian fits. m is the number of good devices
%   (good_devices)
% Versions: - 0.1 (4.7.16) Function created
% - 0.2 Now should be called before goodProfiles()
% - 0.3 (5.15.16) Data between the user selected peak boundaries is now used for the gaussian fit
%   (instead of the entire intensity profile).

```

```

function data_struct = fitPeaks(data_struct, num_peaks, snr_threshold)
%% Check input arguments
switch nargin
    % If only the data_structure is provided, set num_peaks = 1
    case 1
        num_peaks = 1;
    % If provided, ensure the number of peaks is valid
    case 2
        % Exit function if an invalid number of peaks is input
        if ((num_peaks > 3) || (num_peaks < 1))
            error('Invalid number of peaks');
            return
        end
        %If only 2 input arguments provided, user does not want to run the SNR threshold
        apply_snr_threshold=0;
    case 3

```



```

        apply_snr_threshold=1;
    otherwise
        error('Invalid number of input arguments');
        return
    end

%% Get the peaks
%% Get the intensity profiles
try
    intensity_profiles = data_struct.int_prof;
catch
    error('Error accessing data_struct.int_prof');
end

% Find all of the good wells
[x_dim,y_dim,z_dim]=size(intensity_profiles);
%store to the structure the starting number of wells analyzed
struct.total_wells=z_dim;

if apply_snr_threshold==1
    % for loop to filter out SNR<3 lanes with a conservative SNR estimate calculated from the max
    % intensity of a smooth data set and the standard deviation of the last 5 pixels of the lane.
    snr3_devices=zeros(z_dim,1);
    snr_est=zeros(z_dim,1);
    %figure
    for i=1:z_dim
        device=intensity_profiles(:,i);
        xval=device(:,1);
        yval=device(:,2);
        yvalsmooth=smooth(yval);
        noise_est=std(yval(end-5:end));
        signal_est=max(yvalsmooth);
        snr_est(i)=signal_est/noise_est;
        if snr_est(i)<snr_threshold
            snr3_devices(i)=0;
        else
            snr3_devices(i)=1;
            %plot(xval,yval);
            %hold on
        end
    end
    struct.snr_est=snr_est;

    % Get the number of good wells
    num_good_devices = sum(snr3_devices);
    good_indices=find(snr3_devices==1);

    % Exit if there are no good wells
    if (num_good_devices == 0)
        error('No good wells in data_struct');
    end
else
    num_good_devices=ones(z_dim,1);
    good_indices=find(num_good_devices==1);
end

```

```

% Save the good indices
data_struct.good_indices = good_indices;

%% Get the seed parameters
% Let the user select the points for the parameter estimation
bounds_set = false;
while (~bounds_set)
    % Plot the good devices
    figure(1);
    hold on
    for i = 1:num_good_devices
        device_index = good_indices(i);
        plot(intensity_profiles(:,1, device_index),...
            intensity_profiles(:,2, device_index), '-k');
    end
    hold off
    uiwait(msgbox('Please select left and right boundaries of each peak'));

    % Get the limits of the plot
    y_lim = get(gca, 'YLim');

    % Preallocate the nx2 matrix to hold the peak bounds, where n is the
    % number of peaks. Col 1 is the left bound, col 2 is the right bound
    peak_bounds = zeros(num_peaks, 2);
    for peak = 1:num_peaks
        % Get the left peak boundary
        [x1, y1] = ginput(1);
        % Draw the selected peak boundary
        line([x1, x1], y_lim, 'Color', [0, 0, 1]);
        % Get the right peak boundary
        [x2, y2] = ginput(1);
        % Draw the selected peak boundary
        line([x2, x2], y_lim, 'Color', [0, 1, 0]);
        % Save the selected bounds
        peak_bounds(peak, :) = [x1, x2];
    end

    % Ask if the peaks are correct
    choice = questdlg('Are the peak bounds correct?', 'Done with bound selection?', 'Yes', 'No','No');
    close
    % If they are done, exit loop
    if (strcmp(choice, 'Yes'))
        bounds_set = true;
    end
end

% TODO save fitPeaks image
%fn = struct.filename;
%imgname = strjoin(strcat(fn, '_fitPeaks'));
%print(ffigure(2),imgname,'-dtiffn');

close all;

% Save the bounds
data_struct.fit_bounds = peak_bounds;
%% Create the fit options

```

```

% Create the fit options object with the specified number of peaks
switch num_peaks
    case 1
        fit_type = 'gauss1';
    case 2
        fit_type = 'gauss2';
    case 3
        fit_type = 'gauss3';
end
fit_options = fitoptions(fit_type);

% Assign the locations to the fit options object
for peak = 1:num_peaks
    % Get the left and right bound for the peak
    left_bound = peak_bounds(peak, 1);
    right_bound = peak_bounds(peak, 2);
    % Set the sigma bounds
    sigma_min = 0;
    sigma_max = right_bound - left_bound;
    % Set the peak center bounds
    x_min = left_bound;
    x_max = right_bound;
    % Set the amplitude bounds
    a_min = 0;
    a_max = y_lim(2);
    % set the upper and lower bounds. correct for difference in c and sigma terms
    fit_options.Lower = [a_min, x_min, (sigma_min * sqrt(2))];
    fit_options.Upper = [a_max, x_max, (sigma_max * sqrt(2))];
end

%% Fit each peak
% Preallocate the m x 3 x p matrix for the fit coefficients where m is the number of peaks per roi and
% p is the number of ROIs and col 1 is the amplitude, col 2 is the peak center, and col 3 is sigma
data_struct.fit_coefficients = zeros(num_peaks, 3, length(good_indices));

% Preallocate the m x 1 matrix for the R^2 values for each fit where m is the number of good devices
data_struct.R2 = zeros(num_good_devices, 1);

for i = 1:num_good_devices
    device_index = good_indices(i);
    %Display the device number every 50 devices
    %if(mod(i, 10) == 0)
        %fprintf('Fitting lane %d/%d\n', i, num_good_devices);
    %end

    % Get the x and y values
    x = intensity_profiles(:,1, device_index);
    y = intensity_profiles(:,2, device_index);
    %Determine index of x_min and x_max for selection of x and y values in the region of the peak
    left_diff=abs(x-x_min);
    left_data=find(left_diff==min(left_diff));
    right_diff=abs(x-x_max);
    right_data=find(right_diff==min(right_diff));
    %Get the x and y values in the peak region
    x_fit=x(left_data:right_data);
    y_fit=y(left_data:right_data);

```

```

% Fit the peaks
[fit_object, gof] = fit(x_fit, y_fit, fit_type, fit_options);
% Get the coefficients
fit_coeffs = coeffvalues(fit_object);
% Save the coefficients
for peak = 1:num_peaks
    coeff_index_start = (peak - 1)*3 + 1;
    coeff_index_end = peak * 3;
    %get peak center and width for AUC calculation
    center=fit_coeffs(coeff_index_end-1);
    sigma=fit_coeffs(coeff_index_end);
    width=sigma/sqrt(2);
    %determine location of +/- 2 peak widths from the peak center
    auc_left_bound=center-2*width;
    auc_right_bound=center+2*width;
    %Determine index of auc_left_bound and auc_right_bound for selection of x and y values in
    %the region of the peak
    left_diff_auc=abs(x-auc_left_bound);
    left_data_auc=find(left_diff_auc==min(left_diff_auc));
    right_diff_auc=abs(x-auc_right_bound);
    right_data_auc=find(right_diff_auc==min(right_diff_auc));
    % Make sure the left bound is within the array
    if (left_data_auc < 1)
        left_data_auc = 1;
    end
    % Check to make sure the AUC bounds are within the bounds of the array
    if (right_data_auc > length(y))
        right_data_auc = length(y);
    end
    %Sum data within the peak bounds
    peak_region_intensities=y(left_data_auc:right_data_auc);
    AUC(peak,1,i)=sum(peak_region_intensities);
    data_struct.fit_coefficients(peak, :, i) = fit_coeffs(coeff_index_start:coeff_index_end);
    data_struct.AUC(peak,1,i)=AUC(peak,1,i);
end
data_struct.R2(i) = gof.rsquare; % Save the R^2 value
end
end

```

goodProfiles

```

function [data_struct] = goodProfiles(data_struct,r2_threshold)
%perform quality control on intensity profiles, removing lanes with SNR<3
%and allowing the user to select lanes to remove upon visual inspection
% Outputs
%Struct [structure]: A data structure containing objects (indices of "good" lanes, intensity profiles for each
% ROI, 3D matrix with each ROI contained in a different z, and coordinates of the ROIs)
%Inputs
%struct [structure]: A structure containing the intensity profiles generated in intProf
% v04

%% Check input arguments
switch nargin
    % If only the data_structure is provided, set r2_threshold = 0.7
    case 1
        r2_threshold = 0.7;

```

```

% If provided, ensure the r2 value is valid
case 2
    % Exit function if an invalid r2 value is input
    if ((r2_threshold<0) || (r2_threshold > 1))
        error('Invalid R^2 value');
        return
    end
end

int_prof_all=data_struct.int_prof;
[x_dim,y_dim,z_dim]=size(int_prof_all);
r2=data_struct.R2;
good_r2=find(r2>=r2_threshold);

%determine array position of high r2 value fit lanes
good_indices=data_struct.good_indices;
good_fits=good_indices(good_r2);

good_int_profiles=zeros(x_dim,y_dim,length(good_r2));
for i=1:length(good_r2)
    good_int_profiles(:,i)=int_prof_all(:,good_fits(i));
end

%set number of rows/columns of subplots to display in each figure window
n=1; % TODO changed for sclEF, original n=5 (too few lanes in sclEF)
num_subplots=n*n;
plots_display=length(good_r2);
good_devices=ones(length(good_r2),1);
number_subplots=ceil(plots_display/(n*n));
dev_to_analyze=zeros(z_dim,1);
good_subplots = ones(plots_display,1);
disp(number_subplots);

% for loop to generate subplots for user inspection of the intensity profiles
for i=1:number_subplots
    disp(i);
    figure
    if i==1
        devices_subplot=(1:(n*n));
    elseif i*n*n<=plots_display
        devices_subplot=((i*n*n)-(n*n)+1):(i*n*n);
    else
        devices_subplot=((i*n*n)-(n*n)):(plots_display);
    end
    next=0;
    for j=1:length(devices_subplot)
        dev_number=devices_subplot(j);
        device=good_int_profiles(:,dev_number);
        xval=device(:,1);
        yval=device(:,2);
        subplot(n, n, j);
        plot(xval,yval,'LineWidth',2,'Tag', sprintf('%d', dev_number), 'buttndownfcn',...
            @clickTest);

        % TODO label lane & R2
        hold on

```

```

lane = good_fits(dev_number);
r2_lane = r2(lane);
title(strcat('lane=',num2str(lane),' and r2=',num2str(r2_lane)));

% TODO show Gaussian fits
% f(x)=a1*exp(-(x-b1)/c1)^2
pgggg = length(data_struct.fit_coefficients(:,1,lane));
for pGSS = 1:1:pgggg
    a=data_struct.fit_coefficients(pGSS,1,lane);
    b=data_struct.fit_coefficients(pGSS,2,lane);
    c=data_struct.fit_coefficients(pGSS,3,lane);
    x=data_struct.int_prof(:,1,lane);
    gaussFit=a*exp(-((x-b)./c).^2);
    plot(x,gaussFit);
end
legend ('lane','Gaussian fit');
% axis([2500 4000 0 5000]);

hold off
end
next=0;

btn = uicontrol('Style','pushbutton','String','Next','Position',[500 15 50 30],...
    'Callback',@continueButton2);
while next==0
    pause(0.01);
end
%good_devices(devices_subplot(1):devices_subplot(end))=good_subplots;
close(gcf)
end

data_struct.dev_to_analyze = good_subplots;
good_subplot_ind=find(good_subplots==1);
data_struct.index_dev_to_analyze=good_r2(good_subplot_ind);
end

function [next]=continueButton2(qstring,title,str1,str2,default)
qstring='Are you done selecting devices to throw out?';
title='Device Quality Control';
str1='Yes';
str2='No';
default='Yes';
choice = questdlg(qstring,title,str1,str2,default);
    % Handle response
    switch choice
        case 'Yes';
            disp(['choice 'Great, let"s keep going then!'])
            next=1;
        case 'No';
            disp(['choice 'Okay, please finish selecting devices to throw out!'])
            next=0;
    end
end
assignin('caller','next',next);
end

function clickTest(line_handle, event)

```

```

good_subplots = evalin('caller', 'good_subplots');
current_tag = get(line_handle, 'Tag');
%split_tag = strsplit(current_tag, ',');
subplot_num = str2num(current_tag);
%subplot_state = str2num(split_tag{1, 2});
subplot_state = good_subplots(subplot_num);
disp(sprintf('%d, %d', subplot_num, subplot_state));
% Toggle the selection based on the last character in the tag
% (0 = off, 1 = on)
if (subplot_state)
    set(line_handle, 'Color', [1, 0, 0]);
    good_subplots(subplot_num) = 0;
else
    set(line_handle, 'Color', [0, 0, 1]);
    good_subplots(subplot_num) = 1;
end
% disp(good_subplots);
assignin('caller', 'good_subplots', good_subplots);
end

```

Appendix 12: MATLAB script for ultrathin scIEF assay with cells

These MATLAB scripts were modified from the scWB analysis scripts written and provided by Dr. Julea M. Vlassakis and Dr. Kevin A. Yamauchi. Modifications within each script are annotated with a descriptive note preceded by “ %TODO ”.

Commands

```

diary on
struct = scIEF_roiGeneration('run001.tif', 100, 1700, 0);
Wells are right of bands

num_peaks = 3; % I usually analyze 1 peak at a time. This is set up for 3 tGFP peaks.
snr_threshold = 0.5; r2_threshold = 0.5; % set to 0.7 for high selectivity
struct = intProf_cells(struct);
close Figure 1

struct = fitPeaks (struct, num_peaks, snr_threshold);

struct.R2
struct = goodProfiles(struct, r2_threshold);

struct.dev_to_analyze
struct.index_dev_to_analyze

lane = 11; % choose the lane for which you want to report stats
struct.fit_coefficients(:, :, lane)
struct.int_prof(:, :, lane)

save AllVariables_run001.mat

```

scIEF_roiGeneration

```

function [struct] = scIEF_roiGeneration(filename, horzspacing, vertspacing, vert_offset)

```

```

%This function rotates/aligns the raw image and segments the image into ROIs
% Outputs:
%Struct [structure]: A data structure containing objects (3D matrix
%with each ROI contained in a different z, and coordinates of the ROIs)
% Inputs:
%filename [string]: A string containing the name of the fluorescence image to be processed
%horzspacing [num]: Well-to-well spacing (horizontal)
%vertspacing [num]: Well-to-well spacing (vertical)
%vert_offset [num]: Offset from the well center to the end of the separation (vertical)

%% versions
% 0.1-Created April, 2016
% 0.2 (5.15.16): Updated to apply same transform for ROI generation if user
% inputs a struct with the fields "angle" and "rotate".
%0.3 (5.20.16): Added "rows" and "wells per row" fields to structure.
% 0.4 (2017): adapted for single row of microwells for scIEF

% TODO deleted option for inputting script

% TODO suppress warning on resizing image
warning('off','images:initSize:adjustingMag')

%ask the user the name of their protein target
prompt = 'What is the name of your protein target?';
str = input(prompt,'s');
struct.name=str;

%Load the image file in Matlab
img=imread(filename);
%Display more contrasted img in window
contrasted_img=histeq(img);
imshow(contrasted_img);

% TODO remove rotation option
imgrotated=img;
contrasted_img_r=histeq(imgrotated);
imshow(contrasted_img_r);
size(imgrotated)
test=1;

% TODO modified to accommodate only 1 row of microwells
while test==1
    %Prompt user to select the upper right well of the array.
    title('Please zoom in on the middle of the upper left well and press any key.');
```



```

zoom off;
title('Please click on the middle of the upper right well. ');
[x_click,y_click]=ginput(1);
x_upperrightwell=x_click;
y_upperrightwell=y_click; % TODO modified for no rotation
% y_upperrightwell=y_upperleftwell; % TODO modified for no rotation
zoom out;

% Construct a questdlg to ask the user if they are happy with their well selection
choice = questdlg('Are you happy with your well selections?', 'Well selections for array boundaries', ...
'Yes','No','Yes');
% Handle response
switch choice
case 'Yes';
    disp([choice 'Great, let"s keep going then!'])
    test = 0;
case 'No';
    disp([choice 'That"s okay, try again!'])
    test = 1;
end
if (x_upperrightwell<x_upperleftwell)
    test=1;
    title('Oh no! We detected you selected the wells in the wrong order. Please try again. Press any key
to continue')
    pause()
else
    test=0;
end
end

%store the coordinates of the direction vector that extends from the upper left well to the right most point
of the array
dir_vector1=[x_upperrightwell,y_upperleftwell]-[x_upperleftwell,y_upperleftwell];
%store the coordinates of the direction vector that extends from the upper left well to the upper right well
dir_vector2=[x_upperrightwell,y_upperrightwell]-[x_upperleftwell,y_upperleftwell];
%Find angle between the two direction vectors [angle in degrees]
cosangle=dot(dir_vector1,dir_vector2)/(norm(dir_vector1)*norm(dir_vector2));
angle=acosd(cosangle);
if (y_upperrightwell<y_upperleftwell)
    angle=-angle;
end

%Rotate the image so the array is aligned
b=imrotate(imgrotated,angle,'nearest','crop');
b_contrasted=histeq(b);
imshow(b_contrasted); % TODO CHANGE BACK IF YOU WANT
% imshow(b); %
hold on
sz=size(b)/2;
rotation_matrix=[cosd(-angle),-sind(-angle);sind(-angle),cosd(-angle)];
new_upper_left=rotation_matrix*[(x_upperleftwell-(sz(2)))+(y_upperleftwell-sz(1))];
new_upper_right=rotation_matrix*[(x_upperrightwell-sz(2))+(y_upperrightwell-sz(1))];
x_new_upper_left=new_upper_left(1)+sz(2);
y_new_upper_left=new_upper_left(2)+sz(1) - vert_offset;
x_new_upper_right=new_upper_right(1)+sz(2);
y_new_upper_right=new_upper_right(2)+sz(1) - vert_offset;

```

```

%generate matrix to store ROIs
%Determine number of wells per row
wells_per_row=round((x_new_upper_right-x_new_upper_left)/horzspacing)

% TODO only one row of microwells
%Determine number of rows
rows=1;
%Determine total number of wells
total_wells=wells_per_row*rows;
%for loop to fill in the 3D matrix with ROIs from the image (proceeds row by row of the microwell array
from left to right)
mat=zeros(vertspacing,horzspacing,total_wells);
for i=1:rows
    for j=1:wells_per_row
        z=(wells_per_row)*(i-1)+j;
        row_start=(round(x_new_upper_left)-horzspacing/2)+((j-1)*horzspacing);
        row_end=row_start+horzspacing;
        col_start=(round(y_new_upper_left)+((i-1)*vertspacing));
        col_end=col_start+vertspacing;
        x=row_start:1:(row_end-1);
        y=repmat(col_start,1,length(x));
        y2=col_start:1:(col_end-1);
        x2=repmat((row_end-1),1,length(y2));
        mat(:,z)=b(col_start:(col_end-1),row_start:(row_end-1));
        plot(x',y','Color','w','LineStyle','-');
        plot(x',y','Color','k','LineStyle','-');
        plot(x2',y2','Color','w','LineStyle','-');
        plot(x2',y2','Color','k','LineStyle','-');

        % TODO label lane
        text(row_start,col_start,num2str(j));
    end

    % TODO label pixel values (start, 1/3, 1/2, 2/3, end)
    % for ease of consultation for peak identification in fit_peaks
    text(row_end,col_start,num2str(col_start));
    col_t13 = (col_end - col_start) / 3 * 1 + col_start;
    text(row_end,col_t13,num2str(col_t13));
    col_t12 = (col_end - col_start) / 2 * 1 + col_start;
    text(row_end,col_t12,num2str(col_t12));
    col_t23 = (col_end - col_start) / 3 * 2 + col_start;
    text(row_end,col_t23,num2str(col_t23));
    text(row_end,col_end,num2str(col_end));
end
struct.rois=mat;
struct.vert_offset = vert_offset;

% TODO save image, using protein target name & filename, assuming .tif
fn = strsplit(filename,'.tif');
struct.filename = strjoin(strcat(fn(1), '_', str));
imgname = strjoin(strcat(fn(1), '_', str, '_roiGeneration'));
print(figure(1),imgname,'-dtiffn');

figure; imshow(b);
end

```

intProf_cells

```
function [struct] = intProf_cells(struct,backgroundwidth)
%Generate intensity profiles from the ROI stacks in the output of roiGeneration
% and perform background subtraction on the profiles
% Outputs
%Struct [structure]: A data structure containing objects (Intensity profiles for each ROI, 3D matrix with
%each ROI contained in a different z, and coordinates of the ROIs)
% Inputs
%Struct [structure]: The data structure from roiGeneration containing the ROIs for each lane
%backgroundWidth [num]: width of the background region for axial background subtraction (in pixels)
mat=struct.rois;
[x_dim,y_dim,z_dim]=size(mat);
int_profiles=zeros(x_dim,2,z_dim);

%pix_conversion is the number of microns per pixel
pix_conversion=5; % FOR CELLS -- GENEPIX

% for loop to generate the intensity profiles for each ROI in the z-stack of the matrix Mat. The intensity
% profile is an average of the pixel intensities across the short-axis of the ROI. The background regions
% are defined by the parameter backgroundWidth, and the average pixel intensity in the left and
% right background regions are calculated. The background subtracted intensity profile is generated by
% subtracting the mean background intensity at each point along the long-axis of the ROI from the
% average pixel intensity.
figure
for i=1:z_dim
    lane=mat(:, :, i);
    dist=(0:pix_conversion:pix_conversion*(x_dim-1));
    int=sum(lane,2);
    avg_int=int/(y_dim);
    left_backgroundregion=lane(:,(1:backgroundwidth));
    right_backgroundregion=lane(:,((end+1)-backgroundwidth:end));
    left_background_int=(sum(left_backgroundregion,2))/backgroundwidth;
    right_background_int=sum(right_backgroundregion,2)/backgroundwidth;
    mean_background=(left_background_int+right_background_int)/2;

    bsub_int=avg_int-mean_background;
    lane_profile=[dist',bsub_int];
    int_profiles(:, :, i)=lane_profile;

    plot(dist',bsub_int);
    hold on
end
struct.int_prof=int_profiles;
end
```

fitPeaks and goodProfiles

See **Appendix 11**.

Appendix 13: Characterization of background fluorescence in PA gels

Researchers in the Herr lab have observed high background and noise in fluorescence channels in polyacrylamide (PA) gels used in the single-cell Western blotting (scWB) and single-cell isoelectric focusing (scIEF) assays, with the subsequent immunoblot. In these gels, background is defined as the average fluorescence intensity in areas of the gel sufficiently far away from fluorescently-labeled protein bands; noise is defined as the standard deviation of the average fluorescence intensity in the background regions. During the analysis of scWB and scIEF gels, the background is subtracted from the gel, to distinguish the fluorescence signal contribution of the gel from the fluorescence signal of the proteins focused and immobilized in the gel. High noise in the fluorescence channels from the gel affects the signal-to-noise ratio (SNR) of these assays and obscures the fluorescence signal from low-abundance protein isoforms, which increases the lower limit of detection (LLOD) of these assay. In order to use these PA gels for interrogations of biologically relevant proteins, it is important to characterize the source of this high background and noise, especially if this might be due to entropic trapping of antibodies within the heterogeneous PA gel network.⁹³ Thus, in a short study, we interrogated the source of that high background and noise from PA gels used for protein separations with an immunoblot.

Methods

We defined three groups of gels: gels in the “A” group contain BPMA and were exposed to UV; “B” group contain BPMA but were not exposed to UV; “C” group do not contain BPMA and were exposed to UV. The gel formulations used in this study included the 6%T 3.3%C PA gels polymerized with APS/TEMED, termed “standard gel.” In addition, we compared these gels to 6%T 8%C gels polymerized with LAP and with added soluble 0%, 0.5%, 1%, 1.5%, or 2% PEG in the precursor, referred to by the % PEG content. These gels were also used in **Chapter 4**, and are listed in **Table 10-1** and **Table 10-2** for clarity.

This study used the same materials listed in **Chapter 4**. We fabricated a wafer with SU-8 rails of 40 μm , spaced 22 mm apart, coated with GelSlick® to avoid gel adhesion to the wafer. We fabricated gels on the wafer and incubated the gels in 1 \times TBS-T for 12 hours for diffusive removal of soluble PEG. These gels were not exposed to protein at any point. These gels were imaged on the GenePix 4300A microarray scanner (Molecular Devices) for fluorescence in both the 488 and the 647 channels. A subset of gels was UV-exposed to activate the BPMA protein immobilization moieties within the gels, rinsed for 1 hour in 1 \times TBS-T, and imaged a second time. Subsequently, all gels were exposed to a 1:26.6 dilution (final 500 nM) of secondary polyclonal antibody AlexaFluor-647-labeled donkey-anti-mouse (Invitrogen A-31571) for 1 hour, then rinsed for 1 hour in TBS-T. The gels were then imaged a last time. Images were analyzed using an in-house Fiji script. Briefly, each well was segmented into a region of interest (ROI) avoiding edges. For each ROI, we measured average fluorescence intensity, defined as “background,” and the standard deviation of the fluorescence intensity, defined as “noise.” For the images acquired by the GenePix scanner, 1 pixel is 5 μm \times 5 μm .

Table 10-1. Gel nomenclature for the brief study on gel background and noise.

Gel nomenclature	Standard gel	0% PEG	0.5% PEG	1.0% PEG	1.5% PEG	2.0% PEG
Acrylamide content	6%T	6%T	6%T	6%T	6%T	6%T
Bisacrylamide : acrylamide ratio	3.3%C	8%C	8%C	8%C	8%C	8%C
10 kDa PEG	0.0%	0.0%	0.5%	1.0%	1.5%	2.0%
Polymerization chemistry	APS/TEMED	LAP	LAP	LAP	LAP	LAP
BPMA photo-immobilization moiety	5 mM	5 mM	5 mM	5 mM	5 mM	5 mM

Table 10-2. Conditions of gel exposure for the brief study on gel background and noise.

Category	BMPA content	UV exposure	AlexaFluor-647-labeled antibody exposure
C	Yes	Yes	Yes
B	Yes	No	Yes
C	No	Yes	Yes

Results

For the standard PA gels, we observed higher background and noise in the 488 channel than in the 647 channel (**Figure 10-1A, B**). This is of interest, considering that these gels were not exposed to any fluorescently-labeled protein at any point, and were only exposed to an AlexaFluor-647-labeled secondary antibody at the last stage (red bars).

Additionally, we isolated the increased background and noise to gels both containing BPMA and exposed to UV (group “A” in **Figure 10-1C, D**). Minimal contribution to the background and noise was observed from the PA gels not containing BPMA, termed group “C”. After discussions with multiple Herr lab members, interrogation of the literature,^{90,335} and independent research completed by Alison Su, a PhD candidate in the Herr lab, the current hypothesis is that upon UV exposure, the BPMA may form benzopinacol moieties with neighboring BPMA molecules, which would have increased fluorescence. Further research is needed to elucidate the exact source of this UV-induced fluorescence increase in these PA gels.

The background and noise decreased in the LAP-polymerized, PEG-containing gels compared to the standard gels (**Figure 10-2**), indicating a potential use of the LAP-polymerized gels as an improved substrate for immunoblotting. **Chapter 4** includes further characterization of these gels towards application in the scIEF immunoblot.

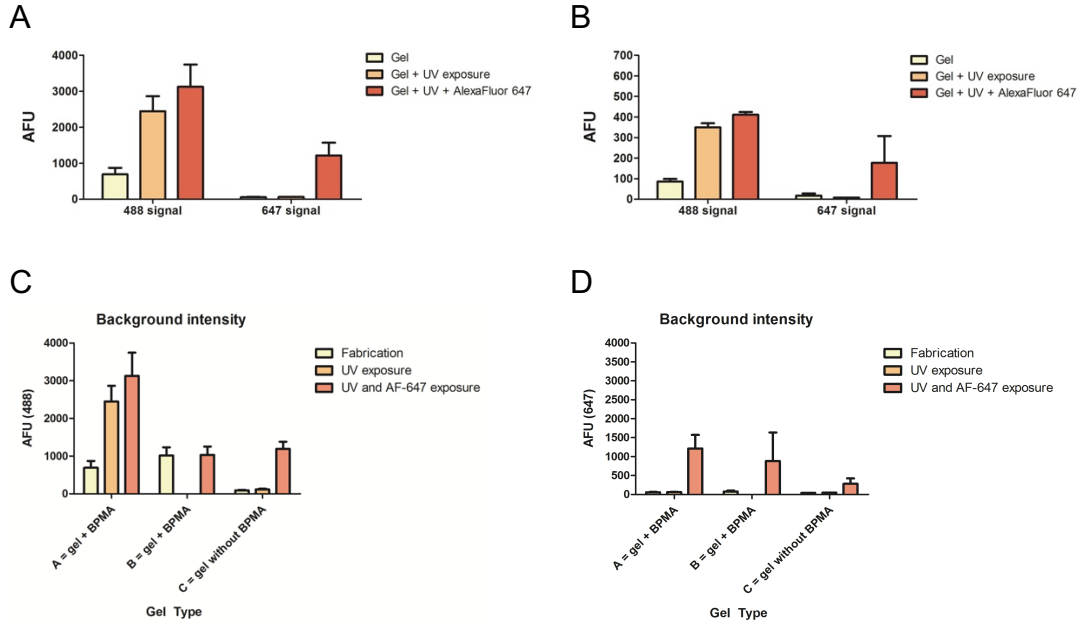


Figure 10-1. Increases in background and noise from standard PA gels were observed specifically from UV exposure of gels containing BPMA.

(A) In the standard 6%T 3.3%C APS/TEMED gel, background signal in only the 488 channel increased 4-fold due to UV exposure alone, and 5-fold due to the combination of UV exposure and exposure to AlexaFluor-647-labeled antibody. The background signal in the 647 channel did not increase after UV exposure alone, and increased 14-fold after both UV and AlexaFluor-647-labeled antibody exposure. (B) The noise in the 488 channel for the standard gels increased 4-fold due to UV exposure alone, and 5-fold from the combined exposure. The noise in the 647 channel did not increase after UV exposure alone, and increased 18-fold after the combined exposure. These increase in background did not occur in gels containing BPMA but not exposed to UV, nor in gels not containing BPMA and exposed to UV, in the (C) 488 channel and (D) 647 channel.

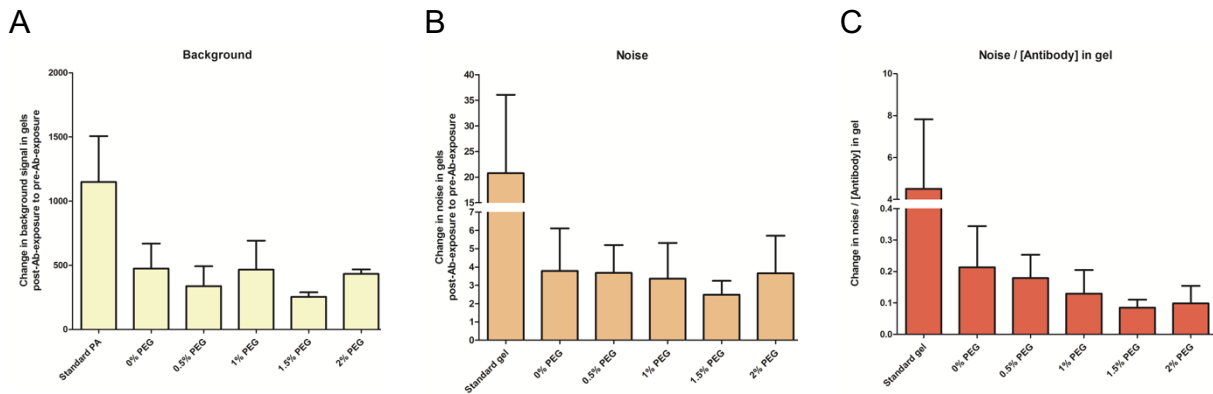


Figure 10-2. High background and noise from the PA gel immunoblots were decreased several fold in the LAP-polymerized PA gels.

Ratio of in-gel fluorescent signal (AFU) post-antibody-incubation / pre-antibody-incubation for polyacrylamide gels in a protein-free platform indicates (A) a 2-fold decrease in background signal, (B) a 4-fold decrease in noise, and (C) more than a 10-fold decrease in noise scaled by the antibody concentration in gel from the standard PA gels to the 2% PEG gels.

Appendix 14: Preliminary efforts towards the delivery of an IEF protein ladder via protein microparticles in the ultrathin IEF assay

This research was conducted in collaboration with Dr. Peggy Chan.

For improved characterization of reproducibility between IEF experiments, we attempted to use the protein microparticles developed by Dr. John Kim, Dr. Peggy Chan, and others¹⁴³ to deliver an IEF protein ladder to the ultrathin IEF assay. Briefly, this method involves the conjugation of His-tagged proteins to microparticles (10 μm diameter) conjugated with a Ni surface chemistry. These microparticles are incorporated in the solution of singularized cells and settled into the microwells along with the cells. The lysis solution with the cell-relevant detergents is supplemented with a high concentration of imidazole, which outcompetes the His tags for the Ni, thus releasing the proteins from the microparticle surface.¹⁴³

Methods

The materials used in this study are all included in **Chapter 4**, as well as imidazole (Sigma 792527), PureProteome nickel magnetic microparticles, 10 μm (Sigma), recombinant Protein G with His Tag (Abcam, 26 kDa), and Alexa Fluor 647 NHS ester labeling kit (Life). His-tagged Protein G was labeled in-house with AlexaFluor-647, and conjugated onto the microparticles.

As described in **Chapter 4**, the same silicon wafer with rails was used to fabricate 6%T 3.3%C PA gels chemically polymerized with APS/TEMED. The ultrathin IEF was conducted as previously described¹⁹ with minor modifications to accommodate purified protein solutions (further details in **Appendix 3**) and the protein-G-laden microparticles. Briefly, gels of height 40 μm were briefly rinsed in DI water, with the fluid layer wicked off the top of the gel, then microparticles were settled on top of the gel for 30 minutes at room temperature, protected from light. The 3-component IEF lid was fabricated using a 1:100 dilution of the stock 40% SinuLyte® ampholytes for a final concentration of 0.4% and 250 mM imidazole. **Table 10-3** lists the components of the lid gel, which was polymerized for 4 minutes per component (in the order of catholyte, anolyte, and focusing region) at 20 mW/cm² light intensity using a 390 nm UV long-pass filter (Edmund Optics) on an OAI Model 30 Collimated UV light source.

The PA gel and lid gel were assembled in the IEF device previously described,¹⁹ and set on an Olympus IX-71 inverted microscope with an Olympus UPlanFi 4 \times (NA 0.13) objective and a EMCCD Camera iXon2 (Andor), with imaging settings loaded into MetaMorph software (7.10.1.161, Molecular Devices). After a 30 second delay for the soluble reagents in the focusing lid gel to diffuse into the PA gel, IEF was conducted by applying 690 V for 12 minutes using the Power-Pac high-voltage power supply device (HVPS, Bio-Rad 1645056). During this focusing period, Protein G was imaged using a Cy5 filter cube (Chroma 49009). The lab markers used to denote the gel edges along the separation axis is visible in brightfield imaging.

Micrographs were analyzed using an in-house MATLAB (R2015b, MathWorks) script^{6,48,49} adapted to this microwell-containing variant of the IEF (code in **Appendix 12**). Briefly, the micrographs were segmented into regions of interest (ROIs), converted into line plots averaged across the width of the ROI (maintaining the separation axis), and background-subtracted using the average background intensity across the ROI. Gaussian curve fitting to the line plots led to the extraction of the peak height, peak location, peak width, area under the curve, SNR, and other assay-specific parameters from each ROI. Validation of the Gaussian curve fits is conducted analytically ($R^2 \geq 0.7$ and signal-to-noise ratio $SNR \geq 3$) and confirmed manually. For the images taken on the Olympus microscope setup, 1 pixel corresponds to 4 μm .

Table 10-3. Composition of IEF lid gel for the protein microparticle study.

Components of the 3-part lid gel used for lysis and electrophoresis in this study.

Lid gel components	pH 4 anolyte	Focusing region	pH 10 catholyte
Polyacrylamide gel	15% T 3.3% C 0.2% VA-086	15% T 3.3% C 0.2% VA-086	15% T 3.3% C 0.2% VA-086
IEF reagents and detergents		0.4% final SinuLyte® ampholytes 1% TritonX-100 250 mM imidazole	
Boundary conditions	13.5 mM pKa 3.6 immobililine 6.4 mM pKa 9.3 immobililine		5.6 mM pKa 3.6 immobililine 14.4 mM pKa 9.3 immobililine

Results

First, we observed disruption of the formation of the pH gradient required for an IEF protein separation, by the inclusion of 250 mM imidazole (**Figure 10-3**). This region of Protein G aligns between the typical locations of the pI 5.5 and 6.6 markers (not shown here). Interestingly, imidazole may be a ampholyte of pI ~ 6.1 .¹⁶ We hypothesized that this high concentration of imidazole overwhelmed the buffering capacity of the 400+ ampholytes in the ampholyte solution, resulting in the observed disrupted pH gradient. Additional characterization with pI markers confirmed the disruption of the pH gradient due to 250 mM or 1 M imidazole (not shown here). In this experiment, the pI markers were diffusively introduced throughout the gels. Upon application of the electric field, the pI markers swept across the separation axis, from both boundary conditions, but formed a leading edge around the pI 5-6 range, instead of resolving into distinct protein bands.

In addition, from the streaky nature of the Protein G bands (**Figure 10-3**), we may have observed continuous loading of Protein G from the microparticles. This indicates a need

for modified lysis conditions for bulk release of the His-tagged Protein G mediated by imidazole within the 30 s lysis timeframe.

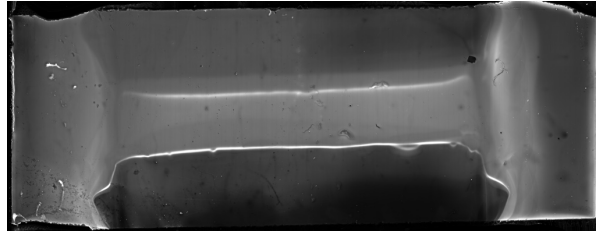


Figure 10-3. Inverted fluorescence micrograph of Protein G indicates a disrupted pH gradient. Gel is oriented with the pH 4 anolyte boundary condition at the top of the image. After 10 minutes of electrophoresis, the Protein G forms a poorly-resolved hazy region across the center of the gel, indicating poor focusing in the pH 5-6 region.

We concluded that this particular method of delivering a protein ladder to the scIEF assay was incompatible with IEF. Subsequent to this study, further research into the development of a protein ladder for the scIEF assay was conducted, documented in **Chapter 6**.

Appendix 15. Research eddies

Throughout the development of this dissertation, several research eddies were noted. For the amusement and possibly even edification of other researchers, a select few are included here.

First, several chapters in this dissertation use the scIEF assay to also characterize photocapture efficiency with BPMA (including **Chapters 3 and 4**). As an attempt to develop a robust platform for characterizing in-gel photocapture efficiency independent of the IEF assay, we attempted to use a Mylar mask (CAD Art Services) to selectively pattern a region of turboGFP purified protein. Extensive exposure of the Mylar mask with UV light using a Hamamatsu LC8 device (Hamamatsu Photonics K.K.) at < 1 cm distance may induce inadvertent removal of the mask material, rendering a hole in the mask itself. Such damage was not duplicated by use of the OAI, nor by use of the Hamamatsu at an extended distance.

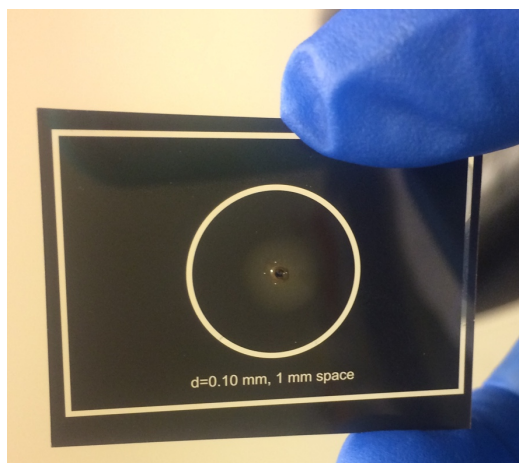


Figure 10-4. Mask inadvertently damaged via exposure to high-intensity UV light.

Next, **Chapter 3** describes the development and utilization of highly-porous, laterally-aggregated PA gels. Directly and visually characterize the porosity of these hydrogels in their hydrated form is an ongoing challenge in the biomaterials landscape. As a proof-of-concept attempt, we interrogated the porosity of the 6%T 8%C APS/TEMED + 2% PEG gel composition, compared to the benchmarking 6%T 3.3%C APS/TEMED gel composition.

Figure 10-5A-B were collected with the assistance of Dr. Andrew Barazia during a demo of the Lattice Lightsheet microscope (Intelligent Imaging Innovations, 3i) through the UC Berkeley CRL Molecular Imaging Center in February 2019. The gels were polymerized on 5 mm coverslips with rhodamine methacrylamide incorporated into the gel matrix for visualization, and maintained in a water bath during imaging. **Figure 10-5A** depicts the benchmarking gel, with no clear gaps in the gel microstructure (fluorescence imaging via rhodamine, false-colored white). In contrast, **Figure 10-5B** depicts gaps in the gel microstructure of the highly-porous 2% PEG gel. By best estimate, these images represent 250 nm resolution within the top 30 microns of the gel material. Timelapse imaging of the 2% PEG gels (not reported here) included movement within the PA gel during imaging, potentially indicative of Brownian motion of the PA gel in a fluid bath.

Figure 10-5C-D are SED images (SEM-like, from dehydrated gels) collected by Dr. Heather Robison, among others, on a multiplexed ion beam imaging (MIBI) platform in spring 2019. Similar to the lightsheet microscopy images, the 2% PEG gels may indicate a porous microarchitecture not seen in the benchmarking gels. The cracks in the benchmarking gels may be attributable to salt content pre-gel-dehydration.

It is essential to note that these are proof-of-concept images, for which significant imaging optimization is required. Nevertheless, these images are promising indicators that the highly-porous 2% PEG gels do contain acrylamide bundles on the order of 200 nm, and large pores on the order of 500 nm, similar to the laterally-aggregated polyacrylamide gels reported by Righetti et al.⁷⁰ Furthermore, the minimal sample

preparation required for these measurements of pore dimensions in hydrated gels is particularly intriguing.

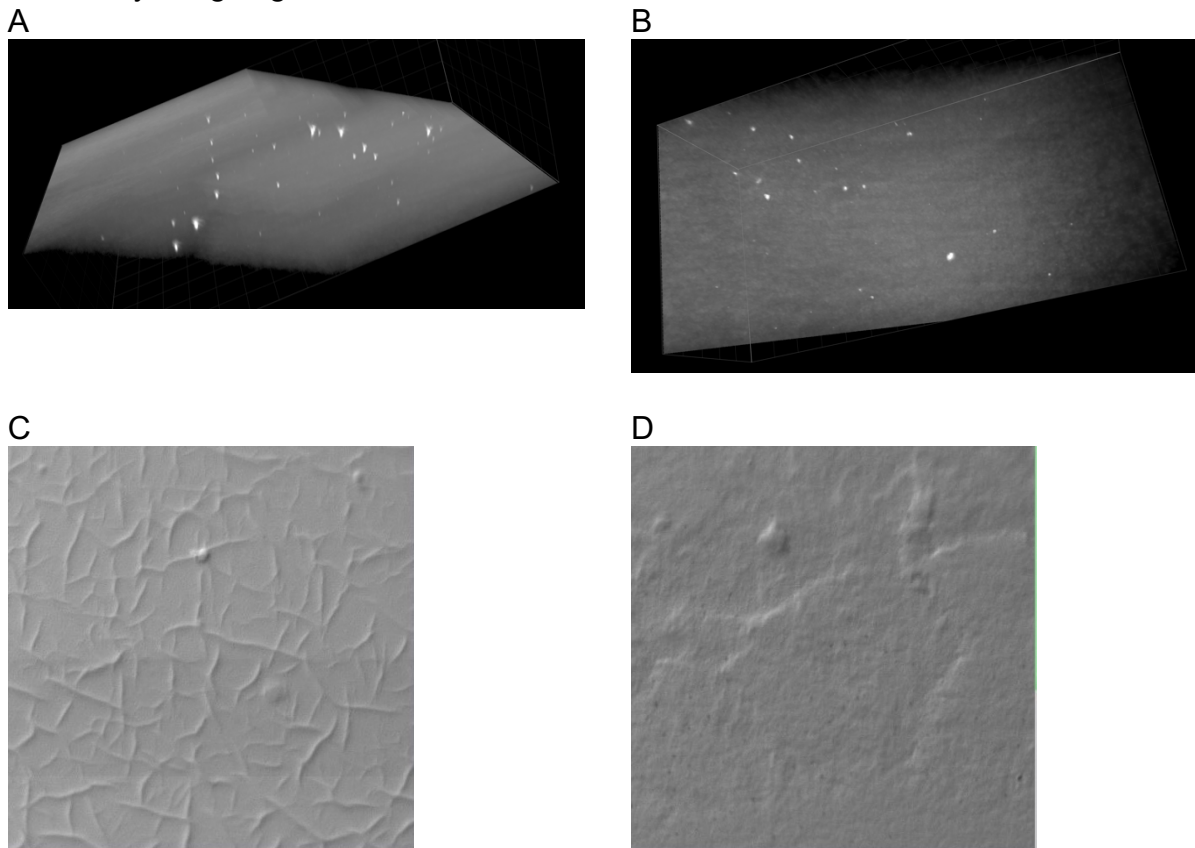


Figure 10-5. Visual characterization of the porosity of highly-porous PA gels.

(A and B) are 2-dimensional depictions of 3-dimensional images collected on the Lattice lightsheet microscope, oriented with the gel surface at the top of the image. (C and D) are 2-dimensional SEM images of the surface of the gels, collected on the multiplexed ion beam imaging platform. The field of view is approximately 400 microns. (A and C) represent the 6%T 3.3%C APS/TEMED gel composition. (B and D) represent the 6%T 8%C APS/TEMED + 2% PEG gel composition. Images are attributable to (A-B) Dr. Andrew Barazia and (C-D) Dr. Heather Robison.

Appendix 16: Development of a lab cybersecurity SOP

After an unfortunate cybersecurity incident in the Herr lab, Dr. Samantha Grist and I developed a lab cybersecurity SOP, with assistance from other Herr lab members, the UC Berkeley Information Security and Policy office, and others at UC Berkeley. We are grateful to John Ives, Craig Carlson, Chris Doane, and many others in the development of this document. The June 2018 version, modified for distribution among other research groups, is included in this dissertation.

This document reports current practices for cybersecurity for the Herr Lab at UC Berkeley, and was designed with UC Berkeley security policies in mind and reviewed by the UC Berkeley ISP office. When adapted for other research groups, please refer to the relevant university ISP/IT services offices and university online resources to ensure

that the group SOP meets minimum security standards for networked devices at the relevant university.

This SOP is separated into sections for all lab members, for superusers of equipment connected to lab PCs, and for cybersecurity superusers.

All lab members

Our group protection against cybersecurity threats is only as strong as the weakest of our individual protections, so it is crucial that we all employ stringent cybersecurity practices in both our personal devices and use of shared lab PCs.

Please review the university's [minimum security standards for all networked devices](#), as well as recommendations on steps that you can take for [protection against ransomware](#), and [best practices for cybersecurity](#). By following this Herr Lab security policy, we are meeting campus policies for minimum security standards.

Accounts and passwords

1. [Current recommendations](#) (please review the link to ensure you are using secure passwords!) suggest that passwords need to be >10 characters in length to ensure security. Use strong and different passwords/passphrases for each of your personal computers as well as all online accounts.
2. Ensure that all personal accounts on lab computers have secure passwords.
3. Consider enabling two-step verification in your CalNet ID for increased security (Dropbox, Gmail, etc. have similar options which add an extra level of security: you cannot login from new devices without having a code from your phone).
4. Consider also using a password manager (e.g. 1password) to make sure you can remember and do not repeat your passwords. Make sure that you are changing passwords from computers that are known to be secure (e.g. clean virus scan from 2+ software for thoroughness, no signs of infection).

Personal computers

1. Ensure that you are promptly receiving and installing all security updates. Prompt security updates are our best protection against vulnerabilities. Ensure that Windows Defender also receives updates.
2. Ensure that you have enabled computer screen lock to ensure no unattended sessions, and set a lock-out threshold to help protect against brute-force attacks.
3. Install Microsoft System Center Endpoint Protection, Malwarebytes, Avast (free for Windows) and/or Sophos (free for Mac OSX) for additional protection.
4. Ensure that Windows Defender and Avast (Windows) or Sophos (Mac) are automatically scanning the PC and receiving updated threat definitions (set it up to scan every day, in the middle of the night).
5. Make sure that the firewall is enabled.
6. Back up your data. It is important to implement automated off-site backups in case of fire/flood/theft (and there is a chance that directly connected external drives could also be compromised in case of ransomware infection). Backblaze

can be used for off-site backup, with automated backup as well as 30-day rollback on backups. There are also other similar services with similar pricing (e.g. [Crashplan](#)), and [UC Backup](#).

7. Report any malware issues promptly to the cybersecurity superusers as well as security@berkeley.edu.

USB drives

USB drives are a primary vector for malware. We need to practice stringent security hygiene with all of our USB flash and hard drives.

1. Where possible, avoid use of USB drives (use cloud share tools to transfer files).
2. Regularly scan your USB drives with antimalware software (particularly after using any computers in shared facilities, and at least once a week during regular use). Please scan your USB **before** opening or transferring files. This will not only protect vulnerable lab PCs but also your personal files, data, and information.
3. If using USB drives with computers that are not connected to the internet and/or running unsupported Windows (XP, Vista, or older than these, as of June 2018), scan your USB drive **both before and after use** with the vulnerable machine to avoid spreading malware. This includes several shared lab computers and all shared facility computers.
4. Report any malware found on your USB drive to the cybersecurity superusers, along with a record if possible of the PCs to which you recently connected.

Use of lab PCs

1. Be careful about websites you access, emails you open, and files you download.
2. See something? Say something! Read all dialogue boxes and report any virus scan or other issues to the cybersecurity superusers.
3. If using USB drives with computers that are not connected to the internet and/or running unsupported Windows (XP, Vista, or older, as of June 2018), scan your USB drive **both before and after use** with the vulnerable machine to avoid spreading malware.

Remote access

Note that on computers with remote access enabled, we have initiated a lockout policy for enhanced security. Take care with typing passwords on these PCs to minimize disruption. Remote access should **only be enabled when necessary** and should only be enabled by the cybersecurity superusers, so discuss with them if you propose remote access should be enabled on any PC.

Superusers of equipment connected to PCs

All superusers are responsible for basic cybersecurity hygiene on the PCs connected to their equipment. This involves making sure that the PCs are as up-to-date as possible and regularly scanned for malware, and verifying that the [computer inventory](#) is current and complete.

First, determine if the PC is running Windows that is [currently supported by Microsoft](#). Then follow the instructions below, depending on whether the Windows version still receives security updates.

Supported Windows (7, 8, and 10, as of June 2018)

1. Make sure that the PC has internet access so that it can receive necessary security updates and threat definitions. Prompt security updates are our best protection against vulnerabilities.
2. Install additional antivirus protection.
3. Ensure that all antivirus software are automatically scanning the PC (set it up to scan every day, in the middle of the night).
4. Make sure that the firewall is enabled.
5. Ensure automatic updates are enabled. If automatic updates are absolutely not possible (e.g. we regularly need to run things overnight on that PC, and cannot handle weekly or biweekly restarts for security updates), disable automatic updates and schedule a time weekly when you will manually check for and install the updates and restart the PC. You are responsible for making sure that this PC is kept up to date. Add PC updates as an event to both the equipment calendar (so others schedule their work accordingly) and to your calendar (so you remember to do this crucial step). Windows updates are released weekly on Tuesday nights.
6. Check the PC every week, looking at the antivirus scan logs and reporting any issues to the cybersecurity superusers.
7. Ensure that you have enabled computer screen lock to ensure no unattended sessions, and set a lock-out threshold to help protect against brute-force attacks.

Unsupported Windows (XP, Vista, older as of June 2018)

All computers running unsupported Windows are a security risk as they do not have access to security updates. We need to work to minimize the number of these kinds of systems that we have as well as mitigate risks associated with their presence.

1. Ensure the PC is not connected to the internet. Deactivate Ethernet connection, WiFi adapters, remote access, and any other ports that could enable internet connection. Remove all unnecessary wiring.
2. Verify that the computer inventory is complete (listed hardware/software incompatibility is preventing us from updating Windows). If not, contact the previous superusers and the equipment manufacturer for all connected hardware to determine whether Windows can be updated.
3. If Windows can be updated, work with the cybersecurity superusers to bring it up to date.
4. If Windows cannot be updated, ensure that the most recent service pack ([Windows 7 and later, XP](#)) and patches for that Windows version are installed. If they aren't, work with the cybersecurity superusers to install them (we may temporarily connect the PC to the internet).

5. If possible, install antivirus protection software and Sophos virus removal tool (via a known clean USB) on the PC.
6. Set up a daily virus scan and check the results once a week, reporting any issues to the cybersecurity superusers.
7. When training users, stress the importance of scanning USB drives before and after use with the at-risk machine.

Cybersecurity superusers

This section describes the cybersecurity superuser duties and recommendations for setting up remote access.

Superuser duties

1. Ensure all lab computers are running up-to-date antimalware.
2. Train all lab members in best practices outlined above.
3. Train equipment superusers on the use of antimalware and Windows updates as outlined above.
4. Assist group members with cybersecurity questions.
5. Keep this document and best practices up-to-date.
6. Set up security settings on all lab PCs.
7. Work with the data storage superusers to ensure that all computers are backed up (automated, off-site backup for maximum reliability).
8. Work with equipment superusers to ensure that PCs are up-to-date.
9. Initiate review of cybersecurity best practices provided by the information security office to ensure that our best practices are up to date.
10. When threats are detected:
 - a. If necessary, report the threat to the information security office and to federal governmental agencies.
 - b. Assist in the [removal of the threat](#) from the device on which it was found (including a complete wipe and reinstall if needed).
 - c. Assist in tracking from where the threat originated and removing it from there as well (for USB drives being infected from other lab or shared facility PCs).
 - d. Quickly report the threat to the group, with necessary next steps (email).
 - e. Summarize the threat and learning points for reporting to our group.
 - f. Make any necessary changes to improve the set of best practices and recommendations in our group's cybersecurity policies.


Setting up remote access

Remote access should **only be enabled when necessary**. Remote access will always make computers more vulnerable to attack, but this risk may be worthwhile in cases with significant benefit in work efficiency (e.g. check and restart long simulations from home, or check on long experiments with monitoring). Remote access should only be enabled by the cybersecurity superusers, so discuss with them if you propose enabling remote access on any PC.

Cybersecurity/IT superusers should review the university's [security recommendations](#) for Windows Remote Desktop. This article should be periodically read by the superusers, and the recommendations below should be updated as needed.

Appendix 17: Cell line authentication and mycoplasma testing certificates

2016 cell line authentication and mycoplasma testing



University of California, Berkeley
Cell Culture Facility

Certificate of Analysis
Cell Line Short Tandem Repeat (STR) Report
Sample name: 2-U251
Date received: 9/2/16
Client: Elaine Su

LOCUS	ALLELE SIZE
TPOX	8,9
D5S818	11,12
D13S325T	10,11
D7S820	10,11
D16S539	12
CSP1PO	11,12
AMEL	15,Y
vWA	16,18
TPDX	8

Results indicate the allele(s) detected at each locus tested. Each allele represents the number of short tandem repeats present at that locus. Generally, a DNA profile uniquely identifies an individual cell line. However, some cell lines may exhibit genomic instability over time leading to slight changes in the DNA profile.

IDENTIFIED CELL TYPE(S)	PERCENT MATCH
U-251 MG	100%


Based on STR analysis, the results indicate a high probability (80% or higher) match with the U-251 MG cell line. Multiple cell lines with 80% match are considered to be derived from common ancestry. Electropherograms are available upon request.

Mycoplasma test: NEGATIVE 9/2/16 Cells were fixed with methanol and stained with Hoechst nuclear stain to visualize nuclei. Small nuclei present in the cellular membrane indicate mycoplasma infection.

Disclaimer: While every reasonable effort has been made to assure the accuracy of these data, no warranty, express or implied, is made by this facility.



Alison N. Killilea, Ph.D. | Bioscience Facility Manager



University of California, Berkeley
Cell Culture Facility

Certificate of Analysis
Cell Line Short Tandem Repeat (STR) Report
Sample name: 1-MCF-7
Date received: 9/2/16
Client: Elaine Su

LOCUS	ALLELE SIZE
TPOX	8
D5S818	11,12
D13S325T	11
D7S820	9,9
D16S539	11,12
CSP1PO	10
AMEL	X
vWA	14,15
TPDX	9,12

Results indicate the allele(s) detected at each locus tested. Each allele represents the number of short tandem repeats present at that locus. Generally, a DNA profile uniquely identifies an individual cell line. However, some cell lines may exhibit genomic instability over time leading to slight changes in the DNA profile.

IDENTIFIED CELL TYPE(S)	PERCENT MATCH
MCF-7	100%


Based on STR analysis, the results indicate a high probability (80% or higher) match with the MCF-7 cell line. Multiple cell lines with 80% match are considered to be derived from common ancestry. Electropherograms are available upon request.

Mycoplasma test: NEGATIVE 9/2/16 Cells were fixed with methanol and stained with Hoechst nuclear stain to visualize nuclei. Small nuclei present in the cellular membrane indicate mycoplasma infection.

Disclaimer: While every reasonable effort has been made to assure the accuracy of these data, no warranty, express or implied, is made by this facility.



Alison N. Killilea, Ph.D. | Bioscience Facility Manager



University of California, Berkeley
Cell Culture Facility

Certificate of Analysis
Cell Line Short Tandem Repeat (STR) Report
Sample name: 11-CHO parent
12-CHO p 95
13-CHO p185
Date received: 9/2/16
Client: Elaine Su

Mycoplasma test: NEGATIVE 9/2/16 Cells were fixed with methanol and stained with Hoechst nuclear stain to visualize nuclei. Small nuclei present in the cellular membrane indicate mycoplasma infection.

Disclaimer: While every reasonable effort has been made to assure the accuracy of these data, no warranty, express or implied, is made by this facility.



Alison N. Killilea, Ph.D. | Bioscience Facility Manager

2017 mycoplasma testing



University of California, Berkeley
Cell Culture Facility

Certificate of Analysis

Mycoplasma Testing

Sample names: U-251-GFP, BJ fibroblasts, BT474, HEK 293, MCF-7, MDA-MB-231, MDA-MB-231 GFP Actin, MDA-MB-231 GFP Actin + sh HSF1B
Date received: 9/22/2017
Client: Alisha Geldert

Mycoplasma test: NEGATIVE 9/22/17: Cells were fixed with methanol and stained with Hoechst nuclear stain to visualize nuclei. Small nuclei present in the cellular membrane indicate mycoplasma infection.

Disclaimer: While every reasonable effort has been made to assure the accuracy of these data, no warranty, express or implied, is made by this facility.

Alisha Killilea

Alison N. Killilea, Ph.D. | Bioscience Facility Manager

2018 mycoplasma testing



University of California, Berkeley
Cell Culture Facility

Certificate of Analysis

Mycoplasma Testing

Sample names: U-205 + Halotag +CTCF C32, U-251 + TurboGFP, HeLa, MCF-7, MDA-MB-231, MCF-7 +GFP, BT474, CHO-p185HER2, CHO-p110HER2, CHO-p95HER2, BJ fibroblasts, MDA-MB-231 GFP Actin
Date tested: 10/30/18
Client: Alisha Geldert

Mycoplasma test: NEGATIVE 10/30/18: Cells were fixed with methanol and stained with Hoechst nuclear stain to visualize nuclei. Small nuclei present in the cellular membrane indicate mycoplasma infection.

Disclaimer: While every reasonable effort has been made to assure the accuracy of these data, no warranty, express or implied, is made by this facility.

Alisha Killilea

Alison N. Killilea, Ph.D. | Bioscience Facility Manager

2019 cell line authentication and mycoplasma testing



University of California, Berkeley
Cell Culture Facility

Certificate of Analysis

Cell Line Short Tandem Repeat (STR) Report

Sample name: U-251 + GFP
Date received: 10/30/19
Client: Alisha Geldert-UCB

LOCUS	ALLELE SIZE
TH01	9,3
D5S818	11,12
D18S51P	10,11
D7S820	10,12
D16S539	12
CSF1PO	11,12
AMEL	X,Y
vWA	16,18
TPDX	8

Results indicate the allele(s) detected at each locus tested. Each allele represents the number of short tandem repeats present at that locus. Generally, a DNA profile uniquely identifies an individual cell line. However, some cell lines may exhibit genomic instability over time leading to slight changes in the DNA profile.

IDENTIFIED CELL TYPE(S)	PERCENT MATCH
U-251	100%

Based on STR analysis, the results indicate a high probability (80% or higher) match with the cell line #1 listed. Multiple cell lines with ≥80% match are considered to be derived from common ancestry. Electropherograms are available upon request.

Disclaimer: While every reasonable effort has been made to assure the accuracy of these data, no warranty, express or implied, is made by this facility.

Alisha Killilea

Alison N. Killilea, Ph.D. | Bioscience Facility Manager



University of California, Berkeley
Cell Culture Facility

Certificate of Analysis

Cell Line Short Tandem Repeat (STR) Report

Sample name: MCF-7 GFP
Date received: 10/30/19
Client: Alisha Geldert-UCB

LOCUS	ALLELE SIZE
TH01	6
D5S818	12
D18S51P	11
D7S820	8,9
D16S539	11,12
CSF1PO	10
AMEL	X
vWA	14,15
TPDX	9,12

Results indicate the allele(s) detected at each locus tested. Each allele represents the number of short tandem repeats present at that locus. Generally, a DNA profile uniquely identifies an individual cell line. However, some cell lines may exhibit genomic instability over time leading to slight changes in the DNA profile.

IDENTIFIED CELL TYPE(S)	PERCENT MATCH
MCF-7	97%

Based on STR analysis, the results indicate a high probability (80% or higher) match with the cell line #1 listed. Multiple cell lines with ≥80% match are considered to be derived from common ancestry. Electropherograms are available upon request.

Disclaimer: While every reasonable effort has been made to assure the accuracy of these data, no warranty, express or implied, is made by this facility.

Alisha Killilea

Alison N. Killilea, Ph.D. | Bioscience Facility Manager



University of California, Berkeley
Cell Culture Facility

Certificate of Analysis

Mycoplasma Testing

Sample names: BT474, SK-BR-3, MCF-7 naive, MDA-MB-231, HEK 293, CHO-p185, CHO-p110, CHO-p95, U-251 + TurboGFP, MDA-MB-231 GFP Actin, MDA-MB-231 - sh scramble GFP Actin, MDA-MB-231 GFP Actin+HSF1 OE, MDA-MB-231 GFP Actin +RFP lenti, MDA-MB-231 GFP Actin+sh HSF1B, MDA-MB-231 GFP control, BJ fibroblasts, U251 naive, HeLa
Date tested: 10/31/19
Client: Alisha Geldert

Mycoplasma test: NEGATIVE 10/31/19: Cells were fixed with methanol and stained with Hoechst nuclear stain to visualize nuclei. Small nuclei present in the cellular membrane indicate mycoplasma infection.

Disclaimer: While every reasonable effort has been made to assure the accuracy of these data, no warranty, express or implied, is made by this facility.

Alisha Killilea

Alison N. Killilea, Ph.D. | Bioscience Facility Manager